Doctoral Dissertation

Fast localization of coalescing binaries with gravitational wave detectors and low frequency vibration isolation for KAGRA

A Dissertation Submitted for the Degree of Doctor of Philosophy

May 2020

Department of Astronomy, Graduate School of Science, The University of Tokyo

Yoshinori Fujii

Abstract

Gravitational waves (GWs) are ripple of spacetime. They are generated by accelerated objects and propagate at the speed of light by stretching/shrinking the space. The direct detection of a GW signal has been achieved for the first time in 2015. This event was due to the merger of two black holes at a distance of the order of 1 billion light years. This detection opened the field of GW astronomy. Two years later, in 2017, the detection of a GW signal from a binary neutron star merger event in coincidence with an electromangetic (EM) transient has been also achieved. This event opened a new era of multi-messenger astronomy.

In this era, in order to expand the multi-messenger astronomy, GW and EM transient observations play an important role. To this purpose it is demanded to effectively conduct the EM follow up as rapidly as possible after the event is detected. From the point of view of EM follow up observation, a fast and precise source localization by GW detectors is quite important. Currently a network made by several GW detectors is being built around the world, with detectors in the US (LIGO), in Europe (Virgo), in Japan (KAGRA) and in India (LIGO-India). This network will drastically improve the sky coverage, the sky localization performance and the identification of the source parameters.

In the real life, however, we are now facing a heterogeneous configuration with GW detectors at different level of development having different sensitivities. Likely, this will continue to be the case with more detectors coming on line in the future. At present, there are two higher sensitivity detectors (Advanced LIGO), a middle sensitive one (Advanced Virgo), and KAGRA which is currently being commissioned. This implies that we have to consider a scheme which enables to make effective use of the less sensitive detector information. In such configuration it is considered that we will have better fast localization performance by analyzing the detector signals hierarchically. This hierarchical analysis approach is important to deal with the heterogeneous network.

In this thesis, we quantitatively simulate the expected fast localization performance by that approach.

In addition to the fast localization aspect, having higher network duty cycle is also important for the EM follow up observation. For this purpose, operating a fourth robust interferometer KAGRA is of paramount importance. Such operation is also important to minimize the chances to miss detectable events. In all the ground-based GW detectors, the mirrors are suspended in order to realize a situation where the test masses are in free-fall condition. This is necessary also

to attenuate the transmission of vibrations from the ground to the mirror. These suspensions have mechanical resonances that, if are not properly damped, can produce large mirror motion at low frequencies. Thus, it is important to damp the mechanical resonances of the suspensions and to freeze the mirrors in order to start GW observation. Consequently, for more robust interferometer operation, we need a system that enables to damp the mechanical resonances rapidly and to reduce the mirror motion amplitude. Such a system is realized by active controls using sensors and actuators implemented on the suspension system.

The second part of this thesis is focused on the control system for the suspension system in the fourth detector KAGRA. The system has been built and it has allowed to proceed with the KAGRA interferometer alignment and locking. This implemented control system allows to start interferometric operation in KAGRA.

In the following, a more detailed explanation of these works is given.

In the first part of this thesis, we investigate the expected performance regarding fast sky localization of coalescing binaries with a network of three or four GW detectors having heterogeneous sensitivities, such as the LIGO-Virgo, LIGO-KAGRA and LIGO-Virgo-KAGRA network. This work is done in collaboration with members of the LIGO-Virgo collaboration. A hierarchical approach can be used in order to make an effective use of information from the least sensitive detector. In this approach, the presence of an event seen in coincidence in the two more sensitive detectors triggers a focused search in the data of the third (and fourth), less sensitive, detector(s) with a lower SNR threshold.

We show the expected fast localization performance when a hierarchical search is implemented into a GW-EM follow-up pipeline. The GW-EM follow-up pipeline has mainly two parts. One is a coalescing binary search algorithm using matched filtering technique. In this thesis work we use one of the algorithms used for low-latency search called multi-band template analysis (MBTA). The other one is a software able to reconstruct sky maps from the outputs of the search algorithms such as MBTA. This second part is called Bayestar.

We confirm that the hierarchical search improves both the fast localization accuracy and precision compared to those achieved by a double coincidence search with the two LIGO detectors alone. The hierarchical network effectively improves the localization accuracy and precision when threshold SNR for the lower sensitivity detector is set to around 3.5 provided that the BNS range of that the detector is greater than 20% of the more sensitive detectors in the case of LIGO-Virgo network. We find that as the sensitivity of Virgo approaches half of the LIGO one, the localization performance can be improved by about a factor of 7 compared to LIGO network.

In the case of LIGO-KAGRA network, we find a sky localization improvement when the relative sensitivity of KAGRA becomes greater than 28% of the more sensitive detectors. We find that as the sensitivity of KAGRA approaches half of the LIGO one, the localization performance can be improved by about a factor of 3.5 compared to LIGO network.

In the case of the four detector network (LIGO-Virgo-KAGRA), the localization performance will be improved when threshold SNR for the lowest sensitivity detector is set to around 3.5 provided that the BNS range of that the detector is greater than 28% of most sensitive detectors. we find that as the sensitivity of KAGRA approaches half of the LIGO one (same as Virgo one), the accuracy and precision of the localization can be improved by about a factor of 2 and 2.5 respectively compared to LIGO-Virgo hierarchical network. This result is obtained on the condition that the sensitivity of the middle sensitivity detector (Virgo) is half of the LIGO one.

Consequently, we conclude that once the sensitivity of the third or fourth detector reaches the required one, the search with this hierarchical approach will be quite useful when adding new, less sensitive detectors to the network, as they are undergoing commissioning.

In the second part of this thesis, a suspension control system for KAGRA detector has been constructed. KAGRA is now being commissioned and is planned to join the network in second half of the observation by LIGO-Virgo network called $O3$, as the fourth detector. We construct an active control system for the KAGRA suspensions, especially for the suspension system which holds the arm cavity mirrors, called Type-A suspension.

The Type-A suspension is 13.5 m in height and has a nine-stage pendulum. The lower four stages are located inside a cryostat and are operated at a cryogenic temperature in order to reduce thermal noise. For cooling, the lower four stages are connected to each other with high purity aluminum wires, called heat links. Through the heat links and their specific vibration isolation systems, the absorbed heat on the mirror is extracted to the cryostat structure. In a nutshell we use quite complex suspensions in order to obtain GW signals.

The target of this thesis work is to implement an active control system for the Type-A suspensions that achieves the performances required for acquiring the interferometer lock. This is quite important to start interferometric operation. Since the suspensions are the hardware to operate the interferometer, we cannot start the operation without controlling the complex suspensions.

In this thesis work, we have design the control filters using feedback and feedforward control technique in a simulation. We then implement the control system to one of the actual Type-A suspensions. Along with the implementation of the control system, we conduct the following measurements for the evaluation of the KAGRA Type-A suspension and of its control system:

1. suspension mechanical response,

2. active control performance for the suspension mechanical resonances damping,

3. active control performance for the mirror motion suppression required to help the interferometer lock acquisition.

The first measurement shows that the assembled Type-A suspension has the expected characteristics of the pendulum. It is also confirmed that the suspension response has no problems for the purpose of constructing the control system to allow the interferometer locking. It is found that some unexpected resonances related to the heat link system are observed. This measurement implies that we have to include the heat link system in the model of the suspension mechanics to more precisely model the system. This model improvement work will be done as the future upgrade.

From the second measurement, we confirm that the installed damping control system satisfies its requirement for the lock-recovery mode.

The third measurement demonstrates the effectiveness of a feed-forward system using seismometer on the ground to suppress the mirror residual motion. This system satisfies the requirement to align and to lock the interferometer. Overall, the local control systems constructed for Type-A suspensions within thesis work allows the interferometer locking of KAGRA. The implemented control system allows to start the interferometric operation.

In conclusion, the work described in this thesis shows the importance of adding KAGRA to the present GW detector network, even in the context of a heterogeneous network of detectors with different sensitivities, and provides a contribution to the commissioning of KAGRA towards the joining of the network.

Acknowledgements

I sincerely thank all of you who have shared the time with me in these five and a half years.

to him.

I also deeply appreciate Masayuki Nakano, Takahiro Yamamoto, and Takaaki Yokozawa, who led the main commissioning work at KAGRA mine. They indeed continuously worked on the commissioning, in terms of the interferometer locking, maintenance of all the digital system infrastructures, and the noise hunting and its debugging. They provide me finely aligned interferometer, and also gave me many chances to break the alignment for my experiment at the upper stages such as the IP-stage of the Type-A. Thanks to them, I could smoothly forget that one day consisted of 24 hours at the site.

The team TAMA/NAOJ, Matteo Leonardi, Eleonora Capocasa, Yuhang Zhao, Naoki Aritomi, Manuel Marchiò, and Simon Zeidler, always made me relaxed and put me away from the highly pressured mind.

The administrative office members in NAOJ, Mihoko Kondo, Mizuho Yoshizumi, Mikiko Harada, Megumi Ohyama, and Eri Sakamoto indeed helped/supported my life a lot. With their kind help, I could make schedule change going to/coming back to Mitaka/Kamioka KAGRA site so easily.

I thank Kyouichi Takayama, Mihoko Okinaka, Yukari Maeda, Yayoi Hara and Miho Iwamatsu, who are the administrative office members in Kamioka KAGRA site. Without their continuous help, I could not spend my life at the site.

Indeed I have countless people who have helped me to have bright lives in these five and a half years. I cannot appreciate all of them more. Thanks to all such people, I could enjoy my life and the experience in these years.

Finally, I sincerely appreciate my family; my father, my mother, my sister, and my sister's family. They allowed me to concentrate on the work in the field of research as whatever I like. Sometimes my nephew kicked away all my worries literally. I truly thank all of them for the thoughtful support at home.

Table of Contents

Abbreviations

Astrophysics

EM   Electro-Magnetic (wave)

BNS   Binary Neutron Star

BBH   Binary Black Hole

BH   Black Hole

CBC   Compact Binary Coalescence

GR   General Relativity

GW   Gravitational Wave

NS   Neutron Star

SNe   Supernovae

Detectors

LIGO   Laser Interferometric Gravitational wave Observatory

Virgo   Virgo detector

KAGRA   KAGRA detector

H, H1   LIGO Hanford detector

L, L1   LIGO Livingston detector

V, V1   Virgo detector

K, K1   KAGRA detector

Pipelines

GstLAL   low-latency CBC search pipeline [1]

pyCBC Live low-latency CBC search pipeline [2]

MBTA   low-latency CBC search pipeline [3]

Bayestar   Bayesian rapid localization algorithm [4]

Interferoemter

IMC   Input Mode Cleaner

PRM   Power Recycling Mirror

PR2   Power Recycling Mirror 2

PR3   Power Recycling Mirror 3

SRM   Signal Recycling Mirror

SR2   Signal Recycling Mirror 2

SR3   Signal Recycling Mirror 3

BS   Beam Splitter

TM   Test Mass

ITMX   Input Test Mass X

ITMY   Input Test Mass Y

ETMX   End Test Mass X

ETMY   End Test Mass Y

FPMI   Fabry-Perot Michelson Interferometer

DARM   Differential Arm

PDH   Pound-Drever-Hall (technique)

KAGRA suspensions

SAS   Seismic Attenuation System

VIS   Vibration Isolation System

IP   Inverted Pendulum

GAS   Geometric Anti-Spring

F0   Top GAS filter

F1, F2, F3, F4, SF Standard GAS filter

BF   Bottom GAS filter

Payload   The lower suspension part

PF   Platform

MN   Marionette

RMN   Recoil Marionette

IM   Intermediate Mass

IRM   Intermediate Recoil Mass

RM   Recoil Mass

HLVIS   Heat Link Vibration Isolation System

L   Longitudinal

T   Transverse

V   Vertical

R   Roll

P   Pitch

Y   Yaw

DoF   Degree of Freedom

Sensors and actuators for KAGRA suspensions

LVDT	Linear Variable Differential Transducer
GEO	Geophone L-4C
ACC	Accelerometer
Oplev	Optical lever
Length-oplev	Length sensing optical lever
PD	Photo Diode
QPD	Quadrant Photo Diode
SLD	Super Luminescent Diode
PS	(Reflective) Photo Sensor

Others

SNR	Signal-to-Noise ratio
ASD	Amplitude Spectral Density
PSD	Power Spectral Density
RMS	Root Mean Square
Q	Quality factor
ADC	Analogue-to-Digital Converter
DAC	Digital-to-Analogue Converter
IPsc	Sensor correction system at IP-stage

Chapter 1

Introduction

The existence of gravitational waves (GWs) was predicted by A. Einstein in 1916 according to his theory of general relativity [5]. 100 years after the prediction, a GW signal from the coalescence of two black holes (BHs) was detected for the first time in 2015 by the Laser Interferometric Gravitational-wave Observatory (LIGO) in the U.S. [6]. In 2017, the two detectors in the U.S. (LIGO) and one detector in Europe (Virgo) became online. Soon later, in 2017, the first detection of a GW signal from the coalescence of two neutron stars by LIGO-Virgo network in coincidence with an electro-magnetic transient was achieved and this opened the era of multi-messenger astronomy [7]. In 2019, the commissioning of the fourth detector (KAGRA) has been started. In the coming years, the detector network by the four detectors will explore the universe.

General introduction is presented in this chapter. More details about this chapter can be found in [8]. The targets and outline of this thesis is also included.

More specifically, this chapter describes the background of detection of GWs and that of the current GW detectors. Section 1.1 summarizes the theoretical aspect of GWs. Section 1.2 introduces GW sources expected to be detected. Section 1.3 describes the interferometric detection method, which is used for the current GW detectors. Section 1.4 describes the optical configuration of the KAGRA detector, which is one of the current GW detectors in the world. This subsection provides information the KAGRA the suspension system, which is one of the main infrastructure. Section 1.5 describes the currently working GW detectors. These are also referred to as second generation detectors. Section 1.6 presents the targets and the outline of this thsis. This section includes clarification of my work within this thesis. Section 1.7 summarizes this chapter.

1.1 General relativity and Gravitational waves

1.1.1 Gravity in general relativity

In general relativity (GR), the Einstein field equation describes the relationship between the metric of spacetime and the energy-momentum density distribution

as:

$$R_{\mu\nu} - \frac{1}{2}g_{\mu\nu}R = \frac{8\pi G}{c^4}T_{\mu\nu}. \tag{1.1}$$

The variables in eq (1.1) are summarized as follows:

- $g_{\mu\nu}$: Metric tensor, which characterizes the geometry of spacetime. $g_{\mu\nu}$ is a dimensionless quantity and is defined as the inner product of basis vectors: $g_{\mu\nu} \equiv \boldsymbol{e}_\mu \cdot \boldsymbol{e}_\nu$.

- $T_{\mu\nu}$: Energy-momentum tensor, which includes the following quantities:
  T_{00}: Energy density,
  T_{i0}: ith element of momentum density,
  T_{0j}: jth element of energy flux,
  T_{ij}: Stress tensor in non-relativistic fluid dynamics $(i, j = 1, 2, 3)$.

- $R_{\mu\nu} \equiv R^\alpha{}_{\mu\alpha\nu}$: Ricci tensor, which is defined by
  $R^\mu{}_{\alpha\beta\gamma} \equiv \frac{\partial \Gamma^\mu_{\alpha\beta}}{\partial x^\gamma} - \frac{\partial \Gamma^\mu_{\alpha\gamma}}{\partial x^\beta} + \Gamma^\mu_{\lambda\gamma}\Gamma^\lambda_{\alpha\beta} - \Gamma^\mu_{\lambda\beta}\Gamma^\lambda_{\alpha\gamma}$,
  where $\Gamma^\mu_{\alpha\beta} \equiv g^{\mu\nu}\left(\frac{\partial g_{\beta\nu}}{\partial x^\alpha} + \frac{\partial g_{\alpha\nu}}{\partial x^\beta} - \frac{\partial g_{\alpha\beta}}{\partial x^\nu}\right)$.

- $R \equiv g^{\mu\nu}R_{\mu\nu}$: Scalar curvature (or Ricci scalar).

- G : Gravitational constant.

- c : Speed of light.

In the eq (1.1), the line element ds between two points x^μ and $x^\mu + dx^\mu$, which are infinitesimally separated from each other, is $ds^2 = (dx^\mu \boldsymbol{e}_\mu) \cdot (dx^\nu \boldsymbol{e}_\nu) = g_{\mu\nu}dx^\mu dx^\nu$, where $\boldsymbol{e}_\mu, \boldsymbol{e}_\nu$ denote the basis vectors of the coordinates. In spacetime which is given by the metric $g_{\mu\nu}$ as defined above, the motion of a free particle is explained by its geodesic equation:

$$\frac{\mathrm{d}^2 x^\alpha}{\mathrm{d}\tau^2} = \Gamma^\alpha_{\mu\nu}\left(\frac{\mathrm{d}x^\mu}{\mathrm{d}\tau}\right)\left(\frac{\mathrm{d}x^\nu}{\mathrm{d}\tau}\right), \tag{1.2}$$

where τ is an arbitrary parameter. By using these equations, GR concludes that what we observe as gravity is a curvature of spacetime. The characteristics of gravity are described by the metric in GR.

1.1.2 Theoretical expression of gravitational waves

The equation which describes the GWs are derived from the Einstein equation. First, we develop eq (1.1) assuming that the gravitational field is weak. Since spacetime is flat if there is no gravity, we assume that the spacetime is mostly flat in the weak gravitational field. In the weak field approximation, the metric $g_{\mu\nu}$

is given by the superposition of a metric of flat spacetime, that is, the Minkowski metric $\eta_{\mu\nu}$ and that of a small perturbation $h_{\mu\nu}$:

$$g_{\mu\nu} = \eta_{\mu\nu} + h_{\mu\nu} + \mathcal{O}(h^2), \qquad (\ |h_{\mu\nu}| \ll 1\ ). \tag{1.3}$$

In the equation above, $h_{\mu\nu}$ describes spacetime as a perturbation from Minkowski spacetime. The quantities in eq (1.3) satisfy the following relations:

$$h^{\mu}{}_{\nu} \equiv \eta^{\mu\lambda}h_{\lambda\nu}, \qquad h^{\mu\nu} \equiv \eta^{\mu\alpha}\eta^{\nu\beta}h_{\alpha\beta}, \qquad h \equiv \eta^{\mu\nu}h_{\mu\nu}. \tag{1.4}$$

By rearranging eq (1.1) using a formula $g^{\mu\nu} = \eta^{\mu\nu} - h^{\mu\nu} + \mathcal{O}(h^2)$, we obtain eq (1.5). Note that $g_{\mu\nu}$ denotes the inverse matrix of $g^{\mu\nu}$, and that terms in h^2 and higher are neglected in this calculation.

$$R_{\mu\nu} - \frac{1}{2}\eta_{\mu\nu}R \simeq \frac{8\pi G}{c^4}T_{\mu\nu}$$

$$\frac{1}{2}\left(-\Box h_{\mu\nu} + \partial_\nu\partial^\alpha h_{\mu\alpha} + \partial_\mu\partial^\alpha h_{\nu\alpha} - \partial_\mu\partial_\nu h - \eta_{\mu\nu}\partial^\alpha\partial^\beta h_{\alpha\beta} + \eta_{\mu\nu}\Box h\right) \simeq \frac{8\pi G}{c^4}T_{\mu\nu}, \tag{1.5}$$

where $\partial_\mu \equiv \frac{\partial}{\partial x^\mu}$, $\partial^\alpha = \eta^{\alpha\nu}\partial_\mu$ and $\Box \equiv \partial^\alpha\partial_\alpha = \eta^{\alpha\beta}\partial_\alpha\partial_\beta = -\frac{1}{c^2}\partial_t^2 + \nabla^2 = -\frac{1}{c^2}\frac{\partial^2}{\partial t^2} + \frac{\partial^2}{\partial x^2} + \frac{\partial^2}{\partial y^2} + \frac{\partial^2}{\partial z^2}$. Here, by applying a gauge transformation which satisfies the following condition:

$$\partial^\alpha h_{\mu\alpha} - \frac{1}{2}\partial_\mu h = 0, \tag{1.6}$$

we obtain the equation below:

$$\Box\left(h_{\mu\nu} - \frac{1}{2}\eta_{\mu\nu}h\right) = -\frac{16\pi G}{c^4}T_{\mu\nu}. \tag{1.7}$$

This equation is called the linearized Einstein equation. By using another tensor $\bar{h}_{\mu\nu} \equiv h_{\mu\nu} - \frac{1}{2}\eta_{\mu\nu}h$, eq (1.7) can be expressed:

$$\Box\bar{h}_{\mu\nu} = -\frac{16\pi G}{c^4}T_{\mu\nu}. \tag{1.8}$$

This $\bar{h}_{\mu\nu}$ is called trace-reversed tensor, and has the relationship below:

$$\bar{h} \equiv \bar{h}^{\mu}{}_{\mu} = -h^{\mu}{}_{\mu} = -h. \tag{1.9}$$

Note that $\bar{h}_{\mu\nu}$ satisfies $\partial_\mu\bar{h}^{\mu}{}_{\nu} = 0$, under the condition of eq (1.6). Eq (1.8) shows that $\bar{h}_{\mu\nu}$, which describes the small perturbation $h_{\mu\nu}$ from the Minkowski metric, satisfies a wave equation. Eq (1.8) also implies that $\bar{h}_{\mu\nu}$ propagates away from the source of the energy-momentum tensor $T_{\mu\nu}$ at the speed of light c. In vacuum condition $T_{\mu\nu} = 0$ ($= R_{\mu\nu} = R$), eq (1.8) becomes

$$\Box\bar{h}_{\mu\nu} = 0. \tag{1.10}$$

Consequently, the expression becomes similar to the wave equation for electromagnetic waves which propagate in vacuum. This ripple of the spacetime $\bar{h}_{\mu\nu}$, which propagates at the speed of light c, describes a GW.

1.1.3 Properties of gravitational wave

We briefly explore the properties of GWs which propagate in vacuum, by considering a monochromatic plane wave:

$$\bar{h}_{\mu\nu} \equiv a_{\mu\nu}e^{ik_\alpha x^\alpha} = a_{\mu\nu}\exp[i(\boldsymbol{k}\cdot\boldsymbol{r} - \omega t)]. \tag{1.11}$$

Here k^α denotes the wave vector $k^\alpha = (\omega/c, k^1, k^2, k^3)$, and $a_{\mu\nu}$ is the wave amplitude. $a_{\mu\nu}$ is described by a 4×4 matrix of constant numbers. Here, we can choose the following gauge conditions so that $a_{\mu\nu}$ (or $\bar{h}_{\mu\nu}$) holds only information about the GWs [8]:

$$\bar{h}_{0\nu} = 0, \tag{1.12}$$
$$\bar{h}^i{}_i = 0, \tag{1.13}$$
$$\partial_j \bar{h}^{ij} = 0. \tag{1.14}$$

The set of conditions eq (1.12) to (1.14) is called the transverse traceless (TT) gauge. In most cases, GWs are discussed assuming this gauge. Under this gauge, we obtain the following properties of GWs:

- Eq (1.12) says that the GW metric has only space element.

- Eq (1.13) says that the GW metric is traceless and thus the difference between $\bar{h}_{\mu\nu}$ and $h_{\mu\nu}$ vanishes ($\bar{h}_{\mu\nu}^{\mathrm{TT}} = h_{\mu\nu}^{\mathrm{TT}}$).

- Eq (1.14) says that GWs are transverse waves.

By inserting eq (1.11) into eq (1.14), we obtain the following equation:

$$k^j a_{ij} = k^j \bar{h}_{ij} = 0. \tag{1.15}$$

This equation describes that the wave vector is orthogonal to $\bar{h}_{ij}$. In addition, if we consider a plane GW which propagates along the z axis, i.e, $k^\mu = (k^0, k^1, k^2, k^3) = (\omega/c, 0, 0, \omega/c)$, $a_{\mu\nu}$ is given by the equation below:

$$a_{\mu\nu}^{\mathrm{TT}} = \begin{pmatrix} 0 & 0 & 0 & 0 \\ 0 & a_+ & a_\times & 0 \\ 0 & a_\times & -a_+ & 0 \\ 0 & 0 & 0 & 0 \end{pmatrix}. \tag{1.16}$$

To obtained eq (1.16), we have used the relationships $a_{12} = a_{21}$ and $a_{11} + a_{22} = 0$. This expression implies that GW have two degrees of freedom.

Polarization

The remaining two degrees of freedom correspond to the two possible wave polarizations. These two polarizations are called *plus* and *cross* mode according to the spacetime metric distortion that they produce. Let's suppose that a set

of free point masses are placed on the plane (x, y) along a circle of radius L. If a GW propagates this system along the z direction, then the line element ds^2 between the origin and one of the masses is given by:

$$
\begin{aligned}
ds^2 &= -(cdt)^2 + dl^2 \\
&= -(cdt)^2 + (1 + h_+)dx^2 + 2h_\times dxdy + (1 - h_+)dy^2. \quad (1.17)
\end{aligned}
$$

The space distance dl^2 becomes:

$$
dl^2 = (1 + h_+)dx^2 + 2h_\times dxdy + (1 - h_+)dy^2. \quad (1.18)
$$

In this condition, the infinitesimal distances between the origin and one of the masses, dx, dy vary as

$$
dl^2 \simeq dx'^2 + dy'^2 \quad (1.19)
$$

$$
\begin{pmatrix} dx' \\ dy' \end{pmatrix} = \begin{pmatrix} 1 + \frac{1}{2}h_+ & \frac{1}{2}h_\times \\ \frac{1}{2}h_\times & 1 - \frac{1}{2}h_+ \end{pmatrix} \begin{pmatrix} dx \\ dy \end{pmatrix}. \quad (1.20)
$$

Finally, if we use $(dx, dy) \equiv (L\cos\theta, L\sin\theta)$, the proper distance l is

- if $h_+ \neq 0, h_\times = 0$;
  according to $dl^2 = (1 + h_+)dx^2 + (1 - h_+)dy^2 \simeq L^2(1 + h_+ \cos 2\theta)$,

$$
l \simeq L \times \left(1 + \frac{1}{2}h_+ \cos 2\theta\right) \quad : \quad + \text{ mode}, \quad (1.21)
$$

- if $h_+ = 0, h_\times \neq 0$;
  according to $dl^2 = dx^2 + dy^2 + 2h_\times dxdy \simeq L^2(1 + h_\times \sin 2\theta)$,

$$
l \simeq L \times \left(1 + \frac{1}{2}h_\times \sin 2\theta\right) \quad : \quad \times \text{ mode}. \quad (1.22)
$$

By inserting $h_+ = a_+ \exp[i(kz - \omega t)]$, or $h_\times = a_\times \exp[i(kz - \omega t)]$ into these equations, the distance between the masses varies as shown in Figure 1.1.

Effect on free point mass

Here, we consider how a GW affects free point masses. If we suppose that a free point mass initially at rest is exposed to a GW (in the TT gauge), its geodesic equation is expressed by:

$$
\frac{dU^\alpha}{d\tau} + \Gamma^\alpha{}_{\mu\nu}U^\mu U^\nu = 0, \quad (1.23)
$$

where U^α denotes the mass four-velocity. Then, due to $h^{TT}_{\beta 0} = 0$, the initial acceleration of the mass is always 0:

$$
\left(\frac{dU^\alpha}{d\tau}\right)_{\text{initial}} = -\Gamma^\alpha{}_{00} = \frac{1}{2}\eta^{\alpha\beta}(\partial_0 h_{\beta 0} + \partial_0 h_{0\beta} + \partial_\beta h_{00}) = 0. \quad (1.24)
$$

23
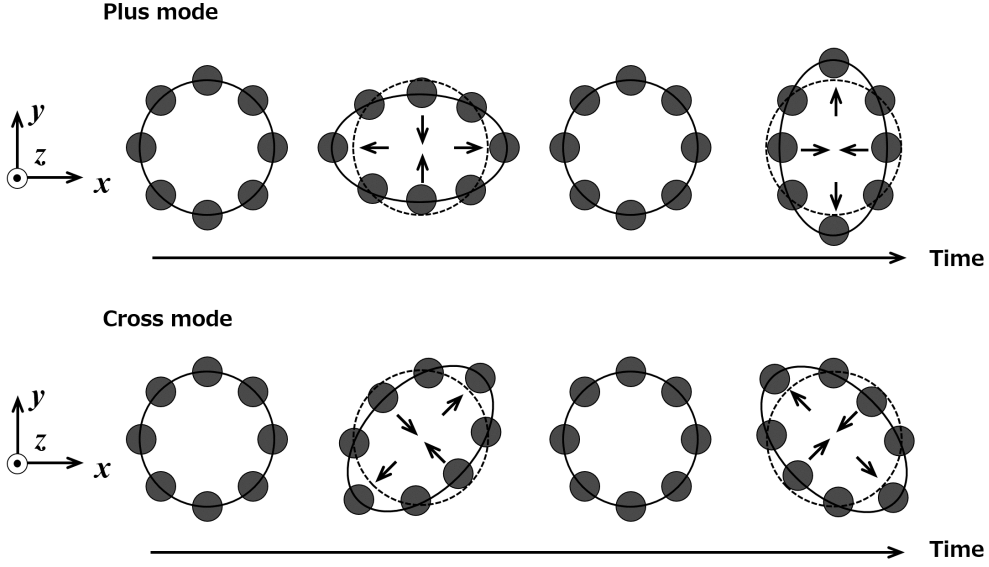
Figure 1.1: Polarizations of a GW. Black points denote free particles. If a GW incidents into $+z$ axis, the positions of free particles arrayed in circle are changed as shown in this figure.

This implies that if we choose the TT gauge, the spacetime metric basis changes so that the each mass stays at the original coordinate position.

Here we examine the behavior of the proper distance between two free point masses. If we place the masses at the origin $(0,0,0)$ and at $(L,0,0)$, the proper distance l is

$$
\begin{aligned}
l &= \int |ds^2|^{1/2} = \int |g_{\alpha\beta}dx^\alpha dx^\beta|^{1/2} \\
&= \int_0^L |g_{xx}|^{1/2}dx \simeq |g_{xx}(x=0)|^{1/2} \times L \\
&\simeq \{1 + \frac{1}{2}h_{xx}^{\mathrm{TT}}(x=0)\} \times L,
\end{aligned}
\tag{1.25}
$$

where $h_{xx}^{\mathrm{TT}}(x=0)$ is a non-zero term. Thus the eq(1.24) and eq(1.25) implies that neither of the two masses move but the proper distance l is changed by the GW. Consequently, we can sense the GWs by observing the proper distance(s) between two (or more) masses. In addition, according to eq(1.25), the length shift due to the GW injection ΔL is described by

$$
\frac{\Delta L}{L} = \frac{1}{2}h,
\tag{1.26}
$$

where h is the spatial distortion in the measurement direction.

1.1.4 Emission of gravitational wave

Here we take a look at the GW emissions according to the linearized Einstein equation. First, we transform eq (1.8) using a Green's function for the d'Alembert operator $G(x^\sigma - y^\sigma)$:

$$G(x^\sigma - y^\sigma) = -\frac{1}{4\pi|\boldsymbol{x}-\boldsymbol{y}|}\delta\left(|\boldsymbol{x}-\boldsymbol{y}| - (x^0 - y^0)\right)\theta(x^0 - y^0), \quad (1.27)$$

$$\Box G(x^\sigma - y^\sigma) = \delta^{(4)}(x^\sigma - y^\sigma) \quad (1.28)$$

where $\sigma = 0, 1, 2, 3$, $\delta(x)$ and $\theta(x)$ denote the Dirac's δ function and the step function respectively. We also assume that $\boldsymbol{x}$ and $\boldsymbol{y}$ are the observing location and the source position respectively. Hence the distance between $\boldsymbol{x}$ and $\boldsymbol{y}$ is $|\boldsymbol{x}-\boldsymbol{y}| = \{\delta_{ij}(x^i - y^i)(x^j - y^j)\}^{1/2}$. Note that $\theta(x^0 - y^0)$ is equal to 1 where $x^0 > y^0$ is satisfied, otherwise it equals to 0. With this settings, if we assume that the observation point is far enough away compared to the size of the source, that is, $r \equiv |\boldsymbol{x}| \gg |\boldsymbol{y}|$, $\bar{h}_{\mu\nu}$ is expressed as below (by using eq (1.8), eq (1.27) and eq (1.28)):

$$\begin{aligned}
\bar{h}_{\mu\nu}(t, \boldsymbol{x}) &= -\frac{16\pi G}{c^4}\int G(x^\sigma - y^\sigma)T_{\mu\nu}(y^\sigma)d^4y \\
&= \frac{4G}{c^4}\int \frac{T_{\mu\nu}(ct - |\boldsymbol{x}-\boldsymbol{y}|, \boldsymbol{y})}{|\boldsymbol{x}-\boldsymbol{y}|}d^3y, \\
&\simeq \frac{4G}{rc^4}\int T_{\mu\nu}(ct - r, \boldsymbol{y})d^3y. \quad (1.29)
\end{aligned}$$

Eq (1.29) can be simplified if we consider the local energy-momentum conservation, i.e., $\partial_\nu T^{\mu\nu} = 0$. Under this condition, we obtain the relationship $\partial_\alpha\partial_\beta(T^{\alpha\beta}x^\mu x^\nu) = 2T^{\mu\nu}$ (virial theorem) and the integration of eq (1.29) gives:

$$\int T^{ij}d^3y = \frac{1}{2c^2}\frac{d^2}{dt^2}\int T^{00}y^i y^j d^3y = \frac{1}{2}\frac{d^2}{dt^2}\int \rho y^i y^j d^3y. \quad (1.30)$$

The last term is the quadrupole mass distribution I_{ij}:

$$I_{ij} \equiv \int \rho y^i y^j d^3y, \quad (1.31)$$

Using eq (1.30) and eq (1.31), $\bar{h}_{ij}$ is given by the following equation:

$$\bar{h}_{ij}(t, \boldsymbol{x}) = \frac{2G}{rc^4}\ddot{I}_{ij}(ct - r). \quad (1.32)$$

In this expression, we find that the amplitude of a GW is proportional to the second derivative of the quadrupole with respect to time. If we consider the TT

gauge, eq (1.32) becomes

$$\bar{h}_{ij}^{\mathrm{TT}}(t, \boldsymbol{x}) = \frac{2G}{rc^4} \ddot{\mathcal{I}}_{ij}(ct - r), \tag{1.33}$$

$$\text{where} \quad \bar{h}_{ij}^{\mathrm{TT}} = \left(P_i^{\ k} P_j^{\ l} - \frac{1}{2} P_{ij} P^{kl} \right) \bar{h}_{kl}, \quad P_j^{\ i} \equiv \delta_j^{\ i} - n^i n_j , \quad n^i \equiv x^i/r,$$

$$\mathcal{I}_{ij} \equiv \int \rho \left(x^i x^j - \frac{1}{3} \delta_{ij} r^2 \right) d^3x.$$

In summary, GWs are generated when the quadrupole moment changes with time.

The amount of power emitted in GW's is given by [8]:

$$\frac{dE_{\mathrm{GW}}}{dt} = \frac{G}{5c^5} \langle \dddot{\mathcal{I}}^{ij} \dddot{\mathcal{I}}_{ij} \rangle. \tag{1.34}$$

If the source is characterized by mass M, size R, emitting time duration T and the velocity $v = R/T$, eq (1.34) can be approximated by:

$$\begin{aligned}
\frac{dE_{\mathrm{GW}}}{dt} &\sim \frac{G}{c^5} \left(\frac{MR^2}{T^3} \right)^2 \sim \frac{c^5}{G} \left(\frac{GM}{Rc^2} \right)^2 \left(\frac{v}{c} \right)^6 \\
&\sim 3.6 \times 10^{59} [\mathrm{erg/s}] \left(\frac{GM}{Rc^2} \right)^2 \left(\frac{v}{c} \right)^6 \\
&\sim 1.0 \times 10^{26} \times L_\odot \left(\frac{r_s}{2R} \right)^2 \left(\frac{v}{c} \right)^6,
\end{aligned} \tag{1.35}$$

where r_s denotes the source's Schwarzschild radius $2GM/c^2$. Moreover, if the virial theorem ($Mv^2 \sim GM^2/R$) is valid in this system, eq (1.35) becomes

$$\frac{dE_{\mathrm{GW}}}{dt} \sim 1.0 \times 10^{58} [\mathrm{erg/s}] \left(\frac{r_s}{R} \right)^5 \sim 2.6 \times 10^{25} \times L_\odot \left(\frac{r_s}{R} \right)^5. \tag{1.36}$$

More particularly, if we consider two equal-mass objects which follow Kepler's law ($2GM \sim (2\pi/T)^2 R^3$), the luminosity is expressed as:

$$\frac{dE_{\mathrm{GW}}}{dt} \sim 1.2 \times 10^5 \times L_\odot \left(\frac{1\mathrm{s}}{T} \right)^{10/3} \left(\frac{M}{M_\odot} \right)^{10/3}. \tag{1.37}$$

We then have the luminosity about 0.14 $L_\odot$ when these parameters are to set $T = 60$ s, $M = M_\odot$. This implies that detectable GWs do not come from events on the earth but from violent celestial events.

Approximate estimation: GW from coalescing binary

Here we consider a system composed by two point-particles orbiting one around the other according to Newton's gravitational low as shown in Figure 1.2. The masses are m_1 and m_2 respectively, and Ω is the angular frequency of the uniform circular motion. In this setting, we obtain the positions of the two particles in the center-of-mass system as:

$$\boldsymbol{r}_1 = \left(\frac{m_2}{M} \, a \, \cos\left(\Omega t + \Phi\right) \;,\; \frac{m_2}{M} \, a \, \sin\left(\Omega t + \Phi\right) \right), \tag{1.38}$$

$$\boldsymbol{r}_2 = \left(-\frac{m_1}{M} \, a \, \cos\left(\Omega t + \Phi\right) \;,\; -\frac{m_1}{M} \, a \, \sin\left(\Omega t + \Phi\right) \right). \tag{1.39}$$

In the above, the quantities are defined as follows: G is the gravitational constant, a is the distance between the two particles, and $M(= m_1 + m_2)$ is the total mass.
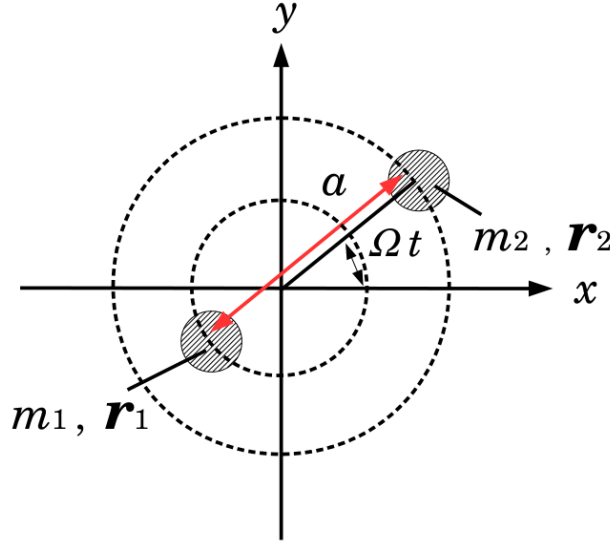
Figure 1.2: A binary system composed by two point-particles in a plane in uniform circular motion with the newton's gravitational force.

In this system, by following eq (1.32), the amplitudes of GW of the *plus*- and *cross*-polarizations h_+, $h_\times$ are described by:

$$h_+ = -\frac{2}{ra} \frac{Gm_1}{c^2} \frac{Gm_2}{c^2} \, \cos\left(2\Omega t_{\mathrm{ret}} - 2\phi + 2\Phi\right) \left(\cos^2\theta + 1\right), \tag{1.40}$$

$$h_\times = -\frac{2}{ra} \frac{Gm_1}{c^2} \frac{Gm_2}{c^2} \, \sin\left(2\Omega t_{\mathrm{ret}} - 2\phi + 2\Phi\right) \, 2\cos\theta, \tag{1.41}$$

where t_{ret} is defined by $t_{\mathrm{ret}} = t - r/c$. For this calculation, the GW amplitudes are calculated at a distance r from the source in the direction (θ, ϕ) respect to

the binary plane. In this configuration, the frequency of the GWs f_{GW} from this system is given by [8]:

$$f_{GW} = 2\Omega = \frac{1}{\pi}\sqrt{\frac{GM}{a^3}} = \frac{1}{\pi}\sqrt{\frac{G(m_1 + m_2)}{(R_1 + R_2)^3}}. \tag{1.42}$$

We then consider the time evolution. Since the energy of the binary system decreases due to the emission of GW, their orbital distance decreases as well, and this causes the frequency of the GWs to increase until the moment of coalescence. By assuming that GW takes away the energy of the system, we obtain the following differential equation for the orbital radius a:

$$\dot{a} = -\frac{64}{5}\frac{G^3 m_1 m_2 M}{c^5}\frac{1}{a^3} \equiv -K\frac{1}{a^3}. \tag{1.43}$$

In the calculation for eq (1.43), we use the following equation [8]:

$$\frac{dE_{GW}}{dt} = -\frac{32}{5}\frac{G^4 m_1^2 m_2^2 (m_1 + m_2)}{c^2 a^5}. \tag{1.44}$$

By choosing a condition where the orbital radius $a = 0$ at $t_{ret} = t_0$, the time evolution of a is written as:

$$a(t_{ret}) = [4K(t_0 - t_{ret})]^{1/4}. \tag{1.45}$$

From eq (1.42) and eq (1.43), the derivative of the frequency of GW is written as:

$$\dot{f}_{GW} = \frac{96}{5}\pi^{8/3}\left(\frac{GM_c}{c^3}\right)^{5/3} f_{GW}^{11/3}, \tag{1.46}$$

where $M_c = (m_1 m_2)^{3/5}/M^{1/5}$ is the so-called chirp mass. We then obtain the following equations for the time evolution of the frequency f_{GW} and of the strain amplitudes h_+, $h_\times$:

$$f_{GW}(\tau) \sim 135 \text{ Hz} \left(\frac{M_c}{1.2 M_\odot}\right)^{5/8}\left(\frac{\tau}{1\text{s}}\right)^{-3/8} \tag{1.47}$$

$$h(\tau) \sim 2.1 \times 10^{-23} \left(\frac{M_{chirp}}{1.2 M_\odot}\right)^{5/3}\left(\frac{r}{200\text{Mpc}}\right)^{-1}\left(\frac{\tau}{1\text{s}}\right)^{-1/4}, \tag{1.48}$$

where τ is $t_0 - t_{ret}$, the time to coalescence.

Figure 1.3 and 1.4 summarizes the time evolution of h_+, a and f_{GW}, assuming a binary system composed by two point masses at a distance of 100 Mpc whose masses are $1.4 M_\odot$. The condition $\theta = \pi/2$, $\phi = 0$ is also assumed. For this example, the GW amplitude becomes larger than 10^{-23} in strain, about 20 sec before the collision. According to eq (1.45) at that time, the separation between the two objects is about 250 km. As it will be in the in the following sections, this final phase of the coalescence is already observable with current sensitivities of the GW detectors.
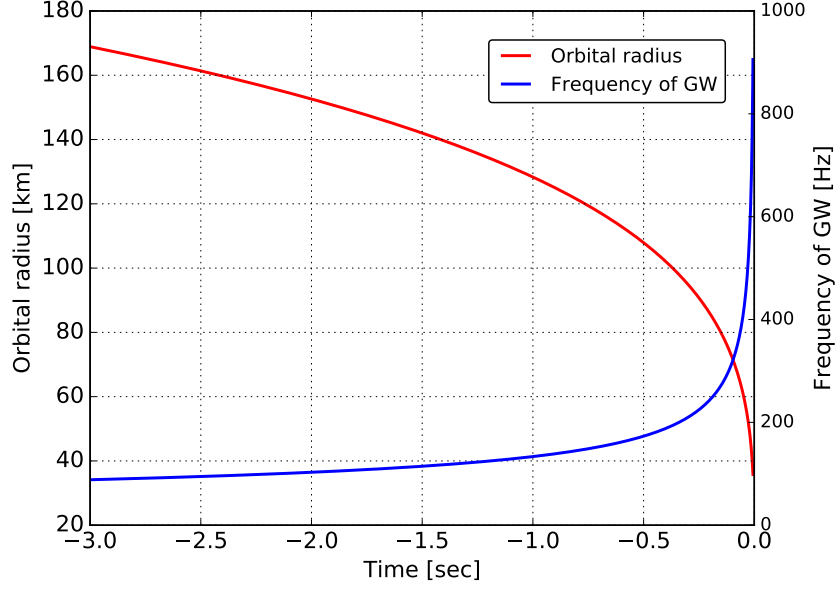
Figure 1.3: Final 3 sec time evolution of the orbital radius a and the frequency of GW f_{GW}, assuming a binary system composed by two neutron stars at 100 Mpc away whose masses are $1.4 M_{\odot}$.
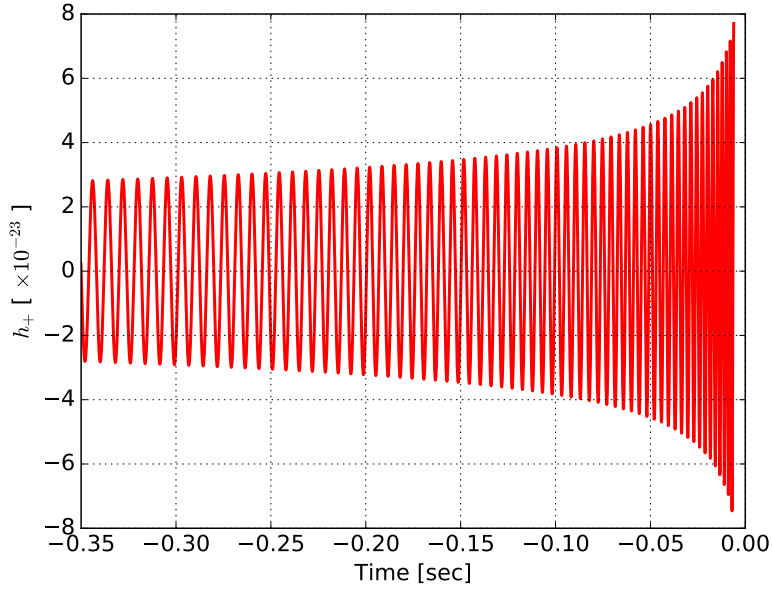
Figure 1.4: Final 0.35 sec time evolution of the strain amplitude of GW h_{+}, assuming a binary system composed by two neutron stars at 100 Mpc away whose masses are $1.4 M_{\odot}$. The final 0.35 sec is drawn.

1.2 Expected astrophysical sources

In this subsection, a few interesting sources and the astrophysical motivations are briefly described. More details can be found in [9].

1.2.1 Compact binary coalescence

As examined in section 1.1.4, the GWs from the compact binary coalescence (CBC) had been well studied and predicted [9]. The expected amplitude of GWs from CBC are quite small, however, CBC is the most interesting sources for the GW detection. The current GW detectors target to detect the GWs from CBC. Indeed the detected GW signals were from the merger of compact objects such as BNS, BBH and NS-BH [6, 10, 11].

By using the GW signals from CBC, we can test GR under strong gravity condition, for example by using polarization of GW [12]. In addition, we can measure Hubble constant [13] independently from usual methods using type Ia supernovae observation [14] and cosmic microwave background observation [15].

In addition, using the GW signals from BNS merger events, we can investigate the mechanism of the kilonovae and its nucleosynthesis [16] more precisely. The equation of state inside NSs can be also investigated using signals from BNS merger [17, 18].

1.2.2 Supernovae

Core-collapse supernovae (SNe) are considered as a promising source of GW's. The explosion will accelerates an huge amount of mass in a short period. Any asymmetrically in the collapse will generate GWs. The prediction of the actual wave forms emitted from supernovae is challenging. However, oowing to progress in the field of numerical relativity, the estimation of GWs from core-collapse SNe are making progress [19, 20]. If we achieve the detection of the GW signal from such SNe events, we can study the explosion mechanisms.

1.2.3 Stochastic background

A stochastic background of GWs is expected from numerous unresolved astrophysical sources such as white dwarf binaries, cosmological origins such as inflation, phase transition in the early universe and cosmic strings [21]. The amplitude and the frequency of the GWs with cosmological origins depends on the theory considered. Detection of stochastic backgrounds is generally conducted by investigating cross-correlation between observations by several detectors.

1.3 Detection with interferometer

This section describes how to detect the GWs with laser interferometric technique.

1.3.1 Basic principle

Given the deformation of the spacetime induced by GW shown in Figure 1.1, their detection can be done by monitoring the differential displacements of two masses in orthogonal directions. The simplest configuration consists in using a Michelson interferometer built with suspended mirrors as shown in Figure 1.5.

As the result of interference, a fraction of the beam goes to the photodiode (PD) and the remainder goes back to the laser source. The output beam intensity at the photodiode P_{out} is then given by

$$P_{\text{out}} = \frac{1}{2} P_0 \left(1 - \cos \delta \phi \right), \tag{1.49}$$

where P_0, λ, and $\delta\phi = 2\pi(L_x - L_y)/\lambda$ represent the incident laser power, the wavelength of the laser beam, and the phase difference between the two optical paths, respectively. Consequently, we can obtain information about the phase shift by monitoring the beam intensity on the photodiode.
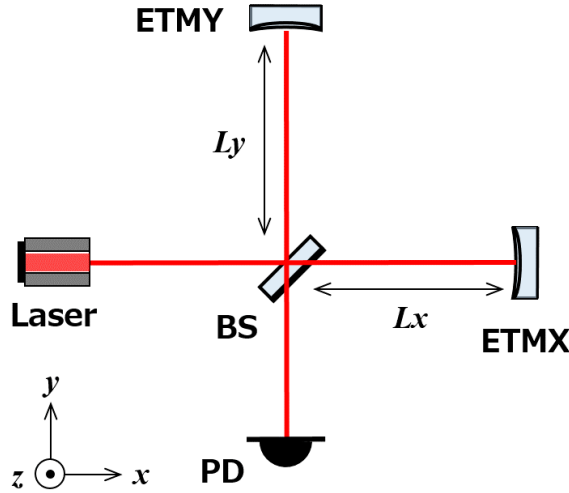
Figure 1.5: An optical configuration of a Michelson interferometer. ETMX(Y), BS, PD denote the end mirrors at X(Y) end, the beam splitter, and the photodetector, respectively.

We then calculate how the GW affects the phase difference between the two optical paths $\delta\phi$. We suppose that a GW which has plus polarization and amplitude $h(t)$ is injected along the $+z$ direction, i.e, perpendicular to the plane of the

interferometer. If we consider one of the photons travelling along the x direction, from eq (1.17), the line element ds^2 of the photon is given by

$$ds^2 = -(cdt)^2 + (1 + h_+(t))dx^2, \qquad (1.50)$$

Since $dy = dz = 0$. By considering that the photons travel on the light cone $ds^2 = 0$, we obtain:

$$\frac{dx}{dt} = \frac{c}{\sqrt{1 + h_+(t)}}, \qquad (1.51)$$

The round trip time Δt_x of a photon between the beam splitter and one end mirror is then given by:

$$\int_t^{t+\Delta t_x} \frac{dt'}{\sqrt{1 + h_+(t')}} = \frac{2L_x}{c}. \qquad (1.52)$$

If we use $(1 + h)^{-1/2} \sim (1 - h/2)$ by assuming $|h_+| \ll 1$, the above equation becomes

$$\Delta t_x = \frac{2L_x}{c} + \frac{1}{2} \int_t^{t+\Delta t_x} h_+(t')\, dt'. \qquad (1.53)$$

Since the first term is much greater than the second term ($|h_+| \ll 1$), on the right hand side, we can set the integral upper limit at $t + 2L_x/c$. Consequently, the phase shift ϕ_x due to Δt_x is given by

$$\phi_x = \frac{2\pi c}{\lambda} \left(\frac{2L_x}{c} + \frac{1}{2} \int_t^{t+2L_x/c} h_+(t')\, dt' \right), \qquad (1.54)$$

where λ is the wavelength of the laser. In the same way, the phase shift ϕ_y along the y-direction:

$$\phi_2 = \frac{2\pi c}{\lambda} \left(\frac{2L_y}{c} - \frac{1}{2} \int_t^{t+2L_y/c} h_+(t')\, dt' \right). \qquad (1.55)$$

By using ϕ_x and ϕ_y, the phase difference $\Delta \phi = \phi_x - \phi_y$ of the two optical paths is

$$\begin{aligned}
\Delta \phi &= \frac{4\pi}{\lambda}(L_x - L_y) \\
&+ \frac{2\pi c}{\lambda} \left(\frac{1}{2} \int_t^{t+2L_x/c} h_+(t')\, dt' + \frac{1}{2} \int_t^{t+2L_y/c} h_+(t')\, dt' \right).
\end{aligned} \qquad (1.56)$$

The first term is the phase shift due to the arm length difference, while the second term is the shift due to the GW transient. By assuming that $L_x \sim L_y = L$ for simplicity, the phase shift due to the GW (the second term) $\delta\phi_{\mathrm{GW}}$ is written by

$$\delta\phi_{\mathrm{GW}}(t) = \frac{2\pi c}{\lambda} \left(\int_t^{t+2L/c} h_+(t')\, dt' \right). \qquad (1.57)$$

In a case where the change of $h_+(t)$ is slow enough, $\delta\phi_{\mathrm{GW}}(t) = 4\pi h_+ L/\lambda$. A more detailed analysis shows that the frequency response of the Michelson interferometer to GWs, $H_{\mathrm{MI}}(\omega)$ is given by following equation:

$$H_{\mathrm{MI}}(\omega) = \frac{\tilde{\phi}_{\mathrm{GW}}(\omega)}{\tilde{h}_{\mathrm{GW}}(\omega)} = \frac{4\pi L}{\lambda} \exp\left(-i\omega L/c\right) \frac{\sin(\omega L/c)}{\omega l/c}. \qquad (1.58)$$

where ω is an angular frequency of the GW. This equation implies that the response $|H_{\mathrm{MI}}|$ is maximized at

$$L = \frac{\pi c}{2\omega} = \frac{c}{4 f_{\mathrm{GW}}}. \qquad (1.59)$$

By following (1.58), ideally the optimal arm length for a GW of 250 Hz becomes 300 km, for example. Even though to construct a Michelson interferometer with large arm is one solution to increase a phase shift caused by GW transient, it is not possible to construct such a large-scale interferometer on the Earth. Thus some technique to increase the effective arm length of the interferometer is necessary for further sensitivity improvement.

1.3.2 Fabry-Perot cavity

One option to expand the effective optical path length is to insert a Fabry-Perot cavity in the arms, in which the light is reflected multiple times. The light incident into the cavity is reflected many times between the mirrors. This optical configuration is illustrated in Figure 1.6. The frequency response of a Fabry-Perot Michelson interferometer (FPMI) to gravitational waves is given by

$$H_{\mathrm{FPMI}}(\omega) = \frac{4\pi L\alpha}{\lambda} \frac{\exp\left(-i\omega L/c\right)}{1 - r_F r_E \exp(-2i\omega L/c)} \frac{\sin(\omega L/c)}{\omega L/c}, \qquad (1.60)$$

when the two Fabry-Perot cavities are in resonance condition [22]. α is given by

$$\alpha = \frac{t_F^2 r_E}{1 - r_F r_E}, \qquad (1.61)$$

where r_F and r_E denote the amplitude reflectivity of the front and end mirrors, and t_F represents the transmissivity of the front mirror. The bounce number in a Fabry-Perot cavity N is given by

$$N = \frac{2\sqrt{r_F r_E}}{1 - r_F r_E} = \frac{2\mathcal{F}}{\pi}. \qquad (1.62)$$

Here $\mathcal{F}$ denotes the sharpness of the resonance of the Fabry-Perot cavity and is called the finesse.

The amplitudes of the frequency responses H_{MI} and H_{FPMI} are shown in Figure 1.7 assuming that the arm lengths are set to 3 km in all cases, and that the Fabry-Perot's finesse $\mathcal{F}$ is set at 80.
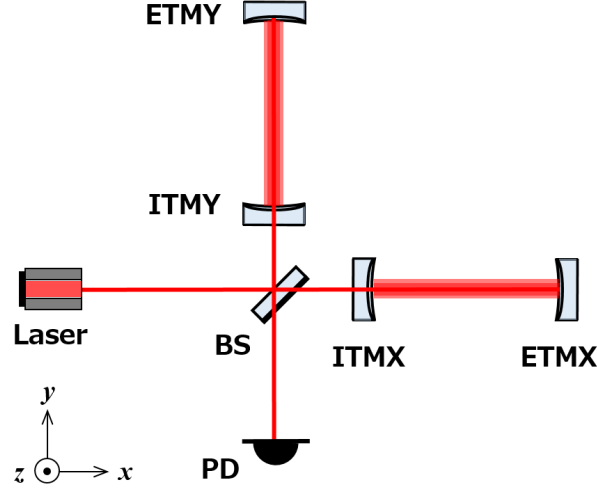
Figure 1.6: An optical configuration of a Fabry-Perot Michelson interferometer (FPMI). The input mirrors labeled ITMX(Y) are added to the configuration in Figure 1.5.

1.3.3 Fundamental noise sources

In a laser interferometric ground-based GW detectors, we have the following noise sources which fundamentally or possibly limit its sensitivity. The sensitivity of the detector is fundamentally limited by the seismic noise, thermal noise and shot noise. The other noise sources are the candidates possibly limiting the sensitivity.

Seismic noise

At the low frequency, the sensitivity of a ground-based detector critically depends on vibrations of the optics induced by the seismic vibration. This is called seismic noise. In order to detect GWs with ground-based detectors, the seismic motion have to be suppressed typically by 10^{-8} to 10^{-10} at 10 Hz. The seismic noise at frequencies higher than about 0.1 Hz is attenuated using vibration isolation systems based on pendulum systems and springs. The seismic noise at frequencies lower than about 0.1 Hz is related to the tidal motion of the ground. This motion can be compensated by using the strain signal sensed by the interferometer itself. As another option to deal with this issue, we can use an additional geophysical interferometer such as the one described in [23], which measures the differential ground motion along the arm (see section 1.4.4).

Thermal noise

Since the mirror and the suspension system are in thermal baths and receive energy from their surroundings, a random energy flow to and from the thermal
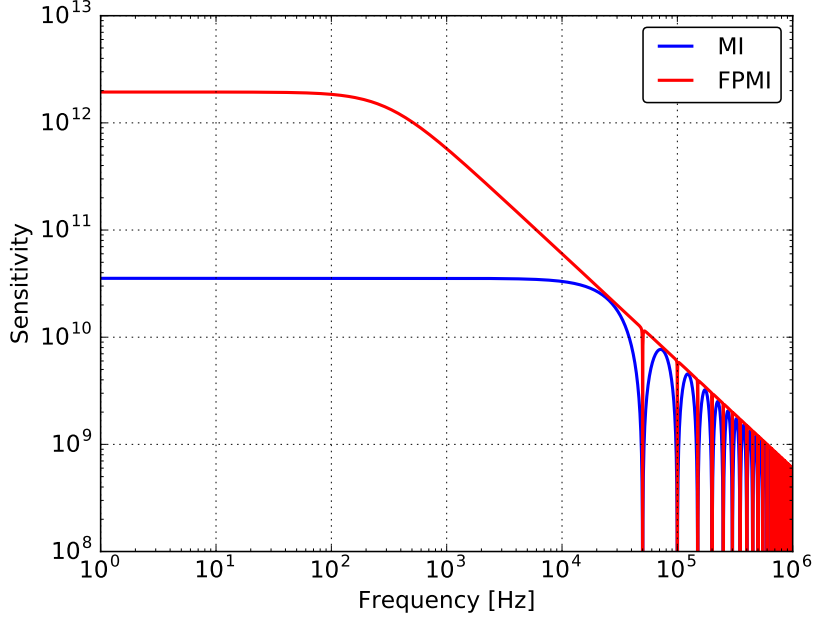
Figure 1.7: Amplitudes of the frequency responses H_{MI} and H_{FPMI} with 3 km arm length. MI and FPMI denotes Michelson interferometer and Fabry-Perot Michelson interferometer, respectively. The finesse $\mathcal{F}$ is set at 80 for FPMI. The wavelength of the laser is assumed the following: $\lambda = 1064$ nm.

baths can take place. This causes a fluctuation of the mirror surface position and so of the optical paths of the interferometer. This noise is called thermal noise. In the field of GW detection, thermal noise induced in mirror substrates or coating is called mirror thermal noise, while the noise caused in the suspension systems is called suspension thermal noise. In order to suppress the impact from the thermal noise, fused silica is typically used for room-temperature mirror substrates [24], while sapphire is a good candidate for cryogenic temperature mirror substrates [25],[26].

Shot noise

A photodetector counts the number of photons and converts it into a photocurrent. In the process, the number of photons counted, or the electrons composing the photocurrent, has a probability distribution, which results in fluctuations of the measured rate. The noise induced by this fluctuation is called shot noise. The shot noise is a fundamental noise in optical power sensing, associated with the quantum nature of light.

This noise in length sensing caused by the probability distribution is proportional to $\sqrt{P_{\mathrm{in}}}$, where P_{in} is the incident power on the mirrors. Since the signal amplitude of the gravitational wave is proportional to P_{in}, the signal to noise ratio is proportional to $1/\sqrt{P_{\mathrm{in}}}$. Consequently the shot noise can be reduced by

increasing the power of the laser.

Radiation pressure noise

The noise caused by the fact that the photons which pushes the mirror randomly, is called radiation pressure noise. The radiation pressure noise is proportional to $\sqrt{P_{\text{in}}}$, where P_{in} is the incident power on the mirrors [8].

Thus we can reduce the shot noise contribution by increasing the incident power. However, by doing this, the radiation pressure fluctuation becomes larger. The shot noise and the radiation pressure noise have a trade-off relationship.

Newtonian noise

At low frequencies it is expected that the interferometer sensitivity will be limited by the direct coupling between the moving ground and the mirrors due to Newtonian gravitational attraction. This is called Newtonian noise. This noise bypasses the vibration isolation system and cannot be reduced by the suspension system. One option to reduce this noise is to place the interferometer underground where the seismic vibrations are smaller. Another option is to subtract the Newtonian noise by calculating the gravity gradient from measurements of the ground motion surrounding the mirrors [27].

Laser noise

Since an interferometric GW detector monitors the distance between the mirrors using the wavelength of the laser as a reference, laser's noises such as frequency and intensity fluctuation, can degrades the detector sensitivity. In order to minimize the impact of the intensity fluctuation, the interferometer is operated at a dark fringe, where the photo-detector receives no light in the absence of GW signals.

Residual gas noise

Random motions of molecules can cause fluctuation of the refraction index in the optical paths of an interferometer and this causes fluctuations of the effective arm lengths. This noise is called the residual gas noise. In order to suppress the impact of this noise, the GW detectors are operated in an ultrahigh vacuum condition.

1.3.4 Power recycling and resonant side-band extraction

For further improvement of the detector sensitivity, additional mirrors are added.

Power recycling

In order to reduce the shot noise, we want to increase the laser power. This is realised by putting a mirror at the incident-laser side. By reflecting the light which comes back from the Michelson interferometer, the laser power at BS is increased. This technique is called power recycling, and the added mirror is called power recycling mirror (PRM). The cavity composed of the PRM and the Michelson interferometer[1] is called power recycling (PR) cavity.

Resonant side-band extraction

If a mirror is put at the anti-symmetric (AS) port[2], and if the cavity composed of the newly added mirror and the interferometer, is kept at resonance, the finesse of the arm-cavities for the differential signal is decreased. By doing this, although the shot noise level at the lower frequency region is increased, at the higher frequency region, the shot noise level would be decreased. The added mirror is called signal recycling mirror (SRM) and the cavity composed of SRM and the Michelson interferometer is called signal recycling (SR) cavity.

The technique described above are used in current ground-based GW detectors, and called dual recycling Fabry-Perot Michelson interferometer (DRFPMI). The schematic view of the optical configuration is shown in Figure 1.8.

---

[1] the Michelson interferometer composed of ITMX(Y) and BS

[2] The port which is not incident-laser side of a Michelson interferometer.
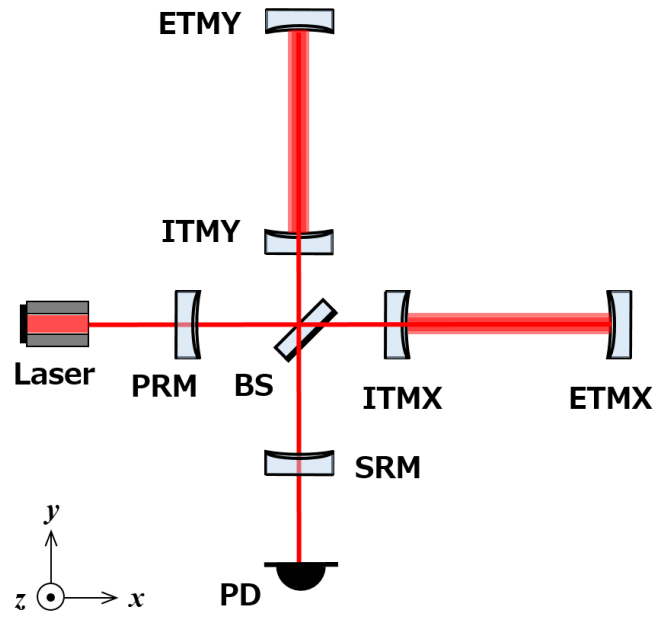
Figure 1.8: Optical configuration of Fabry-Perot Michelson interferometer with the power and signal recycling mirrors. The cavity composed of PRM and the Michelson interferometer is called power recycling (PR) cavity. The cavity composed of SRM and the Michelson interferometer is called signal recycling (SR) cavity.

1.3.5 Interferometer length sensing and lock acquisition

In order to detect GW signals, it is necessary to control the cavity length variation in order to keep the cavities at resonance, and the interferometer output on the dark fringe.

For this purpose, it is required to sense the cavity length displacement. In order to sense the Fabry-Perot cavity length, the Pound-Drever-Hall (PDH) technique is used [28]. In PDH technique, the incident laser frequency (or amplitude) is modulated before entering the cavity. Then the laser beam reflected by the cavity is demodulated. From this process, we can obtain an error signal which contains the information of the cavity length variation.

The error signal becomes proportional to the cavity length change only around the resonant point of the cavity. Thus it is necessary to trap and keep the mirror position in resonance for the interferometer operation.

Conventionally the state where the mirrors are kept at positions where the cavity resonates is called *locked* state. The PDH signal is linear over a ΔL_{lin} given by

$$\Delta L_{\mathrm{lin}} = \frac{\lambda}{2\mathcal{F}}, \tag{1.63}$$

where $\mathcal{F}$ is the finesse of the cavity, and λ represents the wavelength of the laser. Typically the effective width is of the order of a few nanometers, and the mirror displacement has to be kept within this range.

In the real life, we acquire and keep the cavity lock by using an active control system with sensors and actuators. We actuate on the mirror position using a feedback control system. In order to start the observation, we need to lock all the cavities of the DRFPMI. In the process to lock the DRFPMI, particularly it is important to robustly acquire the lock of arm-cavities.

For the lock-acquisition of the X- and Y-arm cavities, KAGRA detector uses the green-lock scheme [29]. This method uses an auxiliary green laser which is the half wavelength of the main laser. This auxiliary laser has a resonance in the arm cavities with finesse of about 50. In this scheme, voltage controlled oscillators (VCOs), which are not affected by the mechanical resonances of the suspensions. VCOs are used to keep the green lasers at the cavity resonance. Then using the correction signals sent to the green lasers, the cavity length is controlled to achieve the resonance condition for the main laser.

Using the VCOs, the control bandwidth can be set up to 10 kHz and the linear regime of the cavity length is expanded.

This lock acquisition system with green laser enables more stable lock acquisition of the arm cavities with the main laser. In addition, we can obtain a looser requirement on the velocity for the arm cavity mirrors.

1.3.6 Calibration

GW signals is extracted from the mirror displacement signals, especially from the differential arm length variation signal, which is called Differential Arm (DARM). The DARM signal in strain h is given by:

$$h(t) = \frac{L_x(t) - L_y(t)}{L},\tag{1.64}$$

where L is the average length of the two arms, i.e, $L = (L_x + L_y)/2$. We then need to obtain the DARM signal h from the interferometer for GW detection.

The error signal obtained with the PDH technique has linear response to the cavity length change if the interferometer is kept locked. Thus for the reconstruction of h we need to know a response function R which satisfies:

$$h(t) = \int R(t - t')\ v_{\mathrm{err}}(t')\ dt',\tag{1.65}$$

where v_{err} represents the error signal in voltage. In the frequency domain eq (1.65) is the response function R satisfies:

$$h(f) = R(f)\ v_{\mathrm{err}}(f).\tag{1.66}$$

Here we reconstruct the GW signal h (in strain) from the DARM control signal. The DARM signal is calculated from interferometer control signal which is used for the mirror actuation to keep the interferometer locked.

The control system uses the feedback control loop. The block diagram of the feedback system for the DARM length control is shown in Figure 1.9. The control loop is characterized by the three components, a sensing function C, a digital filter function D and an actuation function A and.

The sensing function C converts the residual arm length displacements ΔL_{res} to the digital error signal v_{err}. Thus it satisfies:

$$v_{\mathrm{err}}(f) = C(f)\ \Delta L_{\mathrm{res}}(f).\tag{1.67}$$

The digital filter function D converts the digital error signal v_{err} to the digital control signal for the feedback system v_{ctrl}. Thus it satisfies:

$$v_{\mathrm{ctrl}}(f) = D(f)\ v_{\mathrm{err}}(f).\tag{1.68}$$

The actuation function A converts the digital control signal v_{ctrl} to the DARM displacement for the actuation ΔL_{ctrl}. Thus it satisfies:

$$\Delta L_{\mathrm{ctrl}}(f) = A(f)\ v_{\mathrm{ctrl}}(f).\tag{1.69}$$

Consequently, from the diagram in Figure 1.9 we can obtain the response function $R(f)$ as:

$$\begin{aligned}R(f) = \frac{h(f)}{v_{\mathrm{err}}(f)} &= \frac{1}{L}\frac{1 + C(f)D(f)A(f)}{C(f)}\\ &= \frac{1}{L}\left[\frac{1}{C(f)} + D(f)A(f)\right].\end{aligned}\tag{1.70}$$
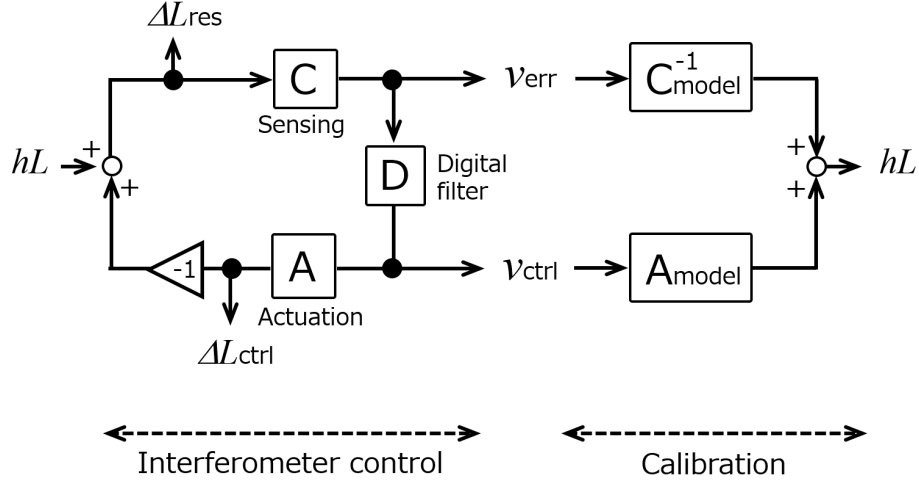
Figure 1.9: Block diagram of the feedback system for the DARM length control.

On the other hand in the time domain the strain signal $h(t)$ is calculated from the the error signal $v_{err}(t)$ and the control signal $v_{ctrl}(t)$.

Since the residual displacements ΔL_{res} is calculated by:

$$\Delta L_{res} = hL - \Delta L_{ctrl}, \tag{1.71}$$

the strain signal h is given as $h = (\Delta L_{res} + \Delta L_{ctrl})/L$. Consequently the time domain strain $h(t)$ is given by:

$$h(t) = \frac{1}{L}\left[\mathcal{C}^{-1}_{model} * v_{err}(t) + \mathcal{A}_{model} * v_{ctrl}(t)\right], \tag{1.72}$$

where $\mathcal{C}^{-1}_{model}$ and $\mathcal{A}_{model}$ are the time domain filters obtained from the modeled frequency domain filters of A and C. More details can be found in [30, 31].

1.4 KAGRA detector

This section describes the optical configuration of KAGRA detector and the requirments placed on the mirror displacement.

KAGRA has been built near Kamioka (Japan) since 2012 [32] and is now being commissioned. The KAGRA detector has been constructed underground in the Kamioka mine. The four Fabry-Perot mirrors are to be cooled down to about 20K. By operating the interferometer underground at cryogenic temperature, the seismic noise and the thermal noise are expected to be reduced and the detector sensitivity is enhanced.

Section 1.4.1 describes the optical design of KAGRA detector. Section 1.4.3 briefly summarizes the required mirror displacement for KAGRA detector in order to get GW signals. Section 1.4.4 shows the seismic motion at KAGRA site. This subsection briefly describes how much the seismic noise has to be attenuated. Finally, section 1.4.5 briefly introduces the seismic attenuation systems in KAGRA detector.

1.4.1 Optical design

The optical layout is shown in Figure 1.10. The laser beam from the pre-stabilized laser source is injected into the main interferometer by passing through the input mode cleaner (IMC). The main interferometer consists of 3 km-long arm cavities, and is operated by using the power recycling and the resonant side-band extraction techniques. The arm-cavity mirrors are called test masses (TMs). In order to improve the spacial mode stability of the power- and the signal- recycling cavities, those recycling cavities are folded in Z-shape by inserting other two curved mirrors in each cavity. The PR cavity is composed of PRM, PR2, PR3 and the input test masses, called ITMs. On the other hand, the SR cavity consists of SRM, SR2, SR3 and ITMs. The beam exiting from the signal recycling cavity passes through the output mode cleaner (OMC) and is detected by photo detectors.
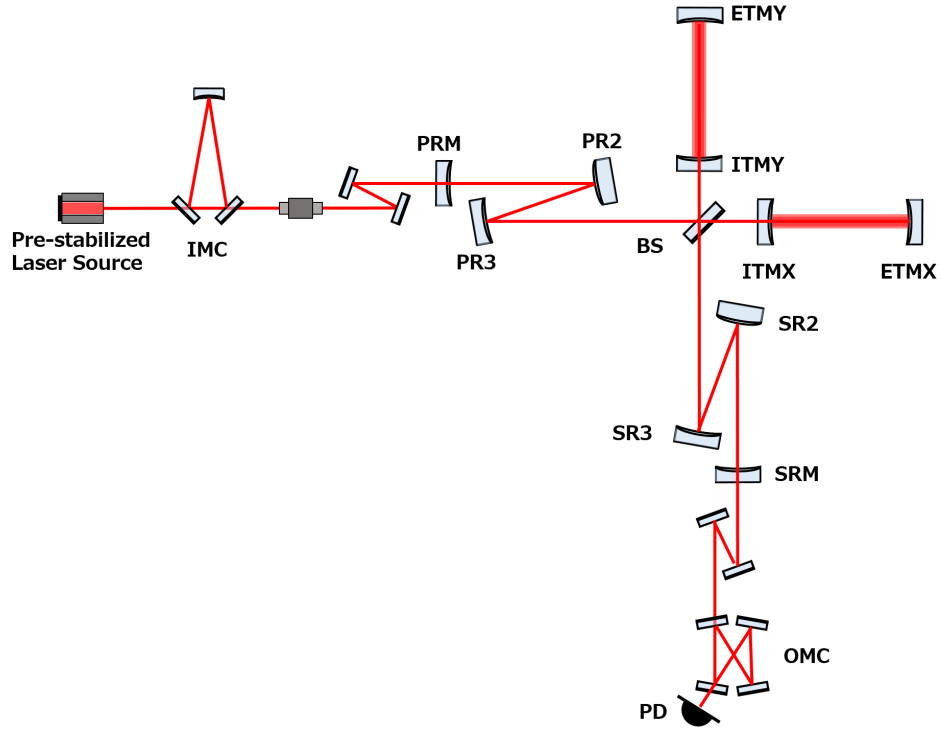
Figure 1.10: The optical layout of KAGRA detector. IMC denotes the input mode cleaner. PRM, PR2 and PR3 are power recycling mirrors, and SRM, SR2 and SR3 are the signal recycling mirrors. Test masses are located at ITMX, ITMY, ETMX and ETMY (Input/End Test Mass X/Y). BS is beam splitter. OMC and PD represent the output mode cleaner and photo diode respectively.

1.4.2 Designed sensitivity

The sensitivity of the KAGRA detector was designed so that the fundamental noises lead the detection limit [32, 33]. Here the fundamental noises represent the seismic noise, thermal noise and the quantum noise. The requirements on other noise contribution are determined to be less than those fundamental noises by a safety factor of 10.

KAGRA has two observation modes called BRSE (broadband resonant side-band extraction) and DRSE (detuned resonant side-band extraction) [34]. Figure 1.11 shows these designed sensitivities of the KAGRA detector. These two modes can be switched by changing interferometer condition, depending on the target GW frequency. DRSE can improve the sensitivity at around 100 Hz, at expenses of worsening the sensitivity at frequencies above a few hundred Hz. By adopting DRSE we can enhance the detector sensitivity to GW signals from coalescing binaries.
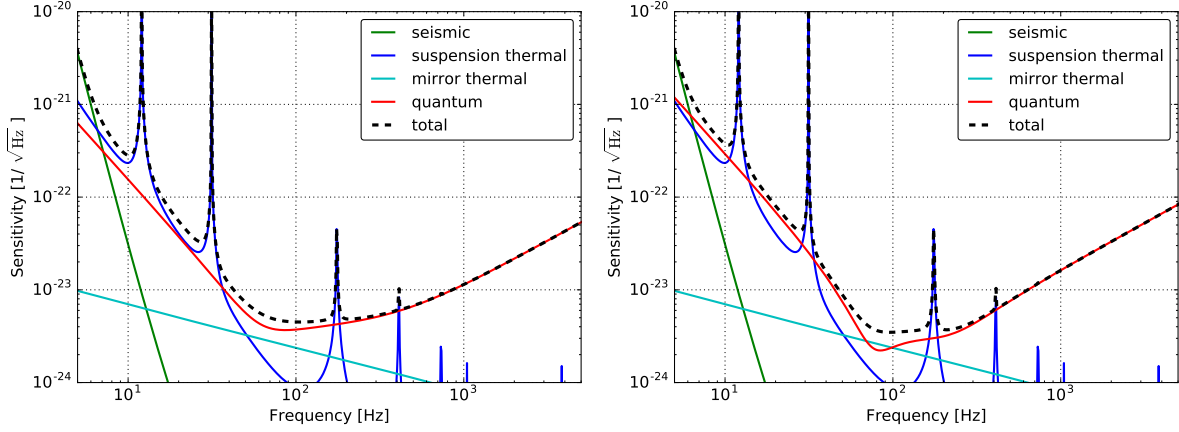
Figure 1.11: Designed sensitivity of the KAGRA detector in BRSE detection mode (*left*) and DRSE detection mode (*right*). The vertical axis show the noise floor.

1.4.3 Displacement noise requirement

GW signal can be found in DARM signal. Thus the spurious displacement of the four TMs have to be sufficiently suppressed. Indeed, not only the TM displacement, but also the displacement of the BS, PR mirrors and SR mirrors have to be suppressed since the displacements induced by those optics can couple to the detector sensitivity[35].

Figure 1.12 shows the required displacement level of the main interferometer mirrors in KAGRA. These plots includes a safety factor of 10. Table 1.1 summarizes the required displacement in spectral density at 10 Hz. The requirement for PR2 and PR3 (SR2 and SR3) are more strict compared to PRM (SRM) case by a factor of 2. This is due to the fact that those mirror displacement can change the optical path of the recycling cavities twice compared to PRM (SRM).
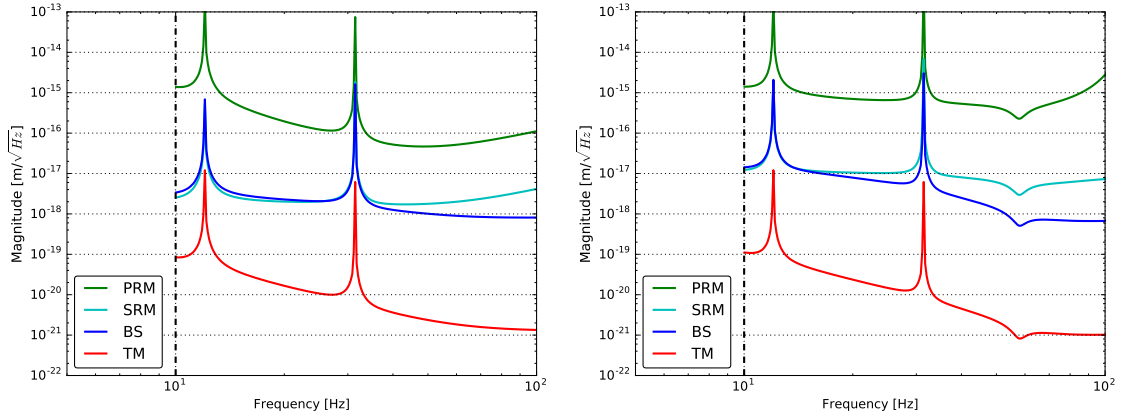
Figure 1.12: Requirement for displacement noise in BRSE detection mode (*left*) and DRSE detection mode (*right*).

Table 1.1: Requirements on longitudinal displacement noise at 10 Hz for the main mirrors of the KAGRA detector.

Optic	Spectrum density at 10 Hz
PRM	1.5×10^{-15} m/$\sqrt{\text{Hz}}$
PR2,3	7.5×10^{-16} m/$\sqrt{\text{Hz}}$
SRM	2.5×10^{-18} m/$\sqrt{\text{Hz}}$
SR2,3	1.3×10^{-18} m/$\sqrt{\text{Hz}}$
BS	3.4×10^{-18} m/$\sqrt{\text{Hz}}$
TM	8.0×10^{-20} m/$\sqrt{\text{Hz}}$

1.4.4 Seismic motion at KAGRA

The ground vibrates continuously and randomly due to oceanic, atmospheric and human activities. The amplitude of the seismic vibration changes by a few orders of magnitude depending on the site and time, as well as on surrounding environment influences such as weather, and human activities.

The worldwide seismic background noise was investigated by J. Peterson [36]. He estimated typical seismic vibration using data from a worldwide network of seismometers and constructed the high and low noise model, according to the upper and lower bounds of the measured power spectral densities.

Figure 1.13 shows the spectra of ground motion of the high and low noise model, compared to that measured at KAGRA site. The spectrum of seismic motion at the KAGRA site shown in Figure 1.13 is obtained from 1 year of measurements [37]. The seismic noise was measured by Trillium120QA [38] at the X-end station in KAGRA underground (shown in Figure 1.10).

The general key features of the seismic-motion spectrum are:

1. At low frequencies below 1 mHz, the amplitude increases due to the tidal deformation of the ground caused by the gravitational attraction from the sun and moon.

2. The peak measured at $0.1 \sim 0.5$ Hz is known as the microseismic peak and is mainly caused by oceanic wave activities. Thus the peak has a large magnitude along the coast while it is smaller in the middle of the continents [39].

3. At frequencies higher than ~ 1 Hz, the typical displacement amplitude spectra of the seismic motions is given by

$$\tilde{x}_{\mathrm{seismic}}(f) \;=\; A \times \left(\frac{f}{1 \text{ Hz}}\right)^{-2} \text{ m}/\sqrt{\text{Hz}}, \qquad (1.73)$$

   The factor A is a constant which depends on sites and is typically about $10^{-9} \sim 10^{-6}$, with thw lowest value obtained underground and the highest value at the ground level.

The seismic vibration at frequencies of microseismic peak produce large motion of the mirrors not coherent between the mirrors placed several km apart and has an impact on stable interferometer operation. One of the main purposes of the vibration isolation system for GW detectors is to reduce the impact of the microseismic peak.

At frequencies lower than about 1 mHz, such low-frequency seismic motion has to be compensated in order to keep the interferometer locked since the test masses (TMs) of ground-based detectors move differentially following to the ground [23]. However, this compensation cannot be done with vibration isolation system since the lowest resonant frequency of the system is typically about a few ten mHz.
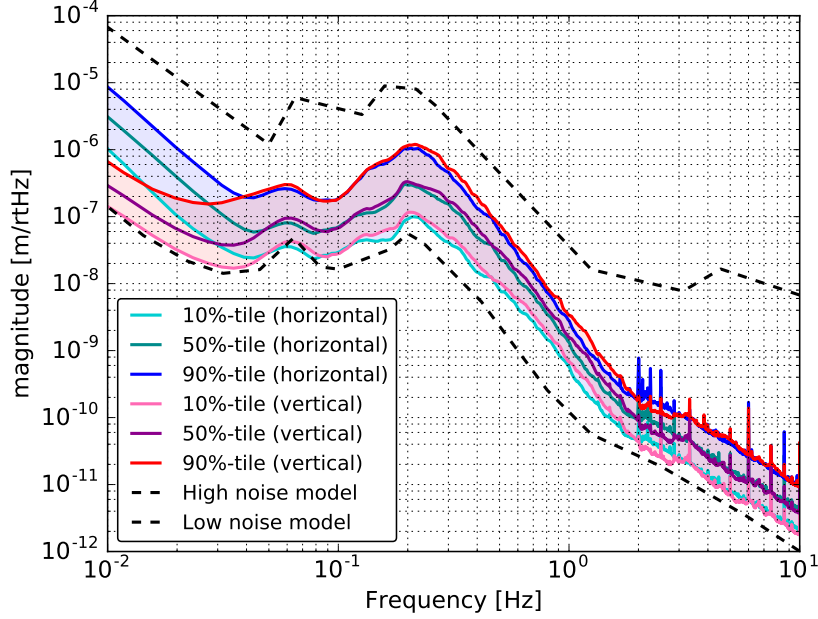
Figure 1.13: Spectrum of measured seismic motion at the worldwide seismic noise from J. Peterson's study [36] (dashed curves), compared to the KAGRA site [37] (solid curves). The colored bands of the spectra of the KAGRA seismic motion denote the range between the 10 percentile to 90 percentile.

For this purpose, we need to use the interferometer signal, or the strain meter signal measured by such as the geophysical interferometer [23].

It is well known that the underground seismic vibration is reduced compared with that on the surface [40]. This reduction of the seismic vibration on underground is effective above 1 Hz, where the atmospheric and human activities dominate. However, the microseismic peak originating from the ocean waves is not reduced much.

At around 10 Hz, the typical amplitude of the seismic vibration at the KAGRA site is a few parts in 10^{-12} m$/\sqrt{\text{Hz}}$. On the other hand, the residual arm-length fluctuation required for KAGRA is on the order of 10^{-20} m$/\sqrt{\text{Hz}}$. Consequently, the displacement of the mirror caused by seismic vibration has to be attenuated by a factor of $10^{-10} \sim 10^{-8}$ at 10 Hz.

1.4.5 Seismic attenuation systems in KAGRA

For the mirrors of the main interferometer of KAGRA, three types of seismic attenuation system (SAS) are used depending on the required displacement noise level above 10 Hz as detailed in section 1.4.3. They are called Type-A, Type-B and Type-Bp suspension, and they are used for the following optics.

- Type-A: for four arm-cavity mirrors (ITMX(Y), ETMX(Y)),

- Type-B: for three SR cavity mirrors and BS,

- Type-Bp: for three PR cavity mirrors.

The location of each suspension system and an overview of the three suspensions are shown in Figure 1.14 and Figure 1.15. This subsection briefly summarizes the mechanics of the assembled KAGRA SAS and their expected mirror displacement. More details about the KAGRA suspension systems is described in chapter 5.
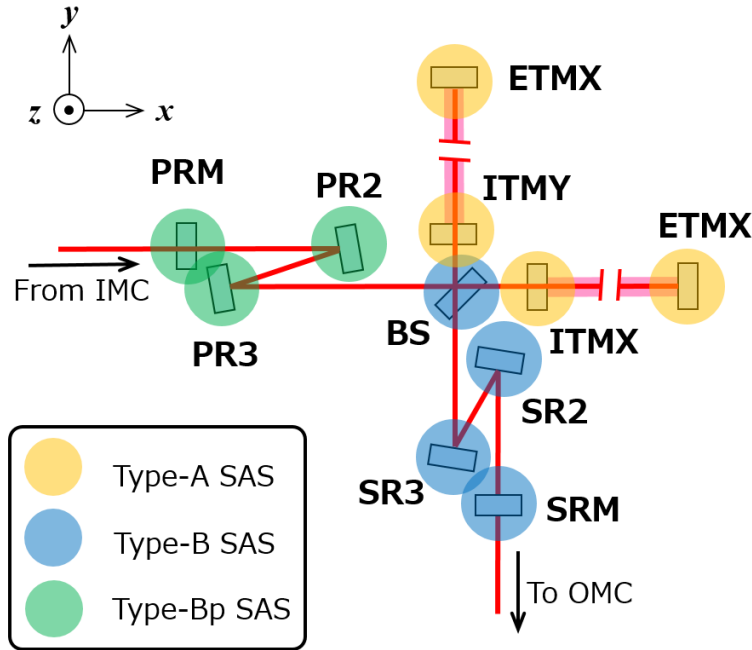
Figure 1.14: The location and the type of suspensions in the KAGRA interferometer. PRM, PR2 and PR3 (the power recycling mirrors) are suspended by Type-Bp system, while SRM, SR2 and SR3 (the signal recycling mirrors) are suspended by Type-B system. The four TMs are suspended by Type-A system.

13.5 m

3.1 m

1.7 m

Type-A   Type-B   Type-Bp
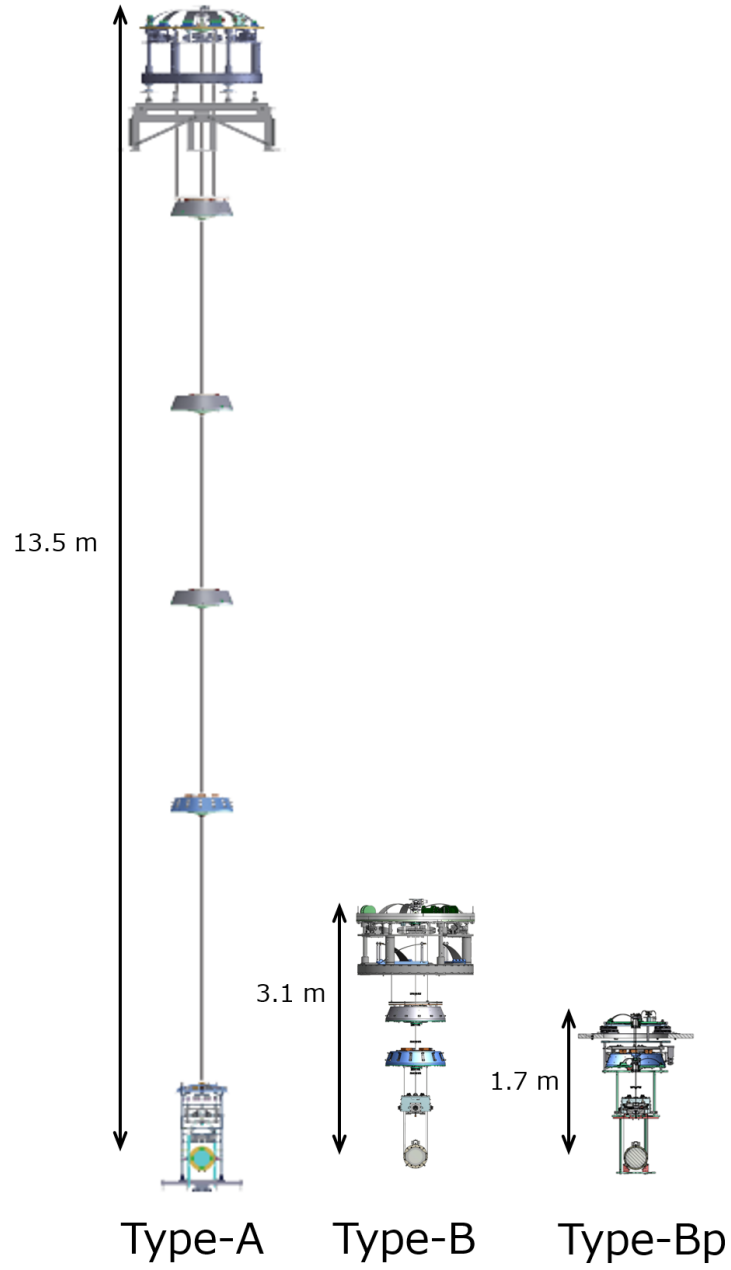
Figure 1.15: Overview of the suspension system for KAGRA detector (originally from [41]). Type-A system is used for TMs, Type-B is for BS and SR mirrors, and Type-Bp system is used for PR mirrors. More details are given in chapter 5.

1.5 Second generation GW detectors

A network of GW detectors composed of km-scale laser interferometers, has been built around the world starting from the 90's. Present ground-based GW detectors are called second generation detectors since they follow a main upgade of initial laser interferometer GW detectors in years 2000's. In the coming years, it is expected that the sensitivities of these detectors will be progressively improved to achieve and then go beyond their design sensitivities.

In the U.S., two detectors called advanced LIGO were built and their operation was started from 2015. The two detectors are located at Hanford, Washington and Livingston, Louisiana, and they have 4 km-length arm. In Europe, Advanced Virgo, which has 3 km-length arms, started the operation from 2017. These detectors have been operated for long periods interrupted by breaks to allow for upgrades and detector sensitivity improvements. The observation periods are called $O1$, $O2$ and $O3$. The first observation period $O1$ was done from September 12, 2015 to January 19 to 2016 with only the two LIGO detectors. The second observation $O2$ was started from November 30, 2016 and terminated on August 25 to 2017. At first, two LIGO detectors had been operating alone. Then Advanced Virgo joined the network in the final one month of the data taking. The third observation $O3$ has been started from April 1, 2019, and is planned to be finished on April 30, 2020.

Starting from 2012, the construction of the KAGRA detector started underground in the Kamioka mine in Japan. KAGRA is planned to join the detector network in the second half of the $O3$.

1.6 Targets and Outline

The previous subsections briefly provides the general background of GW detection, especially about:

1. theoretical aspect of GWs and how they are generated (section 1.1),

2. expected astrophysical GW sources (section 1.2),

3. detection of GWs using interferometer (section 1.3),

4. overview of the KAGRA detector (section 1.4),

5. GW detectors in the current network (section 1.5).

As introduced in the beginning of this chapter, the first detection of GW signal has been achieved in 2015. The natural next step is to start GW astronomy and multi-messenger astronomy. To this purpose GW observation in coincidence with EM observation is crucial. This implies that it is important to have an effective and fast EM follow up program. For the purpose of conducting an effective EM follow up observation, it is quite important:

1. to localize the source position on the sky rapidly and precisely by the GW detectors,

2. to operate the suspensions of the GW detectors with an active control system.

These two topics are selected as the main topics of this thesis work.

The first topic is important in order not to miss the transient events in a short time scale such as days to weeks. In the coming years, the localization performance by the GW detector network is expected to be in the range of 100 deg^2 [42] (chapter 2). In order to achieve this range we need at least three detectors. In the real life, in addition, we are now facing a heterogeneous configuration with GW detectors at different level of development having different sensitivities. Likely, this will continue to be the case with more detectors coming on line in the future. At present, there are two higher sensitivity detectors (Advanced LIGO), a middle sensitive one (Advanced Virgo), and KAGRA which is currently being commissioned. This implies that we have to consider a scheme which enables to make effective use of the less sensitive detector information. In such configuration it is considered that we will have better fast localization performance by analyzing the detector signals hierarchically. This hierarchical analysis approach is expected to effectively work in the heterogeneous network.

In this thesis, we have quantitatively estimated the expected fast localization performance by that approach.

The second topic is important since without a robust operation of the suspensions we cannot start the observation. In addition, a robustly operated detector allows us to have longer detector available time, i.e, it allows us to have more chances to detect astrophysical phenomena. Since the mirrors of ground-based GW detectors (section 1.5) are suspended by multi-stage pendulum systems (section 1.4.5), we have to damp the mechanical resonances of the suspensions as rapidly as possible, and also have to freeze the mirror position and its orientation by isolating the mirrors from the seismic motion. These are necessary to start GW observation. Consequently constructing an system to deal with these issues for the suspension system plays an quite important role for a robust GW detector operation.

In this thesis, we have constructed an active control system, using feedback and feed-forwarding technique, which allows to acquire the KAGRA interferometer lock.

Consequently this thesis work focuses on the following two topics:

1. estimation of the fast localization performance by the current detector network with an on-line approach,

2. construction of active control system for KAGRA suspension system, which allow to start observation.

Section 1.6.1 describes the details of these two topics more specifically. Section 1.6.2 summarises the outline of this thesis.

1.6.1   Targets of this thesis

I have worked on the following two topics. These are motivated to assist conducting more effective EM follow up observation campaign including KAGRA detector. More specifically:

1. I have calculated the fast localization performance of an on-line analysis approach when applied to the localization of a compact binary merger. The approach deals with a network composed of GW detectors with different sensitivities.

2. I have constructed active control system for the KAGRA Type-A SAS, which allows to acquire the interferometer locking.

More details are described in this subsection.

Fast localization by hierarchical approach

The goal of first part of this thesis is to obtain the expected performance regarding sky localization of coalescing binaries in low-latency mode with a network of three or four GW detectors having heterogeneous sensitivities, such as the LIGO-Virgo,

LIGO-KAGRA and LIGO-Virgo-KAGRA network. A hierarchical approach can be used in order to make an effective use of information from the least sensitive detector. In this approach, the presence of an event seen in coincidence in the two more sensitive detectors, triggers a focused search in the data of the third (and fourth), less sensitive, detector(s) with a lower SNR threshold.

So far it was qualitatively considered that such approach will effectively work in the fast localization. In this thesis work I have quantitatively calculated the expected fast localization performance when a hierarchical search is implemented into a GW-EM follow-up pipeline composed of a coalescing binary search algorithm using matched filtering, and a software able to reconstruct sky maps from the outputs of the search algorithms. As the first part of the GW-EM follow-up pipeline, we use one of the algorithms used for low-latency search called multiband template analysis (MBTA) [3]. MBTA is selected since I have been working with MBTA team[3]. As the second part we use Bayestar [4] since it is commonly used for generating the sky maps in low-latency analysis.

This work has started in the context of Advanced Virgo joining to the LIGO network. This work has been done in collaboration with members of the LIGO-Virgo collaboration.

This thesis work is unique in terms of the hierarchical approach with three- and four- detector network. As written in the above, I have worked on the calculation to estimate the rapid localization performance by using MBTA and Bayestar (chapter 3).

Prior works have focused on:

1. LIGO- and LIGO-Virgo-network with a few specific detector-sensitivity cases without considering the hierarchical search [43],

2. LIGO-network using MBTA and Bayestar without considering the hierarchical search [3].

It should be noted that this thesis work does not include the development of the MBTA and Bayestar themselves.

After this estimation, actual implementation of the hierarchical search to MBTA has been done by LIGO-Virgo collaboration members (MBTA team).

Active control of KAGRA Type-A suspension

The second goal of this thesis work is to construct a local control system for the KAGRA suspensions, especially for the arm-cavity mirrors, that is so-called Type-A suspensions. The target is to achieve the required performance in terms of mechanical resonance damping time and of mirror residual motion for acquiring the interferometer lock. This is necessary to start interferometric operation.

---

[3]We have other options for low-latency CBC search algorithm such as GstLAL [1] and pyCBC Live [2]. However, they have mostly same performance.

As it is shown in section 1.3.3, the sensitivity of the ground-based GW detector is limited by the seismic noise at lower frequencies. We adopt vibration isolation systems based on multi-stage pendulum system in order to obtain the required mirror displacement noise level. We then take care of the suspension mechanical resonances of the suspension system. We also have to keep the mirror position and orientation precisely. These two things are quite important to lock the interferometer, i.e. in order to start the observation. For this purpose, we need to construct a system to control the suspensions that is able to:

1. rapidly damp all the mechanical resonances disturbing interferometer lock,

2. reduce the residual motion of the mirror and keep its orientation.

So far there was not such control system for the whole KAGRA Type-A suspensions, including the cryogenic payload part (section 5.1.1). Prior works have focused on the construction of an active control system for the room-temperature part (section 5.1.1) with a dummy payload in terms of damping control [41]. This prior work was done with simple interferometer configuration, i.e, a Michelson interferometer.

For the other KAGRA suspensions called Type-B and Type-Bp suspension (chapter 5), the active control system for them has been already developed in [44, 45, 46]. However, the mechanics of the Type-A suspension and the implemented sensors around the Type-A payload are different from the other suspensions. Thus it is necessary to construct the control system for the Type-A suspensions, especially for whole the Type-A suspension.

In the second part, I have constructed an active control system for the Type-A suspension that deals with the suspensions resonance damping and the residual mirror motion suppression. For the construction I have used feedback and feed-forward control technique. I have designed the feedback and feed-forward filters in a simulation and then have implemented to the actual suspension system.

More concretely, I have worked on the following topics:

1. measuring and estimating the typical sensor noises, for the sensors implemented in the KAGRA suspensions especially for the Type-A suspension (section 5.3),

2. integration of the KAGRA suspensions in terms of installation, maintenance and repairing (section 5.4),

3. designing the control system for the Type-A suspension in a simulation (chapter 6),

4. implementing the control system for the Type-A suspension and its evaluation (in chapter 7).

After implementation of the control system, we could lock the interferometer with FPMI configuration stably. I have used the FPMI as a sensor and verified the vibration isolation performance with FPMI.

I note that the work in this thesis does not include the following tasks. They have been achieved by other KAGRA project members:

1. basic design of the mechanical systems, including the implemented sensors and actuators, for all the KAGRA suspensions,

2. installation of data-acquisition system and real-time digital system infrastructure.

By the work within this thesis, we are able to start the interferometer operation with the Type-A suspensions.

1.6.2 Outline of this thesis

This thesis has mainly two parts as described in section 1.6.1. The first part is the topic about estimating the fast localization with a hierarchical approach with the current GW detector network. The second part is about implementing an active control system to acquire the KAGRA interferometer lock.

The details of the fast localization topic are described in chapter 2 and 3. On the other hand, the details of the topic about the active control system for the KAGRA suspensions, forcusing on the Type-A suspension, are described in chapters 4 to 7.

More specifically, chapter 2 describes the background of sky localization of coalescing binaries with GW detectors. Chapter 3 addresses the fast localization with the hierarchical approach and summarizes the expected improvement. Chapter 4 describes the background of low frequency vibration isolation system for KAGRA detector. Chapter 5 describes the details of the KAGRA seismic attenuation system called KAGRA-SAS. The measured and estimated sensor noise floors are also summarized in this chapter. Chapter 6 sets the requirements for the active control system. This chapter describes the development of the control system for KAGRA Type-A suspension using simulation. Chapter 7 summarizes the implementation and performance evaluation of the installed control system (discussed in chapter 6). Finally, the conclusion and perspectives are given in chapter 8.

1.7 Summary

This chapter briefly describes the general background of detection of GWs. After the brief introduction, the targets and outline of this thesis are presented.

Section 1.1 mentions that the amplitude of GWs is quite tiny; the typical amplitude of GW from a coalescing neutron star binary is about 10^{-23} in strain if the source is 100 Mpc away and its component masses are $1.4 M_\odot$.

Section 1.2 describes some astrophysical phenomena which are the most promising sources for direct GW signal detection.

Section 1.3 indicates that GW can be directly detected by using interferometric technique if we can overcome all the noise contributions. In this section we also show that in order to operate the interferometer, the relative mirror positions have to be controlled within in a nm or less.

Section 1.4 reports the required mirror displacement noise level for the KAGRA detector, and shows that the seismic noise suppression is one of the biggest difficulties in order to realize GW detection on the Earth. This section underlines the necessity to suppress the mirror displacement both at high and at low frequencies. At frequencies above 10 Hz, the residual mirror displacement has to be suppressed sufficiently to measure GW signals. At low frequencies (especially at the microseismic peak), the mirror displacement has to be reduced to about one nm ore less to acquire and keep the interferometer locked. In particular it is important to attenuate the micro-seismic motion.

Section 1.5 describes the ground-based GW detectors that are currently running and being commissioned.

Then section 1.6 summarizes the the target and outline of this thesis specifically, i.e thesis addresses:

1. estimation of the fast localization performance by the current detector network with an on-line approach (chapters 2 and 3),

2. construction of active control system for KAGRA suspension system, which allow to start observation (chapters 4 to 7).

Clarification of my work within this thesis work is included.

Chapter 2

Localization of coalescing binaries

This chapter briefly describes the background of the localization of coalescing binaries by GW detectors. More specifically, the principles at the basis of the sky localization of a compact coalescing binary by means of a network of GW detectors is described. More details can be found in [8].

Section 2.1 explains the essence of the data analysis of the GWs from compact binary coalescence (CBC) which uses the so-called matched filtering. This subsection also describes the antenna pattern of GW detectors. Section 2.2 describes the principle of source localization by means of triangulation. Section 2.4 summarizes the localization performance by the current GW detector network. This subsection includes a discussion about the requirements set on the localization with GW detectors, by the subsequent EM follow up. Section 2.5 describes what is practically demanded role on the fourth detector KAGRA in order to realize more effective EM follow up observation. Section 2.6 summarizes this chapter.

2.1 Data analysis

2.1.1 Matched filtering

Matched filtering is the analysis method commonly used in searching GW signals from CBCs. The matched filter compares the measured signal to the theoretical signal by taking into account the detector noise and it outputs the signal-to-noise ratio (SNR), $\rho(t)$ as a function of time t. For this purpose, the matched filtering needs theoretical wave forms corresponding to all possible masses and spins of the two compact objects. These waveforms are called templates.

We assume that the detector output as the function of time t is given by:

$$x(t) \;=\; s(t) \;+\; n(t), \tag{2.1}$$

where $s(t)$ is the GW signal and $n(t)$ is the detector noise. The SNR $\rho(t)$ is given by[1]:

$$\rho^2(t) \;=\; 4Re\left[\int_0^\infty \frac{\tilde{x}(f)\,\tilde{u}^*(f)}{S_n(f)}\,df\right], \tag{2.2}$$

---

[1]For more details, see [47]

where $S_n(f)$ is the one-sided noise power spectral sensitivity, $\tilde{x}(f)$ and $\tilde{u}(f)$ are the spectra of $x(t)$ and $u(t)$ respectively, and $u(t)$ is the wave form called template. As supplemental note, in this calculation, we assume that $S_n(f)$ meets the followings:

$$\langle \tilde{n}(f)\tilde{n}^*(f')\rangle = \frac{1}{2}\delta(f - f')S_n(f), \tag{2.3}$$

where angle $\langle...\rangle$ denotes an ensemble average. $S_n(f)$ has dimension of Hz^{-1}, and satisfies $S_n(-f) = S_n(f)$. The factor of $1/2$ is inserted in the definition so that the total noise power is calculated by integrating over the range $0 \leq f < \infty$:

$$\langle n^2(t)\rangle = \int_0^\infty df\, S(f). \tag{2.4}$$

Consequently, the data sets which give SNR $\rho(t)$ higher than a SNR threshold, are to be searched. The maximum SNR above the threshold is called a trigger, and the corresponding event is considered as a candidate event. The generated triggers are then used to make the detection network by several detectors.

Signal-to-noise ratio and distance

We briefly check the relationship between the Signal-to-noise ratio (SNR) and the distance to the source. Using eq (2.2), the SNR ρ for a given strain signal h can be given by

$$\rho^2(t) = 4Re\left[\int_0^\infty \frac{\tilde{h}(f)\,\tilde{h}^*(f)}{S_n(f)}\,df\right]. \tag{2.5}$$

By considering eq (1.32), then the amplitude of SNR ρ is proportional to the inverse of the distance between the observation point and the source (not the square of the distance). Here using the distance of an optimally located and oriented source D_{eff}, which is called the effective distance, this is characterized by:

$$\rho \propto D_{\mathrm{eff}}^{-1}. \tag{2.6}$$

The detailed explanation of the effective distance D_{eff} is described in section A.1.

Detection range

In the field of GW detection, to characterize the detector sensitivity, we commonly use the distance, which is called the detection range. The detection range represents the distance at which the signal can be detected with SNR of 8.

In particular we use the distance at which a BNS signal, whose component masses are $1.4\ M_\odot$, can be detected with SNR of 8. This is called the BNS range. More details are described in section A.1.

2.1.2 Antenna Patterns

For the data analysis, we have to consider the angular dependence of the interferometer response to GWs. Let's assume that the source is located at the position (θ, ϕ), and that the source is rotated by ψ (usually called polarization angle), as shown in Figure 2.1. In this configuration, the amplitude of the GW signal $h(t)$ that the interferometer would detect becomes:

$$h(t) = F_+(\theta, \phi, \psi)h_+(t) + F_\times(\theta, \phi, \psi)h_\times(t), \tag{2.7}$$

where $h_+(t)$ and $h_\times(t)$ denote the amplitudes of the GW signal in the two polarizations. The terms F_+ and $F_\times$, in eq (2.7), are called antenna pattern functions. They describe how the two GW polarizations are combined by the detector angular response. In the coordinate system described above, the antenna pattern functions are given by

$$F_+(\theta, \phi, \psi) = \frac{1}{2}(1 + \cos^2\theta)\cos 2\phi \cos 2\psi - \cos\theta \sin 2\phi \sin 2\psi, \tag{2.8}$$

$$F_\times(\theta, \phi, \psi) = \frac{1}{2}(1 + \cos^2\theta)\cos 2\phi \sin 2\psi + \cos\theta \sin 2\phi \cos 2\psi. \tag{2.9}$$

The antenna patterns F_+ and $F_\times$ where $\psi = 0$ are shown in Figure 2.2. The quadrature sums of the F_+ and $F_\times$ where $\psi = 0$, for each of the GW detectors introduced previously, are shown in Figure 2.3 and 2.4.
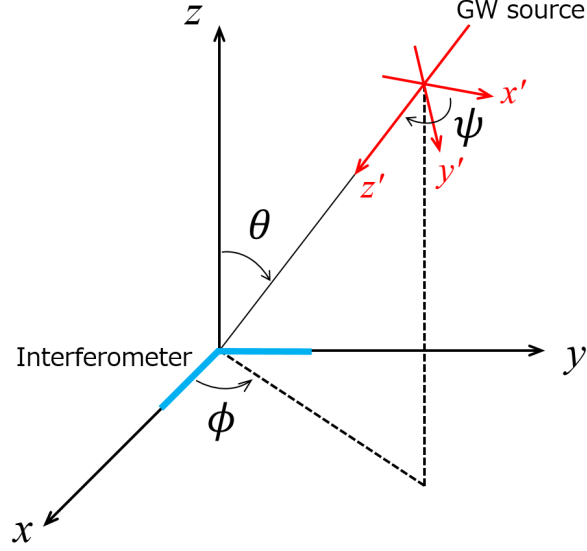
Figure 2.1: Definition of the angles describing the source position and the polarization angle (θ, ϕ, ψ). The interferometer arms are along with the x and y arm.
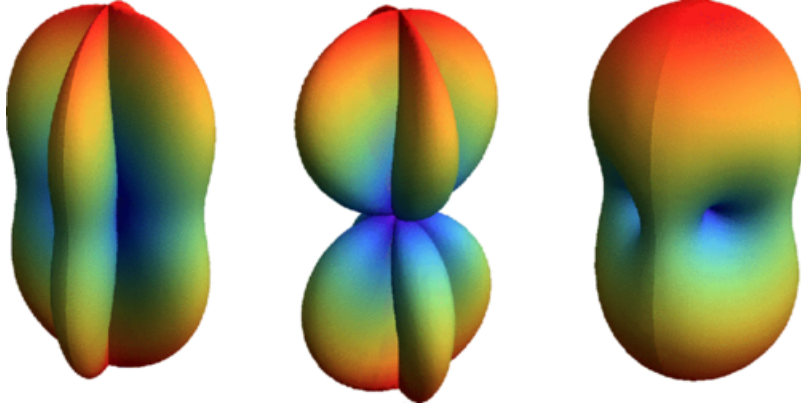
Figure 2.2: The antenna patterns F_+, $F_\times$ and the quadrature sum of them (unpolarized waves), where $\psi = 0$. This figure is reproduced from [48]. *FIG. 2 (color online). Interferometer antenna response for (+) polarization (left), (×) polarization (middle), and unpolarized waves (right).*
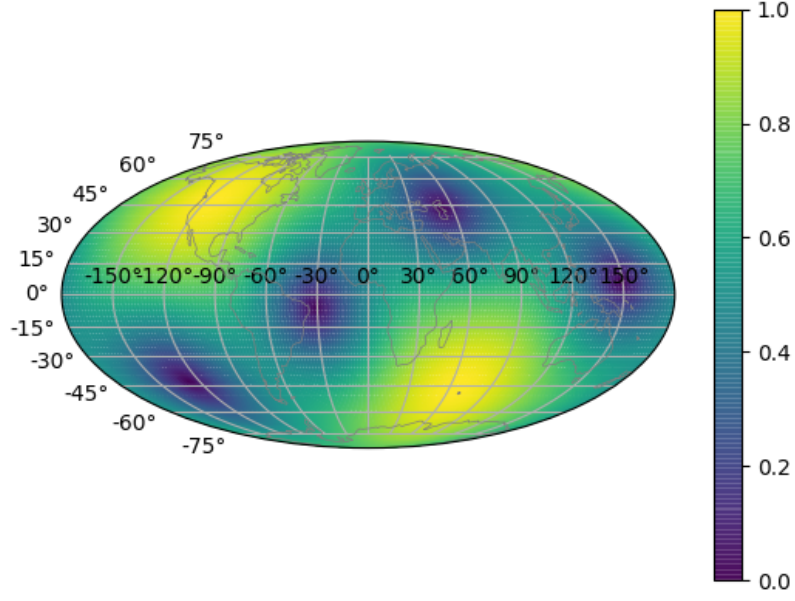
(a) Antenna pattern of LIGO Hanford detector
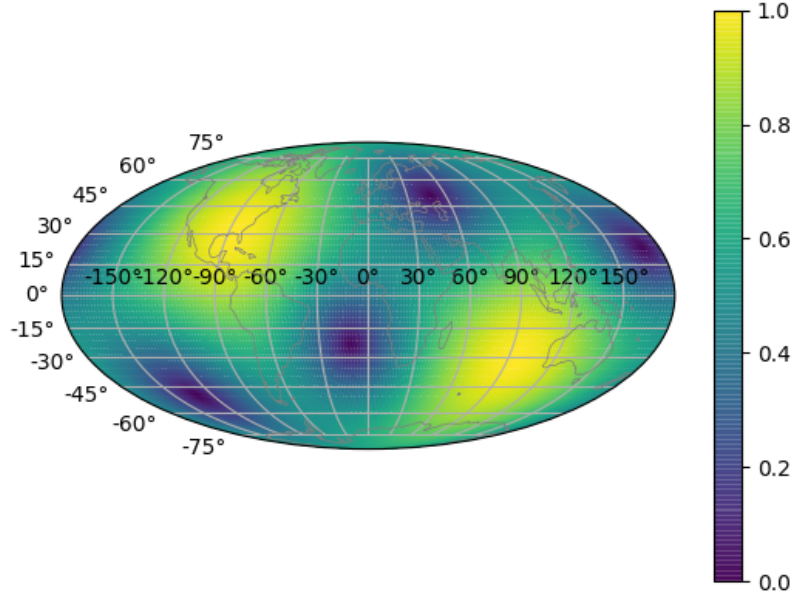
(b) Antenna pattern of LIGO Livingston detector

Figure 2.3: Projection of the antenna patterns of second generation detectors. The quadrature sums of the F_+ and $F_\times$ where $\psi = 0$, i.e, $\sqrt{F_+^2(\theta, \phi, \psi = 0) + F_\times^2(\theta, \phi, \psi = 0)}$ is projected.
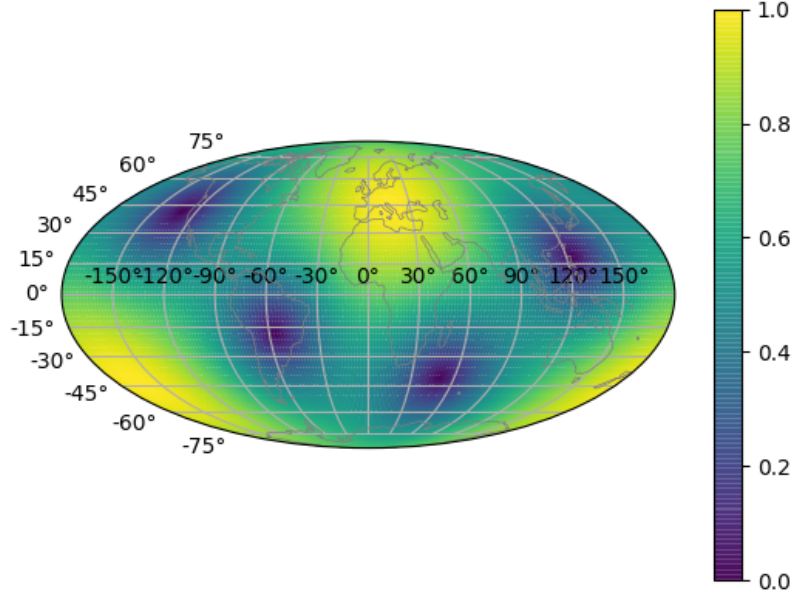
(a) Antenna pattern of Virgo detector
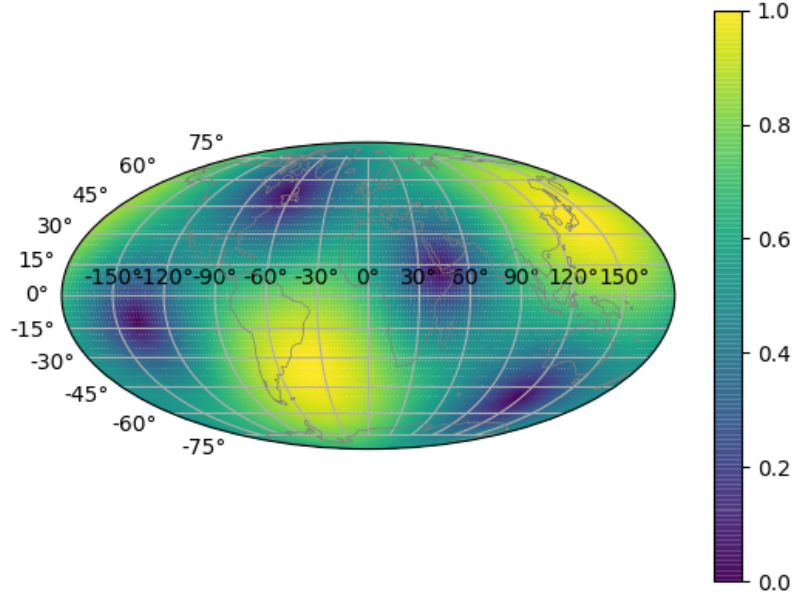
(b) Antenna pattern of KAGRA detector

Figure 2.4: Projection of the antenna patterns of second generation detectors. The quadrature sums of the F_+ and $F_\times$ where $\psi = 0$, i.e, $\sqrt{F_+^2(\theta, \phi, \psi = 0) + F_\times^2(\theta, \phi, \psi = 0)}$ is projected.

2.2 Source localization

The position of the source in the sky is localized by means of a triangulation using the detection time delay at each detector. This is not only of astrophysical interest, but also essential for EM follow-up observation.

Following [49], a two-detector network will give the following distribution. Supposing that the source is located at position $\boldsymbol{R}$ on the unit sphere, and consider two detectors separated by a distance (expressed in light seconds) of $\boldsymbol{D}$, the difference in the time of arrival of the signal at the two sites is given by $(T_1 - T_2) = \boldsymbol{D} \cdot \boldsymbol{R}$. Then assuming that the two detectors have timing accuracies σ_1 and σ_2, and the observed times are t_1 and t_2, the distribution of the reconstructed location $\boldsymbol{r}$ would be given by

$$p(\boldsymbol{r}|\boldsymbol{R}) \;\propto\; p(\boldsymbol{r}) \exp\left[-\frac{(\boldsymbol{D} \cdot (\boldsymbol{r} - \boldsymbol{R}))^2}{2(\sigma_1^2 + \sigma_2^2)}\right], \tag{2.10}$$

where $p(\boldsymbol{r})$ is the prior distribution. In the above, it is assumed that the measured time delay $(t_1 - t_2)$ is given by $\boldsymbol{D} \cdot \boldsymbol{r}$, and the timing accuracy of one detector is expressed as $\sigma \sim (2\pi\rho\sigma_f)^{-1}$, where ρ is observed SNR, and σ_f is the effective bandwidth of the signal in the detector which is calculated by $\sigma_f^2 = \overline{f^2} - \overline{f}^2$ with

$$\overline{f^n} \;=\; 4 \int_0^\infty \mathrm{d}f \frac{|\tilde{h}(f)|^2}{S(f)} f^n. \tag{2.11}$$

The distribution by three-detector network can be given in a similar way by:

$$p(\boldsymbol{r}|\boldsymbol{R}) \;\propto\; p(\boldsymbol{r}) \exp\left[-\frac{1}{2}(\boldsymbol{r} - \boldsymbol{R})^T \boldsymbol{M}(\boldsymbol{r} - \boldsymbol{R})\right], \tag{2.12}$$

where the matrix $\boldsymbol{M}$ which describes the localization accuracy, is given by

$$\boldsymbol{M} = \frac{\boldsymbol{D}_{12}\boldsymbol{D}_{12}^T}{\sigma_{12}^2} + \frac{\boldsymbol{D}_{23}\boldsymbol{D}_{23}^T}{\sigma_{23}^2} + \frac{\boldsymbol{D}_{31}\boldsymbol{D}_{31}^T}{\sigma_{31}^2}. \tag{2.13}$$

In the above, the pairwise timing accuracy is given by $\sigma_{ij}^2 = \sigma_i^2 + \sigma_j^2 + \sigma_i^2\sigma_j^2/\sigma_k^2$, where $k \neq i, j$.

As an example, Figure 2.5 shows the reconstructed region in the case of GW170817 [50]. The blue region represents the localized area by the two LIGO detector network. On the other hand, the green region shows the area reconstructed by the LIGO-Virgo detector network (i.e, three detector network9.

Two-detector network will give a ring-shape reconstructed region since it is only possible to restrict the location of the source in the direction parallel to the separation $\boldsymbol{D}$ between the detectors. In order to have a smaller reconstructed region, we need to have at least three detectors.
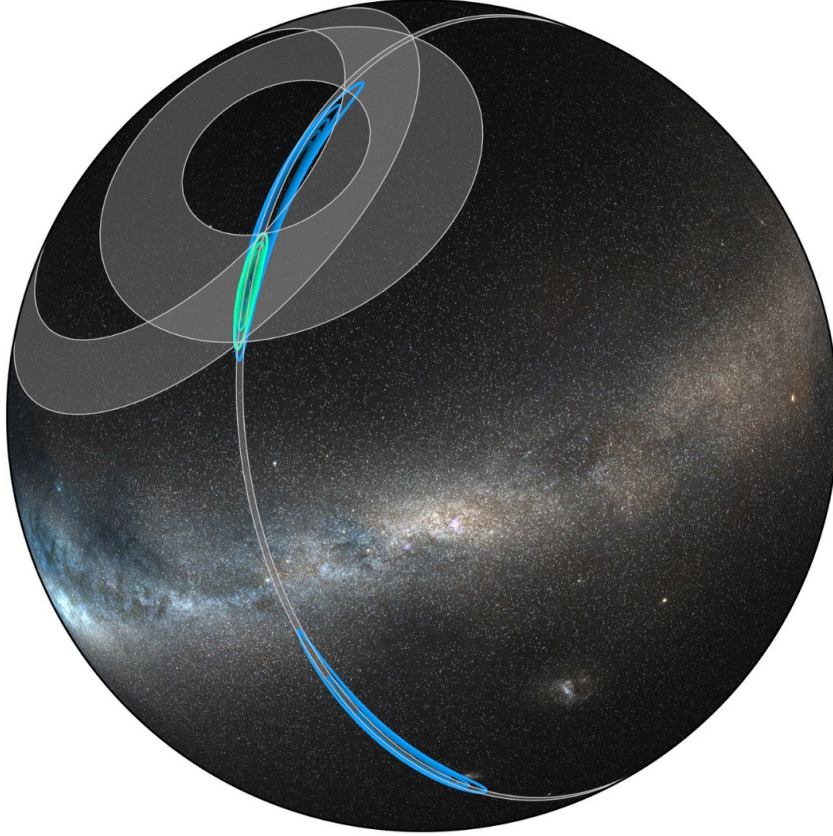
Credit: LIGO/Virgo/NASA/Leo Singer (Milky Way image: Axel Mellinger)

Figure 2.5: *GW170817 localization and triangulation annuli. The rapid Hanford-Livingston localization is shown in in blue, and the final Hanford-Livingston-Virgo localization is in green. The gray rings are one-sigma triangulation constraints from the three detector pairs. Credit: LIGO/Virgo/NASA/Leo Singer (Milky Way image: Axel Mellinger).* This Figure is reproduced from [50].

2.3 Analysis algorithms

The LIGO-Virgo Collaboration has developed several analysis algorithms for the matched filtering and for the sky localization of the sources. The algorithm is called pipeline. Currently, the detector outputs are analyzed using the pipelines introduced in this subsection. The candidate events are uploaded to the GraceDb [11]. Then the candidate events are processed through algorithms for source position reconstruction, which generates probability sky maps.

2.3.1 Compact binary search

As described in above we use the matched filtering technique to search for the GWs from compact binary coalescence (CBC) sources. Currently we use the following pipelines for the actual analysis.

PyCBC pipeline

PyCBC pipeline is a matched filtering algorithm to look for GWs from CBC sources. This pipeline is constructed using the PyCBC software package [51, 52]. *This analysis performs direct matched filtering of the data against a bank of template waveforms to calculate the signal-to-noise ratio (SNR) for each combination of detector, template waveform, and coalescence time [47]* (Italic sentences are cited from [53]). More details can be found in [53].

GstLAL pipeline

A pipeline developed using the GstLAL library [54, 1] (developed by the LIGO-Virgo Collaboration) also performs the matched filtering. More details can be found in [53].

cWB pipeline

Coherent WaveBurst (cWB) is an analysis algorithm used in searches for weakly modeled (or unmodeled) transient signals with networks of GW detectors. Designed to operate without a specific waveform model, cWB identifies coincident excess power in the multiresolution time-frequency representations of the detector strain data [55], for signal frequencies up to 1 kHz and durations up to a few seconds (Italic sentences are cited from [53]). More details can be found in [53].

MBTA pipeline

The Multi-Band Template Analysis (MBTA) pipeline is a low-latency coincident analysis pipeline for the detection of GWs from CBCs. MBTA runs with a low computational cost, and can identify candidate GW events online with a subminute latency.

The MBTA pipeline performs a coincident analysis, analysing each detector in the network separately before the results are combined to identify coincident events. To reduce the computational cost of the matched filtering, which is the most expensive element of the analysis, MBTA uses the novel approach of splitting the matched filter across two (or more) frequency bands (Italic sentences are cited from [3]). More details can be found in [3].

2.3.2 Sky position reconstruction

The source position reconstruction on the sky is done using Bayesian framework [56, 57, 4]. We first generate the sky probability map in a low-latency mode. We then update the sky map with high-latency analysis.

Full parameter estimation

For the precise position reconstruction of the sources, we estimate all the unknown parameters which describe the GWs from CBC sources, using Bayesian inference. For this purpose we use LALInference [56] which is an algorithm for the Bayesian inference applied to GW observation.

It is known that Bayesian inference costs computationally. For the CBC case, we need to estimate 15 parameters[2], and it takes hours to days (or more) with LALInference. More details can be found in [56].

Bayestar

For fast position reconstruction of the source, we use the Bayesian rapid localization algorithm. This algorithm is called Bayestar. Bayestar builds a likelihood function for Bayesian inference using three matched filtering outputs, i.e, the times, amplitudes and phases on arrival at the detectors (see also section 3.2).

It provides the sky maps within a time scale of seconds to minutes. The accuracy is approximately same as the full parameter estimation. More details can be found in [4].

---

[2]The masses and spins of each component, the orientation, distance, arrival time of the signal, inclination angle, polarization angle and coalescence phase. More details can be found in [56, 4].

2.4 Multi-messenger observation

If a precise source position localization by GW detectors is achieved, we can start to observe astrophysical phenomena, such as supernova and BNS mergers with available EM telescopes more effectively. GW detection in coincidence with EM and neutrino detections will play an important role in the discovery and subsequent study of astrophysical phenomena.

Current localization performance and target

In the real life, however, the sky localization provided by GW detectors will be poor by optical telescope standards. With the advanced detectors in the coming years this localization is expected to be in the range of 100 deg^2. The actual size of the area in the sky corresponding to the alerts produced by the LIGO-Virgo network during the first half of $O3$[3] are summarized in Figure 2.6. The median values are about 1600 deg^2 for two LIGO detector network and about 950 deg^2 for LIGO-Virgo three detector network. During this period the detector sensitivities of advanced LIGO Hanford, LIGO Livingston and Advanced Virgo in terms of BNS range were about 120 Mpc, 140 Mpc and 45 Mpc respectively [58].
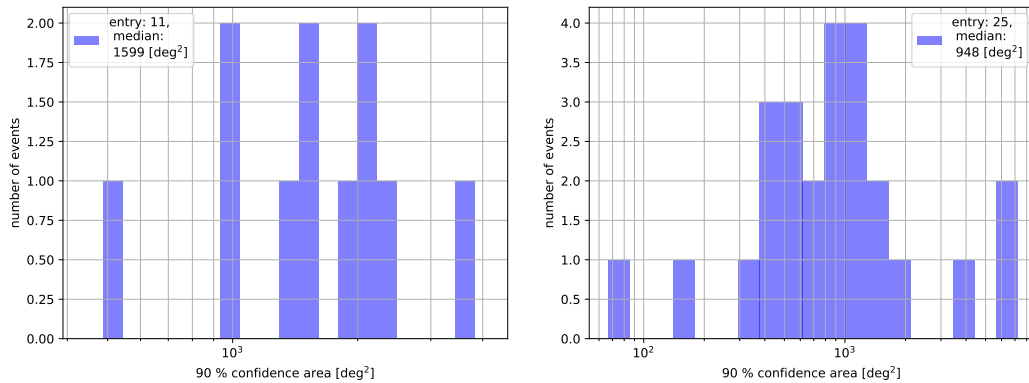
Figure 2.6: The size of 90 % confidence area which are alerted in the first half of $O3$, which is called $O3a$. The events detected by the two LIGO detector network (*left*) and the events by LIGO-Virgo three detector network (*right*) are included.

As an example, if we assume that we search for kilonovae [59] with BlackGEM telescope array, it will take 5 minutes to observe the area of 2.7 deg^2 [60]. Since the luminosity of a kilonova decays in the time scale of days to weeks, it is very important to identify it as soon as possible so as to be able to observe its EM emmission rapidly after the merger. In order to e.g. complete the scan of the sky region given by GW detectors within one night (about 9 hours), it will be necessary that this region is smaller than about 300 deg^2. In order to achieve this localization precision, it is indeed important to detect GW signals with several

---

[3]The information is available from [11].

detectors at the same time. In addition, especially for the coming years, we also need EM telescopes that are able to quickly scan this relatively large area of the sky.

If all the detectors become close to their design sensitivities, the localization by such four-detector network is expected to be in the range of 10 deg^2 [42]. However, currently we have only three detectors (soon we will have four detectors), and they have not achieved their design sensitivities yet. In addition the sensitivities of Advanced LIGO, Advanced Virgo and KAGRA are different from each other.

In this configuration we need a scheme which allows to make effective use of the less sensitive detector information. Otherwise we will have poor reconstructed position. One way to deal with this heterogeneous sensitivity network is to analyze the detector information hierarchically. In this approach, the presence of an event seen in coincidence in the two more sensitive detectors triggers a focused search in the data of the third (and fourth), less sensitive, detector(s) with a lower SNR threshold.

This strategy is discussed in detail in chapter 3.

2.5   Network duty cycle

As described above, in order to achieve a small localization area, it is necessary to detect GW signals with several detectors at the same time. More specifically, for a meaningful localization, at least three detectors are needed. Otherwise the source is localized within a very large area, totally unsuitable for EM follow up observation.

Currently the GW network is composed of the three detectors: the two Advanced LIGO detectors and the Advanced Virgo detector. Soon the KAGRA detector will join this network. However, sometimes these GW detectors are not operational due to interferomenter lock loss and/or maintenance operation.

For example, assuming that all the detectors have an equal duty cycle of 80%, the duty cycle by three detectors in the three detector network would be about 51%. On the other hand, for a network made by four detectors, the the probability to have at least three detectors in operation will raise to about 82%. Indeed the probability to have at least three detectors up and running increases considerably when a fourth detector is added to the network. This is a benefit of adding detectors to the network and reduces the chances to miss detectable events.

Consequently, the operation of a fourth robust interferometer is of paramount importance to achieve high network duty cycle, and to conduct EM follow up observation more effectively.

Operation of fourth GW detector

In order to achieve a robust operation of the fourth detector KAGRA, it is important to have an effective control system for the suspension system. More specifically it is necessary:

1. to damp the mechanical resonance of the suspensions as rapidly as possible,

2. to freeze the mirror position and its orientation.

Constructing a system to deal with the above two issues is quite important to start a robust interferometer operation. Otherwise we cannot start the observation. On the other hand, if we can construct a robust control system for the suspensions, we can increase the duty cycle of the detector. In the current configuration, constructing such system for KAGRA suspensions is quite important.

The details of this work are discussed in chapters 4 to 7.

2.6   Summary

This chapter describes the background of the localization of coalescing binaries with GW detectors.

Specifically, section 2.1.1 describes a typical analysis method to get the signals from CBC. Section 2.1.2 introduces the antenna pattern of the GW detectors. Section 2.2 describes how the GW source position is localized by the GW detectors. Section 2.4 mentions the current localization performance of the worldwide GW detector network for multi-messenger observation. This subsection also explains that we need a way to deal a network composed of detectors with heterogeneous sensitivities. One option is to analyze the data hierarchically. Section 2.5 describes that the network duty cycle by three detectors in four-detector network is improved considerably compared to the case in the three-detector network. This is particularly important when looking for rare astrophysical events.

In chapter 3 we consider a GW source localization strategy using a hierarchical approach, in low-latency search. We then estimate its performance when applied to the current GW detector network.

Chapter 3

Estimation of fast localization with a hierarchical approach

This chapter describes the benefit of adopting an online analysis approach to deal with a network made by GW detectors with different sensitivities, in terms of the fast sky localization of coalescing binaries.

Adding GW detectors to the network benefits both the detection confidence and the sky localization of the source. Especially for the EM follow-up observation, rapid and precise source localization by GW detectors plays a crucial role. As mentioned in section 2.2, as the number of GW detectors increases, the sky localization becomes more precise, since triangulation techniques are used based on the arrival times at the various detectors for the localization of the source in the sky. However, we have to consider a situation where the GW detectors have heterogeneous sensitivities since we are facing such condition as described in section 2.4. Consequently, we need an analysis approach to deal with a heterogeneous-sensitivity detector network especially for rapid source localization. In such configuration, by analyzing the detector signals hierarchically, we will have better fast localization performance.

This work focuses on the sky localization performances, especially in the low-latency mode considering situations where the detector sensitivities are heterogeneous in the network detectors. This setting is motivated since we are already facing this configuration, and, likely, this will continue to be the case with more detectors coming on line in the future. In the US, the Advanced LIGO detectors started operation in 2015 following a decade of commissioning and operation of initial LIGO whose construction started in the 1990's. Advanced Virgo started operation two years later in 2017, after a period of commissioning and upgrade of initial Virgo whose construction had also started in the middle of 1990's. Then KAGRA detector whose construction started much later in 2012, is now being commissioned and is planned to join to the network in second half of O3. As a result, currently there are two higher sensitivity, one middle sensitive and one less sensitive detector.

This chapter addresses the benefit of adding new detectors to the network

made of the two higher sensitive detectors in terms of fast localization performance. The total number of detectors in the network in this work is set to three or four, and the calculation is done assuming 100% duty cycle for each detector.

The following sections describe the details of this study. The discussion for the case of the LIGO-Virgo network with the hierarchical approach is reproduced from [61].

3.1 Fast localization with heterogeneous network

In the upcoming years, it is expected that the detectors in the network will have heterogeneous sensitivities, with detectors still at an early configuration and commissioning stage being less sensitive than more advanced detectors. As written above, in this section, we investigate how to make an effective use of such a network in order to localize coalescing binaries at best with low-latency.

3.1.1 Low-latency search for coalescing binaries

Compact coalescing binaries are sources of particular interest for ground-based GW detectors. When detecting the signals from these events, we perform sky localization in a low-latency mode in order to trigger follow-up observations, especially in the electromagnetic spectrum. In a nutshell, low-latency search pipelines that specifically target compact binary coalescence (CBC) sources operate in the following way:

1. they process the data with matched filtering, based on a discrete set of templates covering a broad source parameters space, and they record triggers when the SNR of the filtered data exceeds some threshold [47].

2. Triggers coincident in several detectors are identified and used to reconstruct the sky location of the source.

3. Events with sufficient significance are then communicated to the astronomy community for follow-up observations.

The LIGO-Virgo Collaboration has been performing low-latency CBC searches with several pipelines: multi-band template analysis (MBTA) [3], GstLAL [1] and pyCBC Live [2].

Candidate events are uploaded to the GraceDb [11]. Then the candidate events are processed through the Bayesian rapid localization algorithm (Bayestar) [4] for fast position reconstruction, which generates probability sky maps.

3.1.2 Hierarchical approach

With three or four detectors of heterogeneous sensitivities in terms of typical detection range for CBC sources, a hierarchical approach can be adopted in order to make an effective use of data from the less sensitive detectors. In this approach,

the presence of an event seen in coincidence in the two more sensitive detectors triggers a focused search in the data of the third (and fourth), less sensitive, detector(s) with a lower SNR threshold. In this process we look for a signal in a small time window around the time of the identified coincidence and having the same source parameters.

So far it was qualitatively considered that such approach will effectively work in the fast localization. In this thesis work I have quantitatively calculated the expected fast localization performance when a hierarchical search is implemented into a GW-EM follow-up pipeline composed of a coalescing binary search algorithm using matched filtering, and a software able to reconstruct sky maps from the outputs of the search algorithms.

The following subsections explores the improvement of fast sky localization performance that can be expected from such a hierarchical approach. Particularly this study is conducted in the framework of the MBTA pipeline, coupled to Bayestar for source localization. However, the approach and results are quite general and could apply beyond the case of a specific pipeline. Section 3.2 describes the settings of the simulation and the figures of merit of the localization performance. Section 3.3 to 3.5 shows the simulated results.

3.2   Calculation set up

This study investigates the localization performance for a set of 248 injections from binary neutron star (BNS) sources (section 3.2.2), in the framework of the MBTA pipeline coupled to the Bayestar, with the following network composed by LIGO, Virgo and KAGRA detectors:

1. three-detector network made by LIGO-Virgo network,

2. three-detector network made by LIGO-KAGRA network,

3. four-detector network made by LIGO-Virgo-KAGRA network.

First, the MBTA is used to apply the matched filtering to the detector outputs. Then, if there is a signal whose signal-to-noise ratio (SNR) exceeds the threshold, MBTA reports the following trigger information for each detector:

1. maximum SNR (as described in section 2.1.1),

2. time of arrival,

3. phase of arrival,

4. noise power spectral density (noise PSD),

for each detector. The time of arrival is the time at which the SNR at the output of the MBTA matched filtering reaches its maximum. Similarly, the phase of

arrival is the phase of the signal at this same time. The noise PSDs assumed for each detector are described in section 3.2.3.

Then, this information measured in each detector (SNR, time and phase of arrival, noise PSD) is provided as inputs to the Bayestar software. The latter builds a sky probability map for the location of the source.

Finally, the figures of merit are extracted from the generated sky maps (see section 3.2.4). We repeat this calculation for different sensitivities and SNR thresholds for Virgo and KAGRA. Then the results are compared.

3.2.1 General configuration

In the matched filtering process (by the MBTA), for the two LIGO detectors:

1. the SNR thresholds are set to 5,

2. the trigger information (SNR, time, phase, noise PSD) is obtained from running the MBTA pipeline on the LIGO simulated data (section 3.2.2).

This was done in [3].

On the other hand, for Virgo and KAGRA we use a different procedure. The Virgo and KAGRA triggers are artificially generated in a way that emulates the result of running the MBTA pipeline (as described in sections 3.2.5 to 3.2.9). This is motivated since we want to explore several relative sensitivities of Virgo and KAGRA compared to LIGO, and several possibilities for the SNR threshold, but we want to avoid running the analysis multiple times.

Then the trigger information of each detector (SNR, time, phase, noise PSD) is used for the calculation by the Bayester. The overview of the main calculation flow is summarized in Figure 3.1.
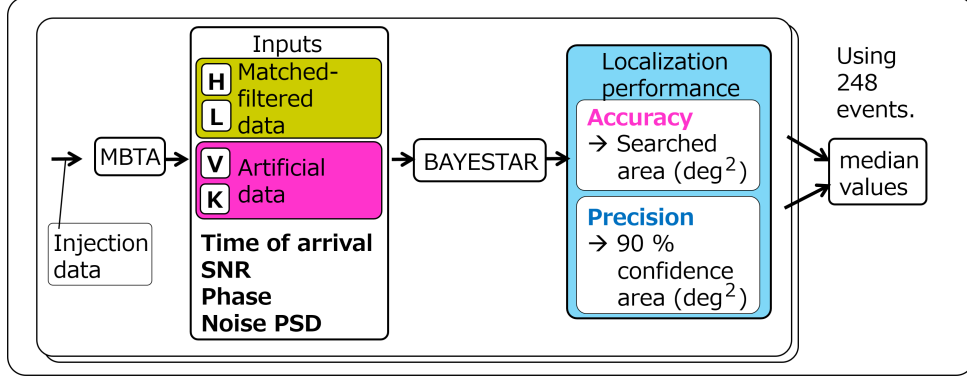
Figure 3.1: Overview of calculation flow. Using sky maps generated for 248 events processed by MBTA and Bayestar, we investigate the accuracy and precision of the localization, quantified by the median values of the searched area and 90% confidence area respectively (see section 3.2.4). We repeat this calculation with different sensitivities and SNR threshold values for the less sensitive Virgo and KAGRA detectors.

3.2.2 Simulated injections

In this study, we use 248 simulated signals from BNS sources. The distribution on the sky of the 248 sources is shown in Figure 3.2 superposed to the LIGO antenna pattern. Figure 3.3 shows the same 248 injection distribution but superposed to the Virgo and KAGRA antenna patterns. The distribution of the distance of the 248 simulated signals is shown in Figure 3.4.

The 248 simulated signals from BNS sources were originally generated in [43]. They were injected into simulated detector noise designed to match the expected initial performance of the Advanced LIGO detectors [43]. Then they were detected using the MBTA pipeline [3] applied to the LIGO-only network.

More specifically, the 248 injections were obtained with the following procedure:

1. originally the locations of 10,000 sources were generated randomly and isotropically over the sky, and uniform in distance cubed[1]. This is done to consider an astro-physically motivated population, since the number of BNS increases as the cube of the distance. The source distribution was cut off at a distance which was far enough away compared to the considering detector sensitivities.

---

[1]For more details, the component masses were uniformly distributed between $1.2 M_\odot$ and $1.6 M_\odot$, and dimensionless component spins of up to 0.05, considering typical configuration.

2. From the events detectable using GstLAL (high-latency CBC search pipeline) with the LIGO network, 250 events were randomly selected.

3. Out of these 250 injections, MBTA found 248 injections in its re-analysis [3]. This set of 248 injections is what we have used in this thesis work.

The first two procedures in the above list were done in [43].

Although the original population of injections composed of 10,000 events was isotropically distributed in space, we consider 248 injections which are detected in the two LIGO detectors, which biases the source directions toward directions favorable for the LIGO detectors.

We use this injection set since this work considers starting from the events detected by LIGO network with MBTA, and then including the less sensitive detector information to the trigger.

Figure 3.2: The sky locations of the 248 injections considered in this work are shown as stars on top of the color-coded combined antenna pattern of the two LIGO detectors. The sources are not uniformly distributed across the sky, but more favorably positioned with respect to the LIGO antenna pattern.

(a) With antenna pattern of Virgo detector
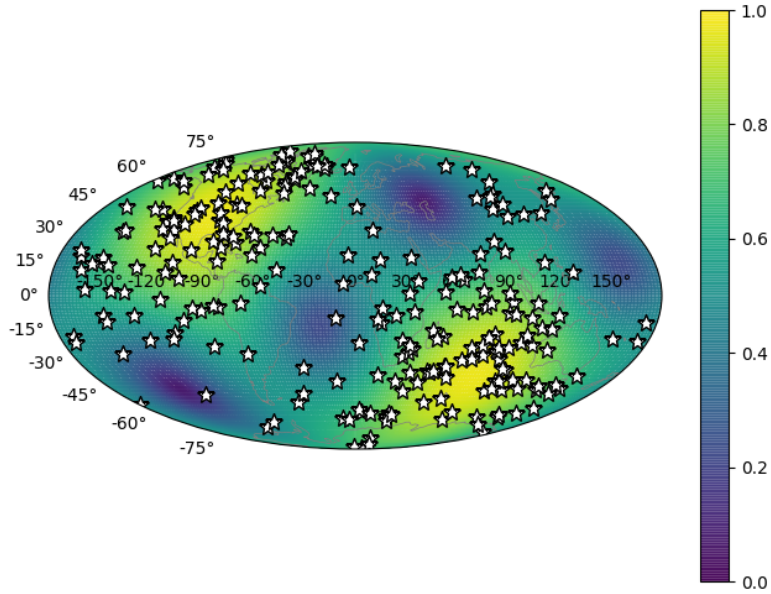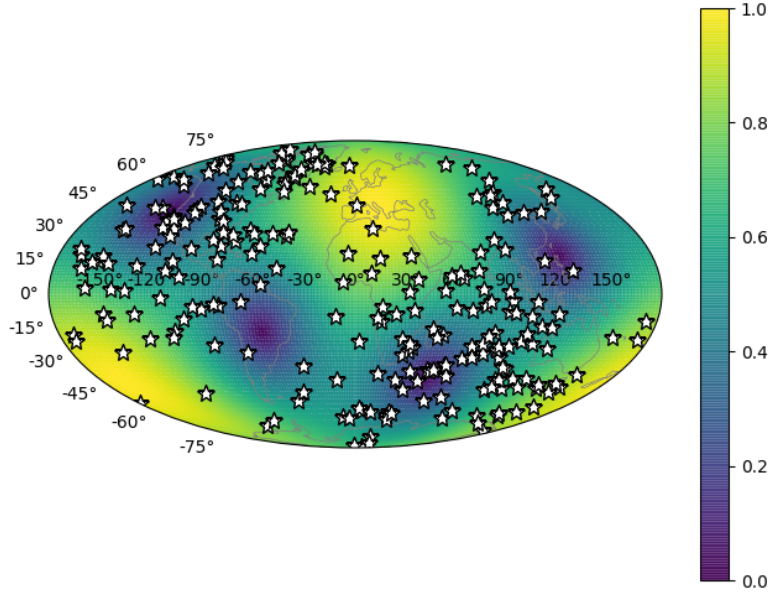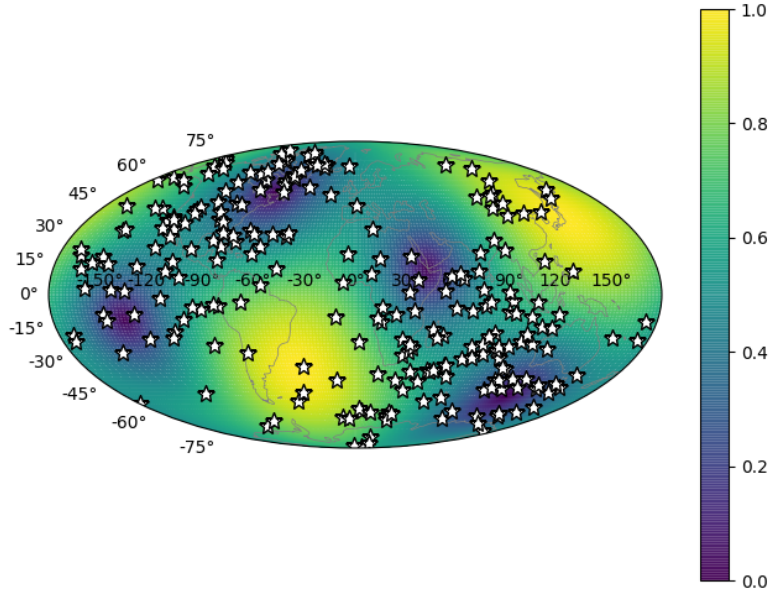

(b) With antenna pattern of KAGRA detector

Figure 3.3: The sky locations of the 248 injections considered in this work are shown as stars on top of the color-coded antenna pattern of Virgo detector (a) and KAGRA detector (b).
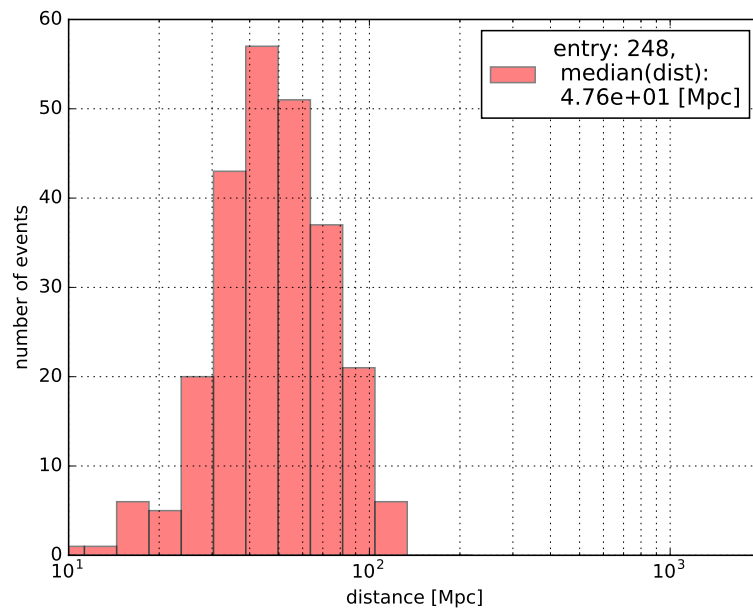
Figure 3.4: The distance distribution of the 248 injections considered in this work.

3.2.3 Detector sensitivity

The simulated data set used in this study was generated assuming noise curves based on early expectations of the 2015 performance of the detectors [43]. In order to explore various cases for the sensitivity of Virgo and KAGRA, the Virgo and KAGRA PSDs were rescaled to correspond to various relative values of the BNS range with respect to LIGO. The noise curves of the network detectors are drawn in Figure 3.5.

Although the corresponding detector sensitivity, which translated into a BNS detection range of 54 Mpc, does not match the more recent performance of the LIGO detectors, this is not an issue for this study, which depends primarily on the relative sensitivities of the detectors in the network and hardly on the absolute value of the BNS range. Therefore our results are relevant for the current and future LIGO-Virgo-KAGRA network.
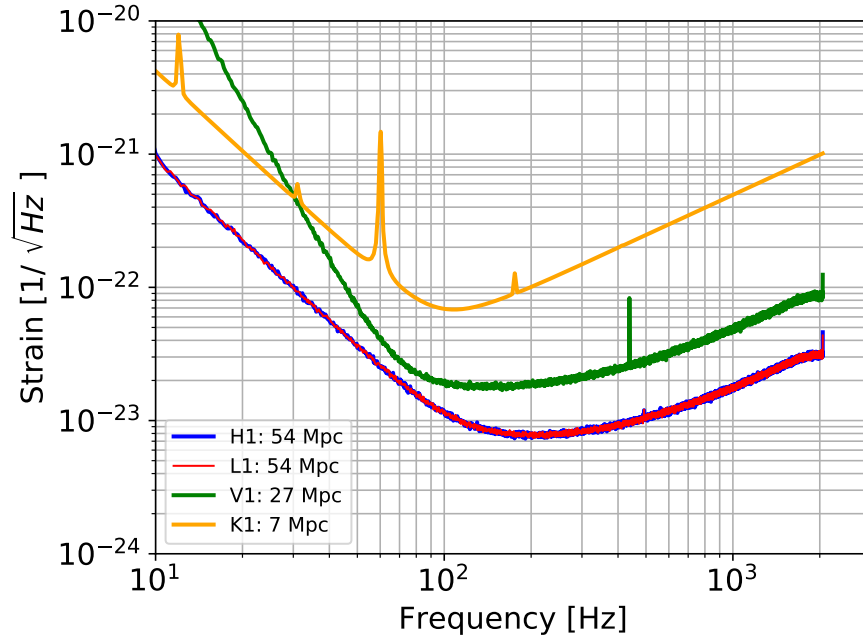
Figure 3.5: The assumed noise curves of the network detectors in amplitude spectral density (ASD). H1, L1, V1, K1 denote the name of the network detectors, i.e., LIGO-Hanford detecotr, LIGO-Livingston detector, Virgo detector and KAGRA detector, respectively. The distances show the BNS range of each detector. The Virgo and KAGRA PSDs were rescaled to correspond to various relative values of the BNS range with respect to LIGO.

3.2.4 Figures of merit

We use the 90% confidence area and the so-called searched area [62] as figures of merit for the performance of the sky localization. The searched area is the area of the highest confidence region around the pixel of maximum probability, that includes the sky location of the injected GW signal. We use searched area since the reconstructed region sometimes has ring shapes, not circle shapes. More details about the searched area can be found in [62] (section 7.2).

The 90% confidence area gives the precision, whereas the searched area quantifies the accuracy of the sky localization. Figure 3.6 shows the schematic view of the 90% confidence area and the searched area.

Accuracy
(Searched area)

Precision
(90 % confidence area)
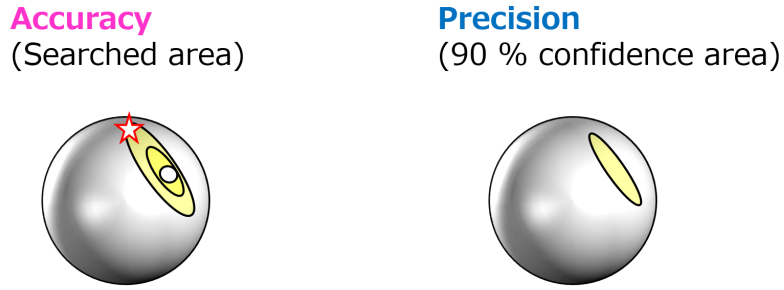
Figure 3.6: The schematic view of the searched area (*left*) and the 90% confidence area (*right*). The searched area quantifies the accuracy of the sky localization, whereas the 90% confidence area gives the precision.

3.2.5 Generating artificial triggers for Virgo

We start from 248 injections detected as HL double coincidences. Depending on the outcome of the targeted search in the Virgo data obtained by looking for a trigger occurring close in time and with the same parameters as the HL coincidence, each of these can either remain a double coincidence if no trigger is found in Virgo (HL case), or else become a triple coincidence (HLV case). The latter case can appear in either one of two possibilities: the trigger found in Virgo is actually related to the injected signal (V_i case) or is related to detector noise (V_n case). The first step of the procedure is therefore to construct a set of injections with appropriate fractions of HL, V_i and V_n cases.

To assess the probability to get a V_n trigger, we need an estimate of the false alarm probability (FAP) in Virgo above a given SNR threshold, for a single template and a time window of 70 ms since we consider Virgo triggers within $\pm$ 35 ms of the LIGO triggers. This is derived from the SNR distribution obtained by running MBTA on representative subsets of O1 data, with about 2×10^5 templates, then assuming that the trigger rate is uniform across templates, and extrapolated below the SNR threshold of 6 applied in these analyses. The extrapolation used a Gaussian function, known to be a good approximation for the distribution of triggers at low SNR, which was confirmed by running small-scale analyses with lower SNR thresholds.

We use two data sets, one corresponding to Virgo showing nominal behavior (quiet case) and one corresponding to a time of excess noise (noisy case). The SNR distributions are shown in Figure 3.7, along with the FAP as a function of SNR threshold that is derived from them.

For each injection, we estimate the SNR expected in Virgo $SNR\,_V^{\text{expected}}$ from the known effective distance D_{eff}^V, allowing for some statistical uncertainty:

$$SNR\,_V^{\text{expected}} \;=\; 2.26 \times (\text{detection range}) \times 8/D_{\text{eff}}^V + \text{Gauss}(0,1), \qquad (3.1)$$

where $\text{Gauss}(\mu, \sigma)$ is a random number derived from a Gaussian distribution with mean μ and standard deviation σ. More details about the effective distance are given in section A.1. In this formula, the factor 8 is the SNR threshold used to define the horizon distance for an optimally located and oriented source. The factor 2.26 connects horizon distance to detection range by averaging on source's location and orientation (for more details see section A.1).

The V_i case applies if $SNR\,_V^{\text{expected}}$ is above the SNR threshold in Virgo $SNR\,_V^{\text{th}}$ and there is no noise trigger louder than the threshold. The probability of such a loud noise trigger is estimated by drawing a random number p_V from a uniform distribution between 0 and 1, and by requiring it to be smaller than $\text{FAP}(SNR\,_V^{\text{expected}})$. The probability of the V_n case depends on the probability of getting a noise trigger above $SNR\,_V^{\text{expected}}$ or above $SNR\,_V^{\text{th}}$ if $SNR\,_V^{\text{expected}}$ is smaller than $SNR\,_V^{\text{th}}$, i.e. $\text{FAP}(max(SNR\,_V^{\text{th}}, SNR\,_V^{\text{expected}}))$. The procedure is summarized in Table 3.1.
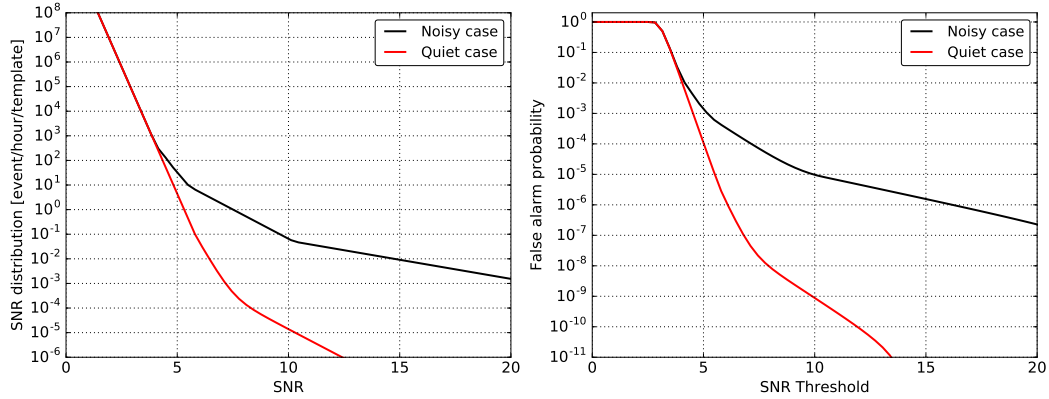
Figure 3.7: (*Left*) SNR distribution of noise triggers per hour and per template using a measurement done during O1 and extrapolated for SNR below 6. The red curve was obtained on quiet data and the black curve on data with excess noise. (*Right*) False alarm probability (FAP) as a function of the SNR threshold, computed as $\mathrm{FAP} = 1 - \exp(-R\,T)$, with R the rate of triggers above threshold per template, derived from the distribution on the left, and $T = 70$ ms. At low SNR threshold, FAP saturates at about 1 since the rate R becomes quite large.

3.2.6 Attributing parameters to Virgo triggers in HLV-network

To produce sky maps for triple coincidences, we need to attribute parameters (SNR, time and phase of arrival) to the V_i or V_n triggers that supplement the HL double coincidence. This is done according to the procedure summarized in table 3.2.

For V_i triggers we use parameters known from the injection metadata, and ad-hoc statistical uncertainties. For the uncertainties we start from educated guesses based on our experience of running the MBTA pipeline, which are then slightly adjusted to get consistent sky localization performances for HLV_i cases, i.e. making sure that the fraction of injections found within the area at a given confidence level matches that confidence level.

More concretely, we compare certain confidence region (searched posterior probability) and the cumulative fraction of the injections as shown in Figure 3.8. The plot in this figure is called probability-probability plot (PP-plot). PP-plot tests if the obtained sky maps have reasonable sizes. If we make a cumulative histogram of the confidence levels corresponding to the searched areas of all the events, it should be found close to a diagonal line in the PP-plot, with small deviations due to finite sample size. For example, 90% of events should have their true locations contained within their respective 90% confidence area, on average.
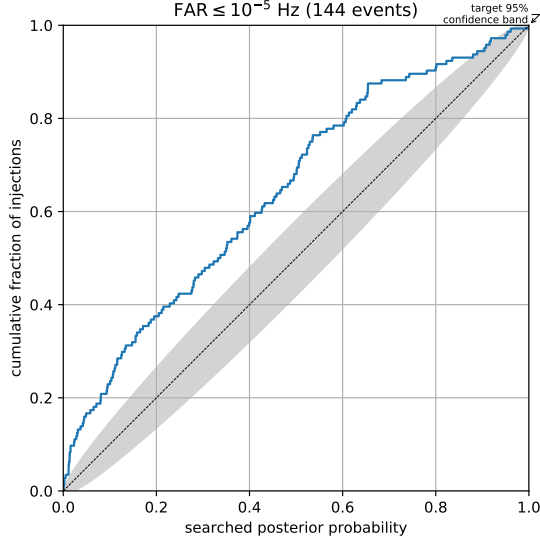
We look for the ad-hoc statistical uncertainties for the time and phase, which give a diagonal line in the PP-plot.

Table 3.1: Procedure for generating coincident events for LIGO-Virgo network. p_V is a random number from a uniform distribution between 0 and 1. FAP$_V$ is the false alarm probability at a given SNR in Virgo.

Conditions	Generated coincidences
if $p_V < $ FAP$_V($ $max(SNR\,_V^{\,\mathrm{th}}, SNR\,_V^{\,\mathrm{expected}})$)	H L V$_\mathrm{n}$
else	
if $SNR\,_V^{\,\mathrm{expected}} > SNR\,_V^{\,\mathrm{th}}$	H L V$_\mathrm{i}$
if $SNR\,_V^{\,\mathrm{expected}} < SNR\,_V^{\,\mathrm{th}}$	H L

Table 3.2: Procedure for attributing parameters to Virgo triggers. $t_{\mathrm{LIGO}}^{\mathrm{measured}}$ and $\phi_{\mathrm{LIGO}}^{\mathrm{measured}}$ represent, respectively, the measured time and phase of arrival at either the LIGO-Hanford or the LIGO-Livingston detector. For these parameters, we use the ones whose SNR is closer to the expected SNR of Virgo detector. $\Delta t^{\mathrm{injection}}$ and $\Delta\phi^{\mathrm{injection}}$ describe the simulated LIGO-Virgo differences of time and phase respectively. Random$[a : b]$ describes a random number uniformly drawn between a and b. We use 0.11 msec and 0.35 rad as typical measurement uncertainties at an SNR of 6 for the time and phase of arrival. These values have been adjusted so that the localization areas at a given confidence level are statistically self-consistent.

V$_\mathrm{n}$: Virgo trigger from noise	
SNR	randomly drawn from the distribution shown in figure 3.7
Time	$t_{\mathrm{LIGO}}^{\mathrm{measured}} + $ Random$[-35\ \mathrm{msec} : 35\ \mathrm{msec}]$
Phase	Random $[0 : 2\pi]$
V$_\mathrm{i}$: Virgo trigger from injections	
SNR	$2.26 \times$ (detection range) $\times\, 8/D_{\mathrm{eff}}^V + \mathrm{Gauss}(0,1)$
Time	$t_{\mathrm{LIGO}}^{\mathrm{measured}} + \Delta t^{\mathrm{injection}} + \mathrm{Gauss}(0, 0.11\ \mathrm{msec} \times 6/SNR\,_V^{\,\mathrm{expected}})$
Phase	$\phi_{\mathrm{LIGO}}^{\mathrm{measured}} + \Delta\phi^{\mathrm{injection}} + \mathrm{Gauss}(0, 0.35\ \mathrm{rad} \times 6/SNR\,_V^{\,\mathrm{expected}})$

(a) without uncertainties
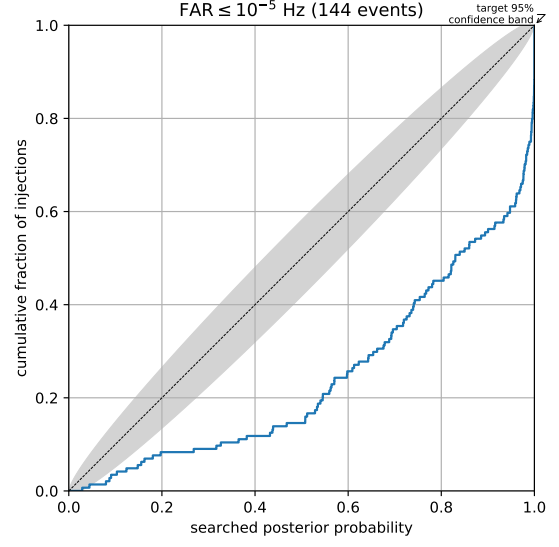
(b) with too much uncertainties
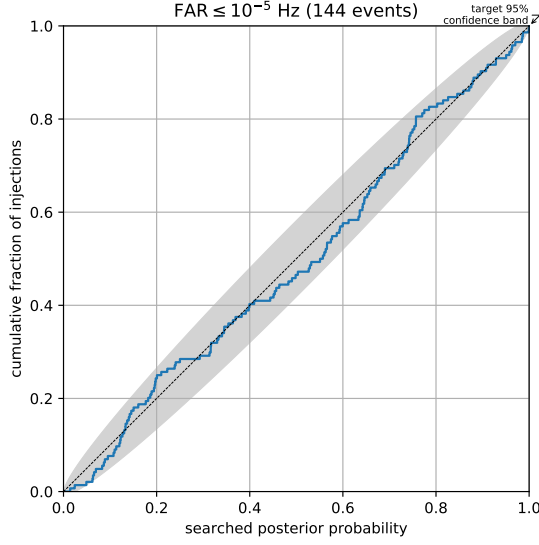
(c) with appropriate uncertainties

Figure 3.8: Examples of the PP-plot used to find the optimal (ad-hoc) statistical uncertainties for the time and phase in the case of HLV_i triggers without uncertainties (a), with too much uncertainties (b) and with appropriate uncertainties (c). The horizontal and vertical axis represents the certain confidence region (searched posterior probability) and the cumulative fraction of the injections respectively. in the case without uncertainties (a), we find 80% of injections within the respective 60% confidence area, while in the case with too much uncertainties (b), we find 25% of injections within the respective 60% confidence area.

84

3.2.7 Generating artificial triggers for KAGRA

The basic idea of generating artificial triggers for KAGRA is same as described in section 3.2.5. We generate K_i and K_n triggers in the same manner as Virgo trigger generation with the parameters for KAGRA. The difference is the time window used for the calculation of the FAP for KAGRA. We used 80 ms as the time window since we consider KAGRA triggers within $\pm$ 30 ms and $\pm$ 40 ms, considering the light flight time between LIGO-Hanford to KAGRA and LIGO-Livingston to KAGRA respectively. Consequently the FAP for KAGRA is slightly different from the FAP for Virgo, as shown in Figure 3.9. Other parameters are defined as:

$$SNR_{\mathrm{K}}^{\text{expected}} = 2.26 \times (\text{detection range}) \times 8/D_{\text{eff}}^{\mathrm{K}} + \text{Gauss}(0,1), \quad (3.2)$$
$$SNR_{\mathrm{K}}^{\text{th}} = (\text{SNR threshold in KAGRA}), \quad (3.3)$$

where $D_{\text{eff}}^{\mathrm{K}}$ is the effective distance for KAGRA. The procedure is summarized in Table 3.3.
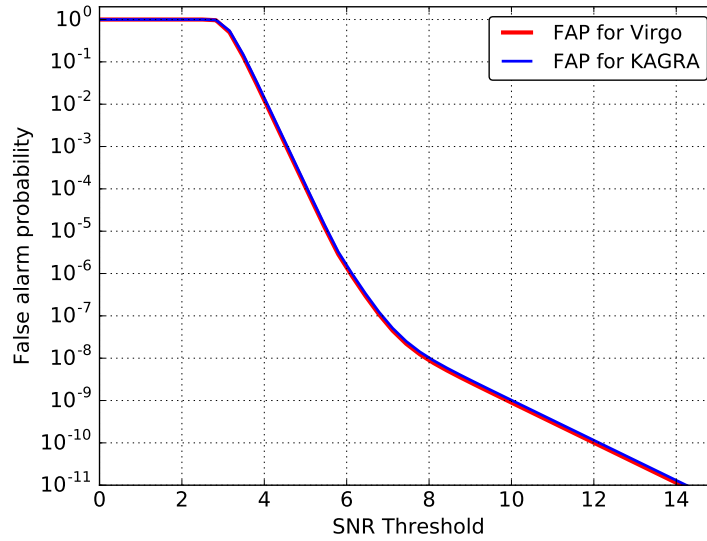
Figure 3.9: False alarm probability (FAP) fir Virgo and KAGRA as a function of the SNR threshold, computed as FAP $= 1 - \exp(-R\,T)$, with R the rate of triggers above threshold per template, derived from the distribution on the left of Figure 3.7, and T for Virgo and KAGRA is set to 70 ms and 80 ms respectively.

3.2.8 Attributing parameters to KAGRA triggers in HLK-network

This process is also done in the same manner as summarized in section 3.2.6. The procedure is summarized in Table 3.4.

Table 3.3: Procedure for generating coincident events for LIGO-KAGRA network. p_{K} is a random number from a uniform distribution between 0 and 1. FAP_{K} is the false alarm probability at a given SNR in KAGRA.

Conditions	Generated coincidences
if $p_{\text{K}} < \text{FAP}_{\text{K}}(\ max(SNR\ _{\text{K}}^{\text{th}},\ SNR\ _{\text{K}}^{\text{expected}})\ )$	H L K_{n}
else	
if $SNR\ _{\text{K}}^{\text{expected}} > SNR\ _{\text{K}}^{\text{th}}$	H L K_{i}
if $SNR\ _{\text{K}}^{\text{expected}} < SNR\ _{\text{K}}^{\text{th}}$	H L

Table 3.4: Procedure for attributing parameters to KAGRA triggers. $t_{\text{LIGO}}^{\text{measured}}$ and $\phi_{\text{LIGO}}^{\text{measured}}$ represent, respectively, the measured time and phase of arrival at either the LIGO-Hanford or the LIGO-Livingston detector. For these parameters, we use the ones whose SNR is closer to the expected SNR of KAGRA detector. $\Delta t^{\text{injection}}$ and $\Delta\phi^{\text{injection}}$ describe the simulated LIGO-KAGRA differences of time and phase respectively. Random$[a : b]$ describes a random number uniformly drawn between a and b. Again we use 0.11 msec and 0.35 rad as typical measurement uncertainties at an SNR of 6 for the time and phase of arrival. These values have been adjusted so that the localization areas at a given confidence level are statistically self-consistent.

K_{n} : KAGRA trigger from noise	
SNR	randomly drawn from the distribution shown in figure 3.7
Time	$t_{\text{LIGO}}^{\text{measured}} + $ Random$[-30$ msec $: 30$ msec$]$, for HK-case
	$t_{\text{LIGO}}^{\text{measured}} + $ Random$[-40$ msec $: 40$ msec$]$, for LK-case
Phase	Random $[0 : 2\pi]$
K_{i} : KAGRA trigger from injections	
SNR	$2.26 \times$ (detection range) $\times 8/D_{\text{eff}}^{\text{K}} + $ Gauss$(0, 1)$
Time	$t_{\text{LIGO}}^{\text{measured}} + \Delta t^{\text{injection}} + $ Gauss$(0,\ 0.11$ msec $\times 6/SNR\ _{\text{K}}^{\text{expected}})$
Phase	$\phi_{\text{LIGO}}^{\text{measured}} + \Delta\phi^{\text{injection}} + $ Gauss$(0,\ 0.35$ rad $\times 6/SNR\ _{\text{K}}^{\text{expected}})$

3.2.9 Generating artificial triggers for Virgo and KAGRA

This is a setting for the investigation of the four-detector case. The artificial trigger generation is processed in accordance with section 3.2.5 and 3.2.7. We also consider the triggers found in Virgo and KAGRA which are actually related to the injected signal (V_i and K_i case), and which are related to detector noise (V_r and K_r case). Parameters are attributed to these triggers as described in section 3.2.6 and section 3.2.8. The procedure is summarized in table 3.5.

Table 3.5: Procedure for generating coincident events for LIGO-Virgo-KAGRA network. p_V and p_K is a random number from a uniform distribution between 0 and 1. FAP_V and FAP_K are the false alarm probabilities at a given SNR in Virgo and KAGRA respectively.

Conditions	Generated coincidences
if $p_V < FAP_V(\ max(SNR_V^{th},\ SNR_V^{expected})\ )$	
if $p_K < FAP_K(\ max(SNR_K^{th},\ SNR_K^{expected})\ )$	H L V_n K_n
else	
if $SNR_K^{expected} > SNR_K^{th}$	H L V_n K_i
else	H L V_n
else	
if $SNR_V^{expected} > SNR_V^{th}$	
if $p_K < FAP_K(\ max(SNR_K^{th},\ SNR_K^{expected})\ )$	H L V_i K_n
else	
if $SNR_K^{expected} > SNR_K^{th}$	H L V_i K_i
else	H L V_i
else	
if $p_K < FAP_K(\ max(SNR_K^{th},\ SNR_K^{expected})\ )$	H L K_n
else	
if $SNR_K^{expected} > SNR_K^{th}$	H L K_i
else	H L

3.3 Expected performance of heterogeneous HLV-network

3.3.1 Sky localization performance

Using the settings in section 3.2.5 and 3.2.6, we generate sky maps of 248 events and investigate the localization performance by collecting the median values of searched area and 90% confidence area. This calculation is repeated with different SNR thresholds in Virgo. First, we assumed that the two LIGO detectors have the same range while the Virgo detector has 39% of the range of the LIGO detectors to roughly mimic the O2 sensitivity. The calculated performance is shown in Figure 3.10. The dots show the median of the localization areas over the set of injections. The uncertainties report the interquartile range, which is the range between 75 percentile and 25 percentile of the localization areas. In order to check that the results were not overly sensitive to a particular realization of the random numbers used in the simulation, the procedure was repeated twice, and since the results were consistent, the figure reports the average (quadratic average) of the medians (uncertainties) obtained in the two trials. The relative detector sensitivities are written down as 1-1-x, with x the ratio of the Virgo sensitivity compared to the two LIGO detectors.

The plots show that the optimal SNR threshold in Virgo is around 3. At this threshold, the localization is improved by about a factor of 4. In this configuration, about 51% of the 248 events are reconstructed as HLV$_i$ triggers, 36% as HLV$_n$ triggers, and 13% are HL triggers. The percentage of these three types of triggers depends on the Virgo threshold (these percentages depend on the Virgo sensitivity and threshold).

Figure 3.10 also includes the localization performance when the lower sensitivity detector generates louder background triggers compared to a stable case. In this noisy case investigation, the SNR distribution and the FAP in Virgo are derived from the black curves instead of the red curves in Figure 3.7. This has no impact on the localization performance and in the following we work only in the quiet case.
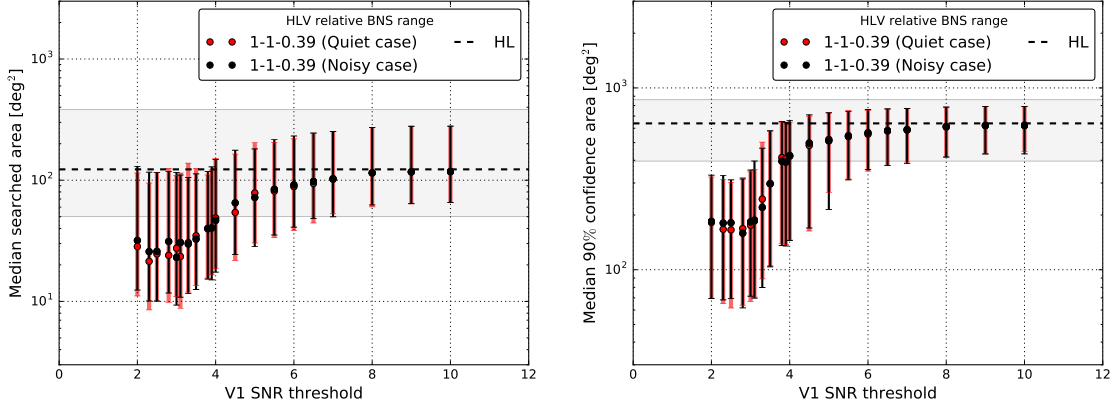
Figure 3.10: The sky localization performance of the heterogeneous network search by three detectors. The searched area is shown in *left* panel, and the 90% confidence area is shown in *right* panel. These plots show the median with its interquartile range. The dashed black line shows the performance using the two LIGO detectors only. The red colored dots are for the case when the detector is quiet, while the black ones correspond to the noisy condition. The performances in the two cases are similar.

As another test, in order to verify the artificial trigger generation in this work, we also actually run MBTA on Virgo data with a SNR threshold ranging from 5 to 10. We obtained consistent median values for the searched area and 90% confidence area compared to the localization performance obtained with artificial Virgo triggers at those threshold as shown in Figure 3.11.
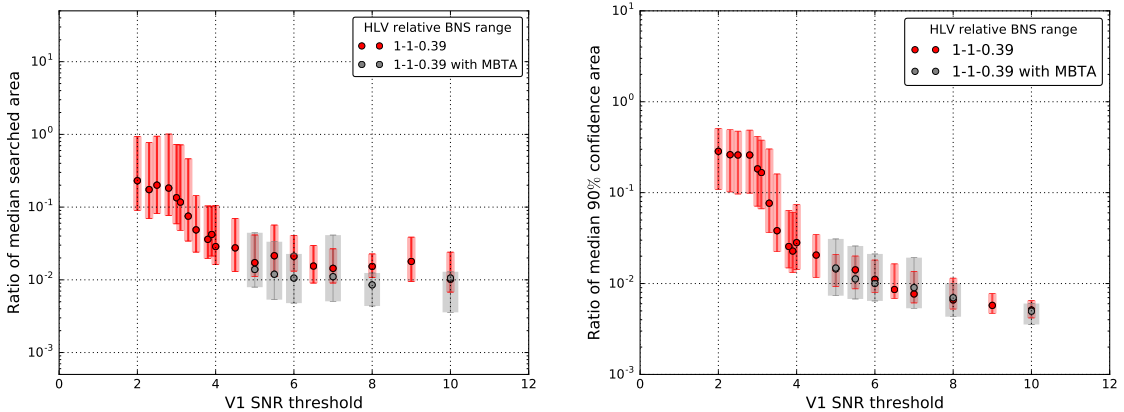

Figure 3.11: Ratio of the median searched area (*left*) and 90% confidence area (*right*) of HLV triggers to that of the same triggers treated as HL coincidences, with the interquartile ranges. The median values of the searched area and 90% confidence area with the artificial Virgo triggers are consistent with the ones obtained by the actual MBTA run with a SNR threshold ranging from 5 to 10.

89

3.3.2 Dependence on the sensitivity of Virgo detector

We calculate the localization performance for various BNS ranges of the Virgo detector. This is obtained by scaling its expected SNR using (3.1) and its noise curve. The other settings are as described in section 3.2. The population of the HL, HLV$_i$ and HLV$_r$ events are summarized in section A.2. The expected performances in terms of searched area and 90% confidence area are shown in Figure 3.13. The hierarchical search with three detectors will improve the precision (90% confidence area) of the localization regardless of the value of the BNS range. On the other hand, if the BNS range for the lower sensitivity detector is too low, the accuracy of the localization will be slightly degraded since it will be more likely to get triple coincidences with Virgo noise triggers. However, this effect will not be so large; noisy Virgo triggers will mainly be found when the sensitivity is much lower than the sensitivities of the LIGO detectors. In this situation, the reconstructed sky maps will be similar to the ones obtained with the LIGO detectors only. This result is due to Bayestar. Since Bayestar uses a Bayesian procedure to calculate the sky map. It takes into account the lower sensitivity of Virgo and then reduces its impact on the sky map. Figure 3.12 shows the improvement in the performance for those events that become triple coincident events when Virgo is added to the network.

Based on Figures 3.12 and 3.13, the lower sensitivity detector begins to improve the localization performance as soon as its sensitivity is 20% of the more sensitive detectors. Then the optimal SNR threshold lies in the range from 3 to 3.5. We select the threshold in Virgo to 3.5 in order to reduce the number of triggers and to make handling the data easier. The dependence on the sensitivity of Virgo detector when its threshold is equal to 3.5 is shown in Figure 3.14. We find that as the sensitivity of Virgo approaches half of the LIGO one, the accuracy and precision of the localization can be improved by about a factor of 7, compared to LIGO network.
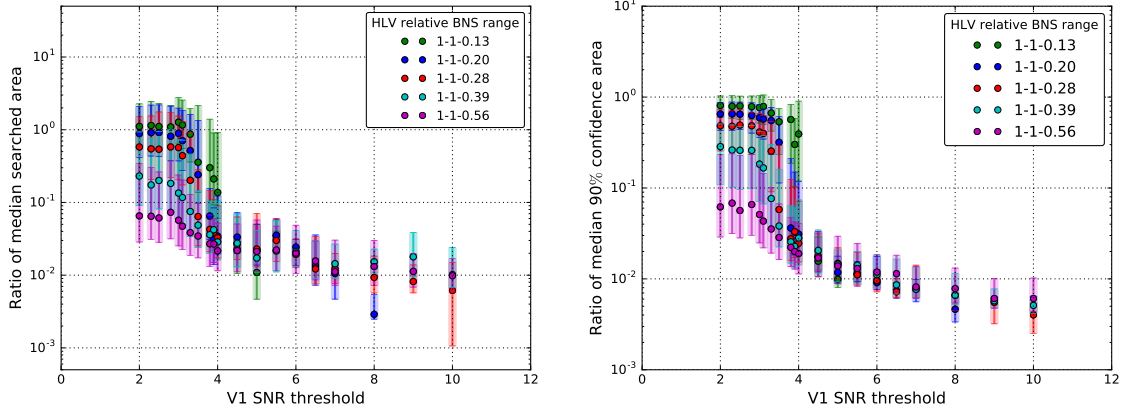
Figure 3.12: Ratio of the median searched area (*left*) and 90% confidence area (*right*) of HLV triggers to that of the same triggers treated as HL coincidences, with the interquartile ranges. As the sensitivity improves, HLV_n triggers become less likely whereas HLV_i triggers become more likely and benefit the localization performance.
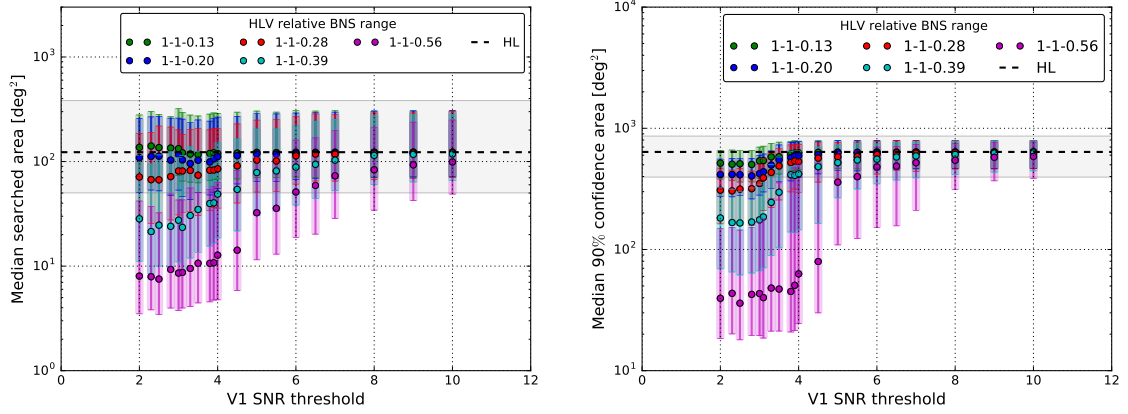

Figure 3.13: The median searched area (*left*) and 90% confidence area (*right*) with the interquartile ranges are shown as a function of the SNR threshold used in Virgo. Expected sky localization performance with the hierarchical search when the sensitivity of the Virgo detector is varied. The colors show the network configuration.
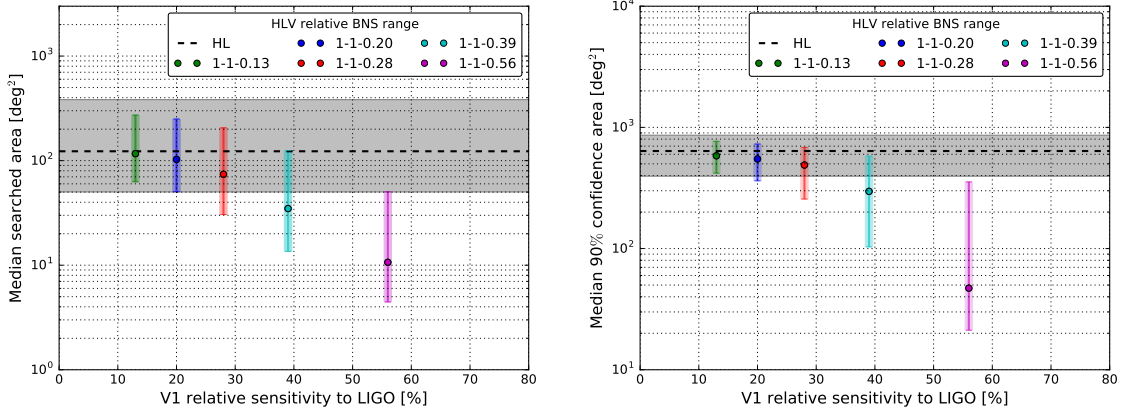
Figure 3.14: The median searched area (*left*) and 90% confidence area (*right*) with the interquartile ranges are shown as a function of the relative sensitivity of Virgo compared to the LIGO one where the Virgo threshold is set to 3.5. The colors show the network configuration.

Concerning the sky maps, the reconstructed region by HLV coincident triggers will be a fraction of the area reconstructed by the two LIGO detectors only. If a coincident trigger is built from two LIGO signals and a noise Virgo trigger, the area pointed by the HLV network starts to shift from the source position, mostly due to the error on the detection time in Virgo. However, if the range of Virgo detector is much lower than the LIGO ones, the reconstructed area remains similar to the ring shape region reconstructed by the two LIGO detectors only even when the Virgo trigger is due to noise. This hierarchical search will find ring-shaped sky maps when the sensitivity of the third detector is much lower than the higher sensitivity ones. As the sensitivity improves, the sky maps progressively turn into point-like regions inside the area identified by the two LIGO detectors only.

3.4 Expected performance of heterogeneous HLK-network

With the same method used for the HLV-network case, we calculate the expected localization performance of heterogeneous HLK-network. Using the settings in section 3.2.7 and 3.2.8, we generate sky maps of 248 events and investigate the performance by collecting the median values of searched area and 90% confidence area. This calculation is repeated with different SNR thresholds in KAGRA. As in the case of the HLV-network, also in this case, the procedure is repeated twice in order to check that the results are not overly sensitive to a particular realization of the random numbers used in the simulation. From the result shown in section 3.3.1, we consider a case where the less sensitive detector KAGRA is in the quiet condition, not in the noisy condition.

3.4.1 Dependence on the sensitivity of KAGRA detector

In the same way as in section 3.3.2, we calculate the localization performance for various BNS ranges of the KAGRA detector, by scaling its expected SNR using (3.2) and its noise curve. The population of the HL, HLK_i and HLK_n events are summarized in section A.2. The expected improvement ratio of the performance of HLK triggers to that of the same triggers treated as HL coincidences is shown in Figure 3.15. The expected performances in terms of searched area and 90% confidence area obtained from all the 248 events are shown in Figure 3.16. The relative detector sensitivities are written down as 1-1-x, with x the ratio of the KAGRA sensitivity compared to the two LIGO detectors.

The obtained results lead qualitatively to the same conclusions as in the HLV-network case. Based on Figures 3.15 and 3.16, the lower sensitivity detector begins to improve the localization performance as soon as its sensitivity is 28% of the more sensitive detectors. Then the optimal SNR threshold lies in the range from 3 to 3.5. By following the LIGO-Virgo network case, we select the threshold in KAGRA to 3.5 in order to reduce the number of triggers and to make handling the data easier. The dependence on the sensitivity of KAGRA detector at the threshold is equal to 3.5 is shown in Figure 3.17. We find that as the sensitivity of KAGRA approaches half of the LIGO one, the accuracy and precision of the localization can be improved by about a factor of 3.5, compared to the LIGO network only.
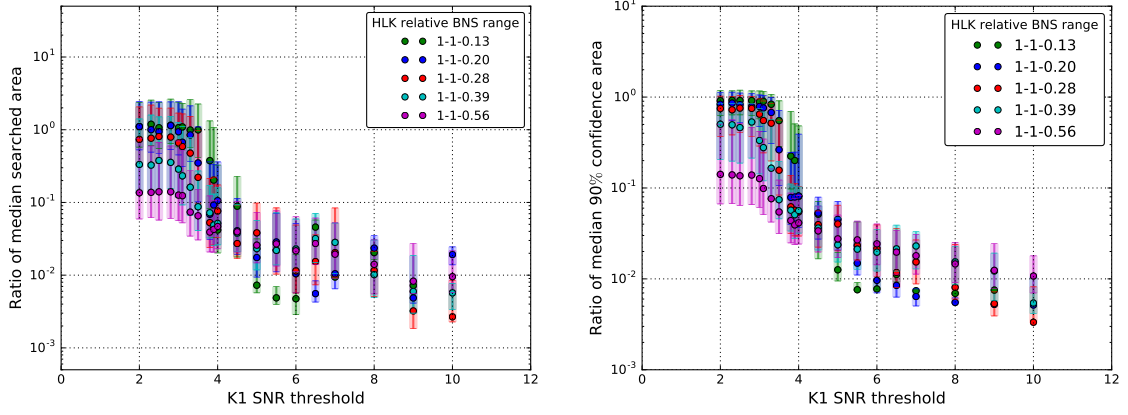
Figure 3.15: Ratio of the median searched area (*left*) and 90% confidence area (*right*) of HLK triggers to that of the same triggers treated as HL coincidences. As the sensitivity improves, HLK_n triggers become less likely whereas HLK_i triggers become more likely and benefit the localization performance.
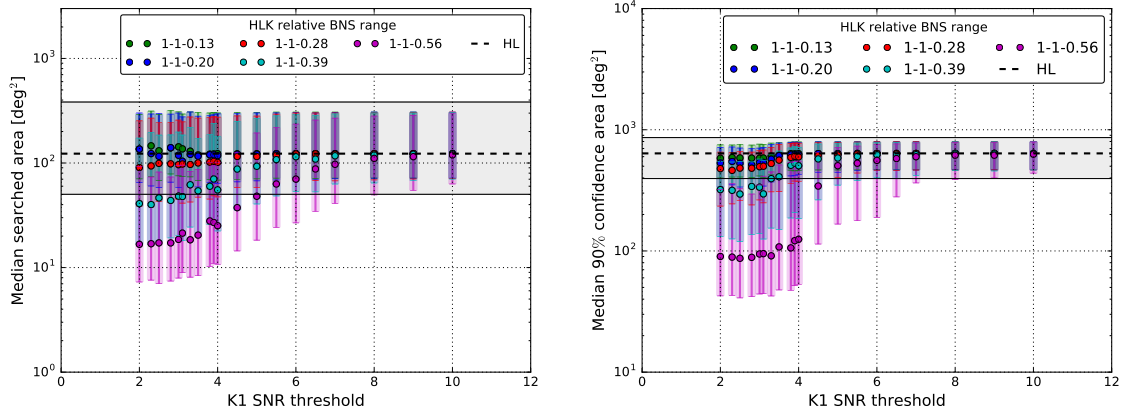

Figure 3.16: The median searched area (*left*) and 90% confidence area (*right*) are shown as a function of the SNR threshold used in KAGRA. Expected sky localization performance with the hierarchical search when the sensitivity of the KAGRA detector is varied. The colors show the network configuration.
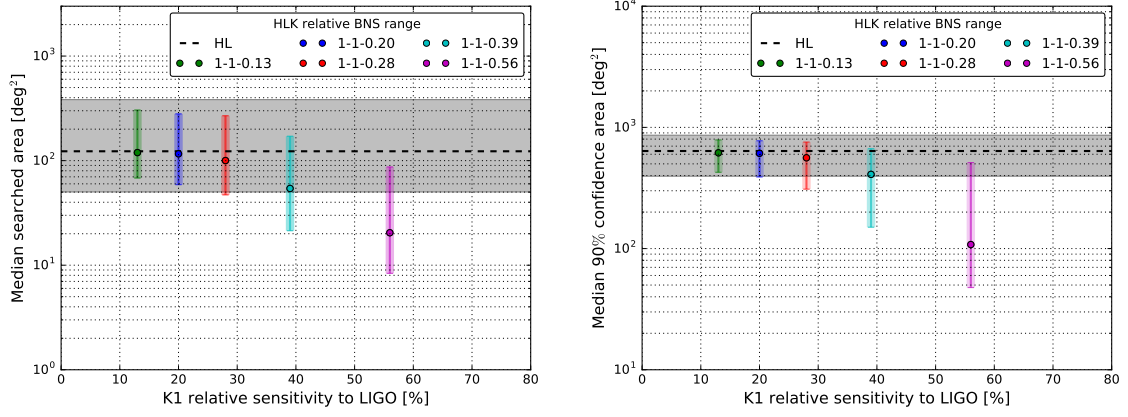
Figure 3.17: The median searched area (*left*) and 90% confidence area (*right*) with the interquartile ranges are shown as a function of the relative sensitivity of KAGRA compared to the LIGO one where the KAGRA threshold is set to 3.5. The colors show the network configuration.

3.4.2 Comparison to HLV-network performance

As seen in Figure 3.13 and 3.16, the size of the reconstructed sky maps by the HLK-network would become larger than that by the HLV-network, by roughly a factor of 2. This feature would come from the geometry of the network detector positions. The geometry of the HLK-network is slightly less favorable than the geometry of the HLV-network.

In order to test this statement, we confirm the followings.

1. The consistent sky localization performances for HLK_i are obtained, i.e. it is confirmed that the fraction of injections found within the area at a given confidence level matches that confidence level.

2. The population of HL, HLK_i, HLK_n triggers are mostly similar to the ones of HL, HLV_i, HLV_n.

3. The SNR distributions of HLK_i, HLK_n triggers are also similar to the ones of HLV_i, HLV_n.

4. This performance does not come from the difference of the used noise curves.

In addition, We investigate the performance by HLV-network and HLK-network with the events whose effective distances are close to each other as shown below.

Examination of localization performance with similar D_{eff} events

We select the HLV- and HLK-events whose difference of the effective distance is smaller than 10% (i.e, with a condition of $| 1 - D_{\text{eff}}^{\text{V}}/D_{\text{eff}}^{\text{K}} | < 0.1$). We then calculate the localization performance with the pure injection parameters without adding the small random number derived from a Gaussian distribution. The result is shown in Figure 3.18. Although we find just 28 such events, on average, this shows that the HLK-network would give larger-reconstructed sky maps compared to the ones by HLV-network. One example of the sky maps are drawn in Figure 3.20. The sky maps show that the reconstructed ring-shaped regions by the HK or LK network are comparably more parallel to the ring deduced from the HL network than the rings from the HV or LV network. As a result, the intersection tends to be larger. This seems to connect to the geometry of the detector position. The detector triangles composed of the two LIGO detectors with Virgo and KAGRA detector is shown in Figure 3.19. This figure shows that the triangle made by the HLK-detectors is flatter than the one made by the HLV-detectors. In addition, the determinants of the matrix $\boldsymbol{M}$ (section 2.2, eq (2.13)), differs by about a factor of 2, which is consistent with the difference observed in the localization performance.

From the above, we conclude that the performance of the HLV-network would be slightly better than that of the HLK-network, due to the geometrical configuration of the detectors. The results obtained for the HLK-network are shown in Figure 3.16. The results are indeed slightly worse than the one for the HLV-network in Figure 3.13.
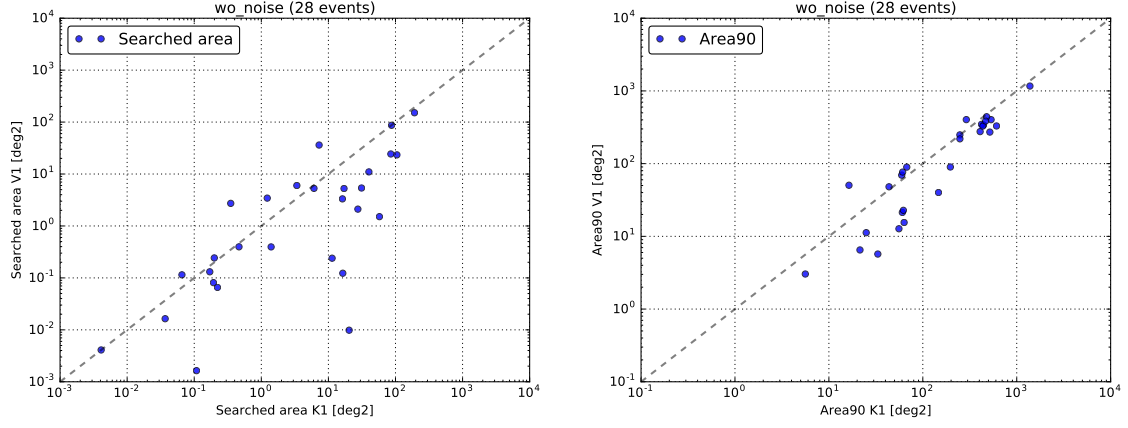
Figure 3.18: The sky localization performance by HLV- and HLK-network with similar D_{eff} events. These plots show the median values.
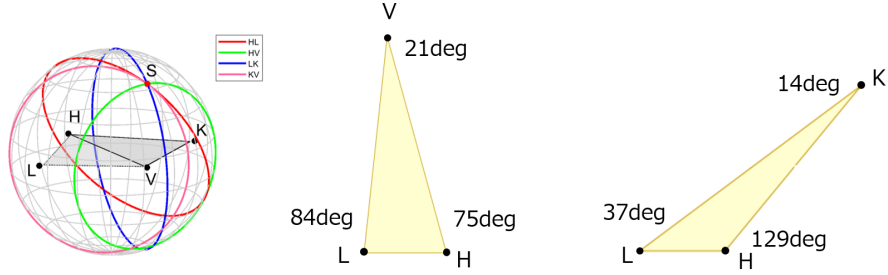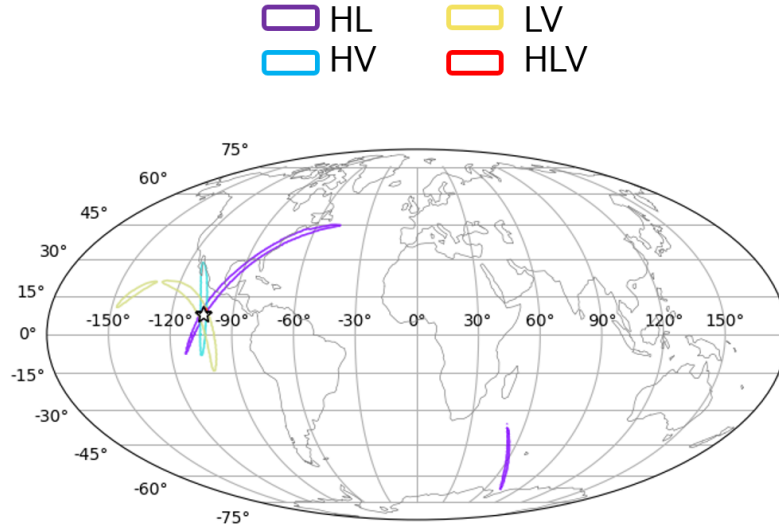

Figure 3.19: The triangles composed of the three detectors. H, L, V and K denote the LIGO Hanford detector, LIGO Livingston detector, Virgo detector and KAGRA detector. The triangle composed of the HLK detectors is more flatter than the triangle composed of the HLV detectors. The most left figure is from [63].

(a) Sky map example obtained by LIGO-Virgo network. The area reconstructed by HLV-network (red) is mostly hidden by the star.
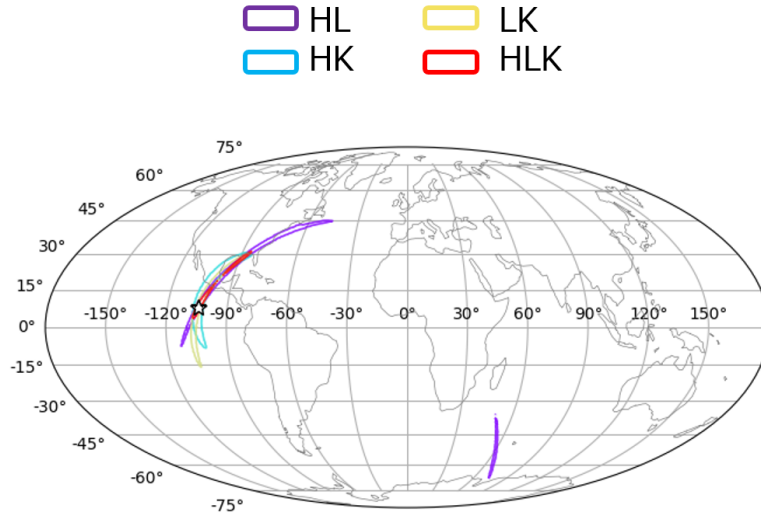
(b) Sky map example obtained by LIGO-KAGRA network

Figure 3.20: Sky map example obtained by LIGO-Virgo network (a) and by LIGO-KAGRA network (b).

3.5 Expected performance of heterogeneous HLVK-network

Similarly what we do for the HLV- and HLK-network cases, we calculate the expected localization performance of heterogeneous HLVK-network. Using the settings described in section 3.2.6, 3.2.8 and 3.2.9, we generate sky maps of 248 events and investigate the localization performance by collecting the median values of searched area and 90% confidence area. In this calculation, we assume that the sensitivity of Virgo detector is half of the sensitivities of the two LIGO detectors. We then consider different sensitivities for KAGRA. The calculation is repeated with different SNR thresholds for KAGRA (from 2 to 10), and for Virgo (3.0, 3.5, 4.0 and 5.0). The procedure is repeated twice in order to check that the results were not too sensitive to a particular realization of the random numbers used in the simulation. We also consider a case where the both less sensitive detectors Virgo and KAGRA are in the quiet condition, not in the noisy condition.

3.5.1 Dependence on the sensitivity of the fourth detector KAGRA

The expected performances of the searched area and the 90% confidence area by the HLVK-network are shown in Figure 3.21 to 3.24. Figure 3.21 shows the expected improvement ratio of the performance of HLVK triggers to that of the same triggers treated as HLV coincidences. Figure 3.22 shows the expected performances of the searched area and the 90% confidence area obtained from all the 248 events. These two figures draws the case where the SNR threshold for Virgo is set to 5.0. We calculate this performance for various BNS ranges of the KAGRA detector, by scaling its expected SNR and its noise curve. The relative detector sensitivities are written down as 1-1-0.5-x, with x the ratio of the KAGRA sensitivity compared to the two LIGO detectors.

Figure 3.23 and 3.24 reports the performance when the SNR threshold of Virgo detector is set to 3.5, with the other parameters same as used in Figures 3.21 and 3.22. The expected performances with other configuration are summarized in section A.3. The population of the HL, HLV_i, HLV_n, HLK_i, HLK_n, HLV_iK_i, HLV_nK_n, HLV_iK_n and HLV_nK_i events are summarized in section A.2.

Figures 3.22 and 3.24 show that, similarly to the HLK-network case, the lowest sensitive detector begins to improve the localization performance as soon as its sensitivity is 28% of the more sensitive detectors. Then the optimal SNR threshold lies in the range from 3 to 3.5. In the case where the SNR threshold of the Virgo detector is set to 5.0, i.e where the information of Virgo detector is not much reflected to the sky maps, KAGRA detector information will contribute to improvement of the localization performance relatively significantly. On the other hand, in the case where the SNR threshold of Virgo detector is set to 3.5, i.e where the information of Virgo detector is already reflected to the sky maps, KAGRA detector information would contribute less to improving the localization performance

It must be noted that, Figure 3.21 and 3.23 report that as the detector

sensitivity of KAGRA increases, the averaged performance by HLVK-network at higher SNR threshold in KAGRA detector becomes worse. This happens since we start from the events detection by the LIGO detectors, which is unfavorable to KAGRA detector, and thus that happens since KAGRA detector finds more events which are less aligned to KAGRA detector as its sensitivity is increased.

Consequently, the lowest sensitivity detector begins to improve the localization performance clearly as soon as its sensitivity is one third of the most sensitive LIGO detectors, which is two third of the sensitivity of the middle sensitive detector Virgo. The optimal SNR threshold lies in the range from 3 to 3.5.

By following the LIGO-Virgo and LIGO-KAGRA network case, we select the threshold in Virgo and KAGRA to 3.5. We also suppose that the Virgo sensitivity is half of the LIGO one. The dependence on the sensitivity of KAGRA detector in these conditions is shown in Figure 3.25. In this configuration, we find that as the sensitivity of KAGRA approaches half of the LIGO one (same as Virgo one), the accuracy and precision of the localization can be improved by about a factor of 2 and 2.5 respectively, compared to LIGO-Virgo network.
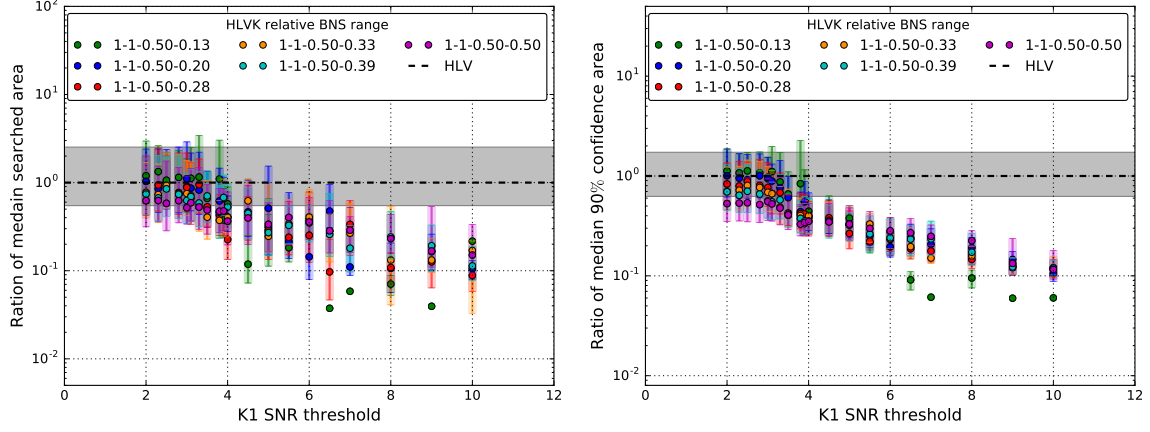
Figure 3.21: Ratio of the median searched area (*left*) and 90% confidence area (*right*) of HLVK triggers to that of the same triggers treated as HLV coincidences, when the sensitivity of the KAGRA detector is varied. The colors show the network configuration. This is the case where the SNR threshold for Virgo is set to 5.0.

Figure 3.22: The median searched area (*left*) and 90% confidence area (*right*) are shown as a function of the SNR threshold used in KAGRA. Expected sky localization performance with the hierarchical search when the sensitivity of the KAGRA detector is varied. The colors show the network configuration. This is the case where the SNR threshold for Virgo is set to 5.0.

Figure 3.23: Ratio of the median searched area (*left*) and 90% confidence area (*right*) of HLVK triggers to that of the same triggers treated as HLV coincidences, when the sensitivity of the KAGRA detector is varied. The colors show the network configuration. This is the case where the SNR threshold for Virgo is set to 3.5.
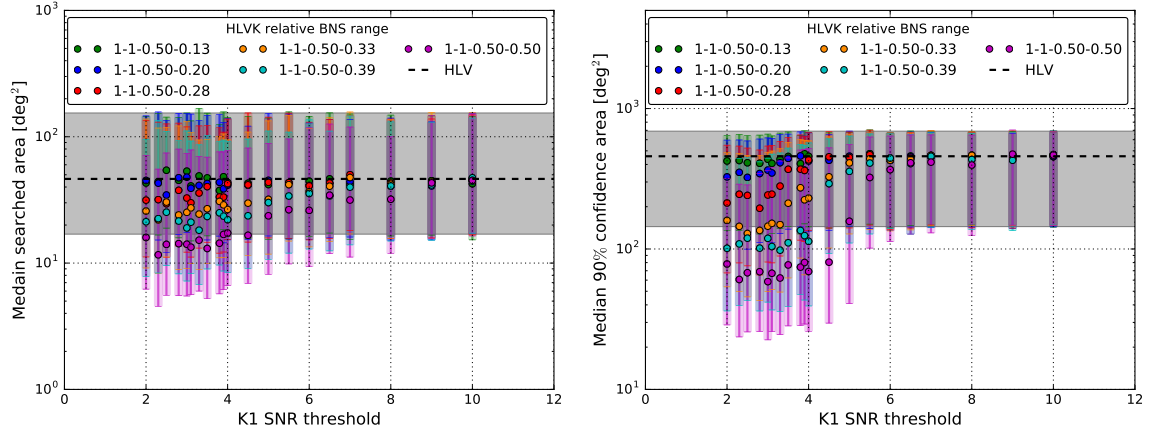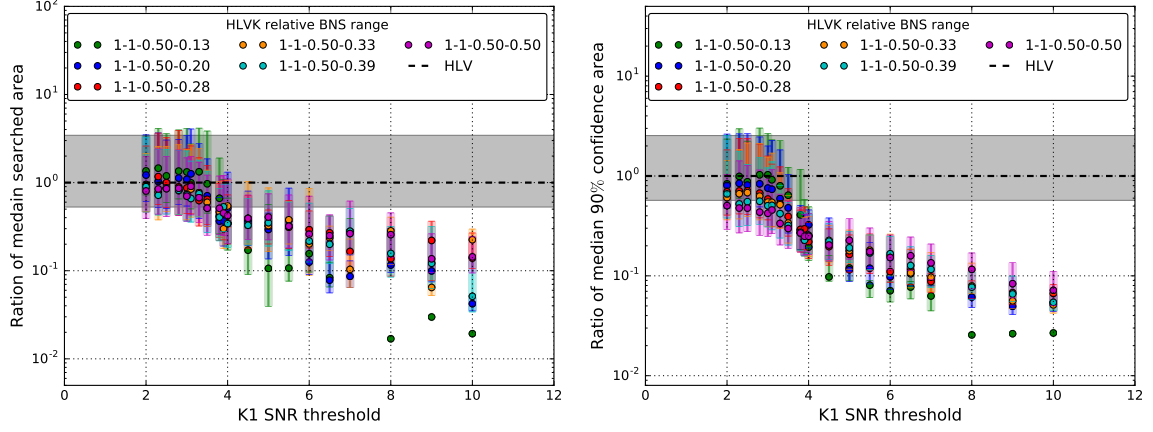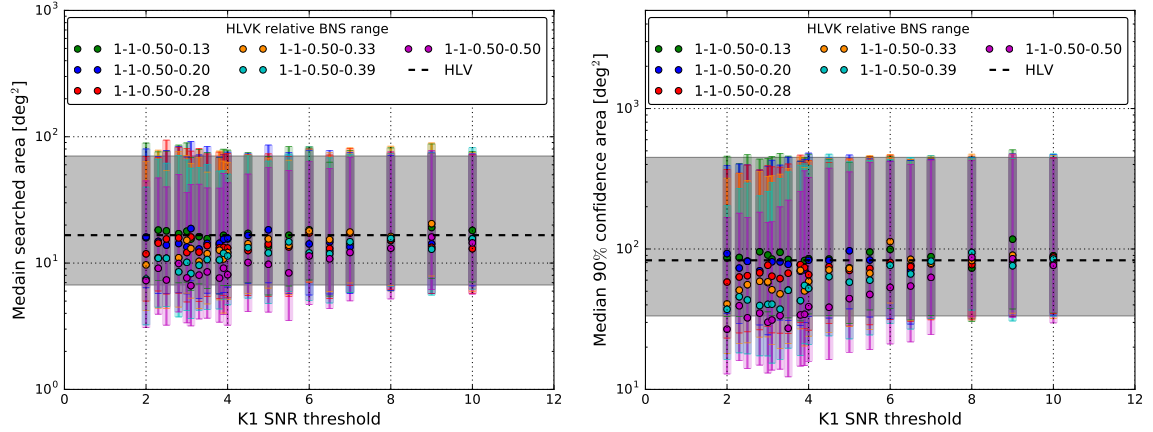

Figure 3.24: The median searched area (*left*) and 90% confidence area (*right*) are shown as a function of the SNR threshold used in KAGRA. Expected sky localization performance with the hierarchical search when the sensitivity of the KAGRA detector is varied. The colors show the network configuration. This is the case where the SNR threshold for Virgo is set to 3.5.

102
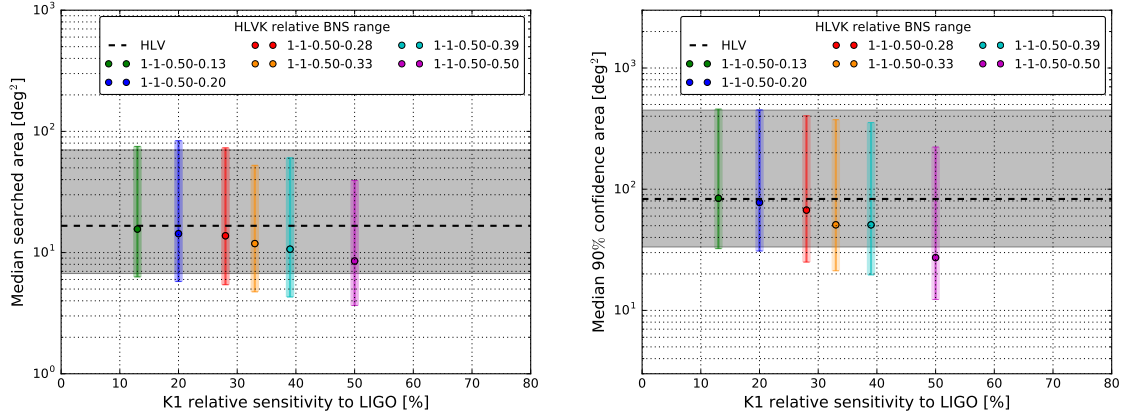
Figure 3.25: The median searched area (*left*) and 90% confidence area (*right*) with the interquartile ranges are shown as a function of the relative sensitivity of KAGRA compared to the LIGO one where the KAGRA threshold is set to 3.5. In this configuration, it is assumed that Virgo has half of the LIGO sensitivity and its threshold is set to 3.5. The colors show the network configuration.

3.6 Summary

Using MBTA and Bayestar, we show the expected fast localization performance for GWs from compact binary coalescence when a hierarchical search is implemented into a GW-EM follow-up pipeline. We confirm that the hierarchical search improves both the localization accuracy and precision in low-latency mode, compared to those achieved by a double coincidence search with the two LIGO detectors alone.

We first consider the case where the detector network is composed of the two LIGO detectors and the Virgo detector. The hierarchical network effectively improves the localization accuracy and precision when the threshold SNR for the lower sensitivity detector is set to around 3.5 provided that the BNS range of that the detector is greater than 20% of the more sensitive detectors. We find that as the sensitivity of Virgo approaches half of the LIGO one, the accuracy and precision of the localization can be improved by about a factor of 7, compared to the LIGO network only (section 3.3.2).

In the case where the detector network is composed of the two LIGO detectors and KAGRA detector, we found a clear sky localization improvement when the relative sensitivity of KAGRA becomes greater than 28% of the more sensitive detectors. We find that as the sensitivity of KAGRA approaches half of the LIGO one, the accuracy and precision of the localization can be improved by about a factor of 3.5, compared to LIGO network (section 3.4.1). The performance difference between LIGO-Virgo network and LIGO-KAGRA network comes from the difference between the geometrical configuration of the two networks (section 3.4.2). Finally we consider the HLVK-network. We find that the hierarchical network composed of the four detectors will improve the localization accuracy and precision when the threshold SNR for the lowest sensitivity detector is set to around 3.5 provided that the BNS range of that the detector is greater than 28% of the most sensitive detectors. This result assumes that the sensitivity of the middle sensitive Virgo detector is half of the LIGO one. In this configuration, we find that, as the sensitivity of KAGRA approaches half of the LIGO one (same as Virgo one), the accuracy and precision of the localization can be improved respectively by about a factor of 2 and 2.5 respectively, compared to the LIGO-Virgo hierarchical network (section 3.5.1).

Consequently, the search with this hierarchical approach will be very useful when adding new, less sensitive detectors to the network, as they are undergoing commissioning.

Realizing higher network duty cycle

This study did not consider the aspect of the network duty cycle. Indeed the probability to have at least three detectors up and running increases considerably when a fourth detector is added to the network. This is another benefit of adding detectors to the network and reduces the chances to miss detectable events. This comes from a fact that sometimes a GW detector is not operational due to interferomenter lock loss and/or maintenance operation. For example, assuming that all the detectors have an equal duty cycle of 80% (which is a typical value), the duty cycle by three detectors in the three detector network would be about 51%. On the other hand, for a network made by four detectors, the duty cycle by three or four detectors becomes about 82%. This implies that in the three- and four-detector network, respectively about 49% and 18% of the detected events would have poor reconstructed sky position, even though all the network detectors have enough sensitivities. This is not suitable to the target of the EM follow up observation of rare events. This fact implies that operating a fourth robust interferometer is of paramount importance to achieve high network duty cycle.

The following chapters of this thesis focuses on the construction of a system to allow a robust interferometer operation of the fourth detector KAGRA.

Chapter 4

Low frequency vibration isolation

This chapter describes the background of vibration isolation system for GW detectors realized by pendulum-based suspension system. This chapter explains the principle of the seismic attenuation first. Then it describes the background of suspension mechanical resonance damping, and of control for mirror position and orientation.

As explained in section 1.3.3, the seismic noise is one of the fundamental noises for ground-based GW detectors. In addition, in order to detect GWs, we have to realize a situation where the test masses are in free-fall condition. To deal with these constraints, we suspend the main optics to pendulum systems called seismic attenuation system (SAS). This implies that it is necessary to take care of the pendulum mechanical resonances in order not to drastically decrease the duty cycle.

More specifically, seismic motion limits the detector sensitivity at low frequency by inducing mirror vibration. In order to detect GWs and to achieve the KAGRA detector target sensitivity, the seismic motion has to be suppressed typically by 10^{-8} to 10^{-10} at 10 Hz. This attenuation is performed by adopting multi-stage pendulum system. In order to bring the interferometer into operation, we need to damp the pendulum mechanical resonances as rapidly as possible.

In addition, for the stable interferometer operation, we also need a system to keep the mirror positions and orientations quiet by isolating the mirrors from the ground motion. The ground motion peaks in the frequency range between 0.1 and 0.5 Hz, which is so-called the micro-seismic peak. Especially the micro-seismic peak affects the RMS mirror residual motion (as shown in Figure 1.13). It is thus important to suppress the mirror motion induced by the micro-seismic motion.

In GW detectors, both the suspension damping and the mirror position control are done by means of active control system.

Section 4.1 describes the background of the passive vibration isolation. The passive vibration isolation is the most basic idea to realize the required seismic attenuation above 10 Hz. This subsection summarizes the physics and the basic techniques used for actual passive vibration isolation system for GW detectors.

Section 4.2 describes the background of active vibration isolation. By utilizing active vibration isolation, it is possible to damp the mechanical suspension resonance, and also to keep the mirror positions and orientations within the narrow ranges needed to acquire and to keep the interferometer locked in the required interference conditions.

4.1 Passive vibration isolation

As described above, the seismic noise has to be attenuated by a factor of 10^{-8} to 10^{-10} at 10 Hz. This attenuation is performed by using multi-stage pendulums. This subsection describes the physics of the pendulum system.

4.1.1 Harmonic oscillator

Isolating optics from ground motion is performed by using mechanical filters. For the simplest case, we consider a single-pendulum system consisting of a mass m, which is suspended by massless wire from a ceiling as in Figure 4.1. Its equation of motion is given by

$$m\ddot{x} = -\frac{mg}{l}\ (x - X),\tag{4.1}$$

where g denotes local gravitational acceleration, l is the length of the wire and x, X are the displacements of the payload and of the suspension point respectively. Taking the Fourier transform, the displacement transfer function from the ground to the mass becomes:

$$H(\omega) = \frac{\tilde{x}}{\tilde{X}} = \ \frac{\omega_0{}^2}{\omega_0{}^2 - \omega^2},\tag{4.2}$$

where $\omega_0 = 2\pi f_0 = \sqrt{g/l}$ represents the resonant angular frequency of the suspension system. The transfer function of this system where the suspension wire length is set to 0.25 m and 1 m are shown in Figure 4.1 (*right*). This figure shows:

1. At low frequencies where $f \ll f_0$,
   The suspended mass follows the motion of the suspension point.

2. Near the resonant frequency, where $f \simeq f_0$,
   the amplitude of the transfer function increases substantially and goes to infinity at the resonant frequency.

3. At higher frequencies where $f \gg f_0$,
   The amplitude of the transfer function decreases as f^{-2}.

4. The attenuation performance at high frequencies is improved if the resonant frequency decreases.
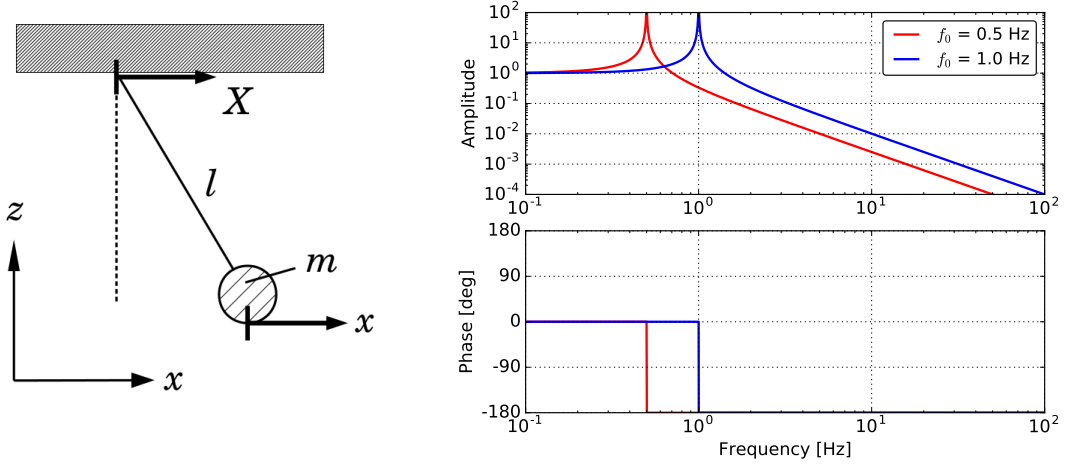
Figure 4.1: A single pendulum system ($left$) and its displacement transfer function ($right$) for the case where the length of the suspension wire is set to 1 m and 0.25 m (corresponding resonant frequencies are $f_0 = 0.5$ Hz, $f_0 = 1.0$ Hz respectively). The lower the resonant frequency is, the more improved the attenuation performance at high frequencies is.

In real life, however, the amplitude of a transfer function of an oscillator at the resonant frequency is finite because of dissipation due to internal friction (at a suspension point for example), a residual gas damping and so on.

The response of the suspended mass when an external force is applied is obtained by solving eq (4.3). The corresponding transfer function is given by eq (4.4).

$$m\ddot{x} = -\frac{mg}{l}\left(x - X\right) + F, \tag{4.3}$$

$$H_{\text{force}}(\omega) = \frac{\tilde{x}}{\tilde{F}} = \frac{1/m}{\omega_0{}^2 - \omega^2}. \tag{4.4}$$

In this thesis we refer to this response function as the force transfer function. The force transfer function is a very useful tool to build active control filters as the ones described in chapter 6.

As a figure of merit to estimate the effective amplitude of a stochastic oscillation, we use the root-mean square (RMS) amplitude. If the random oscillation is described by $x(t)$, the RMS amplitude x_{RMS} is calculated by:

$$x_{\text{RMS}} = \sqrt{\int_a^b d\omega \ S_x(\omega)}, \tag{4.5}$$

where $S_x(\omega)$ is the power spectrum density of $x(t)$. The frequency band of the integration is selected considering the frequency region of interest.

Multi-stage suspension

In a multi-stage pendulum system composed by N stages, the vibration isolation ratio of the N-th stage is proportional to f^{-2N} at a frequencies higher than the resonant frequencies of the system (see Figure 4.2). By implementing a sufficient number of isolation stages and also by using components whose resonant frequency is low enough, it is possible to achieve the required seismic attenuation performance at above 10 Hz.
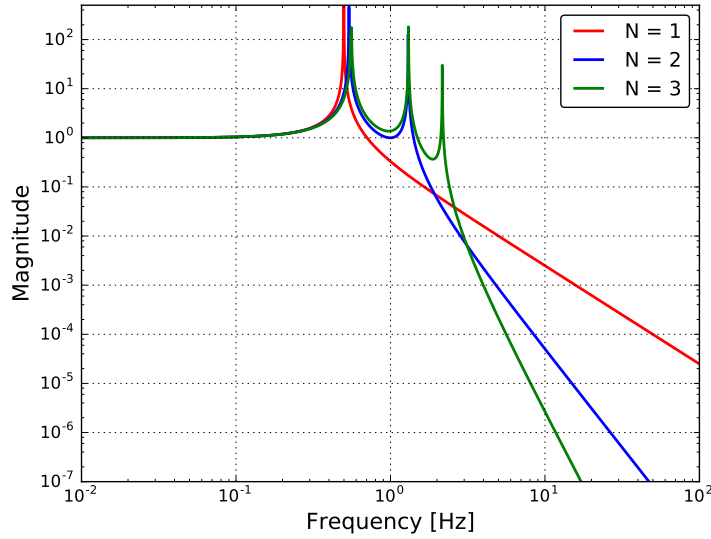

Figure 4.2: The amplitudes of the transfer functions from the suspension point displacement to an N-th stage mass displacement with $N =$1 to 3. The total length of the suspension is set to 1 m in all cases.

Axis definition of suspension motion

For more realistic system, we assume that the each stage of the multi-stage pendulum is described by 3D-rigid body model. In such a system, the motion of each component has 6 degrees of freedoms (DoFs) in total. The axis definition is shown in Figure 4.3. We call the three translational axes longitudinal, transverse and vertical respectively. The three rotational axes are called roll, pitch, and yaw.

Especially we use the 3D-rigid body model when we build active control system for suspension system by ignoring the internal resonances of each stage. We use this assumption since the target control bandwidth is lower than the frequency band where the internal motion becomes dominant, and is in the band where the rigid-body dynamics is a good approximation.
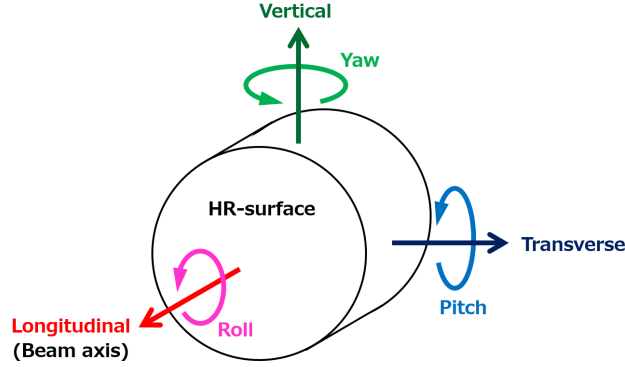
Figure 4.3: Definition of axes used in this thesis. HR-surface indicates the side of the surface of the mirror with high-reflectivity coating (from [45]).

Couplings from vertical and rotational vibration

In an actual system, not only the horizontal ground vibration but also the vertical ground vibration contributes to the mirror displacement. This vertical-to-horizontal coupling is caused by mechanical imperfections in each attenuation stage and also by the non-parallelism of the verticality at locations kilometers apart in the detector. Due to the curvature of the earth, the front and end mirrors of the Fabry-Perot cavities make an angle of $\alpha = L/2R_\oplus$ with the local vertical direction as shown in figure 4.4 (*left*), considering that L is the cavity length and $R_\oplus$ is the radius of the earth. If the optic shifts vertically by δz, it produces a variation $\alpha \delta z$ of the cavity length. Hence assuming a 3-km long interferometer, the minimum coupling caused by earth curvature is $\alpha \sim 2 \times 10^{-4}$. In the case of KAGRA detector, the vertical-to-horizontal coupling is around 0.3 % due to the fact that the arm tunnels have a tilt of 1/300 to help the water drainage.

The rotational motions of the optic can also change the optical path length, as shown in figure 4.4 (*right*). If the laser beam locates at the center of the optic, the rotational motion of a mirror does not change the optical path length. However, the beam spot can be off-centered, and then an angular motion causes a change of the optical path length. Assuming that the beam spot is off-centered by a distance d, an angular shift of the optic $\delta\theta$ translates into a length variation along the beam axis equal to $d\delta\theta$.
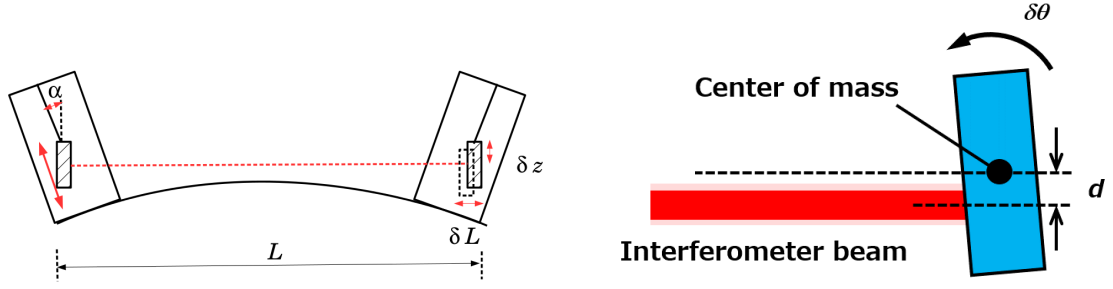
Figure 4.4: Couplings from vertical vibration due to the Earth curvature (*left*) and that from rotational motion due to beam shit (*right*) from [45].

4.1.2 Passive damping system

A multi-stage pendulum system can produce a large motion of the suspended mirror due to the excitation of the pendulum resonances by external disturbances. This has a huge impact on the interferometer operation. It is very important to damp the resonances in order to allow the operation. One option to achieve this goal is to use a passive damping system.

A passive damping system can be modeled by adding a viscous damper which makes a force proportional to the relative velocity between the damper and the suspended mass. The equation of motion of such a system is given by:

$$m\ddot{x} = -k\,(x - X) - \gamma(\dot{x} - \dot{X}), \tag{4.6}$$

where k denotes the spring constant, γ is the damping coefficient of the damper, and X represents the ground motion. The schematic view is shown in Figure 4.5. Taking the Fourier transform, the transfer function from the ground motion to the suspended mass is given by

$$H(\omega) = \frac{\tilde{x}}{\tilde{X}} = \frac{\omega_0{}^2 + 2i\eta\omega\omega_0}{\omega_0{}^2 + 2i\eta\omega\omega_0 - \omega^2} = \frac{\omega_0{}^2 + i\omega\omega_0/Q}{\omega_0{}^2 + i\omega\omega_0/Q - \omega^2}, \tag{4.7}$$

where the damping ratio η is given by $\gamma/2m\omega_0$ and $Q\ (= 1/2\eta)$ is the quality factor of the resonance.

The displacement transfer functions with several quality factors are plotted on the *left* of Figure 4.6. The plot on the *right* of Figure 4.6 shows the impulse response of a mechanical oscillator with a viscous damper, with different Q factors. The *left* panel in Figure 4.6 indicates that:

1. the amplitude of the peak at the resonant frequency gets smaller as the damping force becomes stronger,

2. above the resonant frequency, the amplitude of the transfer function becomes proportional to f^{-1} instead of f^{-2}.
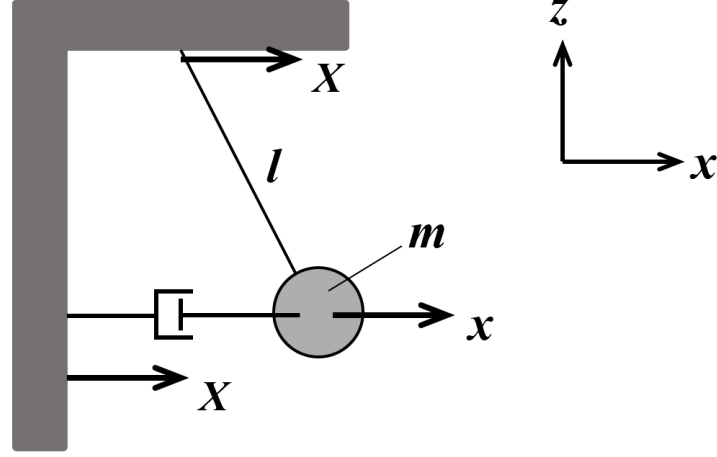
112

Figure 4.5: An example of a passively damped suspension system (from [45]).

Thus, if a damper is attached on the ground, the performance of the mechanical filter is degraded. This attenuation performance with a viscous-damper system can be improved by suspending the damper from the ground with a mechanical filter. This damping method is called flexible damping. By using the flexible damping, the vibration isolation curve will have one additional resonant peak due to the suspended damper, however, the response at higher frequency becomes proportional to f^{-2}, which is same case as a system without viscous damping system. For this reason in GW detectors, passive damping systems are usually suspended.

The *right* panel in Figure 4.6 shows the impulse response of a suspended mass to a driving force assuming different values of Q factor. In the system with a damper, if the damping strength is not too strong, the suspended mass oscillation decays by $1/e$ in the time τ. This decay time is given by $\tau = Q/\pi f_0$. The oscillation amplitude decays faster if the damping factor is greater. In the critical damping condition, i.e, ($Q = 0.5$), the displacement of the suspended mass decays with the fastest decay time $\tau = 1/\omega_0$ without oscillation. In the over-damped condition where $Q < 0.5$, the excited displacement amplitude is decreased but the decay time gets longer compared to the case where the mass is critically damped.

Implementation of viscous damping system

An eddy-current damper [64] is a viscous damping system oftenly used in an actual GW detectors. An eddy-current damping system consists of permanent magnets on one component acting on conductive plate mounted on the component to be damped. A time-varying magnetic field on a conductive material surfaces generates eddy currents in the conductor. Then a magnetic field with opposite
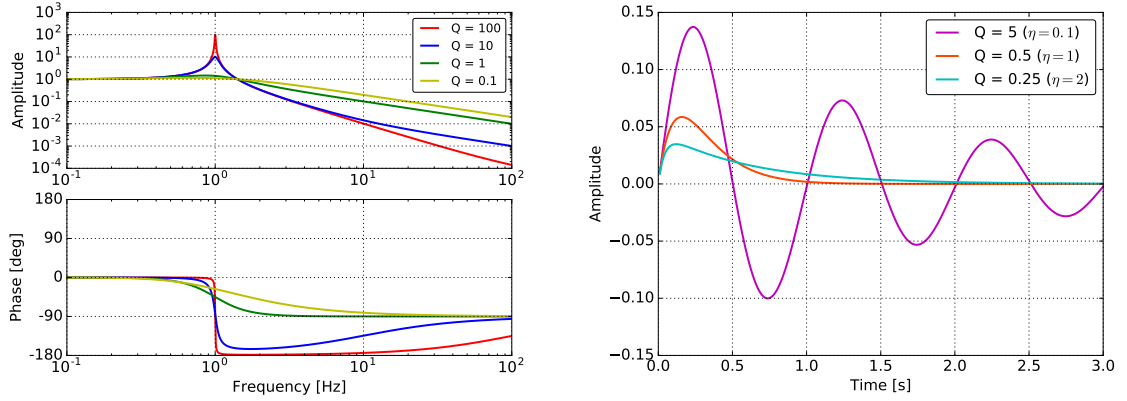
Figure 4.6: The transfer function eq (4.7) (*left*) and the response of a mechanical oscillator with a damper to an impulsive force injected to the suspended mass (*right*), with various Q factors (viscous damping factors) from [45].

polarity of the applied field is induced by the eddy currents, and this makes a delay due to the induced field decay. Consequently a resistive force is generated. Figure 4.7 shows the working mechanism of an eddy current damper with a toy model. The damping coefficient which indicates the damping strength of an eddy current damper is given by

$$\gamma_x = A\sigma B \frac{\partial B}{\partial x},$$

(4.8)

where B is the magnetic field from the permanent magnet, σ denotes the electrical conductivity of the conductor and A represents a factor determined from the geometry of the conductor. Generally, a permanent magnet with strong magnetic field and a conductive object with large electric conductivity are needed in order to get a large damping strength.
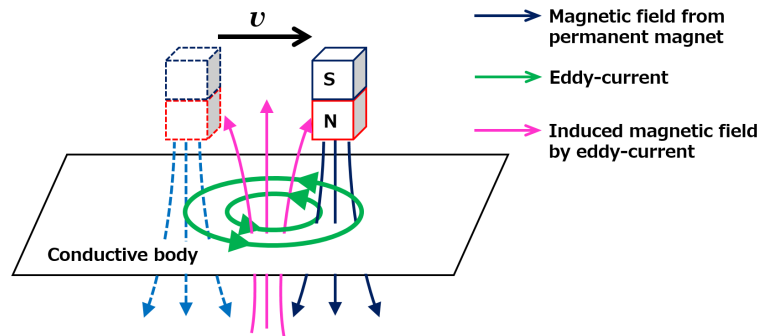

Figure 4.7: Working mechanism of an eddy-current damping system with a toy model (from [45]).

Effect of suspension thermal noise

One demerit of using the passive damping system is that the system can introduce thermal fluctuation of the suspended optics in the detection band of GW detector. According to the fluctuation dissipation theorem, the power spectral density of the spontaneous fluctuations $S_{\text{thermal}}(\omega)$ can be described by using external perturbation forces $(H_{\text{force}}(\omega))$ as:

$$S_{\text{thermal}}(\omega) = -\frac{4k_B T}{\omega} Im[H_{\text{force}}(\omega)], \tag{4.9}$$

where k_B denotes the Boltzmann constant and T is the temperature.

As an example, in the case of the system described by Figure 4.5, the response $H_{\text{force}}(\omega)$ can be deduced as:

$$H_{\text{force}}(\omega) = \frac{1/m}{\omega_0{}^2 + 2i\eta\omega\omega_0 - \omega^2}. \tag{4.10}$$

Then in such a system, the power spectral density of the spontaneous fluctuations $S_{\text{thermal}}(\omega)$ ca be gven by:

$$S_{\text{thermal}}(\omega) = \frac{4k_B T}{m} \frac{2\eta\omega_0}{(\omega_0{}^2 - \omega^2)^2 + 4\eta^2\omega_0^2\omega^2}. \tag{4.11}$$

As a consequence, in an actual multi-stage suspension, we then locate the passive dampers far from the optics so that thermal fluctuations due to their dissipation can be filtered out by the mechanical filters in between, and do not affect the detector sensitivity.

4.1.3 Physics of passive filters for GW detectors

We can improve the attenuation performance at higher frequency by lowering the resonant-frequency of the mechanical filters. In order to obtain sufficiently low resonant frequency with a compact mechanics, passive filters in GW detectors uses the anti-spring techniques.

The key components of such passive filters are inverted pendulum (IP) and so-called geometric anti-spring (GAS) filter. They provide horizontal and vertical vibration attenuation respectively. Since the resonant frequency of IP can be lowered to about 30 mHz, it can passively attenuate the ground vibration at the microseismic peak (at about 0.1-0.5 Hz). IP also mitigates the impact of the microseismic motion on the RMS amplitude of the suspended optic motion. The resonant frequency of the GAS filter can be tuned to about 0.3 Hz. The physics for IP and GAS filter is described in this subsection.

Inverted pendulum (IP)

A toy model of IP is shown in Figure 4.8 (*left*). We consider a system which consists of a flexure fixed to the ground, a cylindrical object connected to the flexure, called IP leg. A mass is mounted on the top of the IP leg. If the top mass displaces horizontally from the vertical point, a restoring force acts on the mass, and the equation of motion can be obtained by

$$M\ddot{x} = -\frac{k_\theta}{L^2}(x - x_0) + \left(\frac{m}{2} + M\right)\frac{g}{L}(x - x_0), \qquad (4.12)$$

where k_θ denotes the bending spring constant of the flexure (for the torque), M and m are the mass of the top mass and that of IP leg respectively, and L represents the length of the IP leg. Then the effective spring constant is given by

$$k_{\text{eff}} = \frac{k_\theta}{L^2} - \left(\frac{m}{2} + M\right)\frac{g}{L}. \qquad (4.13)$$

The second term in eq (4.13) represents a repulsive force due to gravitational anti-spring effect. As a consequence of this term, k_{eff} decreases as the mass of the payload increases. In particular, it goes to 0 when the mass reaches the critical mass $M_c = (k_\theta/gL - m/2)$. The resonant frequency of the IP whose mass is lighter than M_c is given by

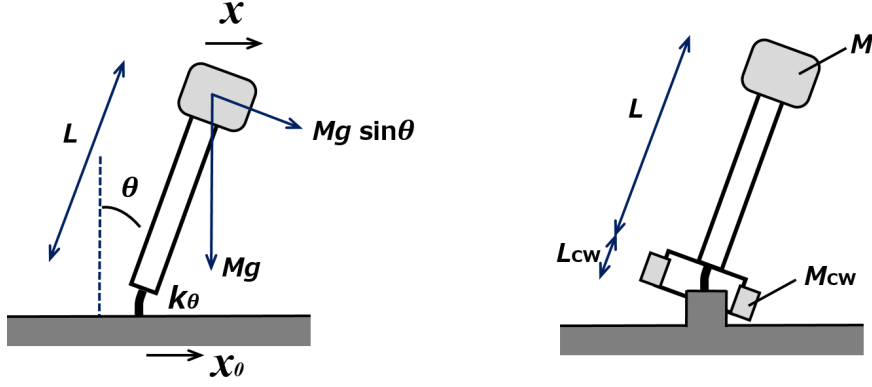$$f_{\text{IP}} = \frac{1}{2\pi}\sqrt{\frac{g}{L}\left(\frac{M_c - M}{M}\right)}. \qquad (4.14)$$

Figure 4.8: Analytic model of an inverted pendulum (*left*) and a schematic view of the inverted pendulum with the counterwight for the compensation of the center of percussion effect (*right*) originally from [45].

Concerning the vibration isolation performance in frequency domain, the displacement transfer function from the ground to the mass on the IP, H_{IP}, is calculated by [65]

$$H_{\text{IP}} = \frac{A + B\omega^2}{A - \omega^2}, \tag{4.15}$$

$$\text{where} \quad A = \frac{k_{\text{eff}}}{M + \frac{m}{4} + \frac{I}{L^2}}, \quad B = \frac{\frac{m}{4} - \frac{I}{L^2}}{M + \frac{m}{4} + \frac{I}{L^2}}. \tag{4.16}$$

In eq (4.16), I denotes the moment of inertia of IP leg. The amplitude of H_{IP} saturates at high frequencies due to so-called the center of percussion (CoP) effect [65, 41]. This can be seen from the coefficient B in eq (4.16). If B becomes smaller, the attenuation from the IP at high frequencies becomes greater. The value of B can be reduced by adjusting the mass distribution along the IP leg. The adjustment is done by implementing a counterweight at the bottom of the IP leg, as shown in Figure 4.8 (*right*).

Geometric Anti-Spring (GAS)

The GAS filter consists of a set of symmetrically arranged cantilever blades (for the actual structure, see section 5.2.2). The one end of the blades is clamped on the base frame and the other end is fixed to the central small disk, which is called the keystone. We then compress the blades horizontally during the installation process, and obtain the anti-spring force. The typical behavior of the GAS filter can be described by a simple analytical model [66] as shown in Figure 4.9, i.e, a combination of vertical and horizontal springs can describe a cantilever spring. The equation of motion and the effective stiffness can be deduced with the following procedure.

If we consider a situation where the suspended payload, whose mass is m, shifts vertically by z, as shown in figure 4.9 (*right*). The equation of motion of the suspended mass is described by

$$m\ddot{z} = -k_z(z - z_{eq} - l_{0z}) - 2k_x(l - l_{0x})\sin\theta - mg, \qquad (4.17)$$

where k_x, l_{0x} are the stiffness and the natural length of the horizontal spring respectively, θ represents the angle between the horizontal axis and the horizontal spring at the clamp point, and l is the length of the horizontal spring when the payload shifts vertically by z. In addition, it is assumed a situation where the working point, which is the height where the forces of the horizontal springs cancel each other is called the working point z_{eq}, is given by $z_{eq} = (mg/k_z + l_{0z})$, where g denotes the gravity acceleration, k_z and l_{0z} are the stiffness and the natural length of the vertical spring respectively. It is also assumed that the force of the vertical spring balances the gravitational force on the suspended mass.

Then assuming x_0 is the horizontal distance between keystone and the clamping point of the spring, eq (4.17) becomes eq (4.19), by using $l = \sqrt{x_0{}^2 + z^2}$, z_{eq} and $k_x{}' = 2k_x$.

$$
\begin{aligned}
m\ddot{z} &= -k_z\left(z - \frac{mg}{k_z}\right) - k_x{}'\left(1 - \frac{l_{0x}}{\sqrt{x_0{}^2 + z^2}}\right)z - mg & (4.18) \\
&= -(k_z + k_x{}')z + k_x{}'l_{0x}\frac{z}{\sqrt{x_0{}^2 + z^2}}. & (4.19)
\end{aligned}
$$

Consequently, the effective stiffness k_{eff} of the modeled GAS filter is obtained as

$$
\begin{aligned}
k_{\text{eff}} &= -\frac{\partial f}{\partial z} = (k_z + k_x{}') - \frac{k_x{}'l_{0x}x_0{}^2}{(x_0{}^2 + z^2)^{\frac{3}{2}}}, & (4.20) \\
&\sim \left[k_z - \left(\frac{l_{0x}}{x_0} - 1\right)k_x{}'\right], \quad (\text{if } x_0 \gg z). & (4.21)
\end{aligned}
$$

Eq (4.21) implies that when the horizontal spring is compressed ($x_0 < l_{0x}$), it makes a repulsive force in the vertical direction and the k_{eff} is reduced from that of the vertical spring ($k_{\text{eff}} < k_z$) due to the anti-spring effect.

About the vibration isolation performance in frequency domain, the displacement transfer function from the frame to the keystone is given by the same form
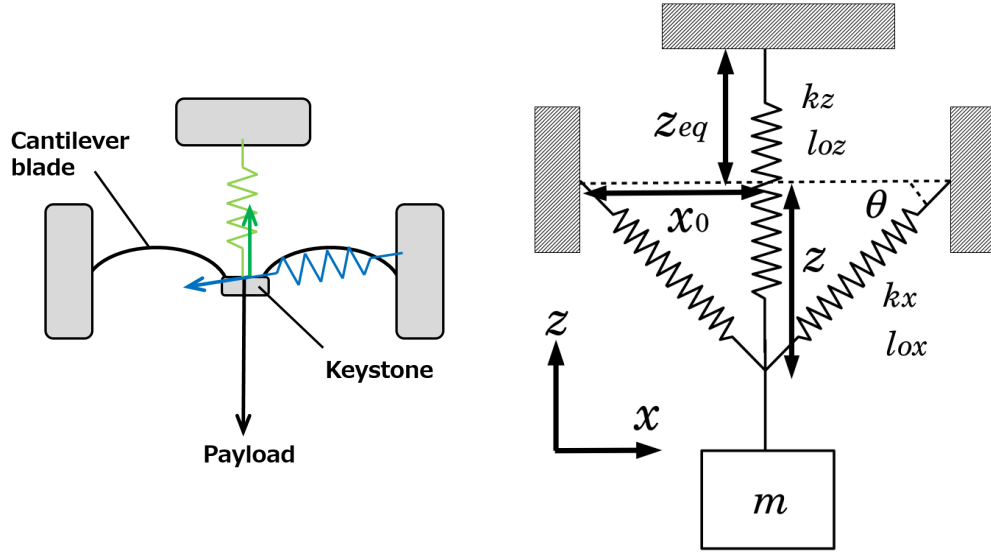
Figure 4.9: A schematic view of an analytical model of the GAS filter ($left$) and the definition of the parameters used in the calculation of the effective stiffness of the GAS filter ($right$) from [45].

as in eq (4.15). The saturation level at high frequencies due to the CoP effect is typically about 10^{-3}. This saturation can be improved by adding a counter weight, which is called magic-wand [67].

4.2   Active vibration isolation

As described in the previous subsections by using the mechanical filters, we can attenuate the seismic noise at frequencies above the resonant frequencies of the multi-stage vibration isolation system. However, in order to reduce the amplitude of the mirror motion at low frequency, we have to damp the mechanical resonances.

Passive damping is one option to deal with this issue. Another option is to implement an active vibration isolation system.

In the real life we often use the active vibration isolation system with feedback and feed-forward control technique. In principle, an active control system can reduce the suspended mass motion amplitude in any frequency. The principle of the active vibration isolation is introduced in this subsection.

Such an active control system can be used not only to damp the resonance but also to steer and maintain the position and orientation of the vibration isolation stage under control in a pre-defined reference position. The main risk associated with the operation of such an active control system is that the noise of the sensors and/or actuators used for the control might affect the attenuation performances of the vibration isolation system.

Feedback control is the most basic system used for this purpose. We construct the desired active control system by implementing appropriate feedback filters for required stages using the Cartesian DoFs. This subsection introduces the basic idea of feedback control and how the noise couplings are estimated, using several control configurations.

The important guidelines for the construction of the suspension control system are summarized the following topics:

1. to close the control loop stably,

2. to damp the suspension mechanical resonances within a given required time,

3. to suppress the suspended mass motion induced by the microseismic motion,

4. to keep the suspended mass displacement induced by the control noise smaller than the required level above 10 Hz.

The following subsections briefly describe how these goals are achieved.

4.2.1 Feedback control with inertial sensor

Here we consider a case where we control a suspended stage with an actuator that applies a force from the ground.
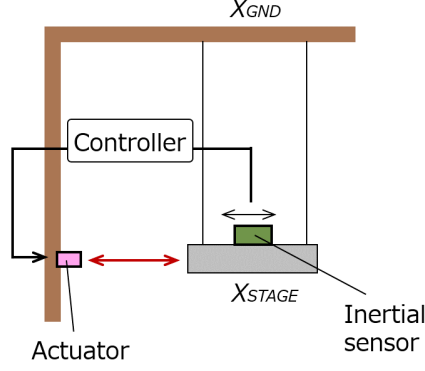

Figure 4.10: A simple model of feedback control with an inertial sensor. Controller represents the feedback control filter. X_{GND} and X_{STAGE} denote the displacement of the ground and the suspended mass respectively.

In this example, we consider a case where we have an inertial sensor which senses the suspended mass acceleration as shown in Figure 4.10. The corresponding block diagram is shown in Figure 4.11. In that diagram, we assume that the displacement transfer function P_s from the ground to the suspended mass motion, and the force transfer function P_a from force on the suspended stage to the suspended stage displacement without feedback are known. The response of the inertial sensor is described by S_{inert} in this system. S_{inert} converts the sensor signal such as in voltage to displacement motion of the suspended stage. F_{fb} denotes the feedback filter for active control. N_{act} and N_{inert} represent the actuator noise and the inertial sensor noise.

In this configuration, the actuator noise N_{act}, the sensor noise N_{inert} and the seismic noise couple to the motion of suspended stage by $X_{\mathrm{stage}}/N_{\mathrm{act}}$, $X_{\mathrm{stage}}/N_{\mathrm{inert}}$ and $X_{\mathrm{stage}}/X_{\mathrm{GND}}$ respectively. These transfer functions are calculated from the diagram respectively as

$$\frac{X_{\mathrm{stage}}}{N_{\mathrm{act}}} = \frac{P_a}{1+G}, \tag{4.22}$$

$$\frac{X_{\mathrm{stage}}}{N_{\mathrm{inert}}} = \frac{-G}{1+G}, \tag{4.23}$$

$$\frac{X_{\mathrm{stage}}}{X_{\mathrm{GND}}} = \frac{P_s}{1+G}, \tag{4.24}$$

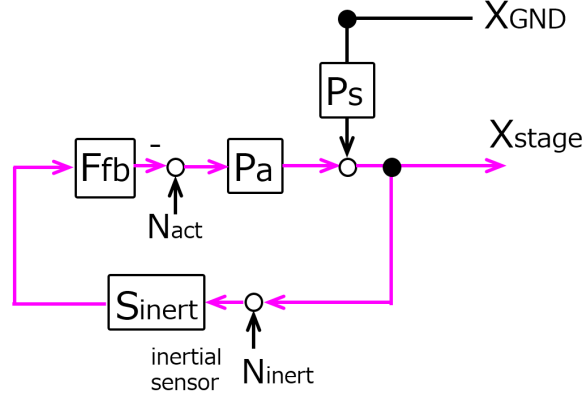where G denote the open loop gain which is given by $P_a F_{\mathrm{fb}} S_{\mathrm{inert}}$.

Figure 4.11: Corresponding block diagram of the system shown in *left* of Figure 4.10.

Then an external disturbance and the seismic noise coupling are to be suppressed by $1/(1+G)$ as described in eq (4.22) and eq (4.24). Thus if we want to damp a resonance, we shape the filter F_fb so that $|G| \gg 1$ in the target frequency band.

However, at frequencies where $|G| \gg 1$, $|X_\mathrm{stage}/N_\mathrm{inert}|$ becomes equal to 1. This indicates that the suspended mass follows the noise of the inertial sensors. Thus in the frequency band where the noise level of inertial sensors are higher than the ground motion, we need to avoid using inertial sensors.

On the other hand, the sensor noise can induce a vibration depending on the feedback filter shape F_{fb} at frequencies where $|G| \ll 1$, since $|X_\mathrm{stage}/N_\mathrm{inert}|$ becomes close to G $(= P_a F_{fb} S_\mathrm{inert})$ there. In this single-stage pendulum configuration, P_a and P_s decreases as f^{-2} at higher frequencies. However, if $|G|$ is not small enough in the high frequency region, the sensor noise coupling can impact the residual motion of the mass.

In addition to the control noise coupling issue, we need to consider the stability of the feedback control loop. The stability of a closed loop system can be tested using the Bode plot of the open loop transfer function. The control loop is unstable if the phase of the open loop transfer function is smaller than -180 deg when its amplitude is equal to 1. The frequency where the open loop gain is equal to 1, is called the unity gain frequency. We need to have at least 30 deg from -180 deg at the unity gain frequency to be able to close the loop stably.

As an example, here we consider the case of a single-stage pendulum suspended from ground, whose resonant frequency is at 1.6 Hz, that is controlled with an inertial sensor. We assume that the ground motion and the sensor noise floor are described by the spectra shown in Figure 4.12. In this configuration, if we want to damp the pendulum resonance, we can shape the servo filter F_fb as shown in Figure 4.13 (*left*) so that the open loop gain is sufficiently greater than

1 at the resonant frequency.

In this shaping process, we need to have enough phase margin in the open loop gain at the frequency where the open loop gain is equal to 1 (the so-called the unity gain frequency). This is important to close the feedback control loop stably.
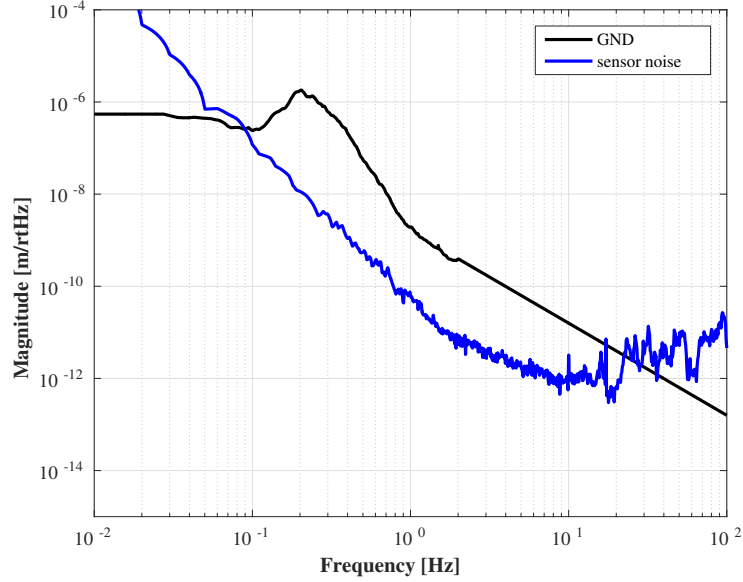

Figure 4.12: Assumed seismic and sensor noise level in the example of the pendulum control with an inertial sensor. The black and blue colored curves show the spectra of the seismic noise and of the sensor noise.
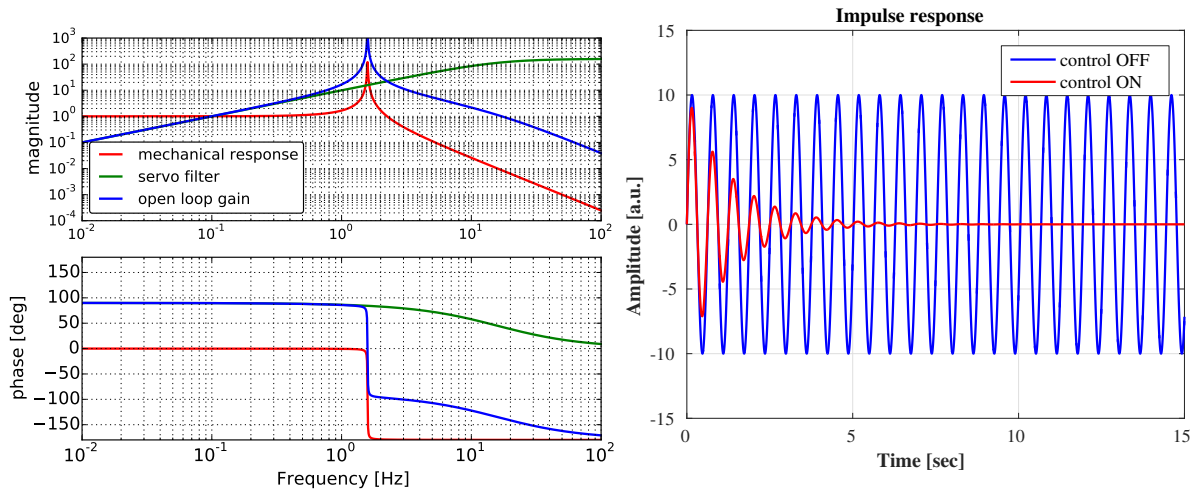

Figure 4.13: An example of the servo filter for damping (*left*) and the impulse response of the suspended mass with and without the control system(*right*).

By using the damping filter shown in Figure 4.13 (*left*), we can damp the mechanical resonance as shown in Figure 4.13 (*right*) and Figure 4.14. We tune the open loop gain so that the decay time of the resonance is shorter than the requirement.

However, we need to keep in mind the control noise coupling to the pendulum motion. Figure 4.14 shows the noise coupling from the inertial sensor control and from the ground motion. At frequencies above 20 Hz in this example, the suspended mass will be shaken by the sensor noise. In the actual GW detectors, we have to sufficiently suppress the mirror displacement noise above 10 Hz. Since the required displacement level of the mirrors is quite strict as described in section 1.4.3, we need to have a roll-off at higher frequencies in the damping filter. Thus we need to carefully shape the control filter in order to avoid inducing the control noise to the mirror above 10 Hz.

In addition, we can also reduce the microseismic noise contribution by setting larger open loop gain. However, we need to keep in mind that such control loops induces lower frequency displacement due to the sensor noise, especially below 0.1 Hz. Thus, inertial sensors can damp the suspended mass motion due to the microseismic motion but we have to properly cut-off the low frequency component due to the sensor noise.
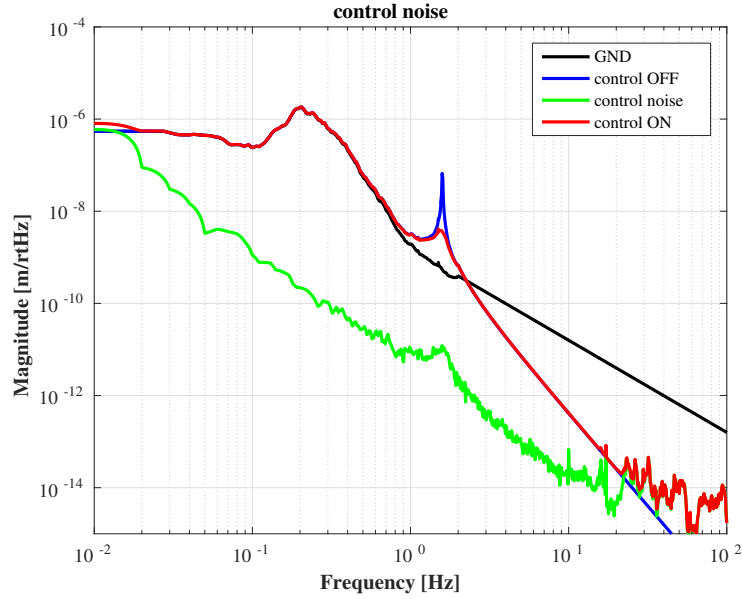

Figure 4.14: Expected motion of the suspended mass with the servo filter shown in *left* of Figure 4.13. The feedback control system reduces the Q factor of the mechanical resonance at 1.6 Hz, i.e, the control damps the resonance successfully. However, the control noise affects the pendulum motion above 20 Hz.

Consequently, we can damp the suspended mass resonance by setting sufficiently large open loop gain in a target frequency band, i.e, around the pendulum resonant frequency. The setting of the open loop gain is done by shaping the

feedback control filter F_{fb}. This filter shaping is done by taking care of phase margin of the open loop transfer function. The stability of a feedback control loop is obtained by having enough phase margin of the open loop gain G at its unity gain frequency, where the open loop gain is equal to 1. In addition we have to have a roll-off filter to minimize the re-injection of control noise at frequencies above 10 Hz.

In addition to the damping control described above, we sometimes have to keep the suspended mass position to a reference point. This low-frequency control is called DC-control. However, for this purpose we cannot use the inertial sensor since the sensor noise level is much higher than the ground motion as shown in Figure 4.12 and will not provides any useful signal at DC. If the suspended mass is actuated in these condition, the mass would just follow the sensor noise. This is not suitable for the interferometer operation. For the purpose of DC-control, it is required to use displacement sensors rather than inertial sensors.

4.2.2 Feedback control with displacement sensor

As a second example, we consider the case of a displacement sensor which senses the motion of the suspended mass with respect to ground as shown in Figure 4.15. The corresponding block diagram is shown in Figure 4.16.
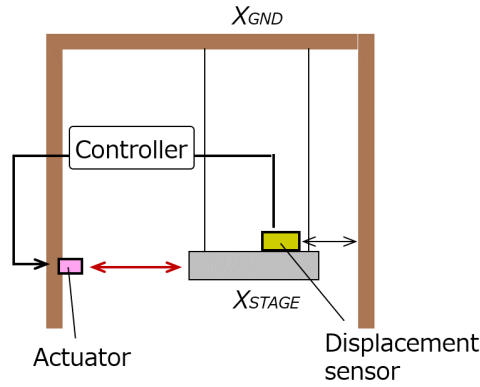

Figure 4.15: A simple model of feedback control with a displacement sensor. Controller represents the feedback control filter. X_{GND} and X_{STAGE} denote the displacement of the ground and the suspended mass respectively.

This configuration is used to damp the suspension resonances and also to keep the suspended mass at a reference position.

In this diagram, we assume that the displacement transfer function P_s from the ground to the suspended mass motion, and the force transfer function P_a from force on the suspended stage to the suspended stage displacement without feedback are known. The response of the displacement sensor is described by S_L, and it converts the sensor signal such as in voltage to displacement motion of the suspended stage with respect to ground. F_{fb} denotes the feedback filter for active control. N_{act} and N_L represent the actuator noise and the displacement sensor noise.
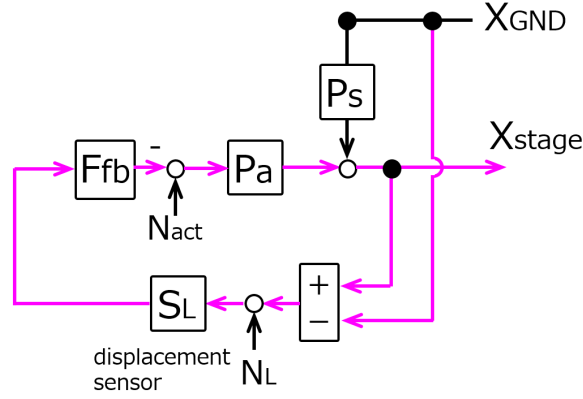
Figure 4.16: Corresponding block diagram of the system shown in Figure 4.15 (*right*).

In this configuration, the actuator noise N_{act}, the sensor noise N_L and the seismic noise couple to the motion of suspended stage by X_{stage}/N_{act}, X_{stage}/N_L and X_{stage}/X_{GND} respectively. These transfer functions are calculated from the diagram respectively as

$$\frac{X_{stage}}{N_{act}} = \frac{P_a}{1+G}, \tag{4.25}$$

$$\frac{X_{stage}}{N_L} = \frac{-G}{1+G}, \tag{4.26}$$

$$\frac{X_{stage}}{X_{GND}} = \frac{G+P_s}{1+G}, \tag{4.27}$$

where G denote the open loop gain which is given by $P_a F_{fb} S_L$. In this case (comparing to the inertial sensor control case), the response from the actuator noise and from the sensor noise to the suspended stage eq (4.25) and eq (4.26) are same as those in the feedback system with an inertial sensor.

The seismic noise coupling has a contribution from the controller as shown in eq (4.27). Especially at $|G| \gg 1$ and $|G| \gg |P_s|$, $|X_{stage}/X_{GND}|$ becomes equal to 1. Thus if the open loop gain is quite large, the suspended mass follows the seismic motion in that frequency band.

On the other hand at $|G| \ll 1$, typically at high frequency, the seismic noise coupling becomes equal to $(G + P_s)$. For a pendulum, P_s become small at high frequency. If $|G|$ is not sufficiently small, the coupling through the feedback control can end up being the dominating term.

Again as an example, here we control a single-stage pendulum suspended from ground, whose resonant frequency is at 1.6 Hz. In this example we use a displacement sensor which observes the relative motion between the suspended mass and the ground. We assume that the spectra of the ground motion and of the sensor noise floor are those shown in Figure 4.17.
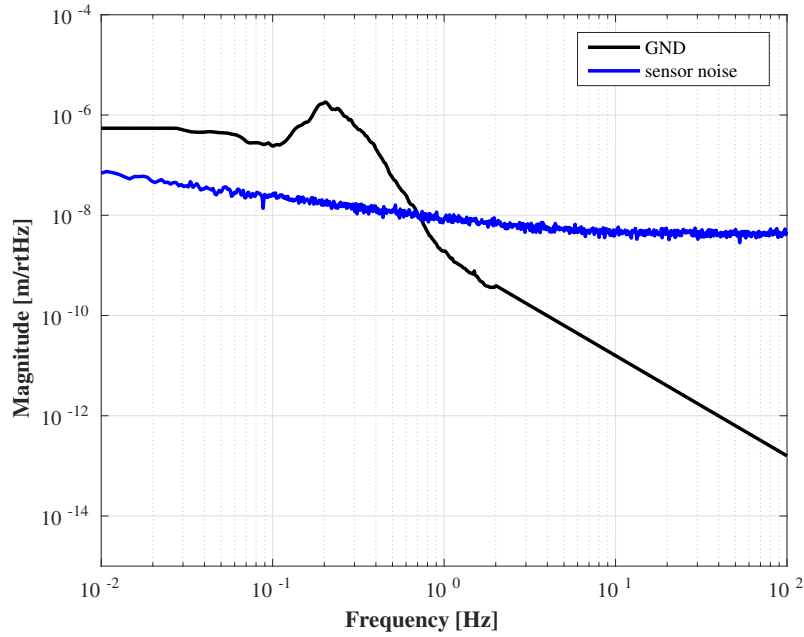
Figure 4.17: Assumed seismic and sensor noise level in the example of the pendulum control with a displacement sensor. The black and blue colored curves show the spectra of the seismic noise and of the sensor noise.

With this configuration, we consider to damp the pendulum resonance and to keep fixed the pendulum position at DC. To this purpose, we can shape the servo filter F_{fb} as shown in Figure 4.18 so that the open loop gain is sufficiently larger than 1 at lower frequencies and around the resonant frequency. The expected displacement of the suspended mass with this control configuration is shown in Figure 4.19 (*left*). The expected displacement of the suspended mass with the same control filter but with the inertial sensor considered in the previous example is shown in Figure 4.19 (*right*).
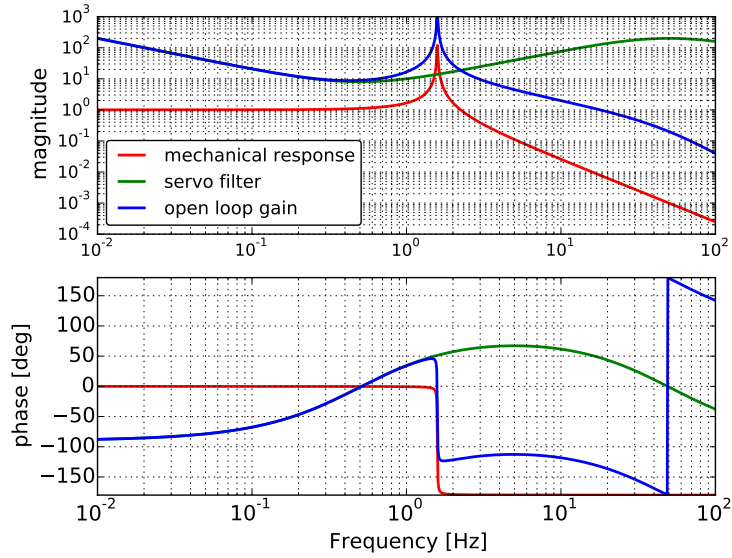
127

Figure 4.18: An example of a servo filter to damp the mechanical resonance and to keep the suspended mass position to a reference.
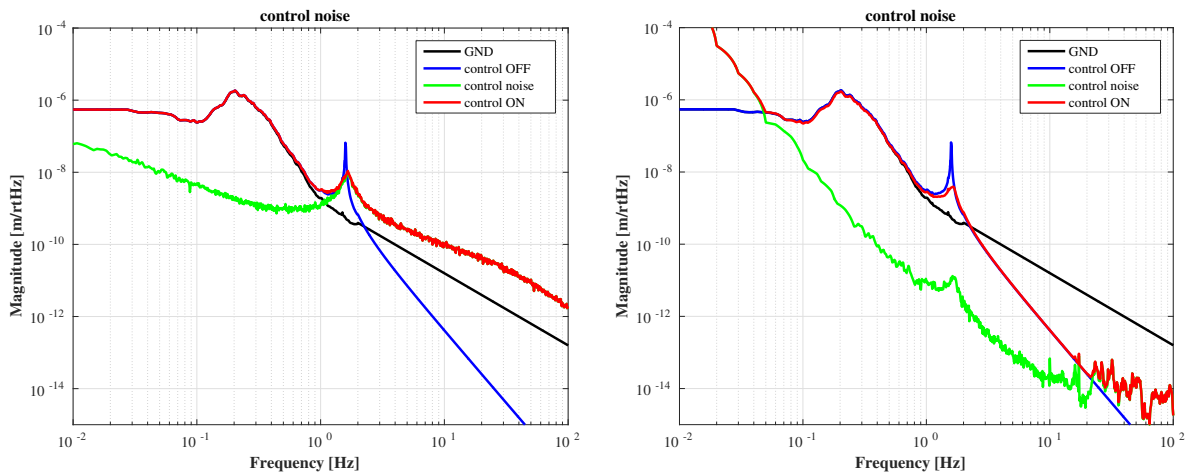

Figure 4.19: Expected motion of the suspended mass using the servo filter shown in Figure 4.18 with a displacement sensor control system (*left*) and with the inertial sensor control system discussed previously (*right*).

Consequently as shown in shown in Figure 4.19, if we include the DC control, i.e control for keeping the suspended mass at a reference position, we need to use displacement sensors. However, the displacement sensor has worse noise level at higher frequencies compared to the noise of typical inertial sensors. Thus we need to use displacement sensors only for control at low frequencies. In addition, the control loop by displacement sensors transmit the ground motion to the suspended mass if the open loop gain is quite large.

In the actual suspension system, in the case of KAGRA detector, inertial sensors are implemented at the level of the top stage (for the main suspensions). We use displacement sensors as the local sensors for all the stages including the top stage. Except for some specific stages we use displacement sensors which measure the relative motion between two suspended objects in order to avoid re-introducing the seismic motion.

We thus use displacement sensors by considering their control noise coupling to the mirror motion above 10 Hz.

In the case of the top stage, we can use both inertial sensors and displacement sensors for the control by using blending technique as described in the next topic.

4.2.3 Feedback control with blended sensor

As described in the previous section, in order to construct a robust mechanical damping system we have to use displacement sensors since displacement sensors are more robust in lower frequency region.

However, displacement sensors couple in the seismic noise and they are much noisier at high frequencies compared to inertial sensors. Thus the inertial sensors are needed in order to suppress the coupling of seismic noise. In particular, we want to use inertial sensors in the microseismic frequency band and above. On the other hand, at lower frequency, inertial sensors are less useful since their output signals become dominated by sensitivity to tilt motions and by their self-noise.

The solution to circumvent these issues is to combine the signals of an inertial sensor and a displacement sensor using high-pass and low-pass filters as shown in Figure 4.20. This is called sensor blending technique [68, 44].

Here we assume that the position of the suspended mass to be controlled is monitored by both an inertial sensor and a displacement sensor, as shown in Figure 4.20. The corresponding block diagram of the feedback control with blended sensors are shown in Figure 4.21. We blend the sensor signals by applying a low-pass filter $F_{\mathrm{LP}}(s)$ to the displacement sensor signal, and a complimentary high-pass filter $F_{\mathrm{HP}}(s) = 1 - F_{\mathrm{LP}}(s)$ to the inertial sensor signal. By doing this we can avoid phase distortion around the blending frequency. As an example, we can select the following blending filters using seventh order polynomial function
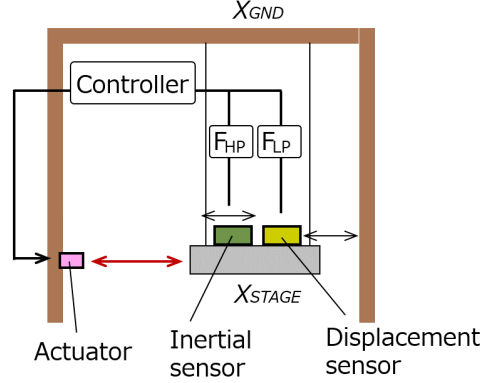
Figure 4.20: A schematic overview of the feedback control system with blended sensor. X_{GND} and X_{STAGE} denote the displacement of the ground and the suspended mass respectively.

of the Laplace variable (s) as

$$F_{LP}(s) = \frac{35\omega_b^4 s^3 + 21\omega_b^5 s^2 + 7\omega_b^6 s + \omega_b^7}{(s + \omega_b)^7}, \tag{4.28}$$

$$F_{HP}(s) = \frac{s^7 + 7\omega_b s^6 + 21\omega_b^2 s^5 + 35\omega_b^3 s^4}{(s + \omega_b)^7}, \tag{4.29}$$

where ω_b denotes the crossover frequency of $F_{\mathrm{LP}}(s)$ and $F_{\mathrm{HP}}(s)$, which is called blending frequency. Since the displacement sensor in this configuration measures the relative displacement between the suspended stage and the ground, the control system will inject the ground vibration to the stage via the displacement sensor. For the purpose of seismic noise attenuation, especially due to the microseismic peak, it is necessary to set the blending frequency below 0.1 Hz. This is required in order to avoid that the large seismic noise due to the micro-seismic peak couples to the suspended test mass motion via the active control. On the other hand, the self-noise of the inertial sensor increases considerably below 0.1 Hz making its use detrimental to the performances of the active control at the lowest frequencies. Thus the blending frequency and the order of the polynomial function in $F_{\mathrm{LP}}(s)$ and $F_{\mathrm{HP}}(s)$ are tuned depending on the sensitivity of the inertial sensor at low frequency.

Using the above blending filters F_{LP} and F_{HP}, the actuator noise coupling $X_{\mathrm{stage}}/N_{\mathrm{act}}$, the sensor noise coupling $X_{\mathrm{stage}}/N_{\mathrm{inert}}$ and the seismic noise coupling

Figure 4.21: Block diagram of the feedback system with blended sensor. It assumes that the position of the suspended mass to be controlled in Figure 4.20 is monitored by both an inertial sensor and a displacement sensor.

$X_{\text{stage}}/X_{\text{GND}}$ are given by the following expressions:

$$\frac{X_{\text{stage}}}{N_{\text{act}}} = \frac{P_a}{1 + G(F_{\text{LP}}S_{\text{L}} + F_{\text{HP}}S_{\text{inert}})}, \tag{4.30}$$

$$\frac{X_{\text{stage}}}{N_{\text{inert}}} = \frac{-GF_{\text{HP}}S_{\text{inert}}}{1 + G(F_{\text{LP}}S_{\text{L}} + F_{\text{HP}}S_{\text{inert}})}, \tag{4.31}$$

$$\frac{X_{\text{stage}}}{N_{\text{L}}} = \frac{-GF_{\text{LP}}S_{\text{L}}}{1 + G(F_{\text{LP}}S_{\text{L}} + F_{\text{HP}}S_{\text{inert}})}, \tag{4.32}$$

$$\frac{X_{\text{stage}}}{X_{\text{GND}}} = \frac{GF_{\text{LP}}S_{\text{L}} + P_s}{1 + G(F_{\text{LP}}S_{\text{L}} + F_{\text{HP}}S_{\text{inert}})}, \tag{4.33}$$

where G is given by P_aF_{fb}. By using a low-pass filter whose crossover frequency is below 0.1 Hz, the coupling of the ground seismic noise due to the control system is suppressed compared to eq (4.27). The sensor blending technique is commonly used system in the GW detectors. However, in order to make use of this solution effectively, it is important to have inertial sensors that have sufficiently good sensitivities at frequencies lower than 0.1 Hz.

If the noise floor of the inertial sensor below 0.1 Hz is low enough, we can decrease the blending frequency and then suppress the suspended mass motion due to the microsesmic peak more effectively, by increasing the open loop gain at that frequency. This gain tuning have to be done by considering the control noise coupling at higher frequency as described in sections 4.2.1 and 4.2.2.

As an example, we consider the control of a suspended mass with both displacement and inertial sensors as shown in Figure 4.20. As before, we assume that the pendulum has its resonant frequency at 1.6 Hz, and that the seismic and sensor noise level are the ones shown in Figure 4.22 (*left*). If we select the blending filters described in eq (4.28) and eq (4.29) with the blending frequency

at 0.15 Hz as shown in Figure 4.22 (*right*), the expected displacement spectrum of the suspended mass is shown in Figure 4.23. In this example, the shape of the feedback filter is same as the one shown in Figure 4.18.
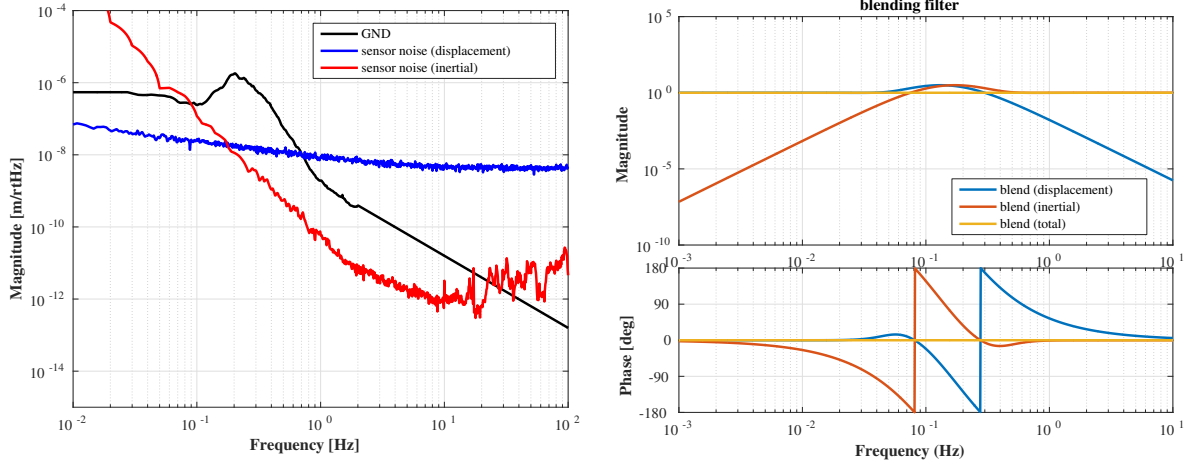
Figure 4.22: Assumed seismic and sensor noise levels in the example of the pendulum control with blended sensor (*left*). The black and blue curves show the spectra of the seismic noise and of the sensor noise. Assumed blending filters (*right*). The blending frequency is set to 0.15 Hz.
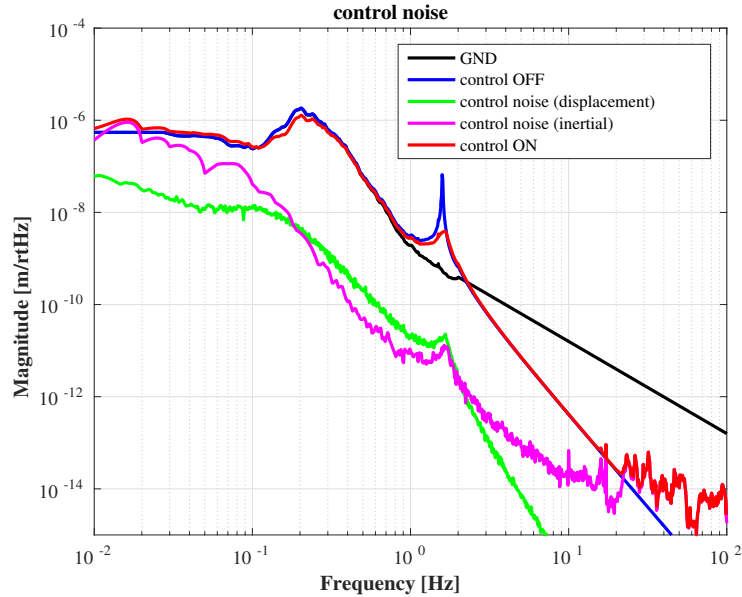
Figure 4.23: Expected displacement of the suspended mass with the servo filter shown in Figure 4.18. The black curve shows the ground motion. The red and the blue curves denotes the suspended mass displacement with and without control system. The light green and magenta curves show the control noise coupling due to the controls with the displacement sensor and the inertial sensor respectively.

In this example case, the noise of the inertial sensor is much larger than the seismic noise at frequencies below 0.1 Hz. We can suppress the contribution from the microseismic peak by increasing the open loop gain as shown in Figure 4.24 even though we introduce some control noise both at low frequencies and at high frequencies. The blending filters and the feedback filter have to be tuned in order to minimize the re-introduction of the noise by the active control loops.
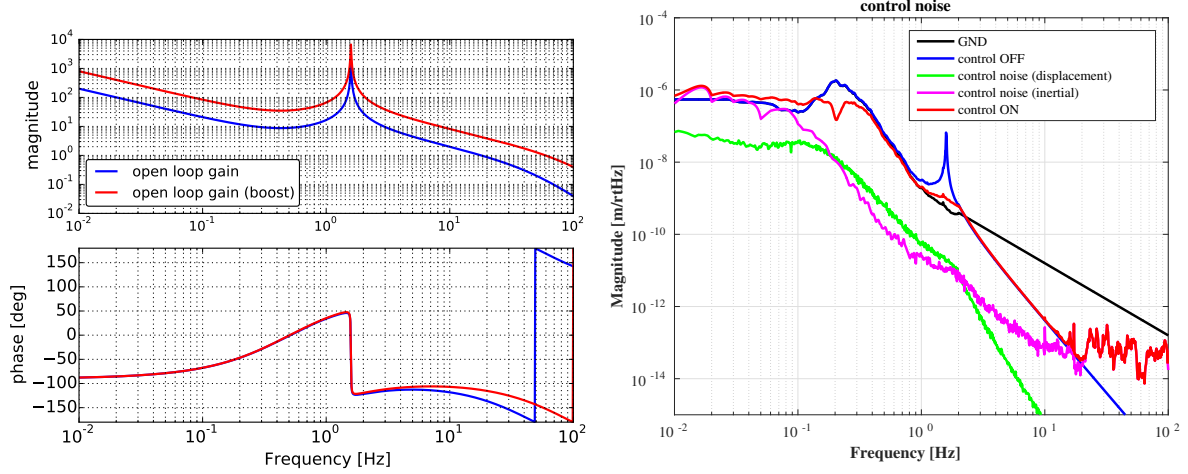
Figure 4.24: A comparison of two feedback filters (*left*) and the expected displacement of the suspended mass with the larger-gain servo filter (*right*). The blue and red colored curves in *left* panel represent the open loop gain used for the calculation of the displacement shown in Figure 4.23 and *right* panel of this figure respectively. The blending frequency is set to 0.15 Hz in the example. By adopting the blending technique we can damp the suspension resonance and can suppress the microseismic peak contribution.

Consequently the feedback control system with the blended sensors can damp the resonance and can keep the suspended mass at a reference position. In addition, this the control with blended sensors can suppress the microseismic noise contribution, especially at frequencies between 0.1 Hz to 0.4 Hz. Such performance is obtained if we blend the sensor signals at sufficiently low frequency compared to the microseismic region. Depending on the noise level of the inertial sensor below 0.1 Hz, we will induce low frequency vibration below 0.1 Hz to some extent. However, we can suppress the effective amplitude of the suspended mass motion.

4.2.4 Feedback control with displacement sensor with feed-forwarding

The control system with the blended sensors can be constructed if the noise level of the inertial sensors is sufficiently lower than the seismic noise. If there are not such inertial sensors on-board of the suspended stage, and if we want to suppress the microseismic contribution in the control system with displacement sensors, we can use feed-forward control. Such system to suppress the coupling of seismic noise is called feed-forwarding technique. In this configuration we use an additional inertial sensor placed on the ground in the proximity of the base of the vibration isolation system as shown in Figure 4.25.
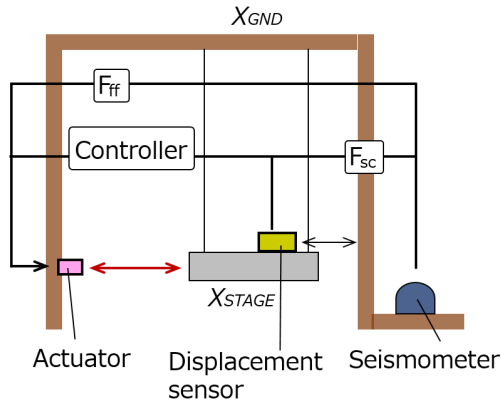
Figure 4.25: A schematic overview of the feedback control system with a displacement sensor with feed-forwarding. X_{GND} and X_{STAGE} denote the displacement of the ground and the suspended mass respectively.

The seismic noise measured by this sensor is then used to subtract the seismic noise coupling from the suspension displacement sensor. Figure 4.26 shows the block diagram of the feedback control system using a displacement sensor combined with feed-forwarding.

In this system, the ground vibration sensed by the seismometer on the ground is used to subtract the seismic noise coupling. This is constructed by sending the seismometer signal to the displacement sensor signal before applying the control filter with a filter F_{sc}, and to the actuation port with a filter F_{ff}. F_{sc} and F_{ff} are called the sensor-correction filter and feed-forwarding filter respectively. The actuator noise coupling $X_{\mathrm{stage}}/N_{\mathrm{act}}$, the sensor noise coupling $X_{\mathrm{stage}}/N_{\mathrm{L}}$ and the seismic noise coupling $X_{\mathrm{stage}}/X_{\mathrm{GND}}$ of this system are given by the following
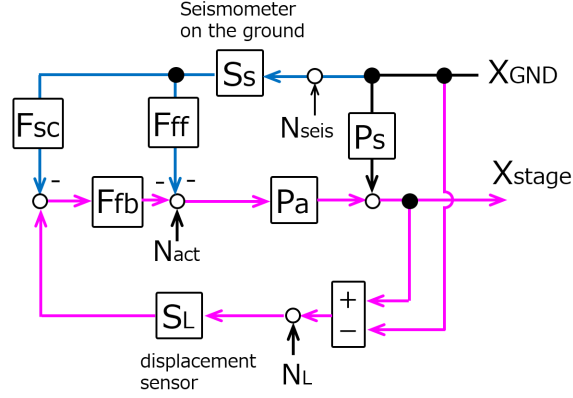
Figure 4.26: Block diagram of the feedback system using a displacement sensor with a feed forward system.

expressions:

$$\frac{X_{\text{stage}}}{N_{\text{act}}} = \frac{P_a}{1+G}, \tag{4.34}$$

$$\frac{X_{\text{stage}}}{N_{\text{L}}} = \frac{-G}{1+G}, \tag{4.35}$$

$$\frac{X_{\text{stage}}}{N_{\text{seis}}} = \frac{S_s P_a}{1+G} \left(F_{\text{sc}} F_{\text{fb}} - P_a F_{\text{ff}} \right), \tag{4.36}$$

$$\frac{X_{\text{stage}}}{X_{\text{GND}}} = \frac{1}{1+G} \left[G \left(1 + \frac{S_s}{S_L} F_{\text{sc}} \right) + \left(P_s - P_a S_s F_{\text{ff}} \right) \right], \tag{4.37}$$

where G is given by $P_a F_{\text{fb}} S_{\text{L}}$. By selecting the condition for the F_{sc} and F_{ff} described by eq (4.38) and eq (4.39), the seismic noise coupling becomes zero in an ideal case.

$$F_{\text{sc}} = -\frac{S_{\text{L}}}{S_{\text{s}}}, \tag{4.38}$$

$$F_{\text{ff}} = \frac{P_{\text{s}}}{P_a S_{\text{s}}}, \tag{4.39}$$

This is a case where the F_{sc} subtracts the ground motion from the displacement sensor, and F_{ff} compensates the mechanical seismic noise coupling P_s. In this condition, the coupling from the seismometer noise becomes

$$\frac{X_{\text{stage}}}{N_{\text{seis}}} = \frac{-P_a}{1+G} \left(S_{\text{L}} F_{\text{fb}} + P_{\text{s}} \right). \tag{4.40}$$

As an example, we calculate the expected suspended mass displacement with the feed-forwarding technique for an example. Again, we assume that the pendulum to be controlled has its resonant frequency at 1.6 Hz. The assumed seismic
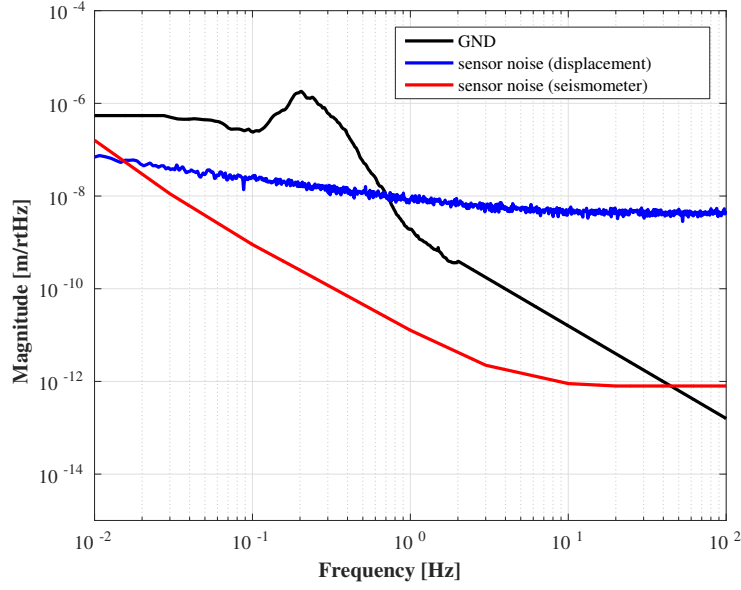
Figure 4.27: Assumed seismic and sensor noise level in the example of the pendulum control with a displacement sensor and feed-forward. The black, blue and red colored curves show the spectra of the seismic motion, the displacement sensor and the seismometer noise.

and sensor noise spectra are shown in the *right* panel of Figure 4.25. The assumed ground motion and the sensor noise spectra are given in Figure 4.27.

The expected displacement of the suspended mass is shown in Figure 4.28. The displacement spectra are calculated by assuming a perfect inter-calibration, i.e, the inter-calibration between the displacement sensor and the seismometer is perfectly done. In this model, the feed-forwarding filters F_{sc} and F_{ff} are set to constant values -1 and 100 respectively. In this example, the feedback control filter shape is the same as the one shown in Figure 4.18 in this example.

By adopting the feed-forwarding technique, both the so-called sensor-correction and feed-forwarding, we can suppress the contribution of the microseismic peak to the suspended stage.

However, the noise coupling from the displacement sensor control is dominant at frequencies above 2 Hz in this example. Thus this configuration can be used only when the noise coupling of the displacement sensor control is acceptable at higher frequencies.

Consequently by adopting the sensor correction and the feed-forwarding technique, we can reduce the suspended mass motion to the sensor noise level. This technique is quite useful to reduce the microseismic contribution.
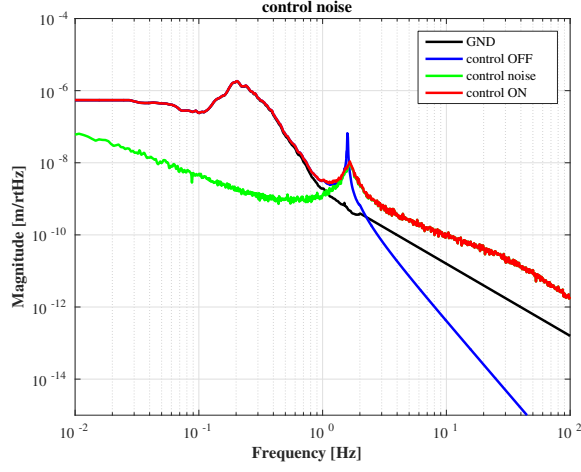
(a) Configuration: $F_{sc} = 0$ and $F_{ff} = 0$ (b) Configuration: $F_{sc} = -1$ and $F_{ff} = 0$
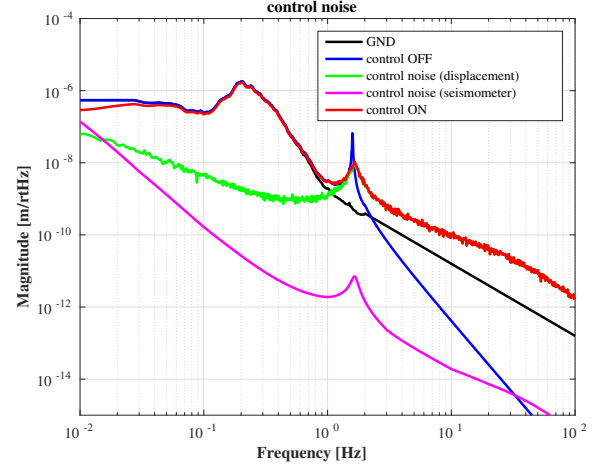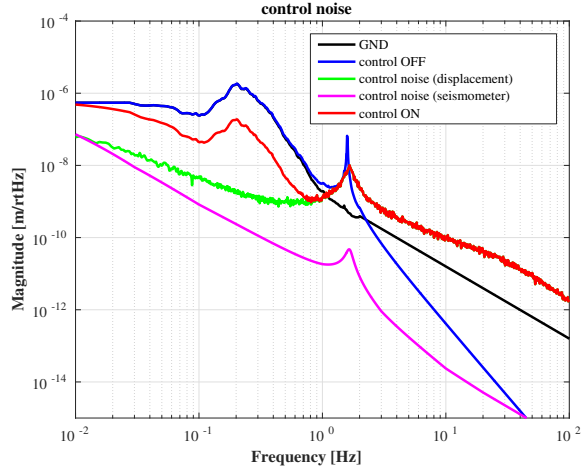
(c) Configuration: $F_{sc} = 0$ and $F_{ff} = 100$ (d) Configuration: $F_{sc} = -1$ and $F_{ff} = 100$
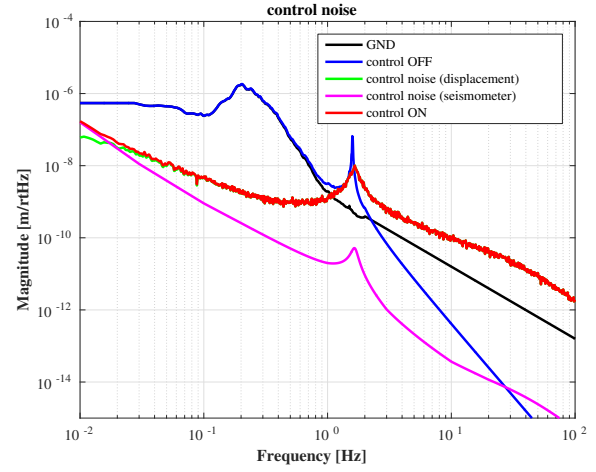
Figure 4.28: Expected motion of the suspended mass with the servo filter shown in Figure 4.18 with the displacement sensor control, without seismometer control (*upper left*), with the sensor-correction technique (*upper right*), with the feed-forwarding technique (*lower left*) and with both the sensor-correction and feed-forwarding technique (*lower right*). The black curve shows the ground motion. The red and blue curves denote the suspended mass displacement with and without control system. The light green and magenta curves show the control noise coupling due to the controls with the displacement sensor and the seismometer respectively.

4.2.5 Feedback control with blended sensor with feed-forwarding

As discussed in [69], further seismic noise suppression can be obtained by means of a feedback control system using both a blended sensor and a feed-forwarding. Figure 4.29 shows the schematic overview of such a system.
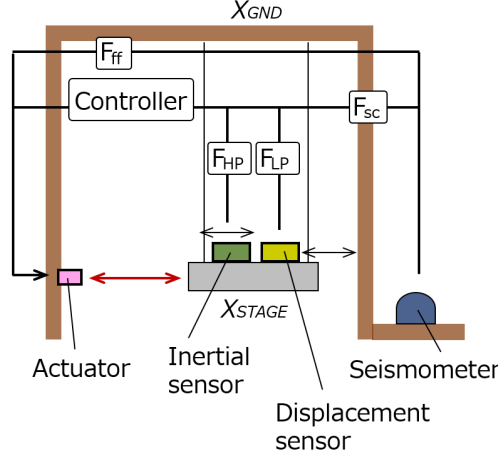
Figure 4.29: A schematic overview of feedback control system with blended sensor and feed-forwarding technique.

In order to suppress the control noise at higher frequencies (compared to the case in section 4.2.4) we can use this configuration.

In practice, it is possible to satisfy the requirements on the control[1] by adopting the feedback control with blended sensors. Even in a case where we do not have sufficiently low-noise inertial sensor (at lower frequencies), we can satisfy the requirements by adopting the feedback control system with displacement sensors and with the feed-forward control. Thus here we skip the detailed discussion about this configuration.

Summary

In GW detectors, by using feedback (and feed-forward) control system, we construct the system to damp the suspension resonances. With such a system we can keep the mirror position and orientation while isolating it from the ground motion. As examples of active vibration isolation systems, the following configurations have been described:

1. feedback control with inertial sensor,

2. feedback control with displacement sensor,

3. feedback control with blended sensor,

---

[1]More details about the requirement on the suspension control is described in section 6.2.

4. feedback control with displacement sensor and feed-forwarding.

A robust control system to damp the mechanical resonances is to adopt the feedback control with with displacement sensor. In order to sufficiently suppress the seismic noise contribution to start the interferometric operation, we utilize inertial sensors either on the suspended stage or on the ground.

In the case of KAGRA detector, inertial sensors are implemented at the top stage for the main suspensions. In addition, we use displacement sensors for all the stages including the top stage. Except for some specific stages[2] we use displacement sensors which measure the relative motion between two suspended masses in order to avoid re-introducing the seismic motion.

In this thesis work, the following control configurations have been used depending on the purpose:

1. feedback control with displacement sensor (sections 4.2.2 and 6.5),

2. feedback control with displacement sensor and feed-forwarding (sections 4.2.4 and 6.6).

4.3 Summary

This chapter describes the background of low frequency vibration isolation systems for GW detector.

Section 4.1 describes the attenuation of the seismic motion by suspending the mirror with a multi-stage pendulum system. This subsection explains that in actual GW detectors we realize passive filters with sufficiently low resonant frequency by using anti-spring technique. The key components are inverted pendulum (IP) and geometric anti-spring filter (GAS filter). Section 4.2 describes the principle of the active control system by using several configurations. By using feedback and feed-forward control, we can damp the suspension resonances and can control the mirror position and orientation.

The following chapters describe the vibration isolation system for the KAGRA suspensions. Chapter 5 describes the actual sensors and actuators implemented for the suspension control. Chapters 6 and 7 discuss the designing and implementation of the feedback and feed-forward control, using the principle described in section 4.2.

---

[2]The most top stage of the Type-A and Type-B suspensions and the fifth stage (from the top) of the Type-A suspension are the corresponding stages. More details are described in chapter 5.

Chapter 5

KAGRA seismic attenuation system (SAS)

As described in chapter 4, in ground-based GW detectors, the main optics are suspended by a pendulum system called seismic attenuation system (SAS) in order to decouple them from the seismic vibration of the ground. An active control system is required in order to damp the suspension resonances that otherwise would drastically decrease the duty cycle.

For the KAGRA detector, three types of SAS are installed depending on the required displacement noise level above 10 Hz as detailed in sections 1.4.3 to 1.4.5.

This chapter briefly summarises the background information about the KAGRA SAS needed to understand the work presented in the following chapters. This chapter also reports the estimated measured and estimated noise floor of the sensors that are developed for the active control system described in chapter 6.

Section 5.1 briefly summarizes the assembled KAGRA SAS mechanics and the expected mirror displacement. Section 5.2 describes each mechanical component of the KAGRA SAS. Section 5.3 introduces the sensors and actuators which are implemented in the KAGRA SAS. This subsection reports the measured and estimated noise floors of those sensors. More details about the three suspension systems can be found in [44, 41, 45, 46].

5.1 Overview of KAGRA SAS

As described in section 1.4.5, in KAGRA detector, three types of SAS are used depending on the required mirror displacement level above 10 Hz. They are called Type-A, Type-B and Type-Bp SAS as described in section 1.4.5. The required displacement of the Type-A SAS is the most strict. This requirement is looser for the Type-B and Type-Bp SAS.

In order to lock DRFPMI, the residual motion of all the mirrors has to be suppressed sufficiently. Suppressing both the mirror displacement and mirror angular motion is quite important. Especially in the locking procedure, it is quite important to robustly acquire the lock of arm-cavities. Thus to actively control the Type-A suspensions, which holds the arm-cavity mirrors, is of paramount importance to start the interferometer operation[1].

This subsection includes the expected mirror displacement spectrum. For the estimate of the mirror displacement, we assume that 1 % of vertical motion couples to the longitudinal displacement. This assumption come from an empirical estimate for the vertical to longitudinal coupling of the mechanics of 0.1-1 % depending on the assembled mechanics. Actually, specifically in KAGRA, at least 0.3 % vertical-to-horizontal coupling is expected due to the fact that the arm tunnel has a tilt of 1/300 for the purpose of water draining. In addition, we use the 90 percentile seismic motion shwon in Figure 1.13 assuming that the ground motion level is high.

---

[1]From this fact, this thesis work mainly focuses on the Type-A suspension system especially in chapters 6 and 7.

5.1.1 Type-A suspension

Type-A suspension consists of nine stages. The mechanical system of Type-A suspension and its schematic overview are shown in Figure 5.1.

The upper five stages are operated at room-temperature and the lower four stages are operated at cryogenic temperature.

Starting from the top stage, the Type-A suspension consists of IP-stage (section 5.2.1), five GAS filters (section 5.2.2) with the damping system at BF-stage (section 5.2.5), and the cryogenic payload (section 5.2.6). The five GAS filters are called Filter 0 (F0), Filter 1 (F1), Filter 2 (F2), Filter 3 (F3) and bottom-filter (BF), from the top. Each GAS filter is suspended by a single maraging wire from the upper stage. At the upper surface of F1, we implement a magnetic damper. The magnet plate is suspended from the IP-stage, and the other copper plate is attached on the F1. The Type-A suspension has the damping system at the BF-stage, composed of sensors and actuators. This system is called BF-stage damping system and its details are described in section 5.2.5

In the payload part, each stage is connected to heat links as introduced in section 5.2.6. Heat links are implemented to reduce the cooling down time making use of conductive heat transfer [70, 71].

Cooling system

The cryogenic payload is cooled down by utilizing both radiation and conductive cooling. For cooling we use four units of pulse-tube cryocoolers. The payload is surrounded by two layered shield whose temperatures are at 8 K and 80 K, and the structure is housed in a cryostat. For heat extraction, the heat links from the cryostat are connected to the payload via a vibration isolation system to avoid transmitting the vibration of the cryostat to the payload.

The overview of the system inside the cryostat and the vibration isolation system for the heat links, which is called heat link vibration isolation system (HLVIS), are shown in Figure 5.2 and 5.3.

Expected mirror displacement

The expected displacement of a mirror suspended by a Type A system is shown in Figure 5.4. In this estimate, it is assumed that the cryostat vibrates as much as the ground. The expected vibration transmitted from the cryostat via the HLVIS is also included. In this calculation, we assume that the cryostat displacement spectra is the same as the ground vibration. However, the cryostat can enhance the vibration at frequency above a few Hz due to its internal resonances and cryocooler operations [72]. Thus the actual mirror displacement especially above 10Hz is to be investigated by using a sensitive interferometer.
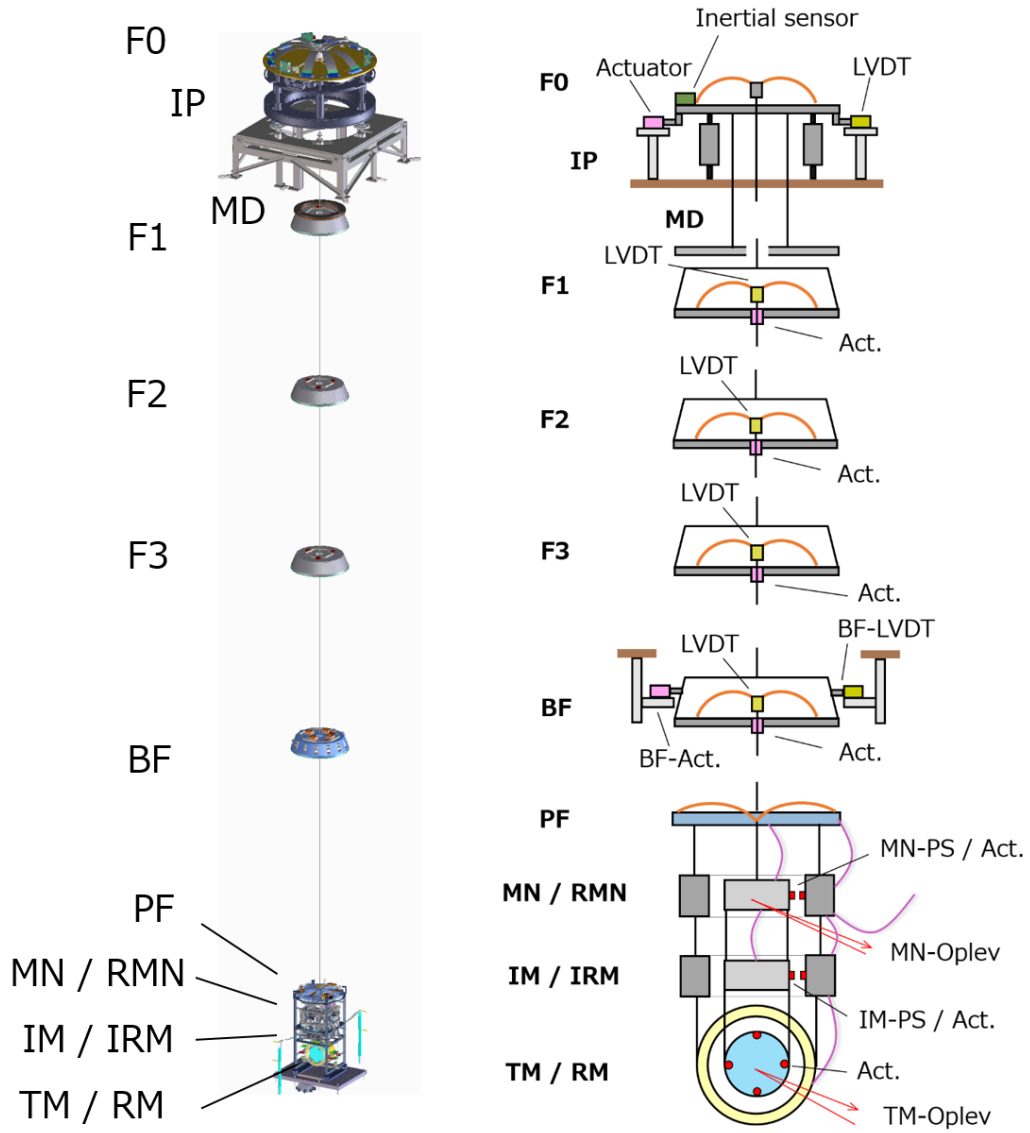
Figure 5.1: The overview of the Type-A suspension system. In the schematic view (*right*), the information about sensors and actuators, described in section 5.3, is included. The boldfaced letters represent the names of the suspension stages, while the small characters show the implemented sensors and actuators.
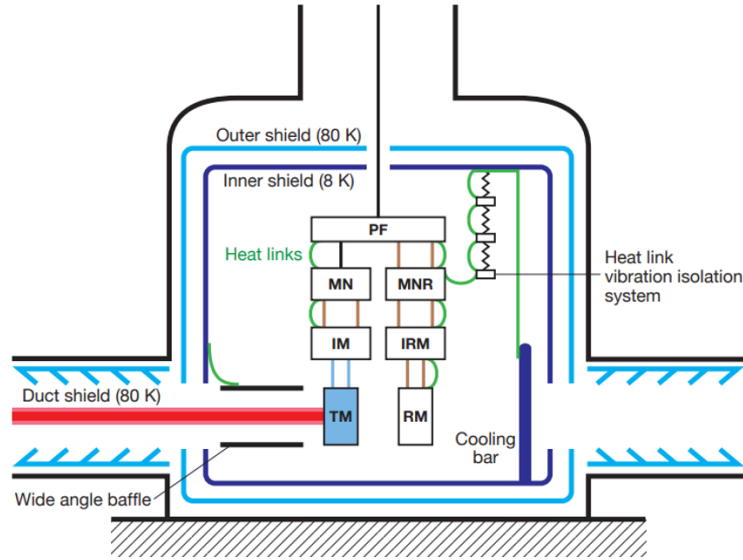
Figure 5.2: A schematic view inside the cryostat. The payload and the vibration isolation system for the heat links (HLVIS) are housed. The heat links from the cryostat are connected to the payload via the HLVIS. This figure is reproduced from [41]. *Schematic diagram of the cooling system around the cryogenic payload.*
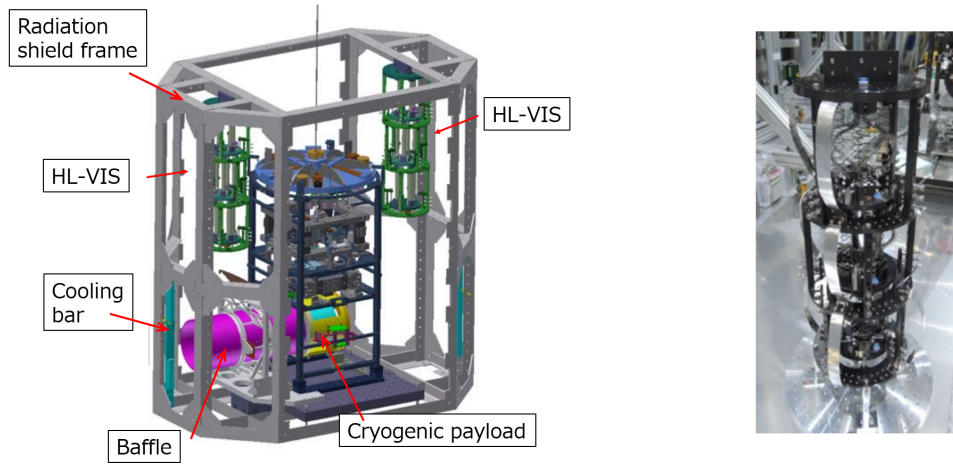
Figure 5.3: 3D-CAD drawing of the system inside the cryostat (*left*) and the actual structure of the vibration isolation system for the heat links (*right*).
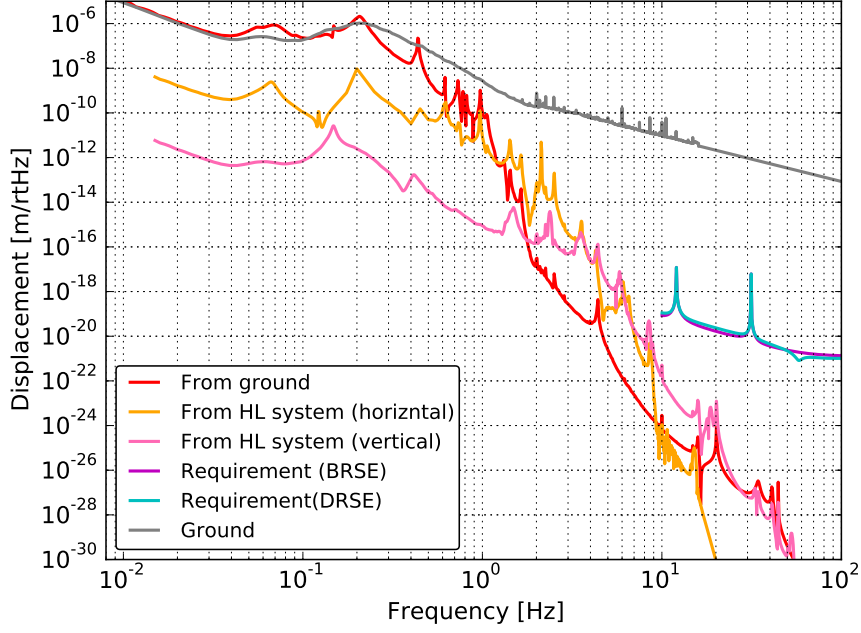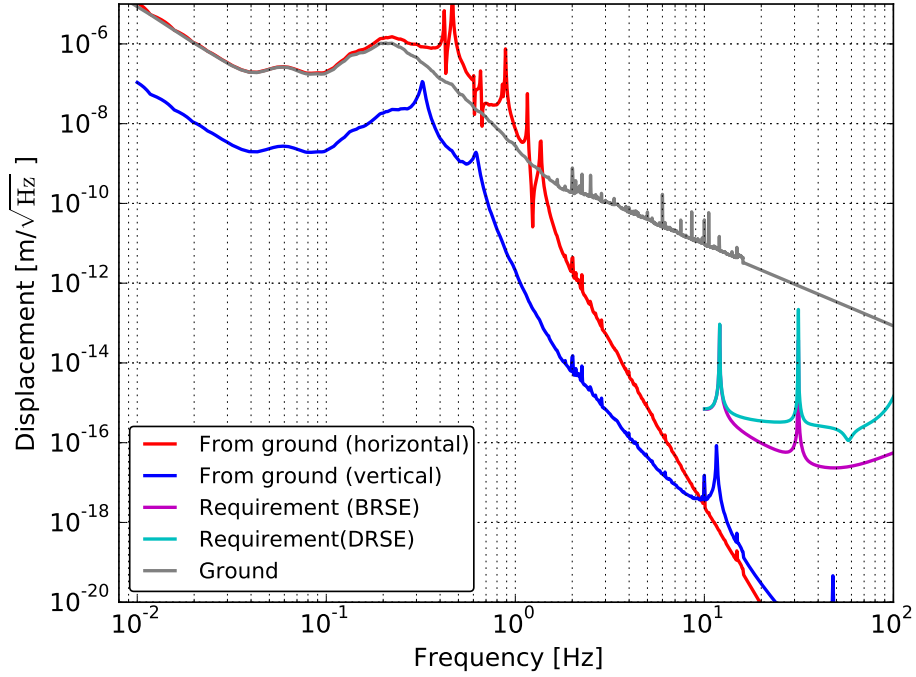
Figure 5.4: Expected mirror displacement spectrum of a mirror suspended by Type-A suspension, assuming 1% vertical to horizontal coupling. The red curve shows the TM displacement induced by ground, and this curve includes the vertical coupling. The orange and pink curves show the horizontal and vertical vibration transmitted from the cryostat via HLVIS respectively, assuming 1% coupling for vertical DoF. The magenta and cyan curves represents the required mirror displacement level for the KAGRA observation modes described in sections 1.4.2 and 1.4.3.

146

5.1.2 Type-B suspension

Type-B suspension consists of five stages. All the stages are operated at room-temperature. The Type-B suspension consists of an IP-stage (section 5.2.1), three GAS filters (section 5.2.2) without the damping system at BF-stage (section 5.2.5), and the room-temperature payload (section 5.2.6). The three GAS filters are called filter 0 (F0), standard filter (SF) and bottom filter (BF) from the top. Each GAS filter and intermediate mass (IM) (see section 5.2.6) are suspended by a single maraging wire from their upper mass. At the upper surface of the SF, we implement the magnetic damper as in the Type-A SAS. The mechanical system of Type-B suspension and its schematic overview are shown in Figure 5.5.
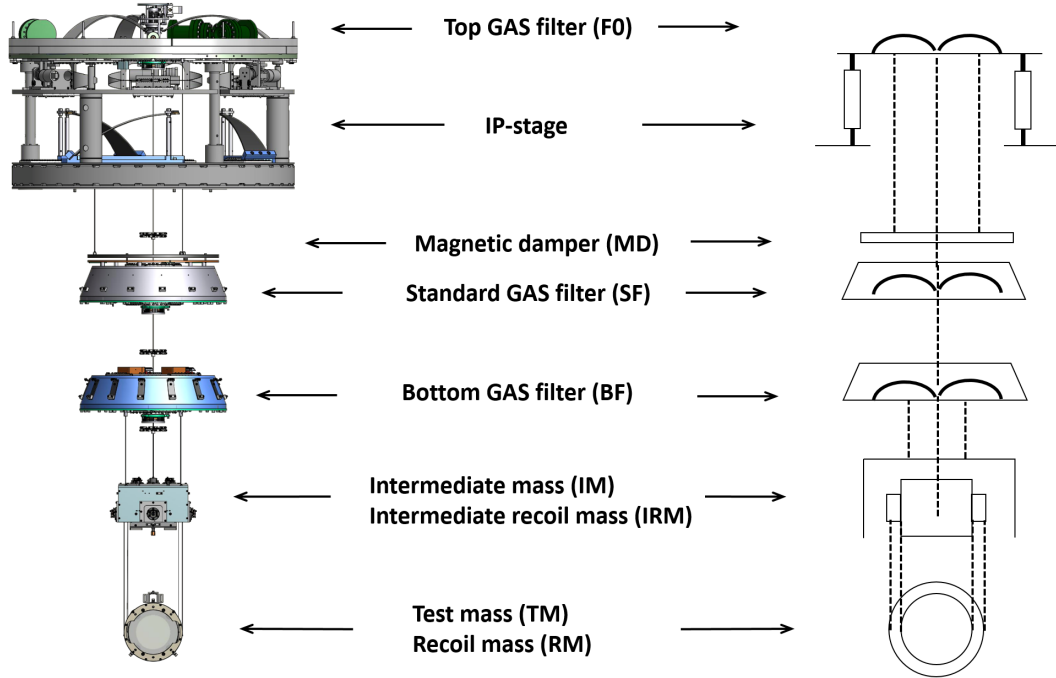
Figure 5.5: The overview of the Type-B suspension system.

Expected mirror displacement

The expected mirror displacement suspended by Type-B suspension is shown in Figure 5.6.
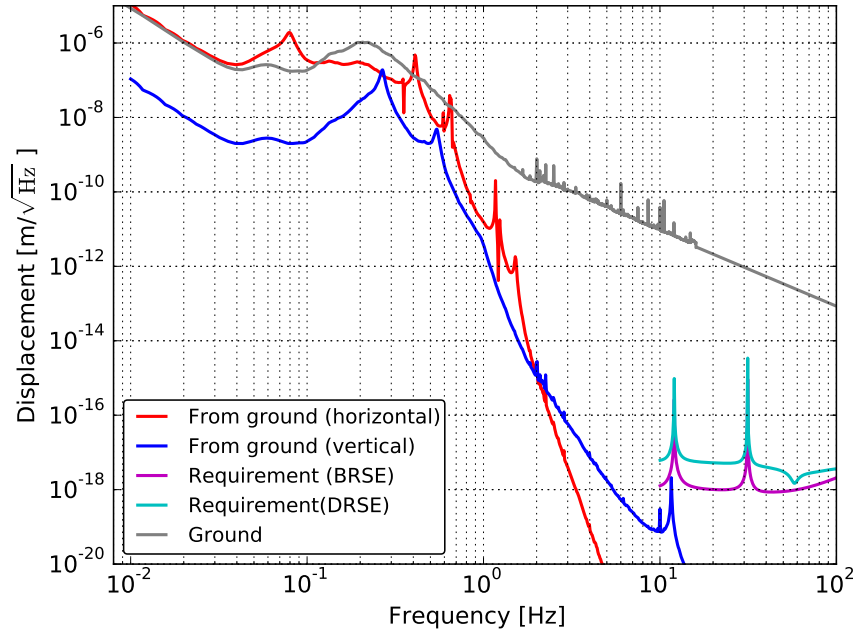
Figure 5.6: Expected mirror displacement spectrum of a mirror suspended by Type-B suspension, assuming 1% vertical to horizontal coupling. The red and blue curves shows the TM displacement induced by ground in horizontal and vertical respectively. The magenta and cyan curves represents the required mirror displacement level for the KAGRA observation modes described in sections 1.4.2 and 1.4.3.

5.1.3 Type-Bp suspension

Type-Bp suspension consists of four stages. The mechanical system of Type-Bp suspension and its schematic overview are shown in Figure 5.7. All the stages are operated at room-temperature. The Type-Bp suspension consists of two GAS filters (section 5.2.2) with the damping system at BF-stage (section 5.2.5), and the room-temperature payload (section 5.2.6). Starting from the top, the two GAS filters are called standard filter (SF) and bottom filter (BF). Each GAS filter and intermediate mass (IM) (see section 5.2.6) are suspended by a single maraging wire from their upper mass. In this system, SF is rigidly mounted on the ground, without IP-stage. For the static horizontal position adjustment, we use a motorized stage which is called traverser, as shown in Figure 5.8. For the BF-stage damping system, we use a recoil mass for the BF, which is called BF-recoil mass (RBF) (see section 5.2.5). In this system, we do not have the magnetic damper.
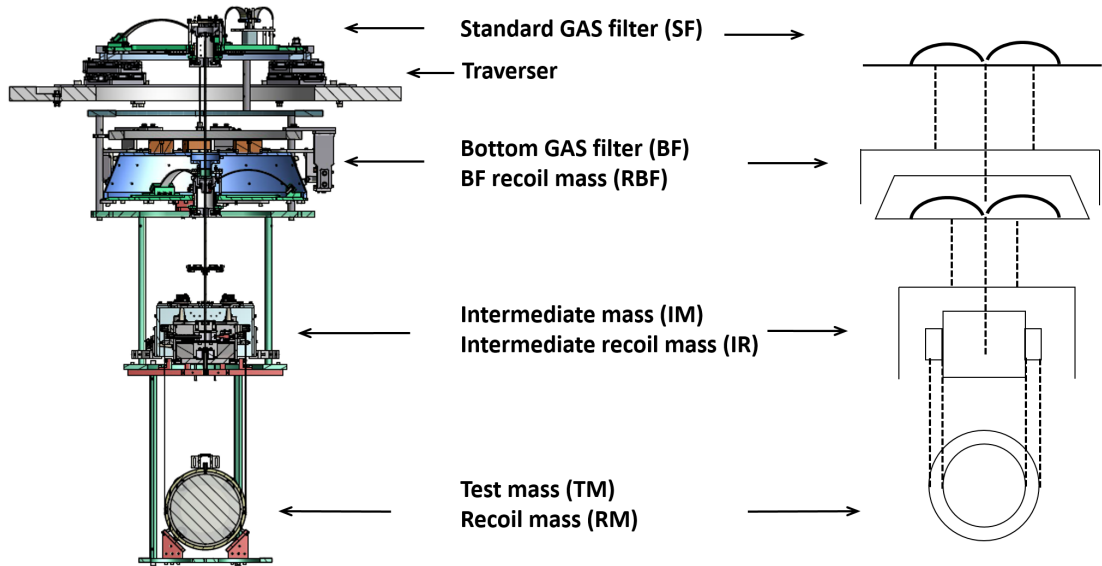
Figure 5.7: The overview of the Type-Bp suspension system (from [45]).

Expected mirror displacement

The expected displacement of a mirror suspended by Type-Bp suspension is shown in Figure 5.9.
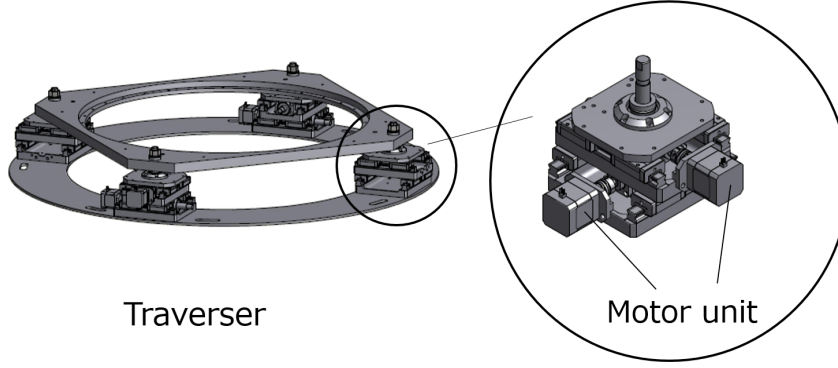
Figure 5.8: Overview of the traverser for Type-Bp suspension.

Figure 5.9: Expected mirror displacement spectrum of a mirror suspended by Type-Bp suspension, assuming 1% vertical to horizontal coupling. The red and blue curves shows the TM displacement induced by ground in horizontal and vertical respectively. The magenta and cyan curves represents the required mirror displacement level for the KAGRA observation modes described in sections 1.4.2 and 1.4.3.

5.2 Building blocks of KAGRA SAS

This subsection describes the mechanical parts of the KAGRA suspensions. The information of the sensors and actuators used for the active control system is summarised in the next subsection.

As introduced in section 4.1.3, we realize sufficiently low resonant frequency SAS with a compact mechanics, using the anti-spring techniques. In this subsection the main components which constitute the three type of SAS are described.

5.2.1 Inverted pendulum (IP) stage

IP-stage is composed of a frame structure on the ground, three inverted pendulums (IPs) and the top-stage where a GAS filter (see section 5.2.2) is mounted. The overview of the IP-stage is shown in Figure 5.10.

The three IPs are 120° separated and they support the top-stage. The detailed structure of the IP leg in shown in Figure 5.11. Each IP leg is supported by a cone bellows on a jack. The jack is placed below the cone bellows outside vacuum. By using the in-air jacks, the tilt of the IP-stage inside the vacuum chamber is adjusted.

IP-stage has three sets of coil-magnet actuators and two kinds of sensors mounted in a pinwheel geometry. The implemented sensors are displacement sensors and inertial sensors. More specifically, as displacement sensors, we use linear variable differential transducer called LVDT (see section 5.3.1). As inertial sensors, we use geophones L-4C for the two ETMs and accelerometers (which were developed for TAMA detector) for the ITMs[2]. The details about these inertial sensors are described in section 5.3.2. These two kinds of sensors on the IP-stage are originally used by combining their signals as introduced in section 4.2, in order to use LVDT signal at lower frequency and inertial sensor signal at higher frequency. The IP-stage can also be used to adjust the equilibrium position of the suspended mirror in the horizontal direction by using a motorized blade spring system.

---

[2]For ITMs, we are planning to replace the TAMA accelerometers to geophones in observation before the next observing run.
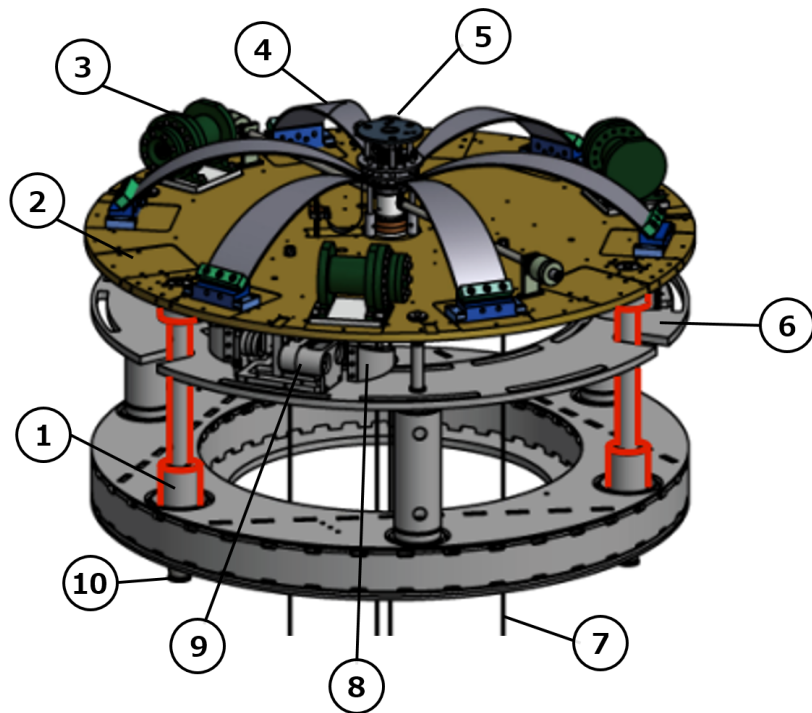
Figure 5.10: The overview of IP-stage. 1) IP leg, 2) top stage, 3) inertial sensor for sensing the IP top stage motion, 4) the cantilever of F0 GAS filter, 5) keystone of F0 GAS filter, 6) frame structure where one end of the LVDTs and the motorized blade spring are attached, 7) suspension wires, 8) motorized blade spring, 9) LVDT and the coil-magnet unit, 10) cup of cone bellows.
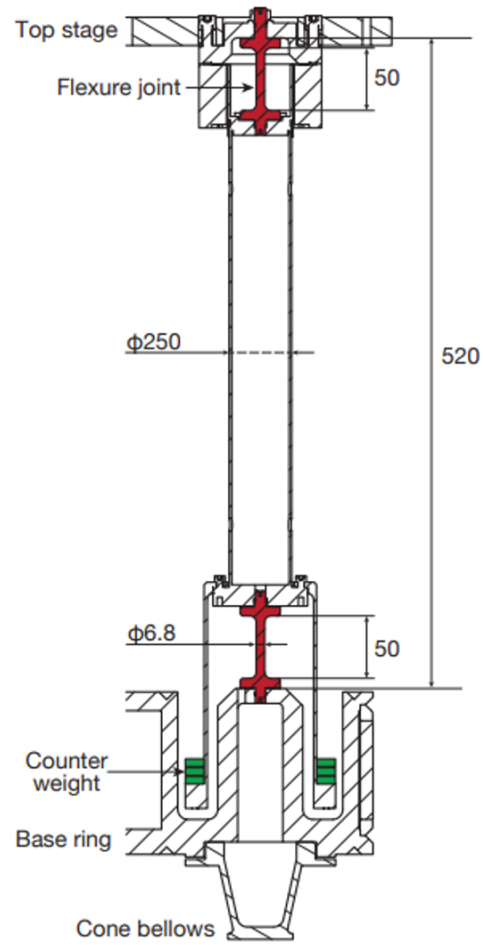
Figure 5.11: The details of the structure around the IP leg. The counter weight is implemented in order to minimize the saturation level in the displacement transfer function as described in section 4.1.3 (This figure is reproduced from [41]).

5.2.2 GAS filters

As introduced in section 4.1.3, a GAS filter is composed of a set of symmetrically arranged cantilever blades. The cantilever blades are made of maraging steel [73]. This material is selected in order to avoid creep deformation, which is the tendency of a material to drift slowly when it is under high stress conditions. Figure 5.12 shows the detailed structure of a GAS filter, known as standard filter (SF). Figure 5.13 shows its cross-section. The width and number of the cantilever blades are tuned in accordance with the weight of the suspended masses. Each GAS filter is covered by a metal cup in order to realize the required mass load and to attach electrical cables on the surface of it. The multi-stage pendulum system in KAGRA is composed of a chain of GAS filters. The number of the GAS filters in the chain is selected with suspension type depending on the required vibration attenuation level.

Each GAS filter has an LVDT and a coil-magnet actuator to actively control it (see section 5.3). LVDT measures the relative height variation between the base plate and the keystone.

The GAS filter has a motorized vertical adjustment system for the keystone position. This system is made out of a blade spring, and is called fishing rod. The top and bottom GAS filters have a motorized Yaw position adjustment system for tuning of the mirror torsional position.
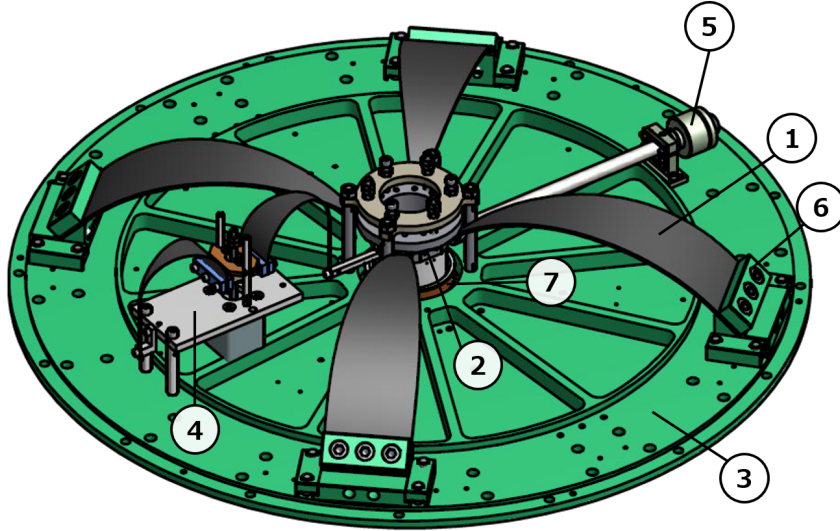
Figure 5.12: The mechanical overview of the typical GAS filter, called standard filter. 1) The cantilever blade, 2) the keystone, 3) the baseplate, 4) the motorized spring for initial positioning of the keystone, 5) the magic-wand for compensating CoP effect (see section 4.1.3), 6) the base clamp, 7) the LVDT to monitor the displacement of the keystone (reproduced from [45]).
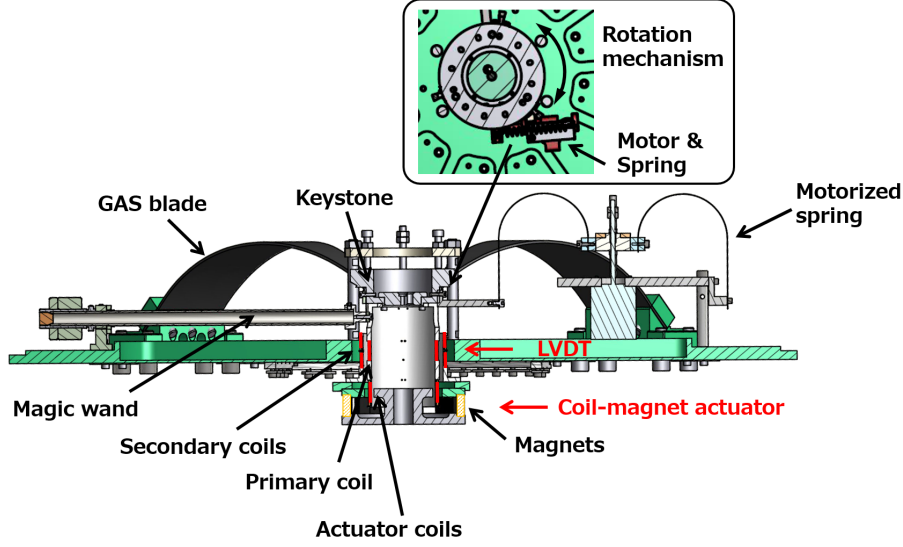
Figure 5.13: The cross-section of GAS filter(from [45]).

Effect of blade compression

The compression of the GAS blades is tuned so that their forces on the keystone balance the suspended mass at the working point. According to eq (4.21), k_{eff} can have a negative value depending on the compression, in which case the system becomes unstable and the GAS filter does not work properly.

Indeed the resonant frequency and the working point depend on the blade compression and the suspended load. The resonant frequency is expressed by $1/2\pi\sqrt{k_{\mathrm{eff}}/m}$, where m is the suspended load with eq (4.20). Concerning the working point, the dependence is explained with eq (4.19). By assuming the equilibrium position of the keystone is shifted by Δz in eq (4.19), we set $m\ddot{z} = (\Delta m)g$ and then obtain the following equation:

$$\Delta m = -\frac{(k_z + k_x{}')\Delta z}{g} + \frac{k_x{}'l_{0x}}{g}\frac{\Delta z}{\sqrt{x_0{}^2 + (\Delta z)^2}} \tag{5.1}$$

$$\sim -\left[\frac{k_z}{g} - \left(\frac{l_{0x}}{x_0} - 1\right)\frac{k_x{}'}{g}\right]\Delta z, \quad (\text{if } x_0 \gg \Delta z). \tag{5.2}$$

Using these equations, Figure 5.14 shows the working point and the resonant frequency as the function of the suspended mass load, for different compression values $C = (l_{0x} - x_0)/l_{0x}$ in the model. Typically, the compression is tuned so that the GAS behaves like the case of 9% compression in Figure 5.14. If the compression value becomes too large (larger than the 9% case in the example shown in Figure 5.14), the oscillator becomes unstable at around the working point as shown in Figure 5.14 (*right*).

Consequently, we have to tune the suspended load very carefully in the actual system.
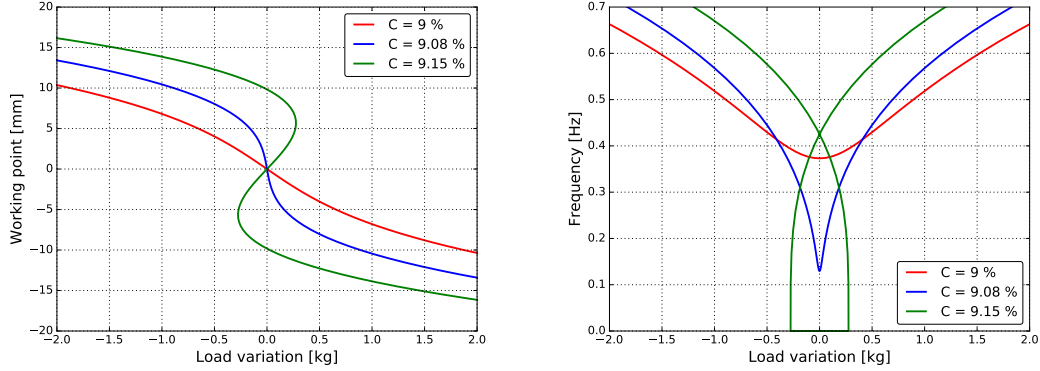
Figure 5.14: Working point height of the keystone (*left*) and its resonant frequency (*right*) as a function of suspended mass load, with various compression of the GAS blade, predicted with the model, when the following setting is used: $k_z = 1.0 \times 10^5$ N/m, $k_x{}' = 1.0 \times 10^6$ N/m and $l_{0x} = x_0 =$ 0.3 m. It is assumed $m_0 = 200$ kg in the *right* panel (from [45]).

Thermal drift

The keystone height can easily drift with small temperature variation of the blade springs. This is due to the temperature dependence of the Young's modulus of the blade spring material. The drift of the keystone can affect the GAS filter operation.

The impact can be estimated as follows. We assume that the GAS filter balances at the working point with a suspended mass of m. In this situation, the height change Δz when the load on the keystone is changed by Δm is given by $\Delta z = g \Delta m / k$, where k and g are the effective stiffness of the GAS filter and gravitational acceleration respectively. In addition, assuming $\Delta m/m = \Delta E/E$ (where E is Young's modulus of the blade), the temperature dependence of the keystone height is given by:

$$\frac{\Delta z}{\Delta T} \;=\; \frac{g}{k}\frac{\Delta m}{\Delta T} \;=\; \frac{mg}{kE}\frac{\Delta E}{\Delta T} \;=\; \frac{g}{\omega_0^2 E}\frac{\Delta E}{\Delta T}, \tag{5.3}$$

where T is the temperature of the blade. Experimentally this dependence was measured as [44]

$$\frac{\Delta z}{\Delta T} \;=\; 0.69\ [\text{mm/K}] \left(\frac{0.33\ \text{Hz}}{\omega_0/2\pi} \right)^2 \left(\frac{\frac{1}{E}\frac{\partial E}{\partial T}}{3.0 \times 10^{-4}\ [1/\text{K}]} \right), \tag{5.4}$$

where ω_0 is the resonant angular frequency of GAS filter.

This implies that even if the temperature in the experimental hall is kept within ± 1 K, the vertical position of the mirror suspended to the Type-A suspension, composed of several GAS filters in cascade, can be changed by several mm. Such a situation can make the interferometer operation difficult. Thus it is

important, not only to keep constant the environmental temperature, but also to keep constant the keystone height by means of an active control system.

5.2.3 Suspension wires

The mechanical components at room temperature are suspended by using wires made of maraging steel. Figure 5.15 shows their detailed structure.

The wire has thicker diameter in its middle part compared to the ends. It is demanded to use larger diameter wire in order to obtain stronger torsional stiffness, which is good for the interferometer operation. On the other hand, if the diameter is too large, the longitudinal vibration attenuation performance can be degraded. This is due to a fact that the elastic force of the wire can become non-negligible compared to the gravitational restoring force. However, the effective bending stiffness depends on the diameter in a few cm from the suspension points. Thus we select the shape as shown in Figure 5.15. The diameter is adjusted depending on the suspended mass.
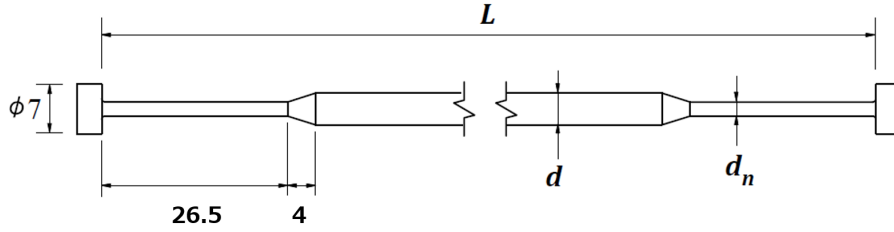
Figure 5.15:   Overview of the typical suspension wire made of maraging steel (from [45]).

5.2.4 Magnetic damper

A passive damper which utilizes the eddy-current as introduced in section 1.3.1 is called magnetic damper. The detailed implemented position for the Type-A and Type-B suspensions are shown in Figures 5.1 and 5.5 respectively.

The damping force acts between two ring-shaped plates. One plate includes an array of magnets (72 magnets in total) as shown in Figure 5.16. Such a magnetic damper works effectively when the distance between the two plates is set to about 2.5 mm in KAGRA SAS.

5.2.5 Bottom filter

The GAS filter at the lowest stage in the GAS-filter chain is called bottom filter (BF). The details about the implemented position for the Type-A and Type-Bp suspensions are shown in Figures 5.1 and 5.7 respectively.

The BF has motorized tilt adjustment system, and is used to set the gap between the intermediate mass (IM) and its recoil mass (IRM) (see section 5.2.6) for the initial alignment of the room-temperature payload. By adjusting the pitch and roll DoFs of the BF, it is possible to adjust the gap between IM and IRM

(see section 5.2.6) respectively in the longitudinal and transverse direction. The schematic of this system is shown in Figure 5.17.

Damping system at BF

Depending on the suspension, we also have an active damping system at BF stage. We implement six sets of LDVTs and coil-magnet actuators around the BF body in order to damp the resonant modes which cannot be damped with the upper stages. The LVDT and actuator unit used for the BF-stage damping is called BF-LVDT (see section 5.3.1).

We have two types of implementation. In the Type-A suspension, one end of BF-LVDT unit is mounted on the ground, i.e, on the security frame structure. In the case of the Type-Bp suspension, this end of BF-LVDT is mounted on a suspended mass. The overview of this system is shown in Figure 5.18.
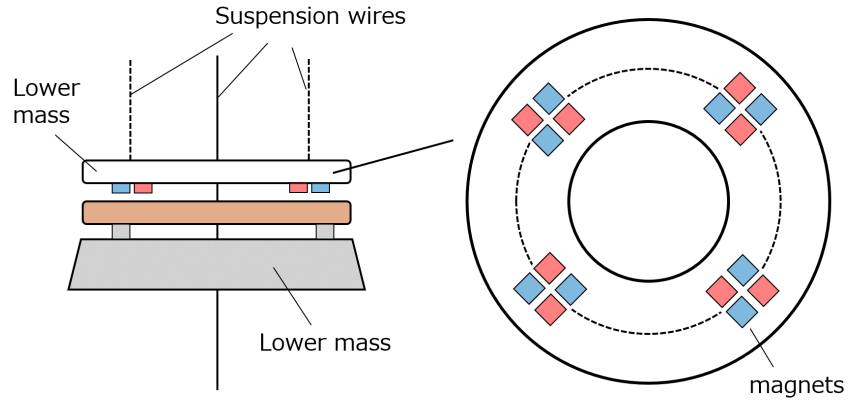
Figure 5.16: Over view of magnetic damper. The magnets are arranged as shown in the picture on the *right*, and the difference of the colors denotes the difference of magnetic pole.
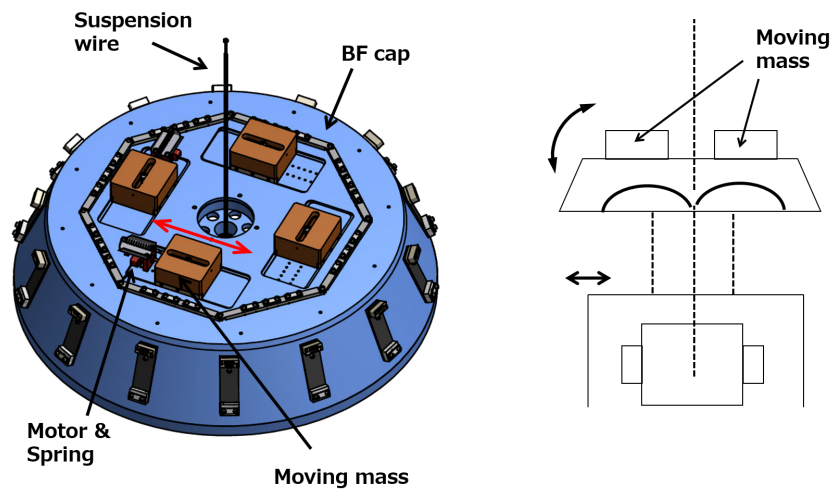
Figure 5.17: Overview of BF tilt adjustment system (from [45]).
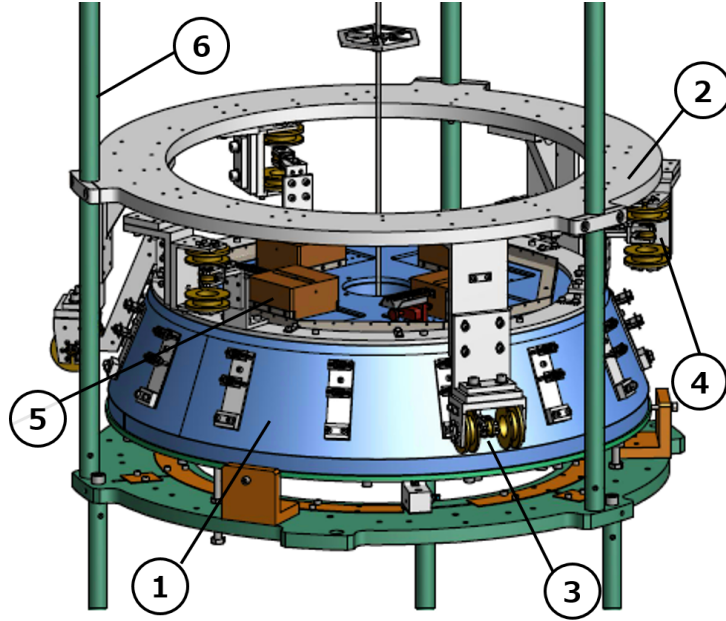
(a) 1) The body of the bottom GAS filter, 2) the BF-damper structure attached to the security frame, 3) the horizontal BF-LVDT and coil-magnet actuator unit, 4) the vertical BF-LVDT and coil-magnet actuator unit, 5) the motorized BF-tilt adjustment system, 6) the security frame.
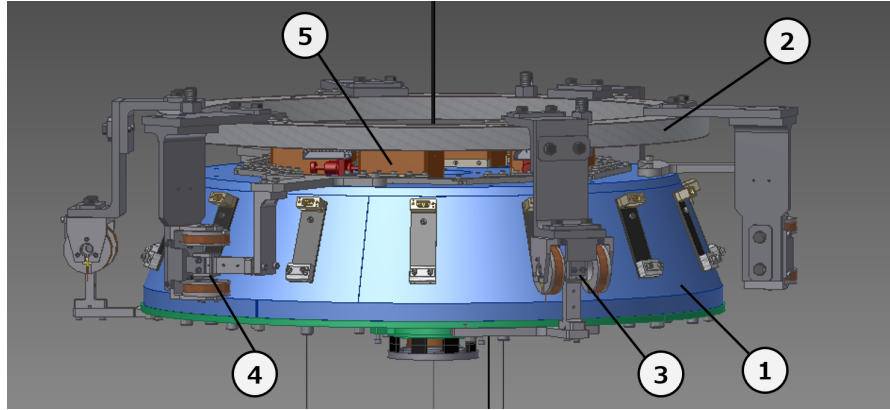
(b) 1) The body of the bottom GAS filter, 2) the suspended recoil mass for the bottom GAS filter, 3) the horizontal BF-LVDT and coil-magnet actuator unit, 4) the vertical BF-LVDT and coil-magnet actuator unit, 5) the motorized BF-tilt adjustment system (from [45]).

Figure 5.18: Overview of damping system at BF for the Type-A suspension (a) and for the Type-Bp suspension (b).

5.2.6 Payload

The lowest part of the suspension system is called payload. The payload is used to:

1. steer the mirror in pitch and yaw for the interferometer alignment,

2. provide additional seismic attenuation,

3. damp the payload resonances.

Depending on the suspension, we have two types of payload; one is used at room-temperature, and the other one is used at cryogenic temperature.

Room-temperature payload

Room-temperature payload is made of two stages and is composed of:

1. an intermediate mass (IM) and an intermediate recoil mass (IRM),

2. a test mass (TM) and a recoil mass (RM).

A drawing of the payload is shown in Figure 5.19. The IM is suspended by single maraging wire from BF keystone, and the IRM is suspended by three magaring wires from below the BF. The TM and RM are suspended from IM by two loop-shaped tungsten wires. As local sensors and actuators, we use an optical sensor and electro-magnetic actuator called OSEM (see section 5.3.3). OSEMs are implemented at the IM-stage. They measure and actuate the relative motion between the IM and IRM in six DoFs. Also the TM stage has the OSEMs but they are only used as actuators. The detailed OSEM positions are shown in Figure 5.20. In addition, an optical lever (see section 5.3.4) is used to measure the TM-stage motion in the longitudinal, pitch and yaw DoFs.
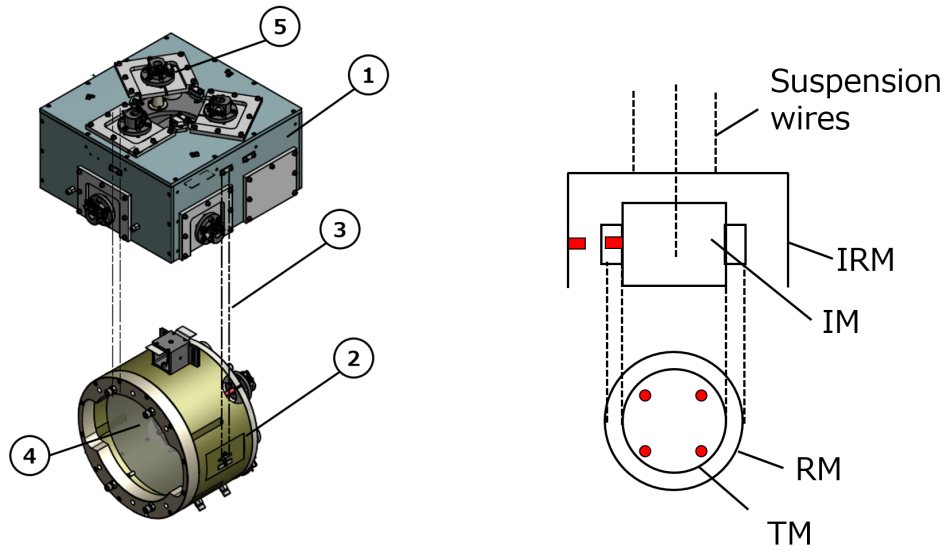
Figure 5.19: Overview of room-temperature payload. 1) intermediate recoil mass (IRM), 2) recoil mass (RM), 3) tungsten wires to suspend RM from IM, 4) test mass (TM), 5) OSEM at IM-stage (in *left*) The red colored dots and the rectangles schematically show OSEM unit positions (in *right*).
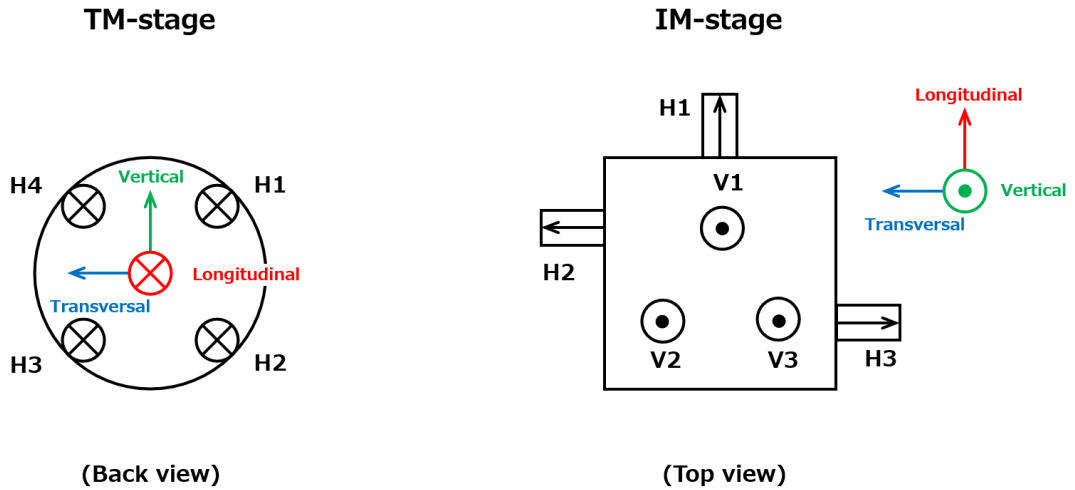
Figure 5.20: Detailed OSEM location. H1, H2, H3 and H4 denote the position of OSEM for horizontal motion sensing, and V1, V2 and V3 show the OSEM position for vertical motion sensing. The arrows show the sensor and actuator polarities. TM-stage has only actuators.

163

Cryogenic payload

Cryogenic payload is developed to operate at cryogenic temperature and, as shown in Figure 5.21, consists of four stages:

1. platform (PF)

2. marionette (MN), recoil marionette (RMN)

3. intermediate mass (IM) and intermediate recoil mass (IRM),

4. test mass (TM) and recoil mass (RM)

In this payload, the PF is suspended by a maraging wire from the BF, and two suspension chains are suspended from the PF. These two chains are called TM chain and RM chain respectively. One chain includes MN, IM and TM, and the other chain suspends RMN, IRM and RM.

MN is suspended from cantilever blades at PF-stage by single maraging. The IM is suspended from MN by four copper-beryllium wires, and the TM is suspended by four sapphire fibers from IM. Each sapphire fiber is hooked to a sapphire blade at the IM-stage.

On the other hand, the RMN is suspended from the underneath of the PF by three wires. The IRM is suspended from RMN by four wires. The RM is suspended by two loop wires from IRM. All the stages of teh recoil-mass chain are suspended by copper-beryllium wires. Each stage is connected with high purity aluminum wires, called heat links (see cooling system in section 5.1.1). These heat links are connected between the stages sufficiently loosely in order to avoid introducing additional stiffness.

As additional local sensors and the actuators, the cryogenic payload uses reflective photo sensors (PS) and coil-magnet actuators specifically developed for the cryogenic environment (see sections 5.3.5 and 5.3.6). The PS measure the relative motion between TM-chain and RM-chain in six DoFs. The detailed PS and the actuator positions are shown in Figure 5.22. As additional local sensor, the TM-stage and MN-stage also have an optical lever (see section 5.3.4), that measures the MN-, TM- chain motion in pitch and yaw. Only at TM-stage, another optical lever which measures the TM-chain motion in longitudinal (see section 5.3.4) is implemented.
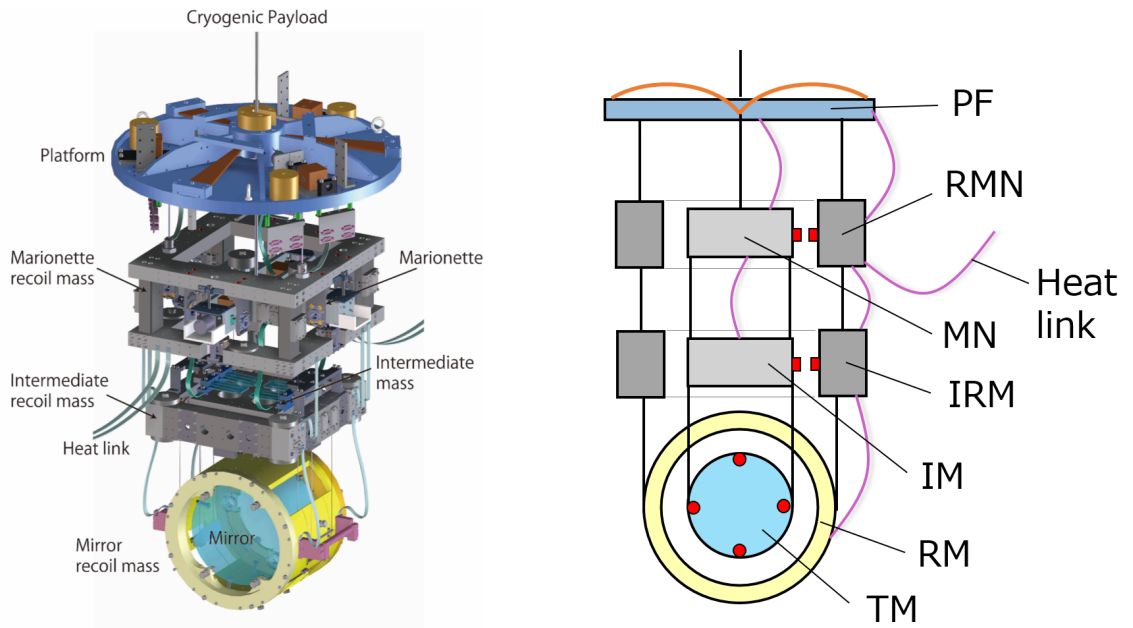
Figure 5.21: Overview of the cryogenic payload. The red colored dots and the rectangles schematically show photo-sensor (PS) and actuator unit positions. For TM-stage, only actuators are implemented.
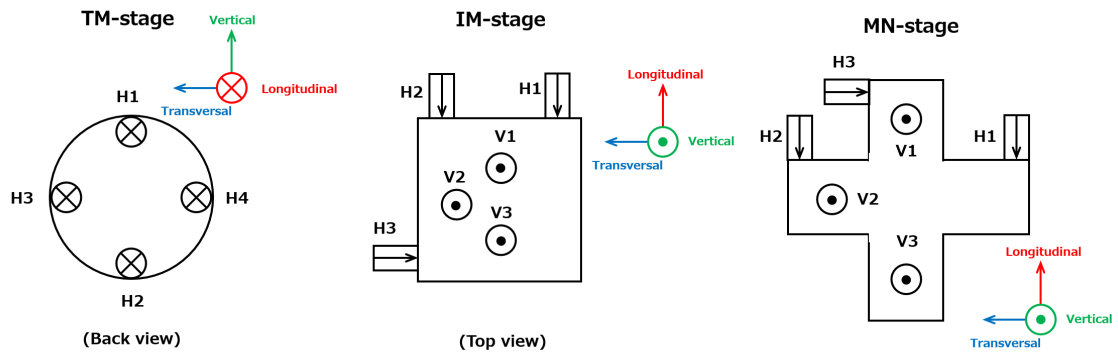
Figure 5.22: Detailed PS and actuator location. H1, H2, H3 and H4 denote the position of the photo-sensor (PS) and actator for horizontal motion, and V1, V2 and V3 show the PS and actuator position for vertical motion. The arrows show the sensor and actuator polarities. TM-stage has only actuators.

5.3 Sensors and Actuators

The sensors and actuators implemented in the KAGRA SAS are briefly introduced hereafter. The measured and estimated noise floors of those sensors are also reported in this section. These measurement and estimation are done to prepare for the construction of the active control system (described in the next chapter).

5.3.1 Linear variable differential transducer (LVDT)

Linear variable differential transducer (LVDT) is a non-contacting relative position sensor using coil inductance and modulated magnetic fields [74]. It is composed of three coaxial coils; a small central coil and two larger lateral coils as shown in Figure 5.23. The smaller coil and the two larger coils are called primary and secondary coil(s) respectively. LVDT measures the displacement of the primary coil from the center of the secondary coils.

We have two kinds of LVDTs in KAGRA; one type shares the coils for sensing and actuation (originally developed for Virgo detector [75]), and the other type does not. The first type consists of the three coils, and has a magnet inside the primary coil holder. The other type has only the three coils and has no actuation capabilities. For this LVDT, we use another coil (and magnet) for the actuation.

The first type is called BF-LVDT since it is used for the damping system at the BF-stage while the other type is simply called LVDT.

We have measured the noise floor and its linear range. The typical noise floor and linear range of these sensors are shown in Figure 5.24.
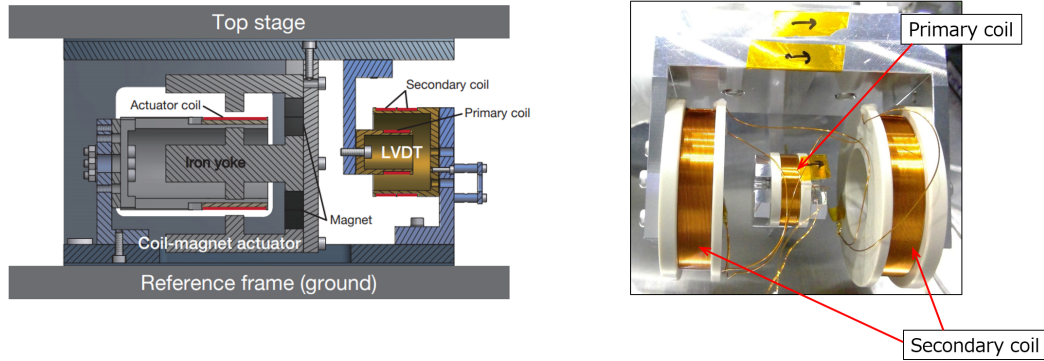
Figure 5.23: The detailed structure of LVDT from [41] (*left*) and that of BF-LVDT (*right*). The structure of GAS-LVDTs is shown in Figure 5.13.
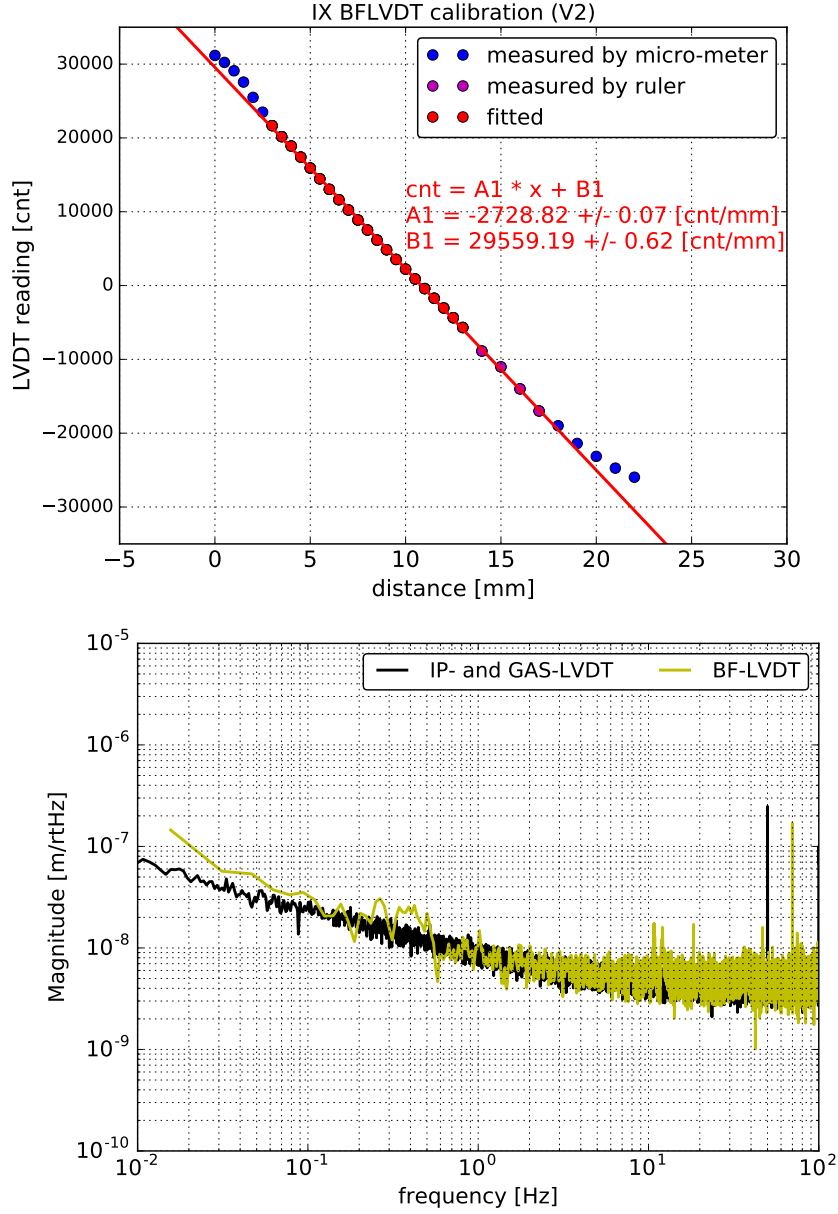
Figure 5.24: The typical linear rage (*top*) and the noise floor (*bottom*) of the LVDTs. The *top* panel shows a measured calibration curve where the value of the vertical axis is proportional to the LVDT output voltage. In the *bottom* panel, the measured noise floors of the LVDTs (referred as IP- and GAS-LVDT) and the floor of the BF-LVDTs are shown.

5.3.2 Inertial sensor

Two different kinds of inertial sensor are currently used. One is an accelerometer developed for TAMA-SAS [65] and the other one is a commercial speed meter known as geophone L-4C. The TAMA-accelerometers are used in the two ITM suspensions, while the geophones are implemented in the two ETM suspensions.

TAMA accelerometer

The accelerometers were originally developed for TAMA-SAS [76]. The overview of the mechanics of TAMA accelerometer is shown in Figure 5.25, The proof mass is supported by a folded pendulum. The leg at one end of the proof mass is a pendulum providing the normal restoring force. The other side of the proof mass is supported by an equal-length inverted leg which produces an anti-spring force. The mechanical resonant frequency can be tuned down to about 0.5 Hz. We obtain the acceleration signal of the proof mass from the feedback control force.

We have measured the noise floor of the implemented ITMX-accelerometer[3] by using the three-channel correlation analysis method [77]. The typical result is shown in Figure 5.26.
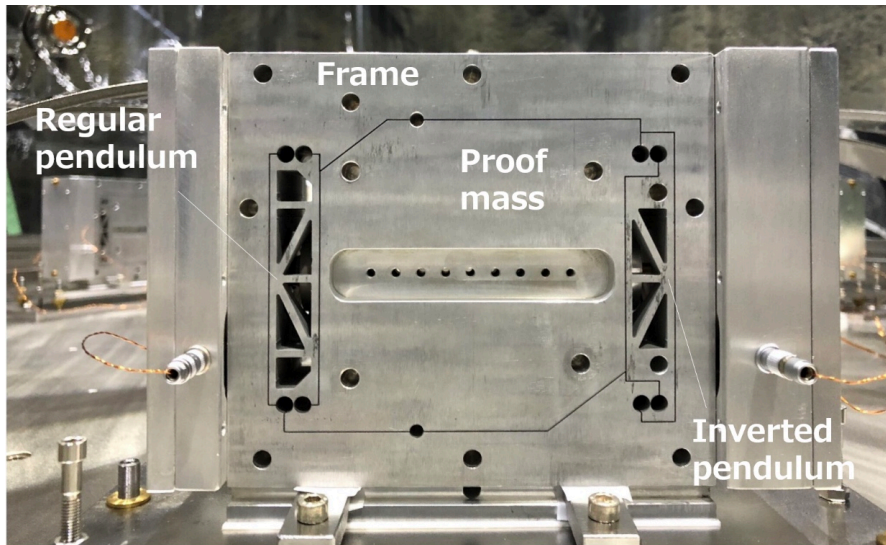
Figure 5.25: Overview of TAMA accelerometer.

---

[3]Due to some technical problems, the accelerometers did not achieve their expected sensitivities. Especially the noise floor of the ones for ITMY suspension was much worse than that of ITMX suspension.
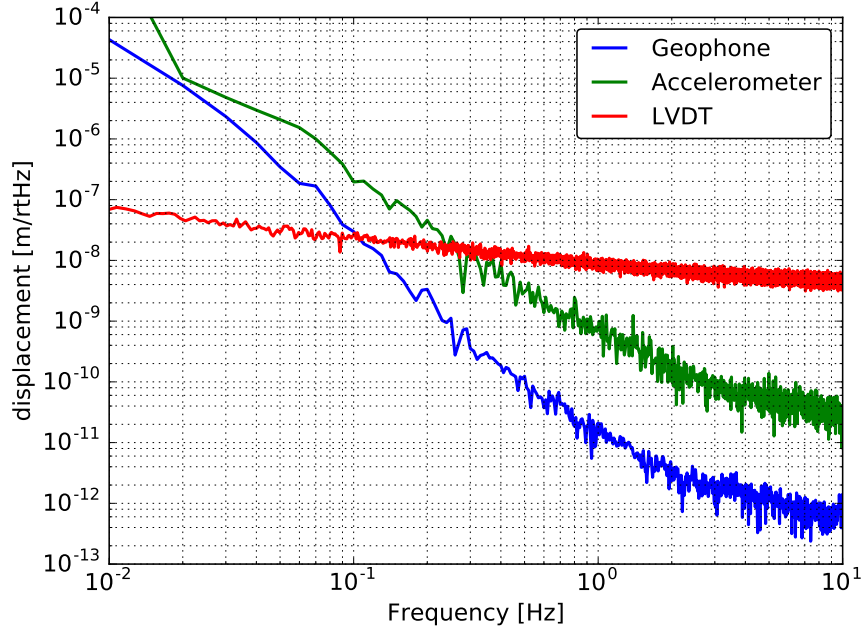
Figure 5.26: The measured noise floor of the implemented inertial sensors compared to that of LVDTs. The blue, green and red curves show the noise spectra of the geophone, the TAMA accelerometer and the LVDT respectively.

Geophone L-4C

A geophone L-4C is a commercial speed meter. It contains a mechanical oscillator and its velocity with respect to its outer frame is measured.

Its response from the velocity to output voltage in frequency domain $H_{\text{geo}}(\omega)$ is given by:

$$H_{\text{geo}}(\omega) \;=\; \frac{G_e \omega^2}{\omega_0^2 + 2i\eta\omega_0\omega + \omega^2}, \tag{5.5}$$

where G_e is called generator constant, η is the damping coefficient, ω and ω_0 are the angular frequency and angular resonant frequency, respectively. G_e represents the sensitivity at frequencies higher than the resonant frequency of the proof mass.

Figure 5.27 shows the response in eq (5.5) with typical parameters. The actual geophones are calibrated with already calibrated seismometers described in section 5.3.7.

We have measured the noise floor of the noise floor of geophones by using the three-channel correlation analysis method [77]. The typical result is included in Figure 5.26.
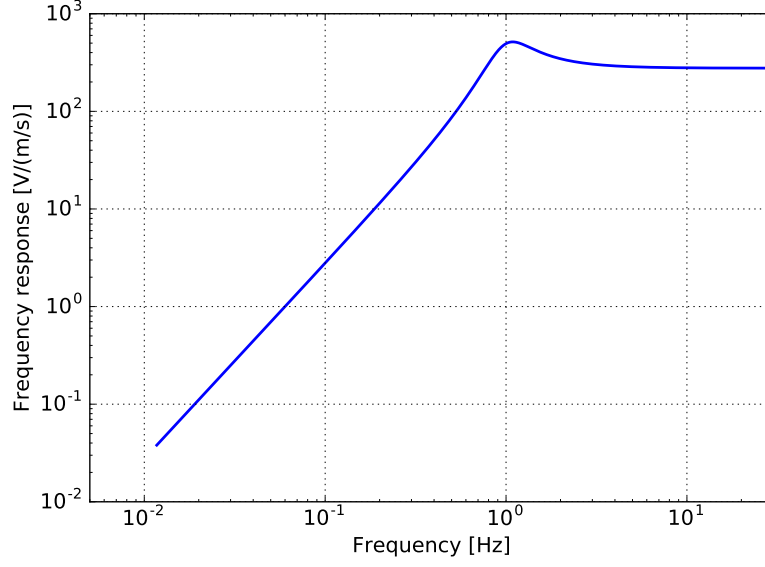
Figure 5.27: The geophone frequency response with the typical parameters. In this plot G_e, f_0, η are set to 276.8 V/(m/s), 1.0 Hz and 0.28 respectively.

5.3.3 Optical sensor and electro-magnetic actuator (OSEM)

Optical sensor and electro-magnetic actuator (OSEM) is a unit composed of a shadow sensor and a coil magnet actuator [78]. In the sensing part, we use a LED, a photodiode (PD) and a flag. We measure the flag position by sensing the detected light on the PD. Typical configuration and its noise floor are shown in Figure 5.28 and 5.29 respectively.

The OSEMs are used only for the payload of the Type-B and the Type-Bp suspension. Thus the details are not described in this thesis. More details can be found in [44].

170
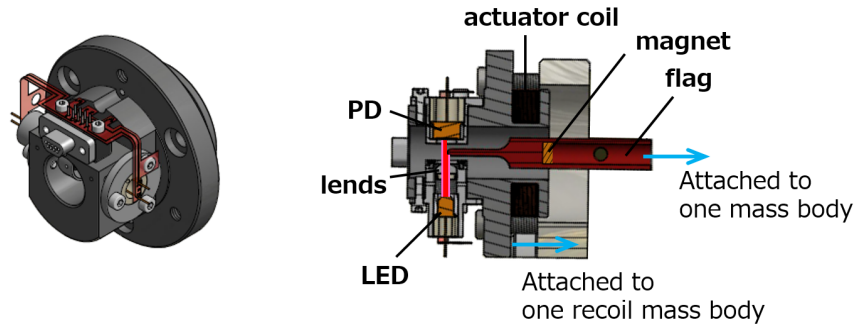
Figure 5.28: Detailed structure of OSEM (This figure is reproduced from [45]).
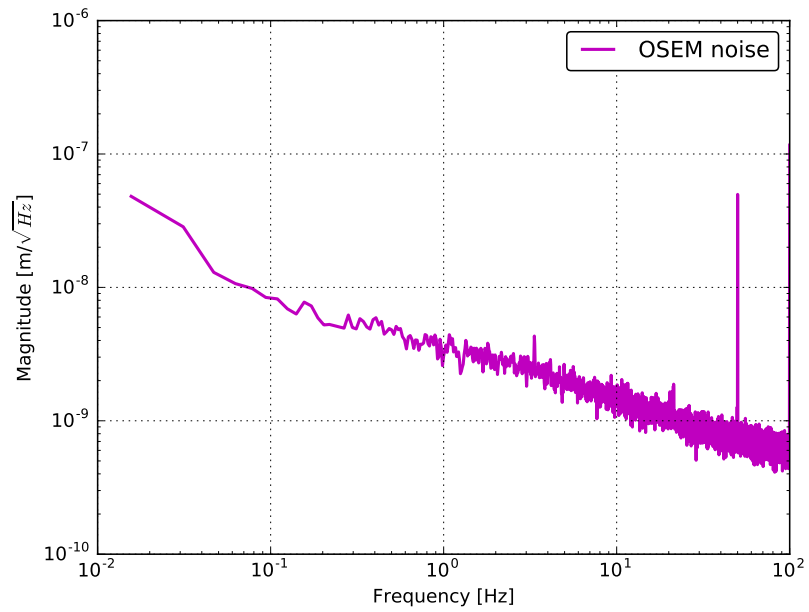
Figure 5.29: Typical noise floor of OSEM (This figure is reproduced rom [45]).

5.3.4 Optical levers

Optical lever (oplev) is a local sensor to measure the angular (and translational) displacement of an object. We have two types of oplevs; one is used for sensing the angular motion, and the other one is for the longitudinal motion. The oplev for the angular motion is called oplev. The oplev for the longitudinal motion is called length-sensing oplev (length-oplev).

The oplev consists of a light source and a quadrant photo diode (QPD). We shine fiber-collimated light from a super luminescent diode (SLD) on a mirror attached to the mass to be measured. From the change in the position of the reflected light on the QPD, we can measure the mirror motion. An example of the geometry is shown in Figure 7.2. The oplev system is implemented outside the vacuum chamber, and an air-shield is installed around both the light source and QPD.

The length-sensing oplev shares the light source with oplev (for angular motion) however uses another QPD and a lens. The details on the working principle can be found in [79].

The linear range of oplev is typically about a few hundred μrad. The noise floor of the optical lever and the length-sensing optical lever estimated from a measurement is shown in Figure 5.30. The noise floors are estimated from a interpolation of free-swinging mirror spectra with the wind-shield.
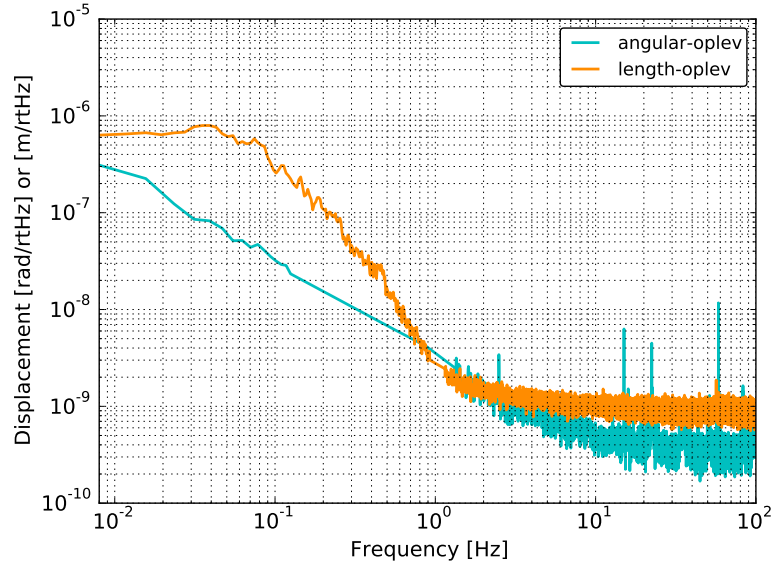
Figure 5.30: Estimated noise floors of the angular optical lever and the length-sensing optical lever.
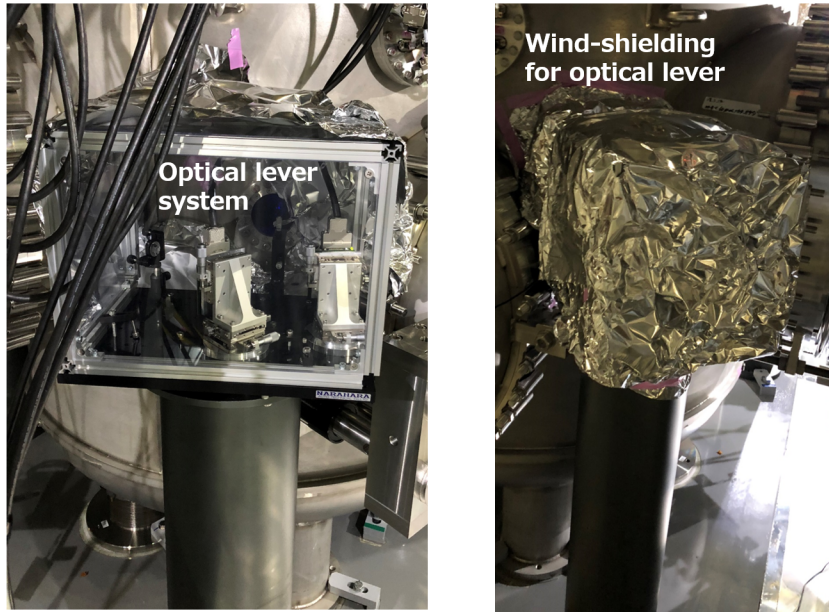
Figure 5.31: An example of the air-shield for the optical levers. The system at PR3 suspension without the shield is shown in $left$, with the shield is in $right$.

5.3.5 Reflective photo sensor

The reflective photo sensor (PS) is a non-contacting sensor which works even at a cryogenic temperature of 20 K. It was developed mainly for the purpose of mechanical resonance damping of the RM-chain modes of the cryogenic payload [80]. A photo-sensor unit consists of a LED and two photodiodes. Six of these photo-sensor units are arranged at each MN- and IM-stage so that they can sense their displacement with respect to its recoil-mass in 6 DoFs.

It is known that these photo-sensors have individual differences in the calibration factors. According to a measurement in [80], the difference can come from the difference of the beam profile of the LED. As another note, the calibration factor depends on the operation temperature.

An estimate of the noise floor of the implemented photo-sensor[4] is shown in Figure 5.33.
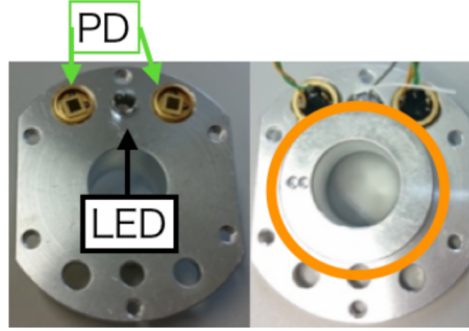
Figure 5.32: Overview of the reflective photo sensor (PS). The front and back sides are shown in the *left* and *right* panel respectively. PD stands for photodetector. The orange colored circle indicates the coil bobin used for actuation. This picture is reproduced from [80], Figure 4.26.

---

[4]Due to time constraint, we could not calibrate each photo-sensor. The calibration factor has been estimated by comparing two force transfer functions. According to a simulation, the low-frequency-gains of the following two transfer functions becomes equal; the transfer function from MN-Yaw excitation to MN-Yaw with PS, and that from MN-Yaw excitation to MN-Yaw with oplev. The calibration factor is obtained by assuming this fact. The noise floor of one PS is then calibrated from the result.
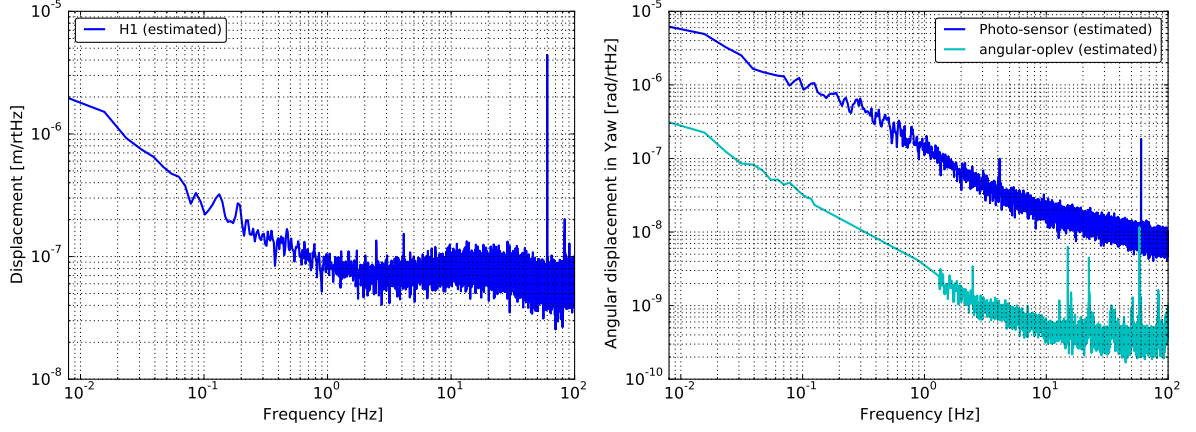
Figure 5.33: An estimation of the noise floor of the implemented photo-sensor (*left*) and a comparison of the noise floor to that of angular optical lever in Yaw DoF (*right*).

5.3.6 Coil-magnet actuator

For the suspension control, it is demanded to use non-contacting actuators in order not to transmit the external vibration to the suspended masses. For this purpose, we implement coil-magnet actuators which are composed of a permanent magnet and a solenoid coil. The magnet is attached on the mirror, and the coil is attached on the recoil mass, for example. By inducing current on the coil, we obtain a magnetic field with electromagnetic induction which apply a force on the magnet. The actuator design details are summarized in [81].

5.3.7 Seismometer

The ground vibration where each Type-A suspension stands is measured by a commercial seismometer Trillium120QA [38]. For the Type-A system, the seismometer is set at the second floor of each station. Its self-noise level compared to the typical noise level of LVDT is shown in Figure 5.34. The noise floor itself is relatively low for the suspension related control even at frequency between 10 mHz to 100mHz. However, the seismometer is affected by local ground tilt change at frequencies below 0.1 Hz. Due to this fact the use of these seismometers below 0.1 Hz is usually avoided.
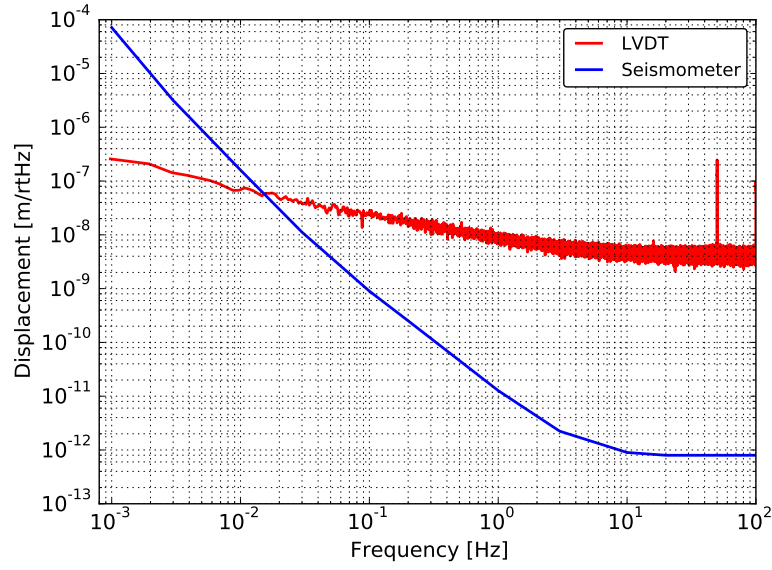
Figure 5.34: Self-noise level of Trillium120QA compared to the typical noise level of LVDT.

5.4 Integration of KAGRA SAS

The eleven KAGRA SASs have been assembled and later transferred into their vacuum chamber where sensors and actuators have been connected to the real-time digital system in order to actively control them. After the mechanical installation has been finished, it has been necessary to perform several adjusting and repairing operations on the mechanics working inside the small vacuum chambers.

Indeed I've devoted more than one and half year of my time to this activity of assembly, installation and repairing for all the three types of suspension from 2018 March[5]. This subsection briefly describes some of the installation steps and my contribution to those works.

5.4.1 Mechanical installation

As the first step, KAGRA SAS is assembled outside its vacuum chamber. The assembly starts from the lower stage (TM and IM stages) and goes to the upper stages, especially for the Type-B and Type-Bp SAS. In the Type-A SAS, the assembly of the room-temperature part and of the cryogenic payload are done independently. The two parts are connected together inside the vacuum chamber. More details can be found in [82, 83].

History

The first KAGRA SAS installation had been done from 2015 October to 2016 February for the initial KAGRA test run (so-called iKAGRA run). At that time only one mirror, the PR3, was suspended by KAGRA SAS, with a simplified Type-Bp configuration. After iKAGRA period, the installation for KAGRA operation started with three assembly teams for Type-A, Type-B and Type-Bp suspensions.

The three Type-Bp suspensions had been installed from December 2016 to December 2017 including test period to assess the installation procedure. Concerning the Type-B suspensions, the test installation of BS suspension started in June 2016 and the installation of all the four suspensions had been finished by December 2018. For type-A suspension, the installation had started on January 2017, and then all the four Type-A suspensions installation had been finished by January 2019 including the cryogenic payload part, heat links and their HLVIS.

Sensor calibration

We calibrated OSEMs, accelerometers, Geophones and BF-LVDTs, which are used in room-temperature part, before they are mounted on the suspensions. The LVDTs for IPs and GAS stages are calibrated during the installation procedure.

---

[5]In master's, I have spent a half year in the tunnel for iKAGRA PR3 installation and its test. I could obtained a knowledge about the mechanics of the actual KAGRA suspension.

Cabling inside/outside chambers

For the purpose of obtaining (sending) the sensor (actuator) signals from (to) the suspension, We lay electrical cables around each stages inside vacuum chamber. It is important to lay the cables loosely so that the additional stiffness due to the cables remains negligible. Figure 5.36 shows examples of in-vacuum cabling around IP-stage of the Type-A SAS and IM-stage of the Type-Bp SAS.

The cables from inside the chamber are connected to ADC/DAC trough appropriate electrical circuits as shown in Figure 5.37.
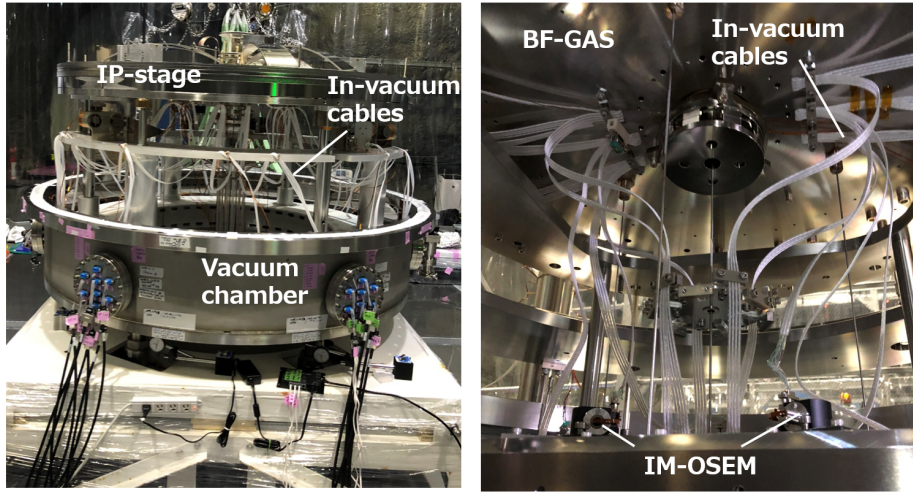
Figure 5.35: Examples of in-vacuum cabling; around IP-stage of the Type-A SAS (*left*) and around IM-stage of the Type-Bp SAS (*right*).

Figure 5.36: An example of in-air cabling around the rack that houses the analog circuits to drive the sensors and actuators.
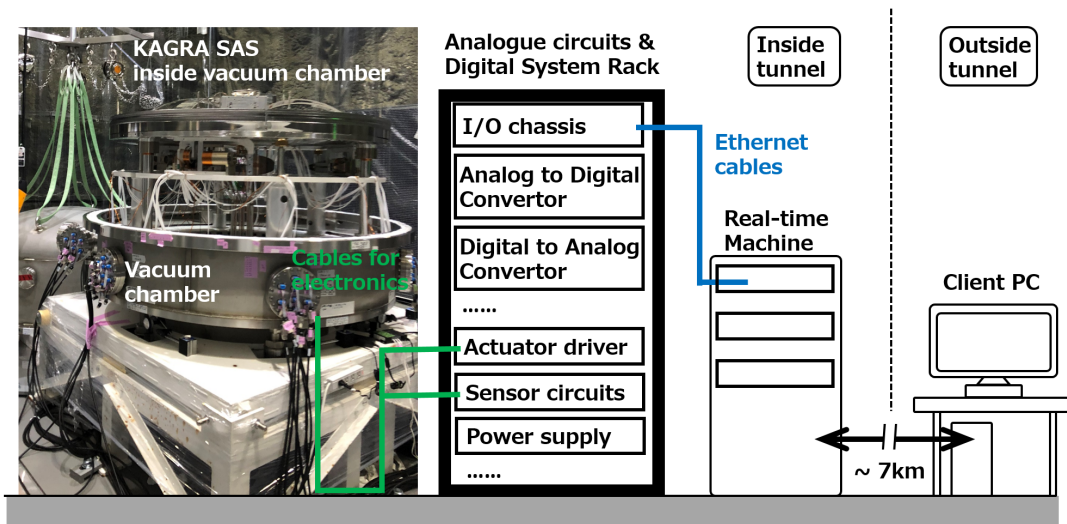
Figure 5.37: Overview of cabling including the digital system connection.

5.4.2 Data acquisition and signal processing

The data acquisition and the active control system implementation in KAGRA are done by using a real-time digital system. The real-time digital system was originally developed for the LIGO project and was imported to KAGRA. The voltage from the sensors are digitalized by Analogto-Digital Converters (ADCs), and then the correction signals are calculated in the digital system. Finally the correction signals are converted to voltage by Digital-to-Analog Converters (DACs) and then the voltage signals are sent to the actuators via appropriate driver circuits. The anti-aliasing and anti-imaging filters which aim to cut the noise due to the digitalization, are applied by using analog circuits. In the digital system for the suspension system, we use 16kHz and 2 kHz as sampling rate for the payload and the other parts respectively, which are enough for the purpose of the KAGRA SAS controls. The sensing and the actuation is limited by the available range of the ADCs and DACs, which are ±20V and ±10V respectively. All the control filters have to be designed not to saturate the ADC and DAC. More details about the KAGRA digital system are provided in [44].

An example of signal flow of the KAGRA digital system especially for the suspensions is shown in Figure 5.38. Each sensor signals are digitalized by ADC and then converted to displacement/velocity/acceleration by digital calibration filter. The calibrated signals are aligned to Cartesian coordinate by matrix operation (with sensor matrix), and then we apply feedback filters for each DoF. Finally we send the correction signals to each actuator through a matrix (actuator matrix).
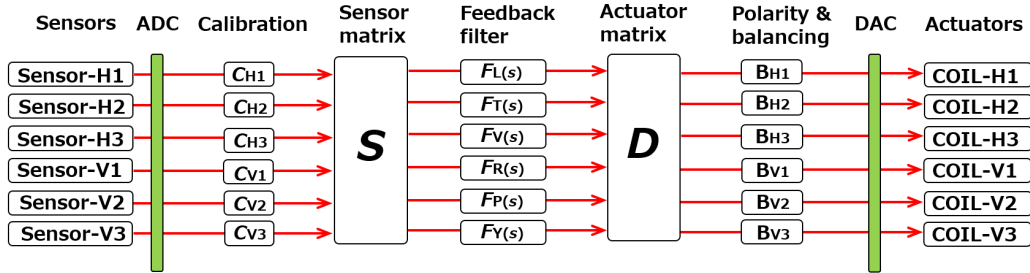

Figure 5.38: An example of signal flow of the KAGRA digital system especially for the suspensions. This is a case where six sensors and actuators are implemented.

5.4.3 Development of real-time digital system model

As described in section 5.4.2, we use real-time digital system to acquire the sensor signals and to send the actuation signals. We first decide and program how the sensor and actuation signals flow before starting the program running. After starting the run, we then develop/implement finite impulse response filters during the running. The operation of the suspensions is performed remotely from a control room located about 7 km away from the tunnel entrance. We work inside the mine if problems are reported.

We first develop the real-time system which enables to sense/actuate the suspensions in order to use the real-time system during mechanical assembly period.

5.4.4 Characterization

At every time when we finish assembling one stage of SAS, we measure the transfer functions from the actuators to the implemented sensors, and then confirm that the mechanical system has been assembled as designed.

After this step is achieved, we can start to implement feedback control systems for the suspensions, by developing the finite impulse response filters.

5.4.5 Maintenance and repairing

During the initial interferometer alignment period, several problems are reported around the suspension system, and we work for the maintenance and repairing whenever such a problem is reported.

Indeed I have contributed to this work a lot, however, this is not the main scope of this thesis work. Thus the details about this work and my contribution for this are summarized in section B.4. More details can be found in [84].

5.5 Summary

This chapter describes the details of KAGRA seismic attenuation systems (SASs). A brief description of the assembled KAGRA SASs and of their expected vibration isolation performances are included in section 5.1. The mechanical parts and the implemented sensors and actuators are summarized in section 5.2 and section 5.3 respectively. The typical sensor noise floors have been measured and estimated to prepare for the construction of the active control system. Section 5.4 describes how the KAGRA SASs are integrated.

After the integration and maintenance work (described in section B.4) has been finished, I have focused on realizing the most important local control system, which is the control system for KAGRA Type-A SAS. The following two chapters describe the development of the servo filters in simulation (chapter 6) and the implementation of them to the actual KAGRA Type-A SAS (chapter 7).

Chapter 6

Designing Type-A SAS control system in simulation

This chapter focuses on the design of an active control system for the Type-A suspension. A pc-based real-time digital servo system is used to the active control system. We use feedback and feed forward control system with the local sensors and non-contacting actuators described in the previous chapter.

The main targets for the suspension control are to damp the mechanical resonances as rapidly as possible, and to keep the mirror at the proper position and orientation. Such control system is developed by implementing appropriately shaped feedback filters. These filters are developed using the ideas described in section 4.2. More concretely we shape and implement the feedback filters (F_{fb} in section 4.2) that are realized by finite impulse response filters in the KAGRA digital system.

Section 6.1 describes the interferometer control phases, since the requirements for the suspension local control system depends on the interferometer control phase. Section 6.2 summarizes the requirements for the suspension local control system for each interferometer control phase. Section 6.3 briefly introduces how the suspension is modeled in the simulation. Section 6.4 describes the overview of the suspension control system. Sections 6.5 to 6.7 summarizes the development of the control system for each interferometer control phase, and the expected performance using simulation. Section 6.8 summarizes this chapter.

6.1 Interferometer control phases

The interferometer control phases can be described by the following three phases:

- the calm-down phase,

- the lock-acquisition phase,

- the observation phase.

The interferometer operation phases are summarized in Figure 6.1.
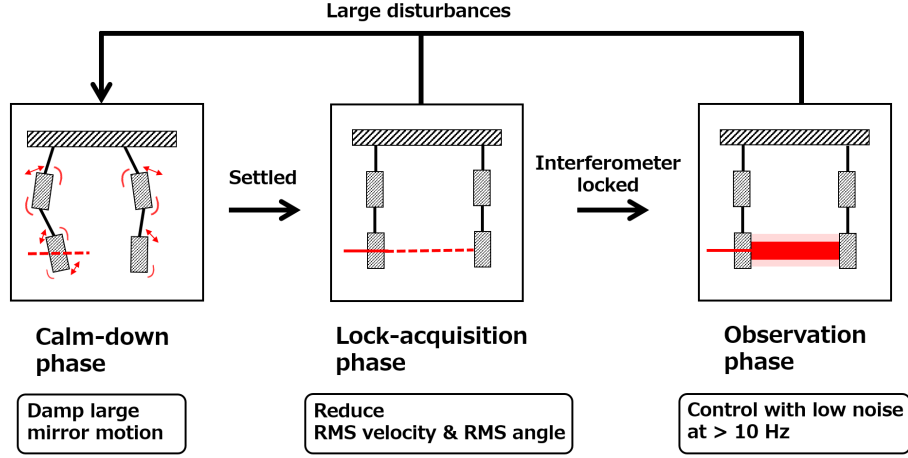
Figure 6.1: Suspension control operation phases categorized into the three phases. The main purposes of the active suspension controls are included.

The calm-down phase denote a phase where the suspended mirrors are oscillating at the resonances with large amplitude due to an external disturbance or the kick by the interferometer lock loss. Thus the target of the local control system in this phase is to damp the mechanical resonances as rapidly as possible. Minimizing the decay time of the resonances allows having fast interferometer lock recovery and, consequently, reducing lock loss time.

The lock-acquisition phase represents a phase where the interferometer lock trials are applied. In this phase, it is required to reduce the RMS mirror displacement and its velocity especially in L DoF. It is also necessary to suppress the RMS amplitude of the angular residual motion of the mirror. In this phase, we steer and hold the mirror position and orientation so that the interferometer is locked to its operating point.

Until this phase we close the control loops using local sensors with large filter gains (especially at the payload stages). We reduce the RMS amplitude of the mirror motion at the expense of the control noise coupling at high frequencies in this phase.

The observation phase is a phase where the interferometer is kept locked in the so-called science mode. What necessary in this phase is to suppress the mirror displacement noise above 10 Hz, which is the detection band of GWs, due to technical noise such as control noise couplings. In addition, we need to keep the mirror position and orientation at the proper interferometer operating point at low frequencies.

For the controls in this phase (especially at the payload stages), we replace some of the local sensor signals to other signals sensed by the photo-diodes and the

wave front sensors, which use the interferomter signal and have higher sensitivity than the local sensors. In this phase we can reduce the control noise coupling using the interferometer signals. We also open some of the local control loops to reduce the control noise coupling.

6.2 Requirements

The description in section 6.2.1 to section 6.2.4, describes each requirement. Section 6.2.5 summarizes the requirements for the local control system and it is summarized in Table 6.2 consequently.

6.2.1 Requirement on damping time

In order to reduce the lock loss time, it is required to damp the the excited mechanical resonances of the suspension rapidly. The requirement is set that the $1/e$ decay time of the mechanical resonances disturbing the interferometer lock acquisition is less than 1 minute. This requirement is set in order to avoid waiting for a long period of time before starting the following lock acquisition trial.

6.2.2 Requirement on RMS velocity

As described in section 1.3.5, the mirror displacement has to be reduced at the level of nm in order to keep the interferometric-locked condition. Since the finesses are set at 38 for the signal recycling cavity, 57 for the power recycling cavity and 1550 for the arm cavities, and the wavelength of the laser is 1064 nm, the effective width of the linear range ΔL_{lin} is calculated as 14 nm, 9.93 nm and 0.34 nm for the signal recycling cavity, for the power recycling cavity and for the arm cavities.

In order to lock the interferometer, it is necessary to reduce the velocity of the mirrors sufficiently. Since the feedback control is available only when the mirrors are in the width ΔL_{lin}, the permitted incident mirror velocity is limited by the control bandwidth. In addition, the maximum actuation force limits the permitted mirror velocity.

Control bandwidth limit

Based on the consideration of control bandwidth, the requirement on the incident mirror velocity is obtained as

$$v_{\mathrm{mirror}} \ \lesssim \ \omega_b \Delta L_{\mathrm{lin}} \ = \ \omega_b \ \frac{\lambda}{2\mathcal{F}}, \tag{6.1}$$

where ω_b represents control bandwidth. The maximum incident velocities due to the control bandwidth limit for the power recycling, signal recycling, arm cavities are summarized Table 6.1.

Actuation force limit

Following the consideration in [81], the force F required in order to stop the mirror can be obtained by,

$$F = \frac{m v_{\mathrm{mirror}}}{\Delta t}, \tag{6.2}$$

where m, v and Δt are the mass, the velocity of the mirror and the time it takes to pass the linewidth ΔL_{lin} of the cavity, respectively. Since the time the mirror takes to pass the width can be given by $\Delta t = \Delta L_{\mathrm{lin}}/v_{\mathrm{mirror}}$, the requirement on mirror velocity limited by the actuation force can be given by

$$v_{\mathrm{mirror}} \lesssim \sqrt{\frac{F_{\mathrm{max}} \Delta L_{\mathrm{lin}}}{m}}. \tag{6.3}$$

The permitted maximum velocities due to the actuation force limit for the power recycling, signal recycling, arm cavities are also summarized Table 6.1. Since we use the green-lock technique for the arm cavity locking as described in section 1.3.5, the velocity for the arm cavity mirrors is not included in that table.

Table 6.1: Requirements on the velocity of the cavity length variation. The control band width is set to 50 Hz, and the values of actuation limit is obtained from [81]. For the lock-acquisition of the arm cavities, the control band width and the finesse are set to 10 kHz and 50 respectively assuming to use the green light source and the laser frequency actuator of the arm-length stabilization system.

Cavity	BW limit [μm/s]	Actuation limit [μm/s]
Arm cavity	330	−
Power recycling cavity	2.9	7.3
Signal recycling cavity	4.4	0.44

RMS velocity requirement

Using the requirement on the mirror velocity v_{mirror}, we set the requirement on the RMS velocity of the mirrors v_{rms}.

Since the mirrors of the optical cavities oscillate randomly, the mirror velocity changes randomly as well. If the mirror velocity has a Gaussian distribution, the probability distribution of the mirror's velocity $f(v)$, when passing through the resonance point, is given by [85]

$$f(v) = \frac{v}{v_{\mathrm{rms}}^2} \exp\left(-\frac{v^2}{2v_{\mathrm{rms}}^2}\right), \tag{6.4}$$

186

where v_{rms} means the RMS velocity of the cavity length variation. Assuming such velocity probability distribution, the RMS velocity that allows acquiring lock with probability p is:

$$v_{\mathrm{rms}} = \left(\sqrt{(-2\log(1-p))}\right)^{-1} v_{\mathrm{mirror}}. \qquad (6.5)$$

In order to have a lock acquisition probability higher than 50%, the RMS velocity v_{rms} has to be lower than 0.72 v_{mirror}. In accordance with these conditions, the requirements on the RMS mirror velocity of the KAGRA suspensions is set to 2.0 μm/s for the type-A SAS, 0.31 μm/s for the type-B SAS and 2.0 μm/s for the type-Bp system. The velocity requirement for the type-A suspensions comes from a fact that PR and SR cavities include the input test masses (ITMs). Even though the requirement on the velocity for the arm cavity mirrors is set to 240 μm/s, the two ITMs are also part of the power and signal recycling cavities. The motion of these ITMs affect the length variation of these cavities, and thus more strict requirement are imposed on the type-A SAS mirror RMS velocity, due to the bandwidth limit of PR and SR cavities.

6.2.3 Requirement on RMS angular fluctuation

For the stable operation of the interferometer, and also for preventing degradation of the sensitivity due to the mode mismatch, we have to suppress the mirror angular fluctuation. This requirement applies to the pitch and yaw DoF, since these angular motions can have a huge impact on the interferometer.

For the lock-acquisition phase, the angular motion has to be reduced below 880 nrad RMS, in order to avoid that the intra-cavity power degrades by more than 5% [86]. During the observation phase, the angular motion has to be smaller than 200 nrad RMS in order to avoid that the beam spot motion on the mirrors becomes larger than 1 mm RMS [87]. In addition, in order to keep the interferometer locked for 1 day, angular beam position drift is required to be smaller than 400 nrad/h [87].

6.2.4 Requirement on longitudinal displacement

In the lock acquisition phase and the observation phase, the mirror longitudinal displacement has to be suppressed so that the interferometer lock is kept. In order to keep the lock, the amplitude of the actuation force should be smaller than the maximum force of the actuators.

It was reported in [81] that the actuation efficiency at MN-, IM- and TM-stage were 3.9×10^{-7} m/V, 1.7×10^{-8} m/V and 1.8×10^{-9} m/V respectively at DC. Since the maximum voltage that the digital-to-analogue converter (DAC) can provide is 10 V (as described in section 5.4.2), the maximum permitted longitudinal displacements for each stage are 3.9 μm, 1.7×10^{-1} μm and 1.8×10^{-2} μm at MN-, IM- and TM-stage respectively.

By assuming that the longitudinal displacement compensation is done at the MN-stage, and considering a margin of a factor of 10, the requirement on the longitudinal displacement of the mirror can be set to 0.39 μm.

6.2.5 Requirement on Type-A suspension control

The requirements for the active controls of the Type-A SAS are summarized in Table 6.2. The requirement for the mirror transverse and vertical displacement is set to 1 mm in order to avoid a mis-centering of the beam spot on the mirror. Based on section 6.2.4 and 1 % vertical-to-horizontal coupling, the permitted requirement of the mirror vertical displacement in the lock acquisition and the observation phase is set to 39 μm RMS. The RMS value is defined as integration of the spectrum density down to 0.02 Hz. This value is selected assuming that the corresponding time scale ($\sim$ 50 sec.) is sufficiently long to cover the lock-acquisition process.

In addition, the control system noise coupling to the mirror longitudinal displacement in the observation band (above 10 Hz) has to be lower than the vibration level required to reach the KAGRA design sensitivity (see section 1.4.3).

Table 6.2: Requirements on the Type-A suspension control. The column labeled as ref. points to the section explaining the reason of the requirements. The RMS value is defined as the integral of the motion spectrum density down to 0.02 Hz.

Items	Requirements	ref.
The calm-down phase		
$1/e$ decay time	< 1 min.	§ 6.2.1
RMS displacement (transverse, vertical)	< 1 mm	§ 6.2.5
The lock acquisition phase		
RMS velocity (longitudinal)	< 2.0 μm/sec.	§ 6.2.2
RMS angle (pitch, yaw)	< 880 nrad	§ 6.2.3
RMS displacement (longitudinal)	< 0.39 μm	§ 6.2.4
RMS displacement (transverse)	< 1 mm	§ 6.2.5
RMS displacement (vertical)	< 39 μm	§ 6.2.5
The observation phase		
Control noise at 10 Hz (longitudinal)	< 8.0×10^{-20} m/$\sqrt{\text{Hz}}$	§ 1.4.3
RMS displacement (longitudinal)	< 0.39 μm	§ 6.2.4
RMS displacement (transverse)	< 1 mm	§ 6.2.5
RMS displacement (vertical)	< 39 μm	§ 6.2.5
RMS angle (pitch, yaw)	< 200 nrad	§ 6.2.3
DC angle drift (pitch, yaw)	< 400 nrad/h	§ 6.2.3

6.3 Mechanical system modeling

For modeling the dynamics of the suspension system, we use a three-dimensional rigid body model. In KAGRA, the mechanical frequency responses of a suspension is calculated with a simulation tool [88]. For the KAGRA suspensions, the rigid body model describes properly the mechanical frequency response up to about 50 Hz [44].

In the simulation tool, we calculate the frequency response by using the linearized equation of motion around the equilibrium point of the system:

$$\boldsymbol{M}\ddot{\boldsymbol{x}} \;+\; \boldsymbol{G}\dot{\boldsymbol{x}} \;+\; \boldsymbol{K}\,(\boldsymbol{x} - \boldsymbol{x_{eq}}) \;=\; \boldsymbol{0}, \tag{6.6}$$

where $\boldsymbol{M}$, $\boldsymbol{G}$, $\boldsymbol{K}$ represent the mass matrix, the damping matrix and the stiffness matrix respectively. These matrices are calculated with:

$$K_{ij} \;=\; \left.\frac{\partial^2 U(\boldsymbol{x})}{\partial x_i \partial x_j}\right|_{\boldsymbol{x}=\boldsymbol{x}_{eq}}, \tag{6.7}$$

$$G_{ij} \;=\; \left.\frac{\partial^2 R(\boldsymbol{x},\dot{\boldsymbol{x}})}{\partial \dot{x}_i \partial \dot{x}_j}\right|_{\boldsymbol{x}=\boldsymbol{x}_{eq}}, \tag{6.8}$$

$$M_{ij} \;=\; \left.\frac{\partial^2 T(\dot{\boldsymbol{x}})}{\partial \dot{x}_i \partial \dot{x}_j}\right|_{\boldsymbol{x}=\boldsymbol{x}_{eq}}, \tag{6.9}$$

where $U(\boldsymbol{x})$, $R(\boldsymbol{x},\dot{\boldsymbol{x}})$ and $T(\dot{\boldsymbol{x}})$ denote the potential energy of the suspension wires, dissipation function and kinetic energy of the system, and the derivatives are calculated at the equilibrium point $\boldsymbol{x}_{eq}$.

Here the potential $U(\boldsymbol{x})$ includes the gravitational potential energy as well as the bending and torsional energies of the wires. The dissipation function $R(\boldsymbol{x},\dot{\boldsymbol{x}})$ takes into account the viscous damping due to the eddy current damper and the internal friction of the materials.

We calculate mechanical transfer functions using eq (6.6). We then use them to confirm that the suspensions are assembled as designed by comparing to the measurement. We also simulate the active control performance assuming that the plant (the suspension) is properly modeled by these equations.

The simulated eigen mode shapes of the KAGRA Type-A SAS are shown in section B.1. As in the following description (section 6.4), we use multiple feedback filters for multiple suspension stages. By referring the eigen mode shapes, we also decide the controlled stages and DoFs, to damp the resonances effectively.

The simulation for the control system of KAGRA SAS is addressed by linear control theory. For this purpose, the equation of motion of the suspension system is transformed into state-space representation. Using this calculation framework, we simulate the suspension system and the control system, and then tune and select the parameters of the control filters. More detailed information about the modeling of the KAGRA suspension can be found in [41].

6.4 Overview of control system

The local control loops for the suspensions are developed using feedback and feed-forward control using the implemented sensors and actuators.

We develop the active control system for single-input-single-output (SISO) system. The actual suspension has multiple sensors and actuators, and thus it is a multi-input-multi-output (MIMO) system. In KAGRA, however, we do not build the control system for the MIMO system as it is. Instead, we make the multiple independent single-input-single-output (SISO) systems by diagonalizing the sensor and actuator basis along the Cartesian coordinates. We then build the active control system for each SISO system. Using SISO system we can construct a simple system as described in section 4.2.

As example, the signal flow of the feedback control system in the case of the IP-stage, is shown in Figure 6.2. We first sense the suspension motion using the implemented sensors, and then convert the sensor-basis signals to the Cartesian signals (in Figure 4.3) by using a matrix. The feedback filters are applied to the Cartesian signals. Then the correction signals are distributed to each actuator by applying the proper matrix, i.e. the matrix that allows transforming the signals from Cartesian basis to the actuator coil basis. Finally we apply the forces to the suspension with the actuators by sending the filtered signals.

In order to realize the active control system, we shape the feedback filters for each required Cartesian DoF and each suspension stage. In the development we estimate the control performance for each feedback loop, such as the noise couplings, following the model presented in section 4.2. We also take care of the stability of the feedback loop using the open loop gain in Bode plot (also described in section 4.2).

The basic idea of the control system is summarized in Figure 6.3. At the IP-stage, we control the static mirror position by controlling the DC position of the IP-sage, and damping the translational resonance. The IP stage is also used by the control system to suppress the mirror residual motion in the lock-acquisition and observation phases.

We implement either DC compensation filter or DC coupled damping filter for the GAS filter stage control, in order to keep the keystone height and to damp the suspension vertical resonances.

For the BF control, we only control the torsional motion (Yaw DoF), in order to compensate the slow torsional drift and to damp the whole chain resonances that cannot be sensed at the IP-stage.

At the payload level, we implement control loops to compensate for the TM and MN angular drift in Pitch and Yaw. In addition, the control damps the payload internal resonances that cannot be sensed by the upper stages.

Figure 6.2: An example of the signal flow of the feedback control system: the case of the IP-stage. H1, H2 and H1 represent each sensor and actuator. L, T and Y denote longitudinal, transverse and yaw respectively.
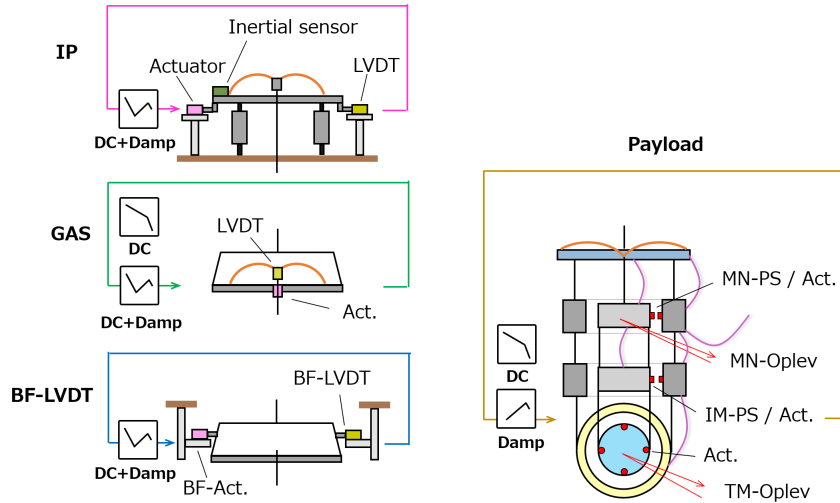
Figure 6.3: Overview of the control system for the Type-A suspension. The curves in the square windows show the schematic view of the filter shapes.

6.5 Suspension control in the calm-down phase

As described in section 6.1, the primary target of the calm-down phase is to reduce large-amplitude motion of the mechanical resonances excited by external disturbances. In this phase, the active controls are required to damp resonances so that the $1/e$ decay time of the mechanical resonances disturbing the interferometer lock acquisition, is less than 1 minute.

According to the rigid-body simulation described in section 6.3, the Type-A suspension has 75 resonant modes; these are listed in section B.1. In this model, the assumption is made that the heat links do not affect the suspension dynamics.

In this work, we concentrate on the resonances at frequencies lower than 30 Hz, since the resonant modes that impact the lock acquisition are the lower frequency modes rather than the higher frequency ones. The value of 30 Hz is set since the suspension sensors (actuators) can sense (actuate) the system up to around that frequency. The resonances whose resonant frequency is higher than 30 Hz contributes less to the RMS displacement (and velocity) compared to the resonances below 30 Hz.

We might have to work on the damping of the resonances above 30 Hz in case they degrade the detector sensitivity. However, for this purpose we need to have another system to damp them since the local sensors and actuators are not enough to damp such modes.

In addition, some suspension resonant modes are excluded from this discussion since they do not affect the interferometer lock-acquisition.

Consequently the total number of resonances to be damped becomes 54.

6.5.1 Servo system

Using the ideas described in section 4.2 we design and simulate the feedback control filters for the suspension damping. We use 18 feedback filters in the control. Table 6.3 summarizes the information of the designed filters in this simulation. For some of the stages, we include DC control in order to steer the mirror position and orientation to the operation point. Figure 6.4 shows one of the designed control filters. This is the case of IP-stage in L DoF using the LVDTs as the displacement sensors.

In the calm-down phase we do not take care of the control noise coupling at higher frequencies. Instead we mainly focus on:

1. closing the feedback control stably,

2. reducing the decay time of the mechanical resonances.

In the case shown in Figure 6.4, we shape the filter so that the open loop gain becomes large enough at the target resonant frequencies and has enough phase margin at the unity gain frequency. In addition, a roll-off is included above 10 Hz in order to avoid making too large the control noise coupling. For the DC-control, the open loop gain is increased below 0.01 Hz.
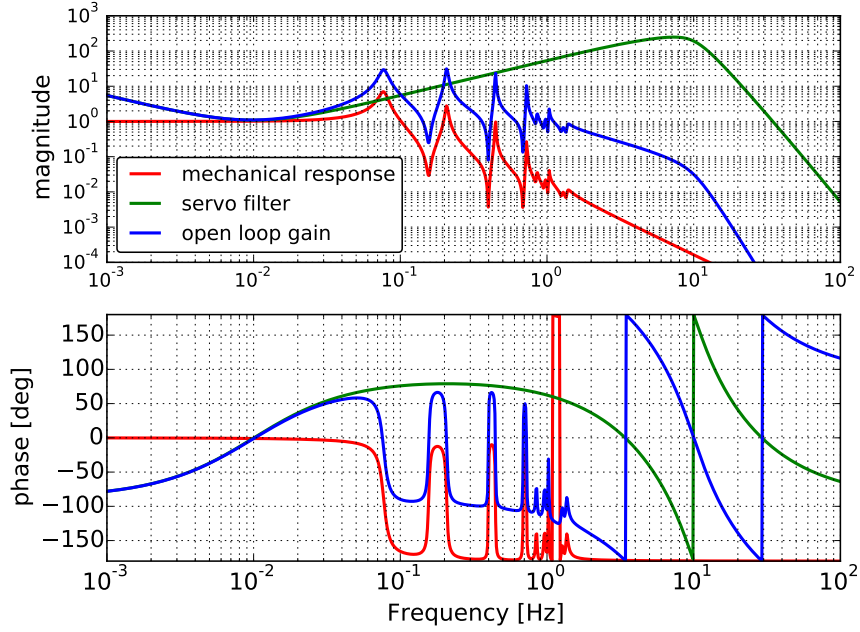
Figure 6.4: One of the designed control filters in the simulation. This is the case of IP-stage in L DoF. The red, green and blue colored curves represent the mechanical response (from the actuator to the IP sensor in displacement), the servo filter and the open loop gain respectively.

To estimate the damping performance, the $1/e$ decay time constant with and without the controls has been calculated. The results are summarised in Figure 6.5. There are four remaining resonances below 30 Hz that exceed the requirement of 1 minute. However, since these are the tilt modes of the F1 and F2 GAS stages (mode #25, #26, #29 and #30 in section B.1) and the coupling to the mirror is small, we do not consider them here[1]. Thus this control system will satisfy the requirement for the calm-down phase.

---

[1]According to the model prediction, the mode #29 and #30 seems to slightly connect to the mirror tilt motion. However exciting the F1/F2 motions by actuating payload is not feasible, and thus we do not consider them.

Table 6.3: The servo loops for the calm down phase and the used sensors. In the below oplev and PS represent the optical lever and the photo sensor. We have the optical levers at MN- and TM-stages and they are labeled as MN-oplev and TM-oplev respectively.

Loop	Loop DoF	Sensor	Actuation DoF	Purpose
IP	L, T, Y	LVDT	IP	DC and damp
BF	Y	BF-LVDT	BF	DC and damp
F0	GAS	LVDT	F0	DC and damp
F1	GAS	LVDT	F1	DC
F3	GAS	LVDT	F3	DC and damp
BF	GAS	LVDT	BF	DC
MN	L, T, V, R, P, Y	PS	MN	damp
from TM to MN	P	TM-oplev	MN-P	DC and damp
from TM to IM	P	TM-oplev	IM-P	damp
from TM to MN	Y	TM-oplev	MN-Y	DC
from TM to IM	Y	TM-oplev	MN-Y	damp
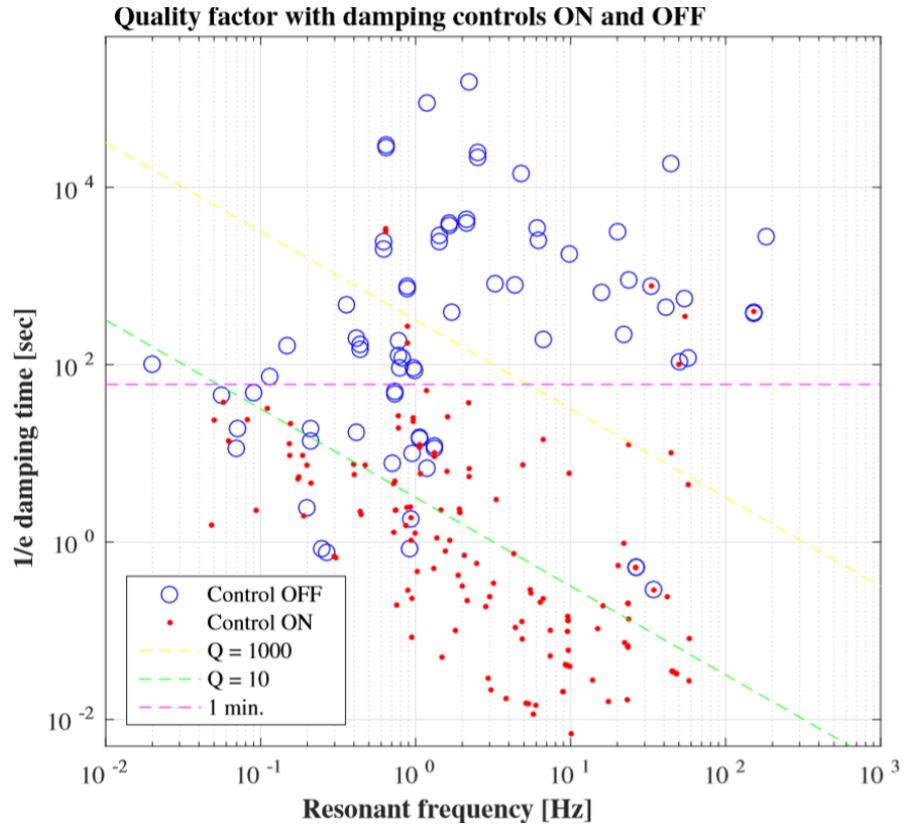
Figure 6.5: $1/e$ decay time constant with and without the designed controls. The blue-edged points and the red dots show the decay time constant without and with the control system. It is confirmed that the designed feedback filters will properly damp the resonances below 30 Hz.

6.6 Suspension control in the lock-acquisition phase

In order to stably acquire (and keep) the interferometer lock, the RMS velocity, the RMS displacement and the RMS angular displacement of the mirrors are required to be smaller than the requirement given in Table 6.2. Typically the biggest contribution to the mirror residual motion comes from the ground motion in a frequency band around 0.2 Hz, around the so-called micro-seismic peak.

For suppressing sufficiently the mirror residual motion at low frequency, we consider a feedback system with feed-forwarding using the sensor correction scheme introduced in section 4.2 (especially in Figure 4.26).

In the calm-down phase, we use LVDTs for IP-stage control. However, the LVDTs measures the relative displacement between the ground and the IP-stage. This implies that the control loops with the LVDTs inject the seismic noise to the suspension and then shakes the suspension at low frequency, especially at the microseicmic peak region.

In order to avoid the re-injection of the seismic noise to the suspension, we consider to remove the seismic motion signal from the LVDTs. For this purpose, we use a seismometer Trillirum120QA (see section 5.3.7) attached to the ground. By combining the LVDT and seismometer signals, we subtract the ground motion signal from the LVDTs. We call this technique sensor correction. The expected suppression is discussed in this subsection.

Here, we consider that the sensor correction system is implemented to the IP-stage. For the other control loop, especially for the payload and the GAS stages, we use same filters as the ones used in the calm-down phase. In the following subsection, the sensor correction system at the IP-stage is abbreviated as IP_{sc}.

6.6.1 Suppression with sensor correction technique

Filter for sensor correction at IP-stage

The block diagram of the IP-stage feedback control system with the sensor correction system is shown in Figure 6.6. This system is the one in Figure 4.26 but without the path from the seismometer to the actuator (which corresponds to the case where $F_{\mathrm{ff}} = 0$). In this system, the sensor correction part is shown by blue-colored part, and is additionally implemented to the feedback control of the IP-stage.

In this configuration, the seismic noise coupling will be most effectively subtracted when the sensor correction filter F_{sc} satisfies $F_{\mathrm{sc}} = -S_{\mathrm{L}}/S_{\mathrm{s}}$ where S_{L} and S_{s} are the sensor response of the LVDT and the seismometer, as discussed in section 4.2 (especially in the topic of feedback control with feed-forwarding).

Assuming the inter-calibration between the IP-LVDT and the seismometer sensors are perfectly done, i.e, $|S_{\mathrm{L}}/S_{\mathrm{s}}| = 1$, the sensor correction filter F_{sc} should have gain of 1 in the frequency band where we want to subtract the seismic motion.

In the real life, the seismometer signal is dominated by the local tilt motion at

frequencies below 0.1 Hz. Thus in F_{sc} we need to include a high-pass filter which adds a phase shift as small as possible in the frequency band where we want to efficiently subtract the seismic noise from the LVDT. Using an elliptic high-pass filter with 10 mHz cut-off, the F_{sc} can be shaped as shown in Figure 6.7.
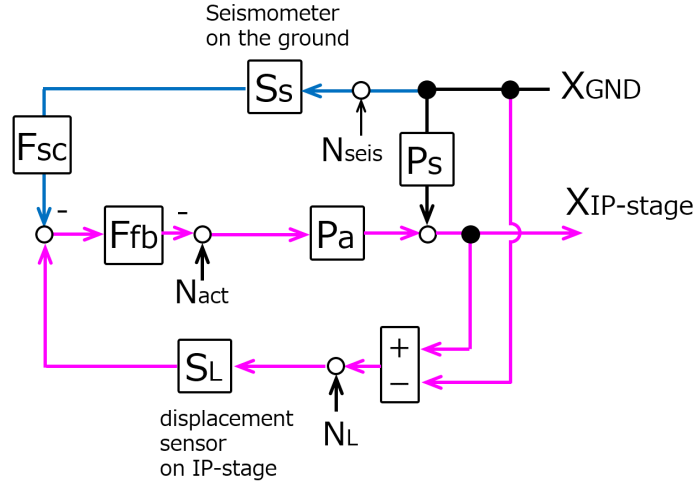
Figure 6.6: Block diagram of the feedback control with the sensor correction system at the IP-stage. All parameters are defined as described in section 4.2. This is the case where F_{ff} is set to zero. By implementing the appropriate filter F_{sc}, we realize the sensor correction system that subtracts the seismic noise from the displacement sensors (LVDTs).
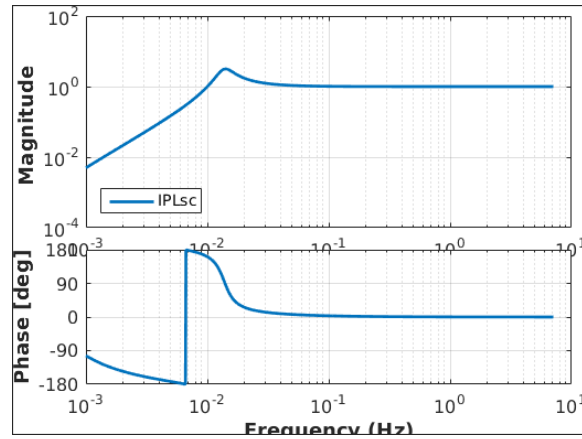
Figure 6.7: Designed sensor-correction filter for the IP-stage. The horizontal axis shows frequency in Hz.

Expected mirror suppression

Using the filter shown in Figure 6.7 and the filter sets used in the calm-down phase (see section 6.5), we calculate the expected velocity and displacement in L DoF. The results are shown in Figure 6.8. In this calculation, high seismic noise level (90 percentile seismic motion level) is assumed. The blue colored curves show the case where no controls are applied. The orange ones represent the case where the IP-stage is controlled with IP-LVDTs (without IP_{sc}). The red ones show the case where the IP-stage is controlled with IP-LVDTs with IP_{sc}.

Table 6.4 summarizes the RMS velocity and displacement integrated down to 20 mHz.

Figure 6.8 and Table 6.4 indicate that the RMS velocity satisfies the requirement for the lock acquisition phase, even without the sensor correction system at IP-stage.

On the other hand, the RMS displacement requirement (down to 20 mHz) will be satisfied by using the sensor correction system. The RMS displacement will satisfy the requirement even if the integration is done down to 13.5 mHz (time scale is about 75 sec). Figure 6.8 (*bottom*) shows that the sensor correction system at IP-stage will also satisfy the displacement requirement at 10 Hz. This implies that the sensor correction can be used even in the observation phase.

The RMS displacement requirement will not be satisfied if the integration is done down to below 13.5 mHz due to the seismometer self-noise contribution. Since this displacement amplitude enhancement comes from the tilt motion coupling from the seismometer Trillium120QA, for the further stabilization at such frequency we have to implement another system.

For example, this issue can be solved by implementing a sensor correction system for the seismometer using a sensor which senses the local tilt motion. As another option, we can compensate the displacement drift by feeding back the interferometer signal to the upper stage such as IP-stage, once the interferometer lock is acquired.

Since the interferometer lock can be acquired within the time scale of about 1 minute, the displacement drift compensation is treated by the control system in the observation phase. The primary target of the sensor correction system is to suppress the motion at the frequency region where the micro seismic peak is dominant.

Figure 6.9 shows the expected mirror velocity and displacement in L DoF with IP_{sc} when the inter-calibration between IP-LVDTs and the seismometer Trillium120QA is not perfect. From these plots and considering the RMS values at 20 mHz, the permitted maximum mis-match between those sensors is obtained as 40%. The target inter-calibration mismatch is then set to be smaller than 10%.

Consequently, the calculated results indicates that the sensor correction system at IP-stage will suppress the RMS velocity and displacement of the mirror. Then it will satisfy the RMS requirement for both the velocity and the displacement in the lock-acquisition phase. In addition, we can keep using the sensor correction system at IP-stage even in the observation phase.

Table 6.4: The estimated RMS displacements and velocities of the mirror with the integration down to 20 mHz. IP_{sc} in the labels denote the sensor-correction system in this work.

Configuration	velocity [μm/s]	Displacement [μm]
Without any controls	0.48	0.56
with IP control, without IPsc	1.1	0.99
with IP control, with IPsc	0.15	0.14
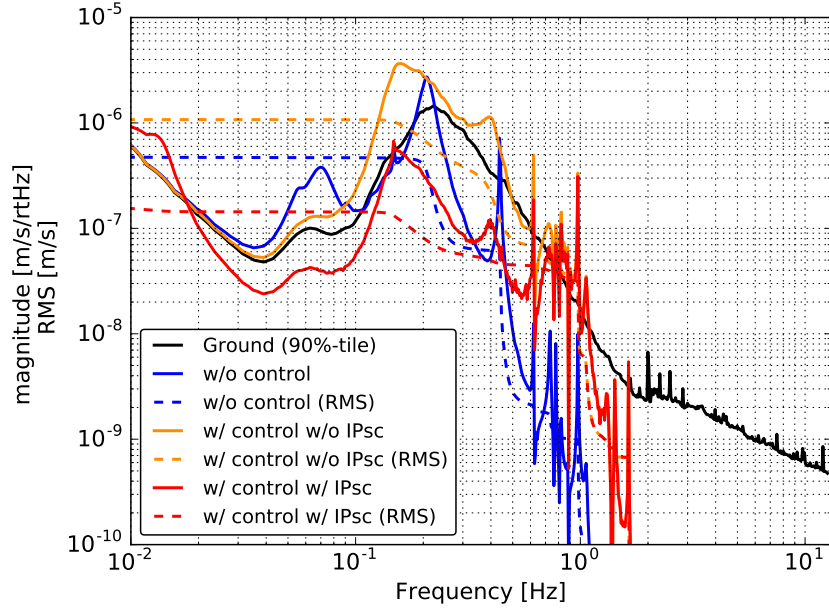
(a) Expected mirror velocity
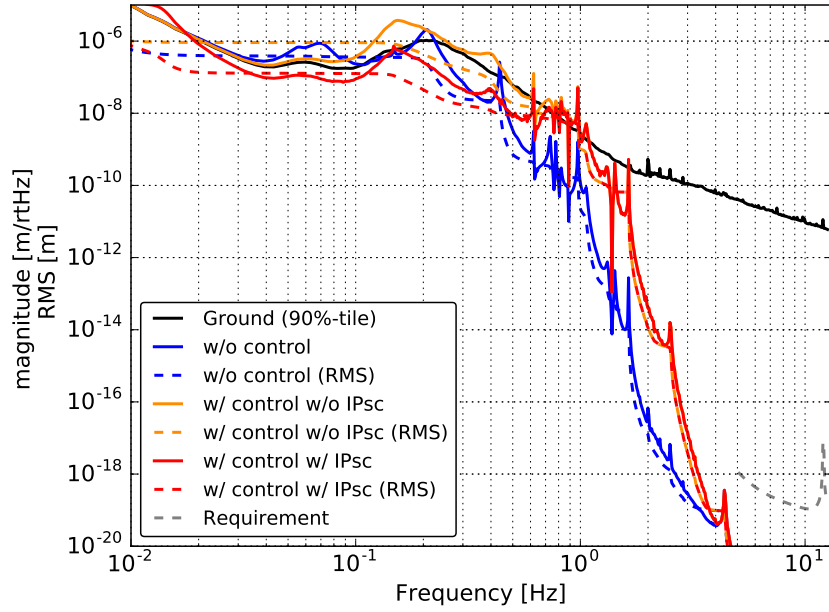
(b) Expected mirror displacement

Figure 6.8: Expected mirror residual motion in L DoF in velocity (*top*) and in displacement (*bottom*) with and without the IP-stage control. The colors show the difference of the control configuration. The dashed curves draw the RMS values integrated from high frequency down to the frequency f. In this calculation, high seismic noise level (90 percentile seismic motion level) is assumed. The grey colored dashed curve at around 10 Hz shows the requirement of the mirror displacement.
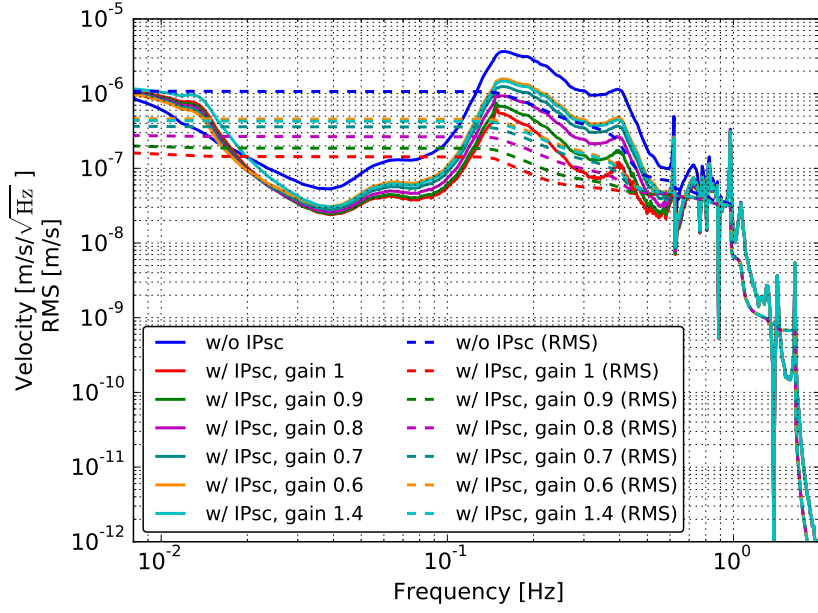
(a) Expected mirror velocity
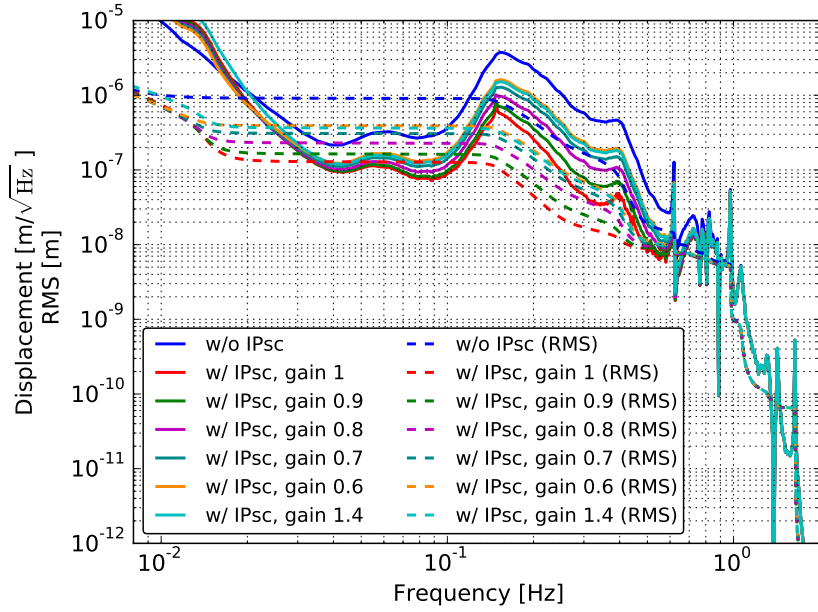
(b) Expected mirror displacement

Figure 6.9: Expected mirror residual motion in L DoF in velocity (*top*) and in displacement (*bottom*) with IP-stage control with IP_{sc}. The colors show the mismatch of the inter-calibration between the IP-LVDTs and the seismometer Trillium120QA. The dashed curves draw the RMS values integrated from high frequency down to the frequency f. In this calculation, high seismic noise level (90 percentile seismic motion level) is assumed. The gain denotes the mismatch level between the LVDTs and the seismometer.

6.7 Suspension control in the observation phase

In this phase, we do not need strong damping since the mirror motion is already calmed down enough. Rather than damping, we need to keep the mirror position/orientation without injecting control noises to the mirror motion. For this purpose, the mirror displacement above 10 Hz has to be sufficiently suppressed in order to meet the requirement. Especially for the Type-A SAS, the permitted maximum mirror displacement at 10 Hz is 8.0×10^{-20} m$/\sqrt{\text{Hz}}$ (as described in section 1.4.3).

Figure 6.10 shows an estimated mirror displacement in L DoF with the controls used in the lock acquisition phase (that is developed in sections 6.5 and 6.6). In this figure, the dashed black curve show the requirement, and the other colored curves represent the couplings to the mirror displacement from all the sensors used in the controls. According to this plot, the contribution from the following loops exceed the required displacement noise level above 10 Hz:

1. MN to MN loop with the photo-sensors (PSs),

2. TM to MN loop with TM optical lever

3. F3GAS to F3GAS and F0GAS to F0 loops with the LVDTs.

Based on this calculation, it is found that the control loops by PSs have to be opened in the observation phase. This is since their contribution above 10 Hz is much larger than the requirement (by factor of 10^8 at 10 Hz). It is also required to use only DC-filters for the GAS filter loops, without damping filters. In addition, the filter shape of the optical lever loop also has to be tuned, or to be opened.

The control system for the observation phase depends on the main interferometer control. Actually we use the interferometer signal for the control in this phase.

The interferometer control scheme was under development and in 2019 when the thesis work was ongoing. Thus the construction of the control system for the observation phase is set as further step after this thesis. However, at least, it is expected that the above listed loops will be issues in the control in the observation phase. The filter shapes and the controlled DoFs are to be further considered.
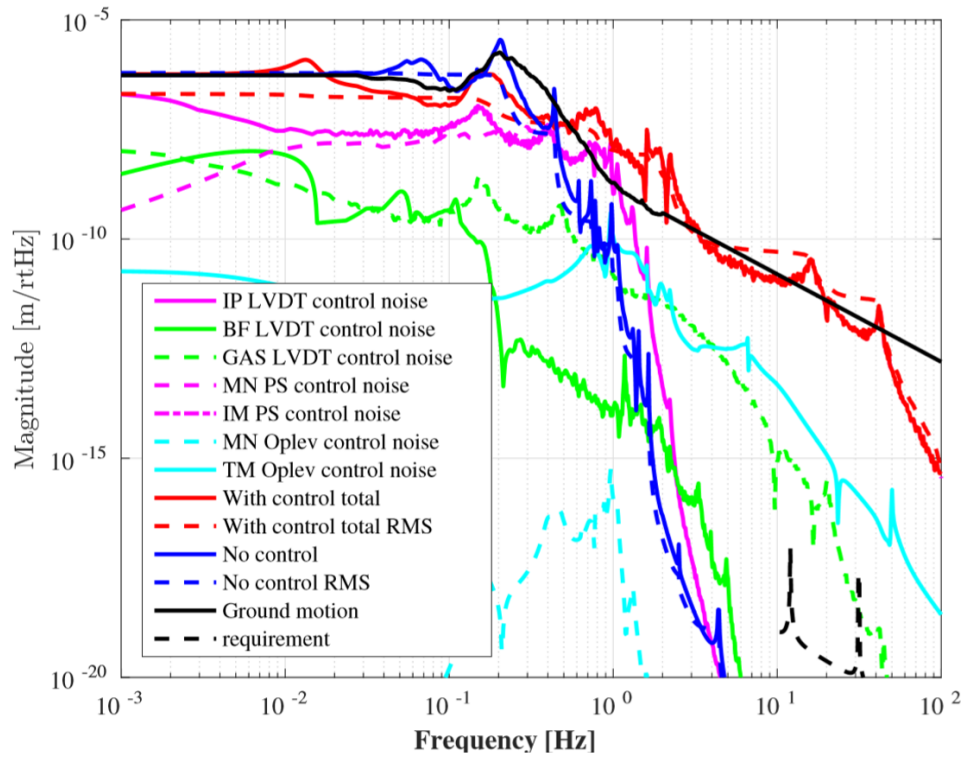
Figure 6.10: Expected mirror residual motion in L DoF in displacement including the contribution from all the control loops in the lock-acquisition phase. The blue and red colored dashed curves show the RMS values integrated down to 1 mHz, and the other curves show the spectra of mirror displacement induced by each control loop.

6.8 Summary

First this chapter describes:

1. the interferometer control phases (section 6.1),

2. the requirements for the Type-A SAS control in each interferometer control phases (Table 6.2).

Second this chapter reports the development of the servo filters which will satisfy the requirements (in simulation), especially for the calm-down phase (section 6.5) and the lock-acquisition phase (section 6.6). Some of these filters cannot be used in the observation phase (section 6.7). However, it is important to construct a control system which allows to lock the interferometer first. This thesis work focuses on constructing the control system for the calm-down phase and the lock-acquisition phase.

The next chapter summarizes the implementation of the simulated control system and the performances achieved.

<div align="right">

Chapter 7

</div>

<div align="right">

Implementation of Type-A SAS control system

</div>

This chapter describes the performance of the implemented active control system (developed in chapter 6) and its evaluation. The target is to realize the local control system for the Type-A SAS that allows to acquire the interferometer lock. More concrete goal is to confirm that the suspensions have the designed mechanical response, and also to verify if the control system meets the requirements for the calm-down phase and lock-acquisition phase summarised in section 6.2, especially in Table 6.2. This implementation and evaluation is conducted with ETMX suspension which is one of the Type-A SAS.

The key components of this chapter are summarized in the following topics:

1. check of the suspension's mechanical frequency response to confirm if the active control system can be constructed,

2. implementation of the damping control system and its performance evaluation,

3. implementation of the sensor correction system and its performance evaluation,

4. verification with interferometer.

Section 7.1 gives the information about ETMX suspension configuration during the measurement. Section 7.2 summarizes the measurement of the mechanical frequency responses of the Type-A suspension. This is done in order to confirm if the suspension has the characteristics of pendulum, and if it is enough for building the active control system. Section 7.3 describes the performance of the implemented control filters for the calm-down phase control. This section confirms that all the mechanical resonances disturbing the interferometer lock are damped within the required time in the lock recovery mode. Section 7.4 summarizes the performance of the control system for the reduction of the mirror residual motion focusing on the frequency region around the micro-seismic peak. This is done for

a robust interferometer operation.

Since the stable FPMI lock is achieved by implementing the control filters described in the above subsections, the measurement with the interferometer becomes possible.

We then measure the overall frequency response of the Type-A suspension with FPMI around a few Hz, which cannot be measured with the local sensors. Section 7.5 reports the result of the measurement with FPMI.

7.1 Suspension configuration

7.1.1 Mechanical and environmental configuration

During the measurement, it was known that one of GAS filter, which is the third GAS filter from the top and is called F2-filter, was mechanically stuck for a technical reason[1]. It was also known that this could not be solved without disassembling the upper structure, and there was not enough time to solve this issue. We then decided to keep using the ETMX suspension with the F2 GAS filter stuck, since the requirement for the displacement noise at 10 Hz should be satisfied even in the configuration (as shown in Figure B.7).

Concerning the other setting, the temperature of the payload during the test was about 250 K.

---

[1]Even though all the coils of the sensors and actuators were electrically connected and the expected resistances were measured, no free-swinging was observed when a actuation was sent. In addition to this, it seemed that one peak disappeared from the force transfer function in vertical DoF. We then started to believe that the keystone of the GAS filter somehow hit the lock screws which had been installed for a safety.

7.1.2 Sensor and actuator arrangement

The implemented sensor positions for the ETMX suspension are shown in Figure 7.1 and Figure 7.2.

IP and BF stage

In the ETMX suspension, the positions of each inertial sensor, LVDT and actuator unit at the IP-stage are arranged as shown in *left* of Figure 7.1. As reported in section 5.3.2, the ETMX suspension uses three geophones as the inertial sensors. The sensor actuator units at the BF-stage are placed as shown on *right* of Figure 7.1.
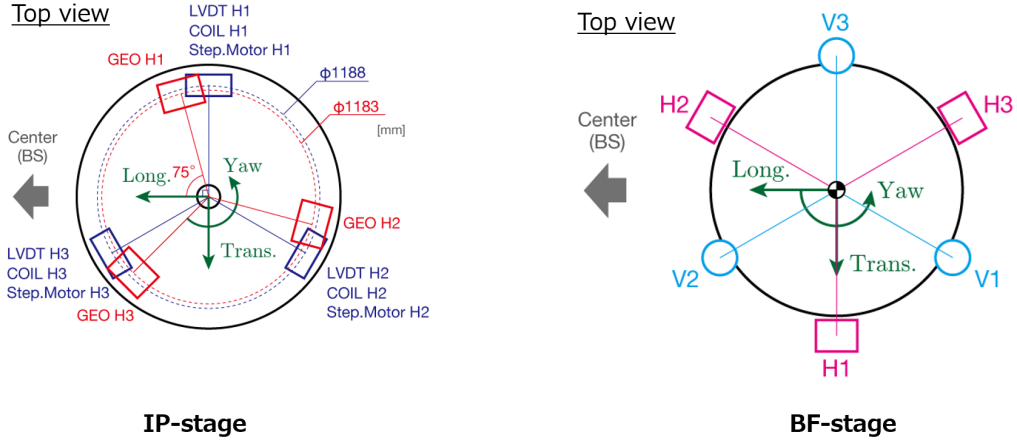
Figure 7.1: Geometrical position of the installed sensors and actuators at IP-stage(*left*) and BF-stage (*right*) for ETMX suspension case [89]. GEO and COIL denote the geophone and actuator respectively. Three LVDTs are installed at IP-stage and measure the horizontal 3 DoFs (longitudinal, pitch and yaw). Six BF-LVDTs senses the displacement in the six DoF.

Optical levers

An angular optical lever and length-sensing optical lever are installed at the TM-stage, and they sense the TM motion in three DoFs: i.e, longitudinal, pitch and yaw. On the other hand, only the angular optical lever is implemented at the MN-stage. In the MN-stage optical lever, the incident light beam is sent to the mirror attached on the MN-body and it is reflected to the same place where it is injected. In addition, since the mirror is mounted onto the MN-body with an angle, this MN-stage optical lever is sensitive to a superposition of the MN-body motion in pitch and roll. As a consequence the motions along these two DoF cannot be distinguished.
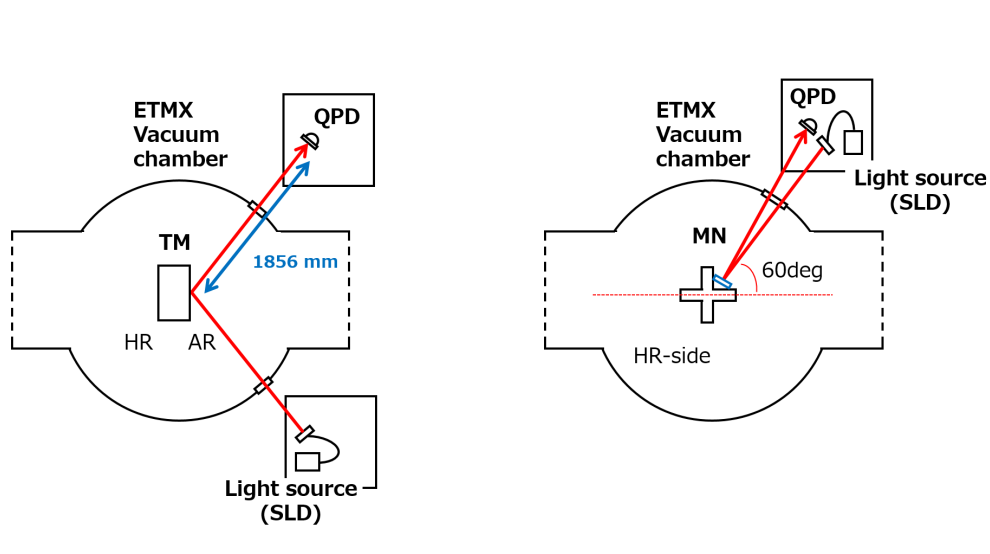
Figure 7.2: Geometrical configuration of the installed optical lever systems at the TM-stage (*left*) and MN-stage (*right*). HR and AR denote high-reflectivity coating and anti-reflectivity coating respectively.

7.2 Mechanical response measurement

In order to confirm if the assembled suspension works as designed, its mechanical response is measured and compared with the simulation.

7.2.1 ETMX suspension model

In this check, we use a rigid-body simulation without considering the heat link system and its HLVIS. We thus assume that the heat link stiffness is sufficiently soft and does not impact the main suspension dynamic. In addition, one spring for F2 GAS is removed in the simulation in order to take into account that the F2 GAS stage is mechanically stuck.

7.2.2 Transfer function measurement

We measure the force transfer function of each component by injecting white noise at each component actuator. The result is then compared to the simulation.

IP stage

Before the measurement, the LVDT sensors at the IP-stage are diagonalized to the Cartesian basis by measuring their geometrical position. The coil-magnet actuators are diagonalized along with the LVDTs by checking the transfer function from each actuator to the L, T and Y DoF defined by LVDTs with an injection of a sinusoidal signal at 2 Hz. This frequency is selected since the highest mechanical resonance is about at 1 Hz. The inertial sensors, i.e, geophones for ETMX suspension, are then inter-calibrated to LVDTs by comparing the transfer function from LVDT signal in yaw DoF to each geophone signal. After the operation, the sensor matrix for the geophone is diagonalized using the transfer function from LVDT signal in L, T, Y to each geophone signal with an injection of a sinusoidal signal at 2 Hz.

After the procedure described above, we measure the mechanical transfer function from the diagonalized actuators to the diagonalized sensors, i.e, along the Cartesian coodinates. The results are shown in Figure 7.3. Even though it is found that the Q factors of some of the peaks in the model have to be tuned more precisely, basically the measured resonant frequencies and the transfer function slope at high frequency agree with the rigid-body simulation.
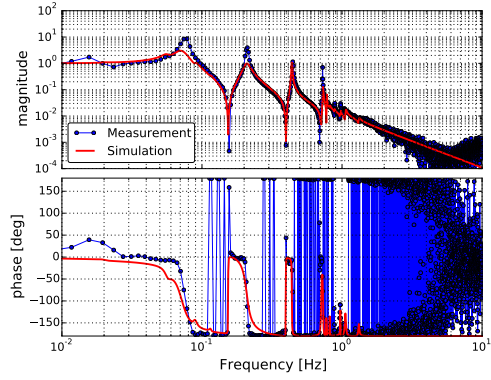
(a) Longitudinal
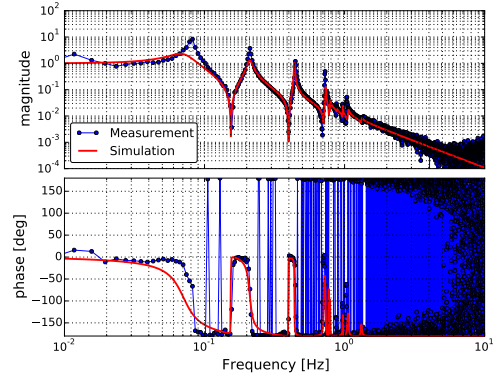
(b) Transverse
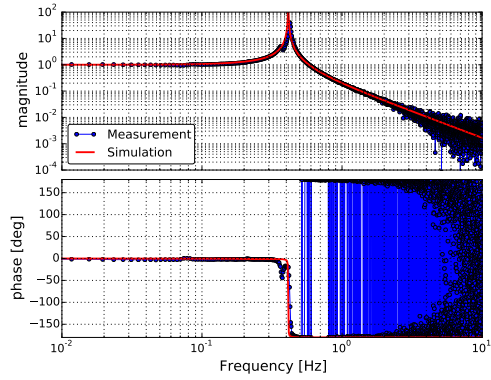
(c) Yaw

Figure 7.3: Diagonalized mechanical transfer functions of the IP-stage in longitudinal (a), transverse (b) and Yaw (c) DoF with the simulated curve. The dots and the curves show the measured result and the simulated one.

GAS stages

The measured transfer functions of each GAS stage are shown in Figure 7.4. The noise becomes dominant at frequency higher than about 7 Hz. As Figure 7.4 indicates clearly, the model fails to explain the actual system. This is so since the resonant frequencies of each GAS filter are not estimated well enough. For the three modes at lowest frequencies (about the 180 mHz, 410 mHz and 480 mHz modes), the model could be tuned to fit the data. However, the model fails to predict the the resonances at 1.29 Hz and 1.44 Hz. Also a peak at 4.4 Hz mode, which is the payload vertical resonance, is not found. In addition, a resonance at 9.7 Hz is found.

Consequently, the current model cannot explain the actual GAS filter responses and it has to be modified for more precise modeling. In case this issue limits the interferometer sensitivity, we might have to investigate further about the system. We then might have to verify if the discrepancies are due to the heat link system, and/or if the F2-GAS treatment is good enough.

Even though this model fails to explain the actual resonant frequencies, the measured slopes at high frequency agrees with the model. This implies that the vibration isolation performance above 10 Hz will satisfies the requirement.The details of the high frequency performance will be confirmed with high sensitive sensor such as the main interferometer.
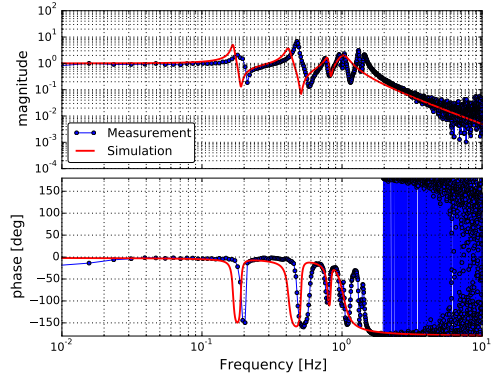
(a) F0 GAS
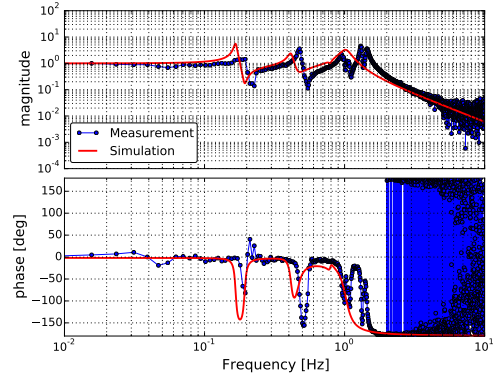
(b) F1 GAS
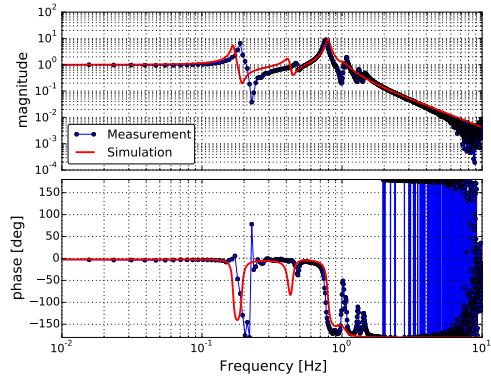
(c) F3 GAS
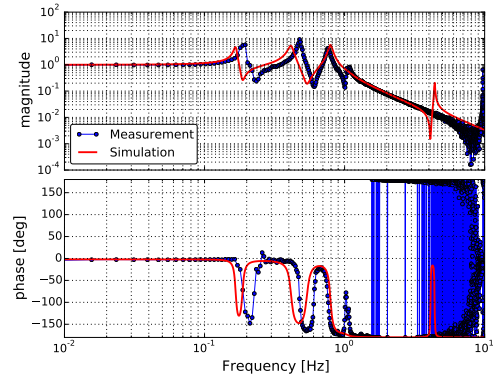
(d) BF GAS

Figure 7.4:   Mechanical transfer functions of F0 GAS (a), F1 GAS (b) F3 GAS (c) and BF GAS stage with the simulated curve. The dots and the curves show the measured result and the simulated one.

BF stage

In the BF-stage, both the sensors and actuators are diagonalized by measuring the geometrical LVDT-unit position. Figure 7.5 shows the measured transfer function in the 3 horizontal DoFs.

At high frequencies above about 1.5 Hz in L and T, 2 Hz in Yaw DoF, all the transfer functions increases as f^2. This is due to a spurious coupling in the BF-LVDT. The actuation signals seems to directly couple to the sensor coils due to a fact that the actuation coil and the sensor coils are co-axially aligned [44, 41].

For L and T DoF, the measurement agrees with the simulation, except for the Q factors and the resonant frequencies of the first and the second modes, similar to the IP-stage case. Concerning the Yaw DoF, the used model totally fails to predict the frequency response. In addition, for all the L, T, Yaw DoFs, this measurement do not agree with the previous measurement which was conducted when payload and the heat link system were not installed. This issue is discussed in section 7.2.3.
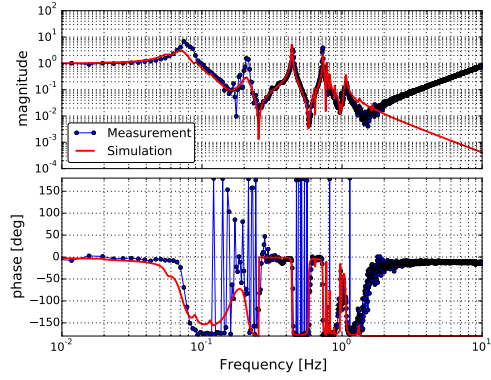
(a) Longitudinal
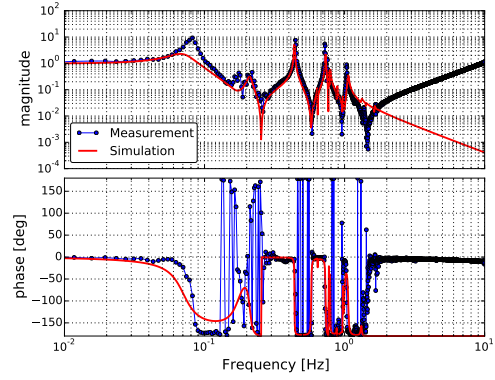
(b) Transverse
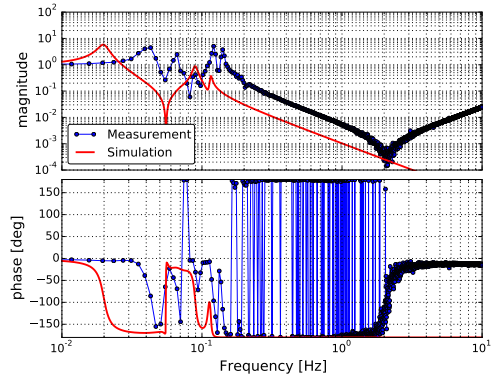
(c) Yaw

Figure 7.5: Diagonalized mechanical transfer functions of the BF-stage in longitudinal (a), transverse (b) and Yaw (c) DoF with the simulated curve. The dots and the curves show the measured result and the simulated one.

MN stage

For the payload part, the actuators are balanced by using the already calibrated optical lever so that the each coil pushes and pulls the mass by the same amount. The photo-sensor diagonalization is done using the geometrical information of the sensor and actuator position. Figure 7.6 and 7.7 show the measured response of the MN-stage sensed by the optical lever and by the photo-sensors respectively.

The measurements fail above about 20 Hz for the transfer functions measured with the optical lever, and above a few Hz for the ones using the photo-sensors. This is so since the induced MN-stage (TM-stage) displacement becomes comparable to the sensor noise level.

Figure 7.6 indicates that the model can explain the actual system, except for the two modes observed at 0.32 Hz in the Yaw DoF and at 7.5 Hz in the Pitch DoF. The 0.32 Hz in Yaw DoF can come from the discrepancy of the material parameters since this model uses the parameters at 20 K. Another possible reason would be the heat link system, however, we do not have good explanation for this in this work. The discrepancy of the 7.5 Hz in Pitch DoF, which is the TM-chain mode, can be connected to the details in the suspensions not considered in the simulation. The TM is suspended with four sapphire fibers bonded to the mirror by means of sapphire ears [71]. This can make uneven tension in the four fibers, and can explain the discrepancy. The fiber material parameter can be also one of this reason.

Figure 7.7 shows that the model agrees with the measurement except for:

1. the two modes already observed in Figure 7.6, i.e, the 0.32 Hz mode in yaw DoF and 7.5 Hz in pitch DoF,

2. the highest resonance in L and T DoF at 5.2 Hz and 5.0 Hz respectively as shown in Figure 7.7a and 7.7b,

3. vertical DoF as shown in Figure 7.7c.

The discrepancy of the L and T DoF, which are the RMN resonances, might come from the hanging condition. This can happen if one of the wires is floating, the effective stiffness in pitch and roll can become softer. Even though for a more detailed explanation, we have to do further investigation. The failure of the vertical DoF come from the failure of the photo-sensor diagonalization. The vertical photo-sensor signal is obtained by the matrix operation using the geometrical sensor and actuator position information. Actually it senses the yaw motion as shown in Figure 7.7c and as shown in Figure 7.7f. Thus the vertical DoF cannot be tested with the photo-sensor. In order to sense the vertical motion with the photo-sensors further sensor matrix diagonalization is necessary.
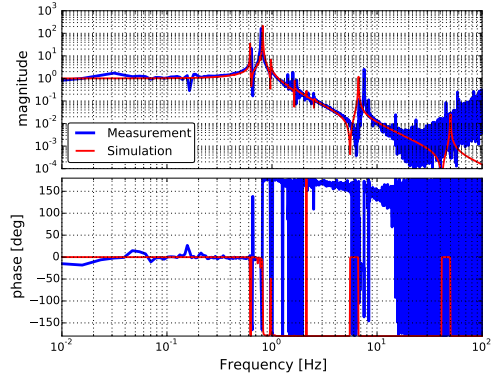
(a) MN to MN in pitch
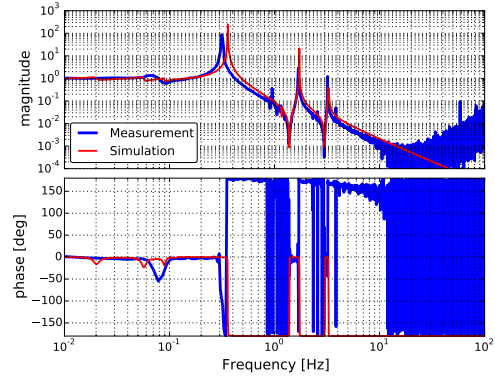
(b) MN to MN in yaw
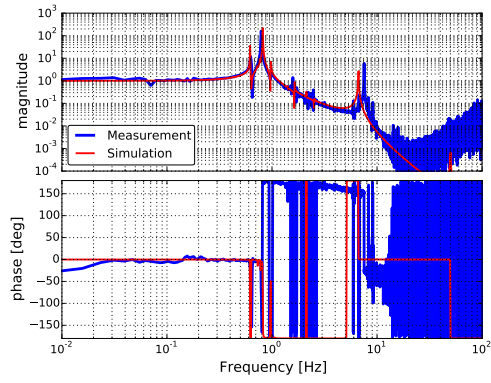
(c) MN to TM in pitch
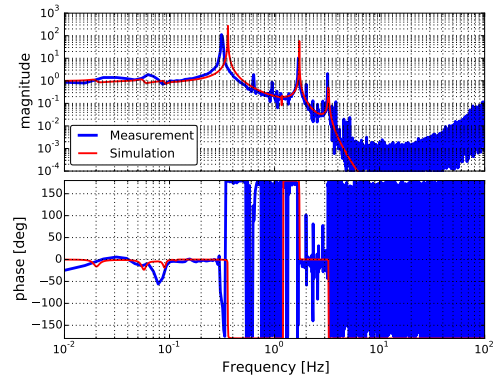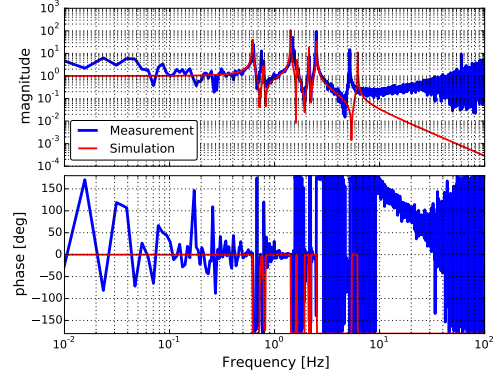
(d) MN to TM in yaw
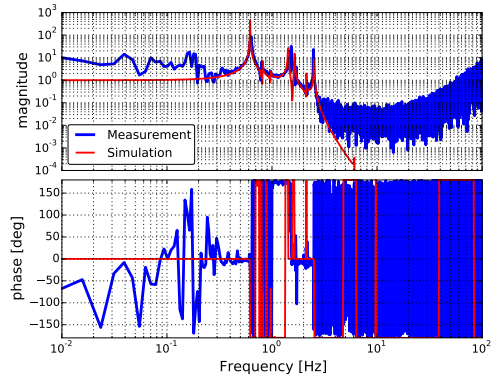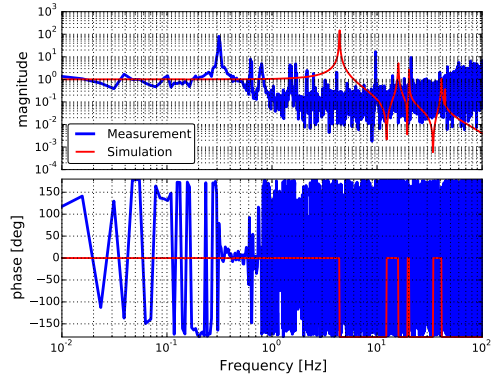
(e) MN to TM in longitudinal

Figure 7.6: Diagonalized mechanical transfer functions of the MN-stage in pitch (*left*) and yaw (*right*) sensed by the optical lever. The upper panels show the response from MN to MN, while the lower panels represent the ones from MN to TM.
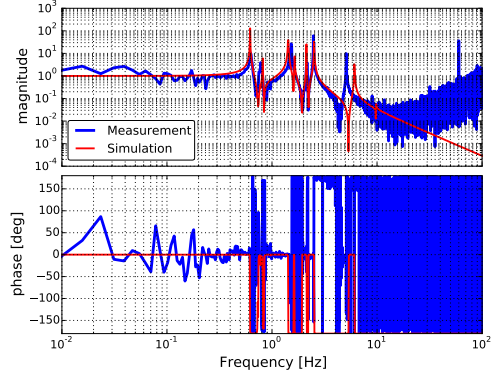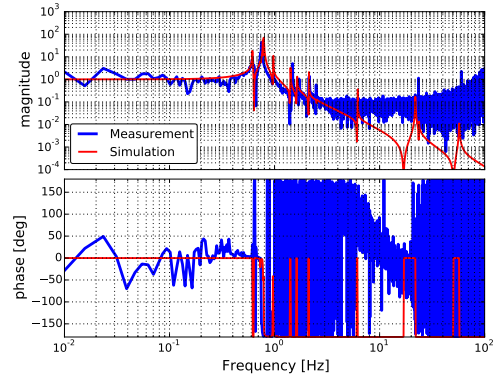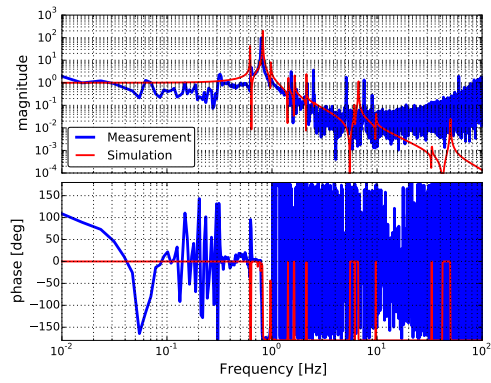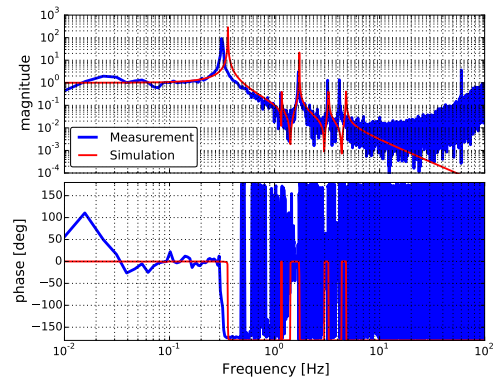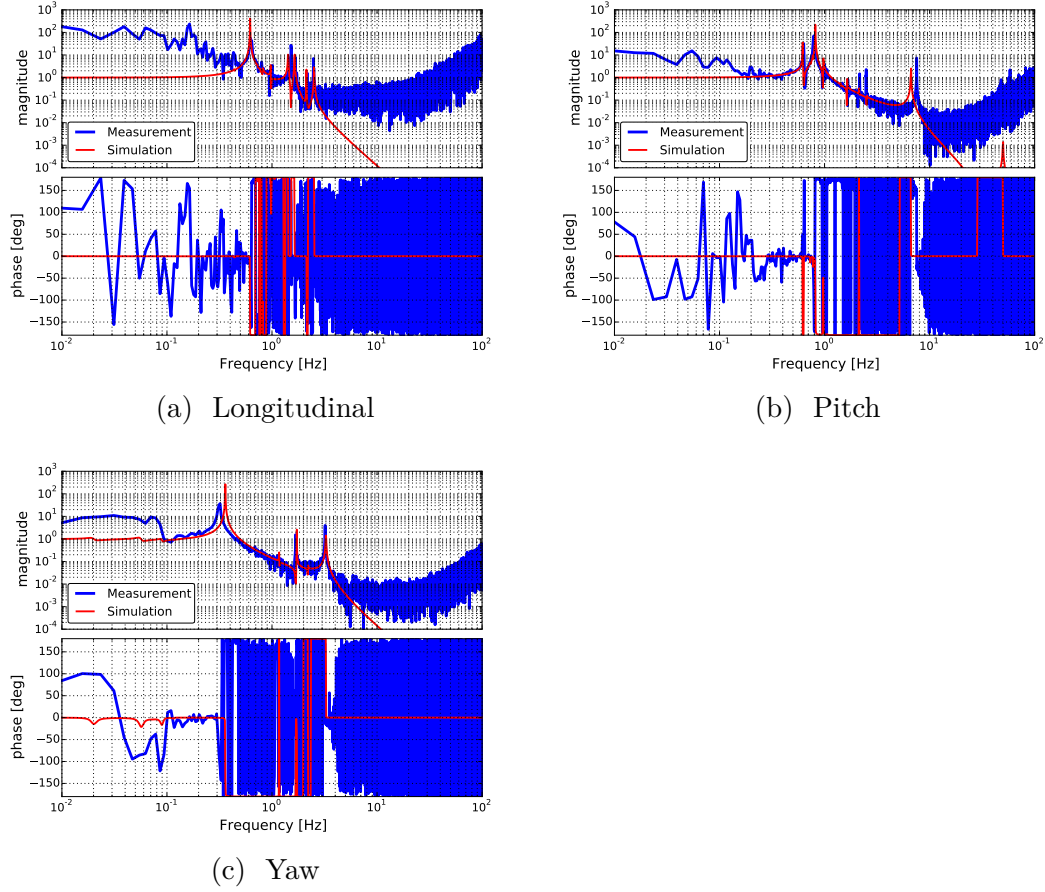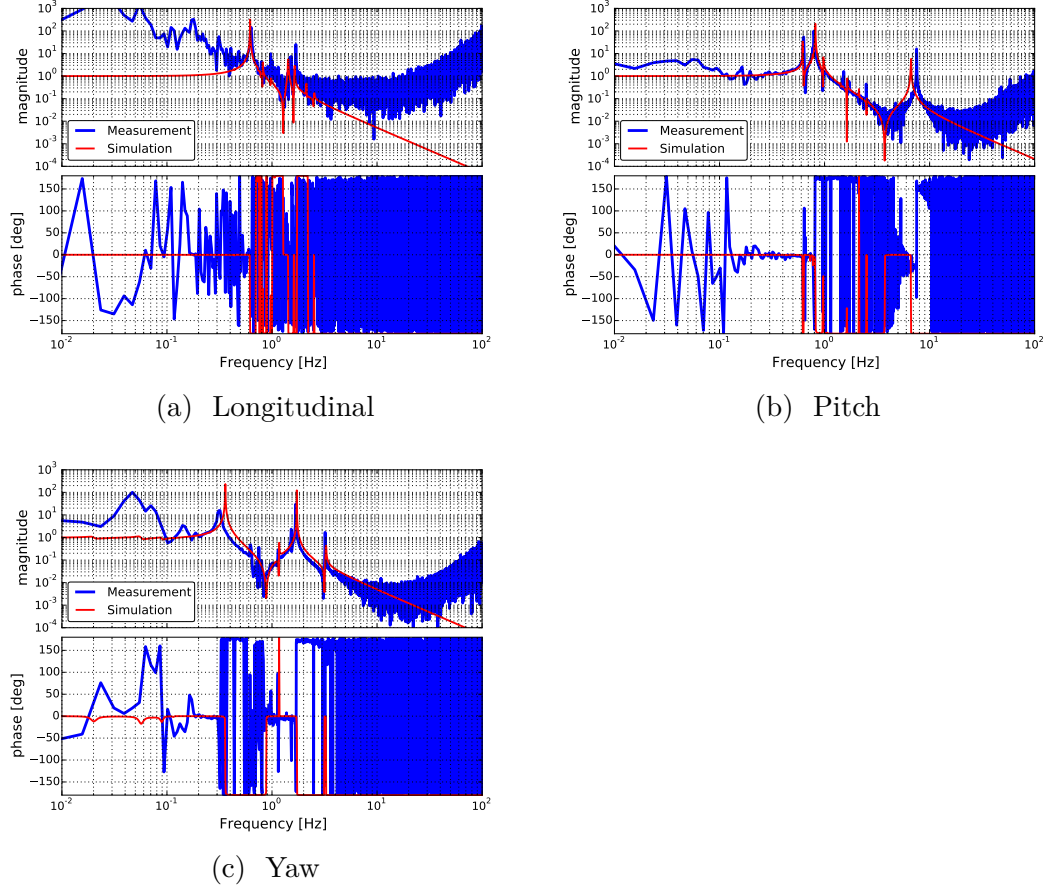
(a) Longitudinal

(b) Transverse

(c) Vertical

(d) Roll

(e) Pitch

(f) Yaw

Figure 7.7: Diagonalized mechanical transfer functions of the MN-excitation to MN-stage sensed by the photo-sensors.

IM stage

Figure 7.8 shows the measured response from the actuators of the IM-stage to the optical lever at the TM-stage.

Basically the model agrees with the actual system except for the two modes at 0.32 Hz in yaw DoF and 7.5 Hz in pitch DoF.

(a) Longitudinal

(b) Pitch

(c) Yaw

Figure 7.8: Diagonalized mechanical transfer functions from IM-stage excitation to TM in longitudinal (a), transverse (b) and Yaw (c) DoF compared with the simulated curve. All the transfer functions are measured with the optical levers at the TM stage.

TM stage

Figure 7.9 shows the measured response from the actuators of the TM-stage to the optical lever at the TM-stage.

Similar to the transfer functions excited at the IM-stage, basically the model agrees with the actual system except for the two modes, i.e, the resonance at 0.32 Hz in yaw DoF and at 7.5 Hz in pitch DoF.

(a) Longitudinal

(b) Pitch

(c) Yaw

Figure 7.9: Diagonalized mechanical transfer functions from TM-stage excitation to TM in longitudinal (a), transverse (b) and Yaw (c) DoF compared with the simulated curve. All the transfer functions are measured with the optical levers at the TM stage.

7.2.3 Effect of heat-links and its vibration isolation system

According to the force transfer function measurement reported in the previous section, some significant discrepancies from the model without heat link system are visible at the BF-stage as follows:

- The first resonant frequency of the BF-stage transfer functions in the Yaw DoF is higher than the one predicted by the model. The first resonant frequency measured for the Yaw DoF is 40 mHz, while the model predicts 20 mHz.

- One peak at 0.14 Hz found in the BF-stage transfer functions in the Yaw DoF. This peak is found in all the sensors when the BF-stage is excited in Yaw. On the other hand, this peak is not observed with the optical levers when lower stages such as MN-stage are excited.

Similar measurement was already done in [41] and it reports that if there is not payload, heat link nor the heat link vibration isolation system, the first resonant frequency in L, T and Yaw DoF is found at 55 mHz, 65 mHz and 20 mHz, respectively. It was also reported that the measured results were in agreement with simulation [41]. On the other hand, the frequencies newly measured in this work are at 74 mHz, 82 mHz and 40 mHz for L, T and Yaw DoF respectively. Compared to the suspension configuration in [41], the total length of the suspension is longer in this work. Thus it is more natural to predict that the fist resonance would be at lower frequencies. The resonant frequency also depends on the temperature, and the temperature during the measurement is actually lower than the room-temperature, 250 K. However, this is not enough to explain a difference of the elastic constant by factor of about 4 in the Yaw DoF.

Thus this implies that the current system should have additional springs compared to the one in the model. The most probable origin of this additional spring is the heat link system.

7.2.4 Summary of mechanical system characterization

Most of the measured frequency responses agree with the rigid-body simulation (which does not include the heat link system) apart from some resonant frequency and the Q factors. This is not true for the frequency responses of the BF-stage and GAS filters. In particular, the model fails in predicting the frequency response of the BF-stage, especially in the yaw DoF.

Consequently, it is confirmed that each suspension component has the characteristics of a pendulum, and this is enough for the purpose of building the local control system to allow the interferometer lock. However, the details of the mechanical system will have to be more precisely identified and modeled for further better understanding. Especially the rigid-body modeling without including heat link system fails to explain some of the actual Type-A suspension response and resonant frequencies.

7.3 Performance of damping control

The previous section confirms that the installed Type-A suspension has the characteristics of the pendulum. This is enough for building the active control system (described in section 6.5). This section describes the implementation of the suspension control in the calm-down phase.

The target is to damp the mechanical resonances quickly. More specifically, the requirement is to damp the resonances so that the $1/e$ decay time of the mechanical resonances disturbing the interferometer lock acquisition is less than 1 minute.

In this phase, the filters to keep the position of the suspension components at room-temperature as well as the mirror orientation are also engaged.

The installed feed-back servo system for the calm-down phase is summarized in section7.3.1 and its performance evaluation is described in the section7.3.2.

7.3.1 Control system

As shown in Figure 6.3, the upper part (IP and BF) has DC-coupled damping filters for the horizontal and the vertical DoF. On the other hand, the control of the lower part (payload) damps the payload modes and does DC-control of the mirror angle. The implemented servo filters and the used sensors are summarized in Table 7.1. The corresponding open loop transfer functions are shown in Figure 7.10.

In this system we use the optical levers both at the MN-stage and the TM-stage. The optical lever at the MN-stage senses the two angular motion in P and Y. The MN-stage optical lever is also used to sense the MN motion in the Roll DoF (see section 7.1.2). On the other hand the optical lever at TM-stage senses the L, P and Y DoF.

Table 7.1: The implemented servo loops with the used sensors. The loops for the IP- and BF-stage and the GAS filters are closed in each stage. In the table oplev represents the optical lever. There are optical levers at MN- and TM-stages and they are labeled as MN-oplev and TM-oplev respectively.

Loop	Loop DoF	Sensor	Actuation DoF	Purpose
IP	L, T, Y	LVDT	IP	DC and damp
BF	Y	BF-LVDT	BF	DC and damp
F0	GAS	LVDT	F0	DC and damp
F1	GAS	LVDT	F1	DC
F3	GAS	LVDT	F3	DC and damp
BF	GAS	LVDT	BF	DC
from MN to MN	Y	MN-oplev	MN-Y	damp
from TM to MN	Y	TM-oplev	MN-Y	DC
from TM to MN	P	TM-oplev	MN-P	DC and damp
from TM to IM	P	TM-oplev	IM-P	damp
from MN to MN	R	MN-oplev	MN-R	damp

Due to a technical issue found in the photo-sensor signals of ETMX suspension (shown in section 7.3.3), the control system for the payload uses mainly the optical levers, even though they provide a smaller linear range compared to the photo-sensors. The resonant modes of #51, #52, #55, #56 and #57 are the exception. They are damped using the photo-sensors at the MN-stage, since the optical levers cannot sense the motions with a good signal-to-noise ratio. The implemented filters are shown in Figure 7.11 (*top*).

We also use fourth order Butterworth band-pass filters for the payload damping [90]. We refer to this as band-pass comb filters. This control system is implemented in order to damp the RM chain modes which were to be sensed by the photo-sensors in the original design. This band-pass filter can also minimize the control noise re-injection at higher frequency region. The filter is designed with band-pass response in the target frequency band $(f_0 - \Delta f_1, \ f_0 + \Delta f_2)$ where f_0 is the resonant frequency of the mode to be damped. Δf_1 and Δf_2 set the frequency bandwidth. We select an optical lever signal sensitive to the target resonance. We then tune the gain the phase by adjusting Δf_1, Δf_2. The optimization is done manually so that the decay time of the mode becomes smaller than the requirement. The implemented band-pass comb filters are summarized in Table 7.2 and shown in Figure 7.11 (*bottom*).

Table 7.2: List of the implemented band-pass comb filters for the payload modal damping. For each filter the table gives the sensors and actuators used, and the frequencies of the target resonances. Sensors and actuators are identified by the stage and by the DoF (written as by stage-DoF).
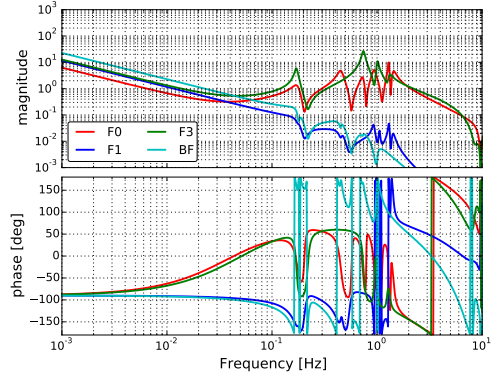
ID	Sensing	Actuation	Target frequency [Hz]
BP-comb 1	TM-P	MN-L	1.53 Hz (#44)
BP-comb 2	MN-P	MN-R	23.5 Hz (#63)
BP-comb 3	TM-L	IM-L	2.17 Hz (#49)
BP-comb 4	TM-P	MN-V	9.69 Hz (#59)
BP-comb 5	TM-L	MN-L	2.5 Hz (#52)
BP-comb 6	TM-P	MN-P	7.5 Hz (#58)
BP-comb 7	TM-Y	MN-Y	3.21 Hz (#53)
BP-comb 8	TM-Y	MN-Y	1.15 Hz (#39)
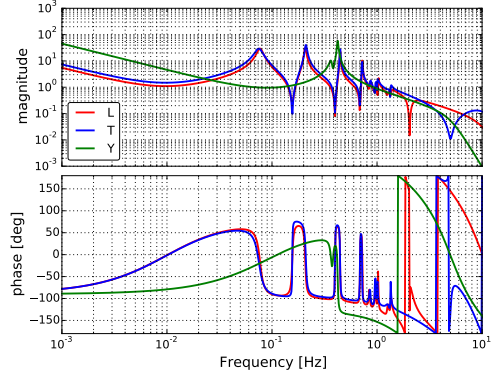
(a) IP loops in L, T and Y DoF.
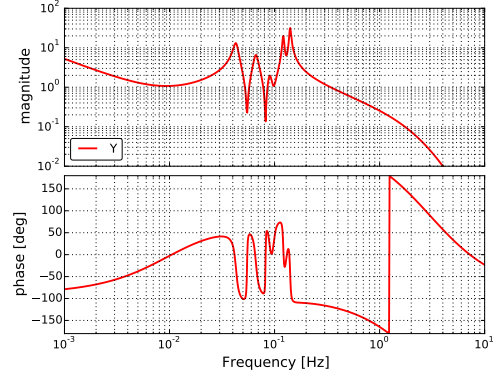
(b) BF loops in Y DoF.

(c) F0, F1, F3 and BF GAS loops.
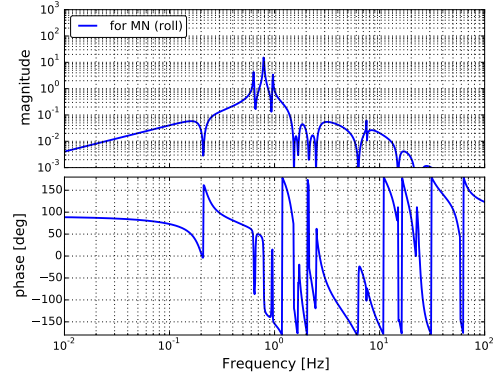
(d) Payload loops in R DoF.
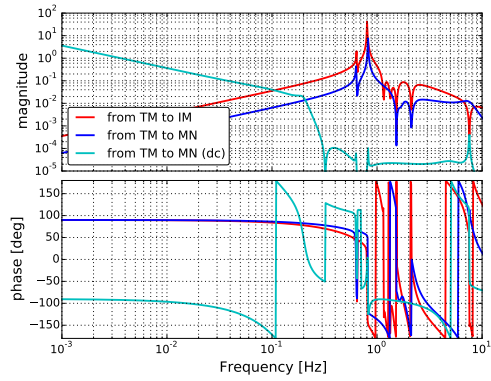
(e) Payload loops in P DoF.
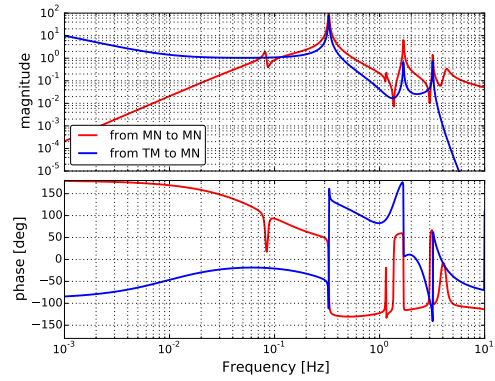
(f) Payload loops in Y DoF.

Figure 7.10: Open loop transfer functions of the implemented servo filters for the calm-down phase.
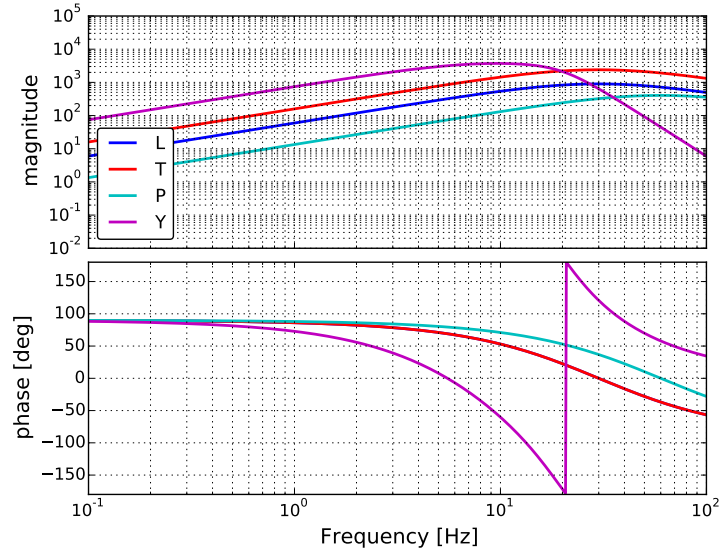
(a) PS loop filters at MN-stage in L, T, P and Y DoF.
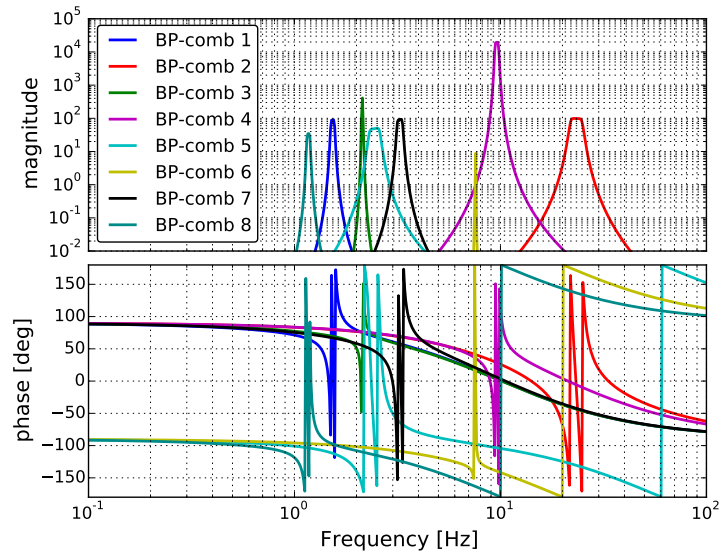
(b) Implemented band-pass comb filters.

Figure 7.11: Implemented servo filters in addition to the ones in Table 7.1.

7.3.2 Decay time measurement

In order to check that the installed control system satisfies the requirement ($1/e$ decay-time constants < 1 min.), the decay-time constant of each mechanical resonance is measured.

Since the goal is to damp all the mechanical resonances which disturbs the lock acquisition, the modes which are expected to have small coupling to the mirror, such as the ones shown in Figure 7.12 (a), are not considered. In addition, only the modes whose resonant frequencies are lower than 30 Hz are examined, since the resonances which disturbs interferometer locking are basically the lower frequency modes. Moreover it is difficult to sense and damp the resonances at frequencies higher than 30 Hz, with the local sensors. Then the total number of the measured resonances are 53.

The decay time measurement is conducted as follows: first, we excite a target resonant mode by using an appropriate actuator with a sinusoidal signal at the target frequency. Then after confirming the resonance is sufficiently excited, we turned off the actuation and measure the decay signal by the built-in sensors. The measured decay time series is approximately fitted by an exponential-decay sine wave function eq (7.1): When a beating signal of two or three resonances is measured, a double or a triple decay sine wave function is used for the fitting. This situation occurs when some modes have close resonant frequencies.

$$f(t) = \sum_i^n \left[A_i \exp\left(-\frac{t}{\tau_{e,i}} \right) \sin\left(2\pi f_{0,i} t \right) \right] + x_0, \quad (n = 1, 2 \text{ or } 3) \qquad (7.1)$$

where τ_e is the $1/e$ decay time.

An example of this measurement is shown in figure 7.13. These are obtained by exciting MN-stage in Yaw DoF and by measuring with the optical lever.

The measured $1/e$ decay time constants for each resonant frequency are plotted in Figure 7.14. They include the resonance modes whose resonant frequencies are below 30 Hz. The detailed values of the measured decay time constants are summarized in section B.5.

I note that one resonance at 4.4 Hz (as shown in Figure 7.12 (b)), is not found in this work (see also section 7.2.2 GAS stages). That resonance is the vertical mode predicted with the model which does not have heat-link system. Further investigation for this mode would be important for a better understanding of the whole suspension system. In this work, however, the detailed investigation is not done since no vertical resonances which disturbs the lock acquisition, are observed in the 4 to 5 Hz region.

According to Figure 7.14, the requirement is satisfied for all modes except for two cases.

For the one case found at 1.5 Hz, this would not be a problem for the lock acquisition since the resonance is the mode in the Roll and Transverse DoF labeled
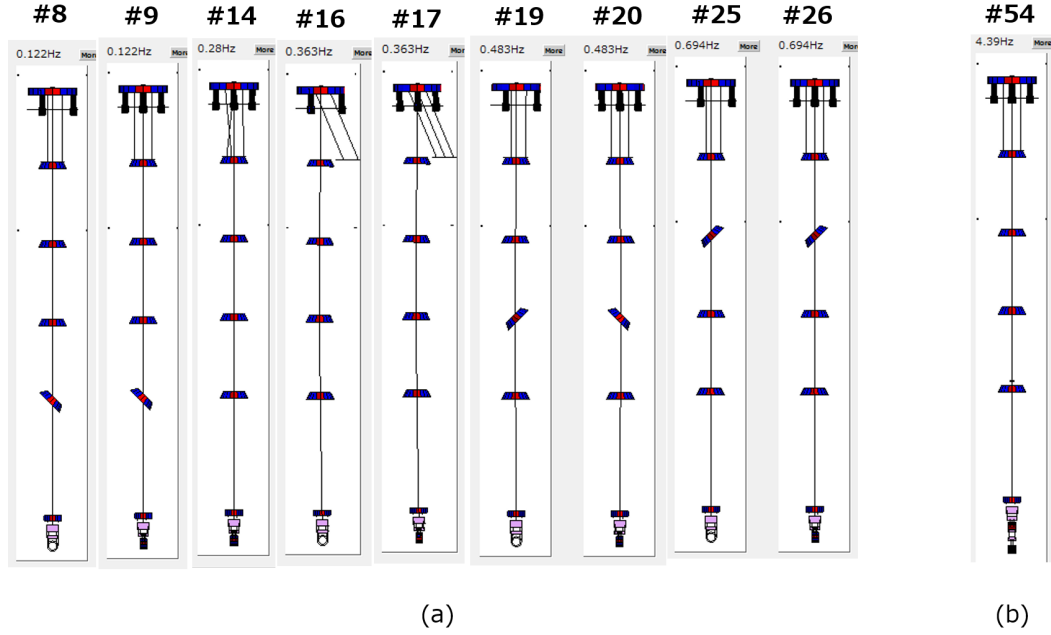
Figure 7.12: The gigen modes which are not considered in this test (a), and the eigen mode which is not found (b). Only the frequency region below 30 Hz has been considered.

mode #43 in section B.1. This resonance would make a small impact on the interferoemter lock acquisition. Thus the case at 1.5 Hz does not break the requirement.

Concerning the case at 0.14 Hz, this mode is found in the Yaw motion of the BF-stage. Thus, in principle, this mode has to be damped quickly.

I note that this mode is not identified by the model which does not have the information of the heat-link system. Thus the counterpart of this mode is not found in the table in section B.1. In the characterization, this is the resonance observed at 0.14 Hz in the force transfer function from BF-stage excitation in Yaw DoF to BF-stage in Yaw DoF as shown in Figure 7.5c.

Since the BF-stage Yaw control loop failed to damp this mode effectively while the open loop gain is larger than 1 (as shown in Figure 7.10b), we suspect that this issue is connected to the payload part, and in particular to the heat-link system.

Generally speaking, further investigations would be necessary to have a better understanding of this resonance. This peak is visible in the BF-Yaw and TM-chain-Yaw sensors, when the BF-stage is excited in Yaw (see in Figure 7.15a). On the other hand, when the MN-stage is excited in the Yaw, the peak is observed in the BF-stage sensors, while both the optical lever at MN-stage and the photo-sensor do not sense it (see Figure 7.15b). This implies that if the BF-stage is not kicked, this resonance would not be excited. Since the feedback signals for the global control is fed back to the TM- and MN-stage in the current interferometer
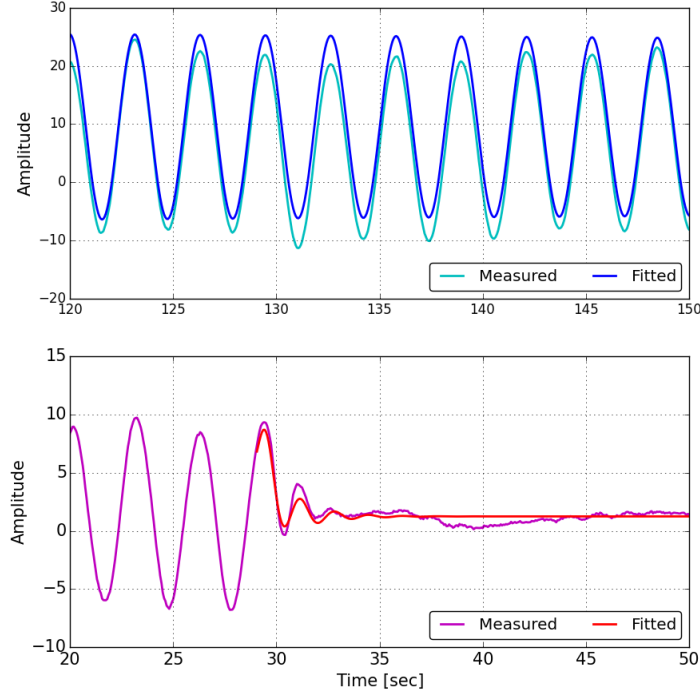
Figure 7.13: An example of the $1/e$ decay-time measurement. The time series, when one resonant mode is excited by a sinusoidal injection and when it is cut off. The upper and the lower panel show the case where the control is off and on respectively. Yaw motion excited at MN-stage and sensed by the optical lever. The (cyan, magenta) colored curves show the measured time series, while the (blue, red) colored time series represent the fitted time series.

control, we do not kick BF-stage at the lock loss.

These observed facts lead to a conclusion that this mode would not be problematic for the lock acquisition in the lock-recovery mode. Although this 0.14 Hz Yaw motion would be problematic when the upper stages such as BF- and IP-stages are used for the interferometer control, that consideration is to be done as further improvement.

Consequently, the control system described above satisfies the requirement in the lock-recovery mode.
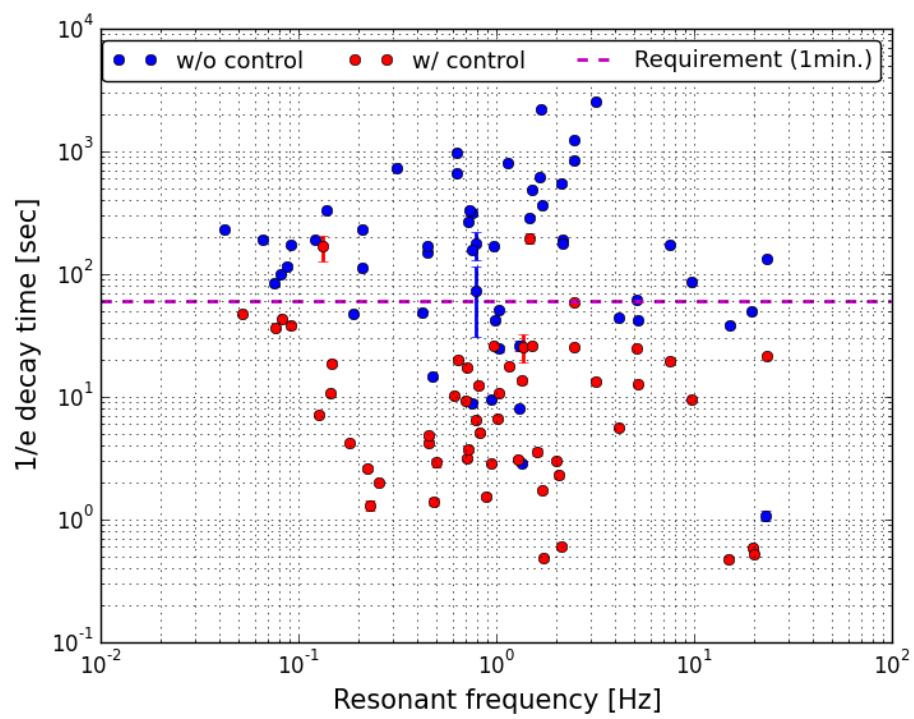
Figure 7.14: The result of the $1/e$ decay time constant as the function of the measurable mechanical resonances. The dashed line shows the requirement of 1 minute.
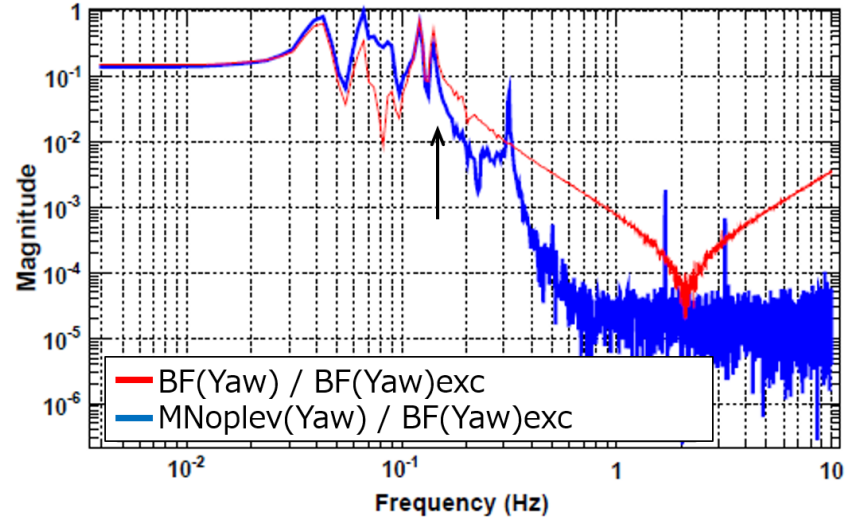
(a) Force transfer function from BF-Yaw excitation to BF-Yaw (blue) and to MN-Yaw measured by the optical lever (red). The unit is a.u.
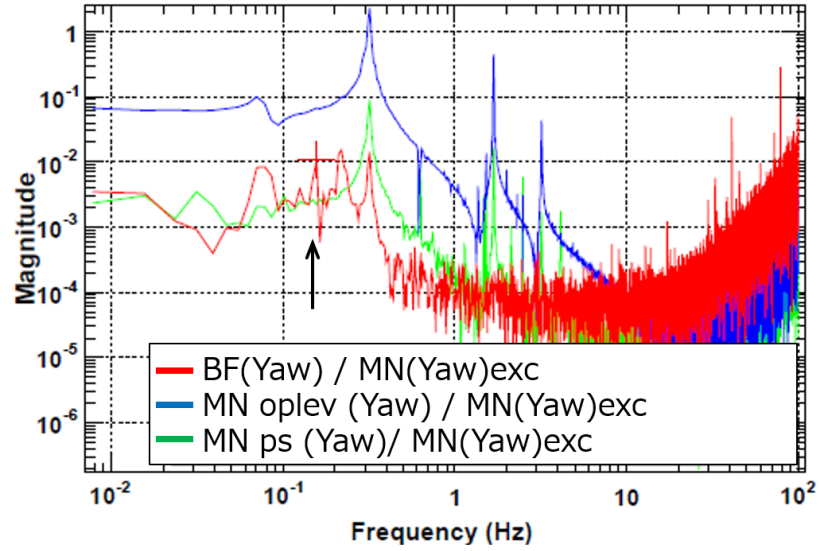
(b) Force transfer function from MN-Yaw excitation to BF-Yaw (blue), and to MN-Yaw with the optical lever, and to MN-Y with the reflective photo-sensors at MN-stage (blue and green respectively.).

Figure 7.15: The measured force transfer functions in Yaw. The unit is a.u. The arrows point the peak at 0.14 Hz.

7.3.3 Further steps for the damping system

As described above, the damping control system implemented using mainly the optical levers satisfies the requirement. However, this system is not robust enough when a relatively large disturbance takes place, such as an earthquake or a large kick during an interferometr lock loss. This is so since the linear range of the optical lever is relatively small. The typical range is about a few hundred μrad, and the signal can go outside of this range when such a large disturbance occurs. In order to construct a more robust damping control system, it is needed to include the damping controls with the photo-sensors since these sensors have linear range wide enough.

In the actual system, we mainly use the optical levers, and the photo-sensors are used only for a few resonant modes, which the optical levers cannot measure with a good signal-to-noise ratio. This solution has been adopted since sometimes the photo-sensors become quite noisy[2]. The typical photo-sensor spectra when it becomes noisy is shown in Figure 7.16. In order to use the photo-sensors more widely, we need to solve this issue.

It must be noted that we use such photo-sensors in this thesis work, since this photo-sensor noise issue was found only in the ETMX suspension. Also, we use them since such high noise level is not observed during the implementation period.
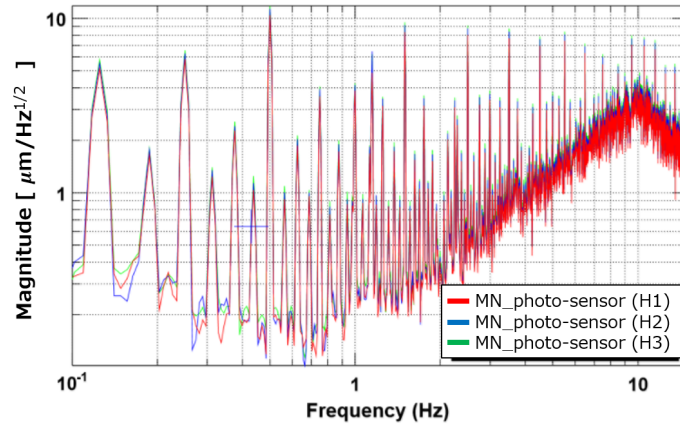
Figure 7.16: Typical spectrum of the photo-sensor when it is noisy.

Another issue concerning the use of the photo-sensors, is their relatively low sensitivity. The current photo-sensors are not sensitive enough to measure the suspension motions when the motion amplitude becomes smaller than about 1μm

---

[2]It is suspected that this issue comes from the electrical circuits. However, further investigation is necessary in the future to solve this issue.

and 1μrad. Thus meaningful photo-sensor signals are available only when a large disturbance occurs.

If we improve the photo-sensor sensitivity to be comparable to the one of the optical lever, then we can construct a more robust damping control system.

The implementation of better-sensitivity photo-sensors will also help to remove the current difficulties with the design and maintenance of the band-pass comb filters.

Indeed, the band-pass comb filter is quite sensitive to the resonant frequency. If the temperature of the payload is changed, the resonant frequencies will be shifted. We then have to tune the filter accordingly. During commissioning of the interferometer, we sometimes have to change the temperature. This sensitivity of the comb filters make their use quite inconvenient.

Thus if we can construct the damping control system without the band-pass comb filters, we can avoid this maintenance work and make the interferometer operation easier and more robust. Such damping control system can be constructed using better-sensitivity photo-sensors. This will be very helpful in particular during the commissioning period.

7.4 Performance of seismic noise suppression control

This section describes the implementation of the seismic noise suppression control. The feedback control with sensor-correction system (described in section 6.6.1) is implemented for this purpose. This is done in order to reduce the RMS velocity and displacement of the mirror especially at the frequency around 0.2 Hz. The concrete target is to reduce the RMS velocity and the RMS displacement of the mirror below 2.0 μm/sec and 0.39 μm respectively (in Table 6.2).

As anticipated in the design (see section 6.6.1), the sensor correction system is added to the feedback controls at the IP-satge level. For the other control loops such as the one acting on the payload and on the GAS stages, we use same configuration used in the calm-down phase.

7.4.1 Control system for sensor correction

The ground vibration signal measured by a seismometer Trillium120QA [38] at the second floor of the X-end station is sent and added to the LVDT signal with a sensor correction filter F_{sc}. Then the corrected LVDT signals are used for the feedback control system. Figure 7.17 show the main signal flow of the system, while Figure 7.18 draws the corresponding block diagram with a schematic view of the actual control system.

The signals sensed at each IP-LVDTs are converted to the Cartesian signals with the sensor matrix. The filtered seismometer signal on the ground is added to the Cartesian signals and then the combined signals are used as the error signal of the feedback system. The correction signals are sent to each coils after applying the force distribution matrix.
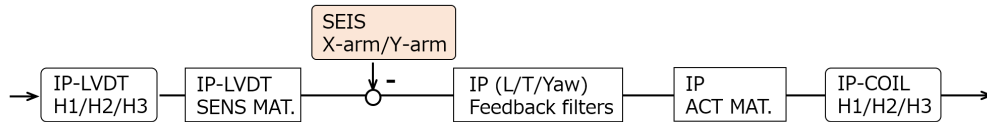
Figure 7.17: Main signal flow of the feedback control with the sensor correction system at the IP-stage. The signals sensed at each IP-LVDTs are converted to the Cartesian signals with the sensor matrix (SENS MAT.). The filtered seismometer signal on the ground is added to the Cartesian signals and then the combined signals are used as the error signal of the feedback system. The correction signals are sent to each coils after applying the force distribution matrix (IP ACT MAT.).

Shaping of sensor correction filter

The optimal sensor correction filter is obtained by using $F_{sc} = -S_L/S_s$ where S_L and S_s are the sensor response of the LVDT and the seismometer. Thus we inter-
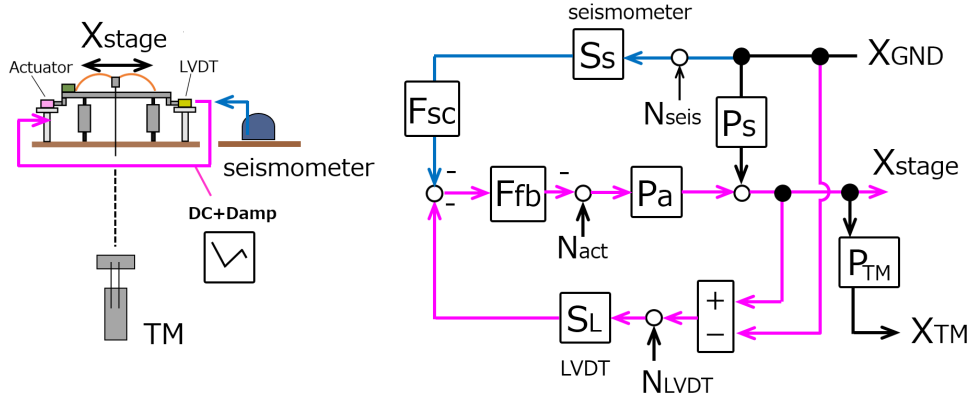
Figure 7.18: Schematic view of the feedback control with the sensor correction system at the IP-stage (*left*) and its Block diagram (*right*). All symbols are defined as in section 4.2. This is the case where F_{ff} is set to zero. P_{TM} denotes the displacement transfer function from IP-stage to TM-stage.

calibrate the signals between the IP-LVDT and the seismometer on the ground so that the seismometer signal has same unit as the LVDT one. This is done by measuring the mechanical displacement transfer function from ground to IP-stage by LVDT. We first find the amplitude where the transfer function is flat. At frequencies higher than the IP resonance, it is expected that the IP-LVDT signal will have only the seismic motion signal. Thus in this frequency region, the amplitude of the transfer function from the seismometer to the IP-LVDT is expected to be equal to 1. Such frequency region is expected to be found above 0.6 Hz as shown in Figure 7.19. Since the sensor noise of the LVDT becomes dominant at frequency above ~ 0.7 Hz, we then select the gain at 0.6 Hz and tune the F_{sc} gain. As the result, we obtain the factors 0.99 and 0.93 for the L and T DoF respectively.

After the gain tuning, the seismometer is high-pass-filtered with cut-off frequency of 10 mHz in order not to inject too much seismometer noise. In order to avoid large amount of phase shift above 0.1 Hz, we select a second order elliptic high-pass filter whose passband ripple and attenuation are set to 10 dB and 100 dB respectively.

In addition we include one more high-pass filter at 0.5 mHz to F_{sc} for the compensation of the calibration filter of the seismometer S_s. The calibration filter S_s has a f^{-1} response in order to convert the seismometer the velocity signal into a displacement signal. A fourth order Butterworth filter has been chosen for this purpose.

The sensor correction filter F_{sc} is shown in Figure 7.20. The phase shift at 0.1 Hz due to the filter F_{sc} is 3.3 deg which gives 0.2 % difference compared to the ideal signal which we want to subtract.
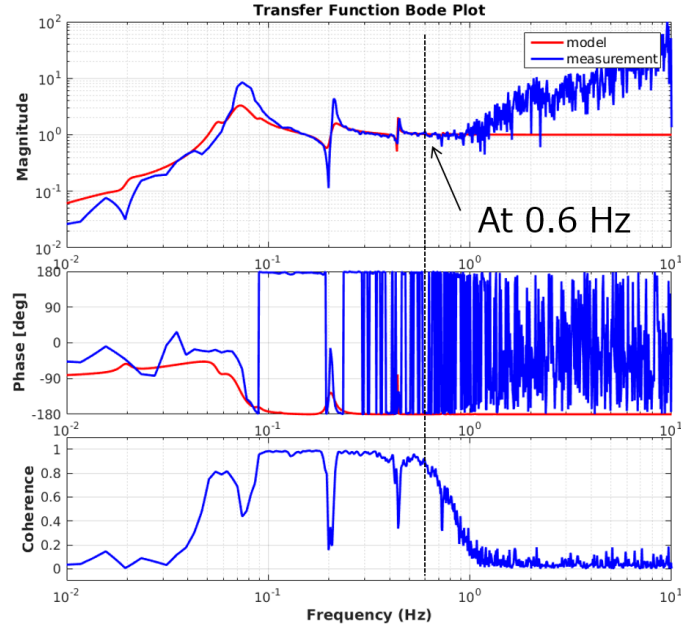
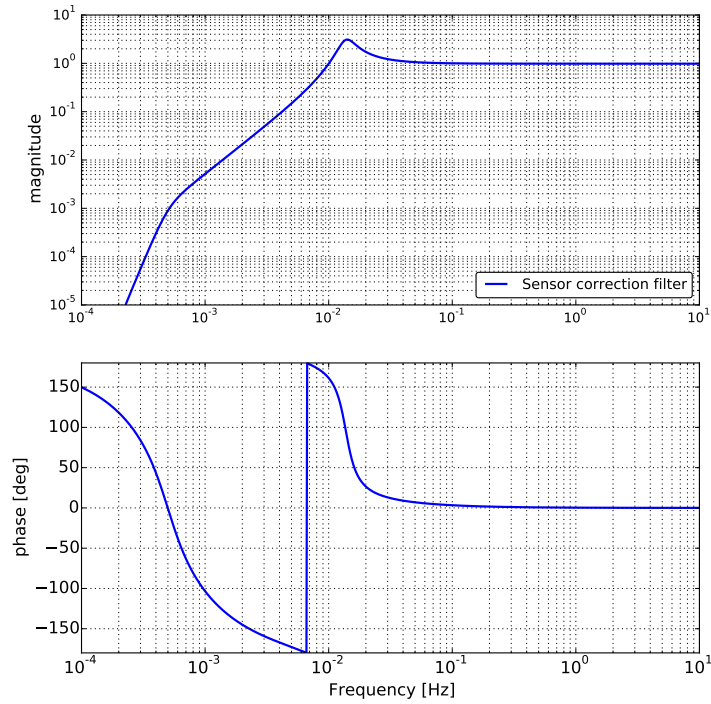Figure 7.19: Displacement transfer function from ground to IP-stage by LVDT.

Figure 7.20: The sensor-correction filter F_{sc} used in ETMX suspension. This filter is applied to the displacement seismometer signal.

7.4.2 Verification of sensor correction performance

After implementing the sensor-correction filter at the IP-stage, we measure the suppression performance with the local sensors which are implemented around the ETMX suspension. We test if the residual mirror RMS velocity and displacement satisfy the requirements on them. In the following subsections the sensor-correction system at the IP-stage by the seismometer on the ground is abbreviated to IPsc.

IP-stage spectra

First we measure the performance in the case where the IPsc is implemented along the the L DoF only. Figure 7.21 shows the comparison of the IP-stage displacement spectrum measured by the inertial sensor, geophone (*left*), and by the LVDT (*right*), when the IPsc is on and off. The seismometer signals are included in order to confirm that the ground motion can be regarded as identical between the two measurements, since the ground motion always affect the shape of the spectra.

Figure 7.21 (*left*) shows that the displacement of the IP-stage is suppressed especially between 0.1 Hz to 0.7 Hz by using the IPsc. At around 0.2 Hz the amplitude is reduced by a factor of 5.

Figure 7.21 (*right*) shows that the IP-stage motion as measured by the LVDT is suppressed by the IPsc at frequencies below 1 Hz, i.e, where the LVDT signal is larger than its noise level when the IPsc was off. Indeed in this frequency range, the LVDT signal is above noise in both conditions (IPsc ON/OFF). On the other hand, however, the sensor corrected IP-LVDT signal indicates that the LVDT is less corrected at frequencies below 70 mHz. Especially at frequencies below 40 mHz, the amplitude becomes larger compared to the case where the IPsc is off. This is due to the seismometer noise and the sensor-correction filter shape.

This performance in the low frequency region is unavoidable in the sensor-corrected system since the seismometer sensitivity to the horizontal motion becomes poor at very low frequencies. Since the main target of this work is to reduce the RMS motion connected to the micro-seismic peak, which is around 0.1 to 0.5 Hz, we do not discuss the performance at very low frequencies (in particular below 0.1 Hz) here.

Figure 7.22 shows the comparison between the sensor-corrected IP-LVDT signal and the geophone signal when the IPsc is on. As shown in Figure 7.22, there is a discrepancy between the geophone signal and the sensor-corrected IP-LVDT signal. The amplitude is different by factor of 2 at around 0.2 Hz. In addition, the frequencies of the dips are different from each other. This seems due to the fact that the geophone also sense the tilt motion, while the LVDTs do not. This happens since the two sensors are not sensing the same motion.

A more detailed investigation for this issue will be necessary. However, in this work we use the geophones for the passive spectra measurement of the IP-stage
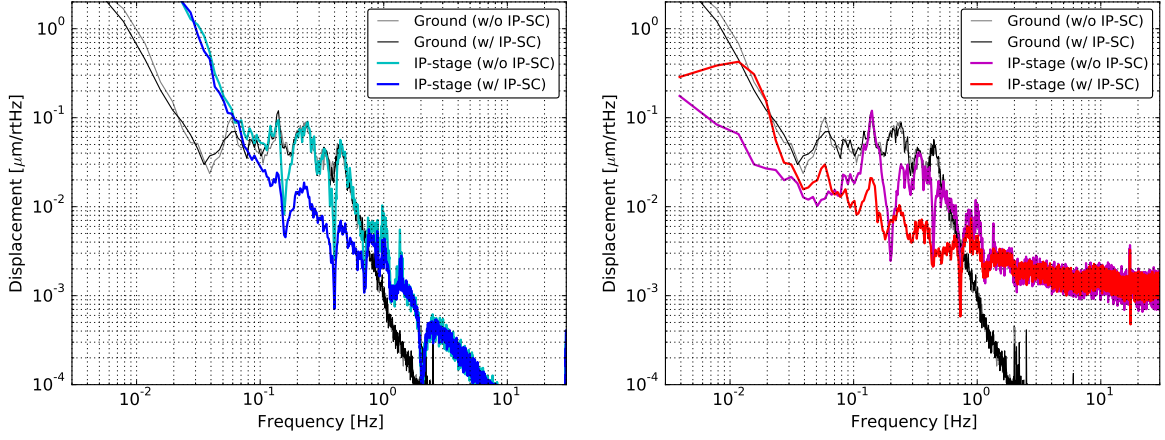
motion.

Figure 7.21: Comparison of the IP-stage displacement spectrum measured by the inertial sensor geophone (*left*) and by the LVDT (*right*) when the IPsc is on and off. I note that in the *right* panel, the LVDT signal with and without IPsc are not comparable since one measures the displacement between the IP-stage and the ground, while the other one observes the inertial motion of the IP-stage basically.
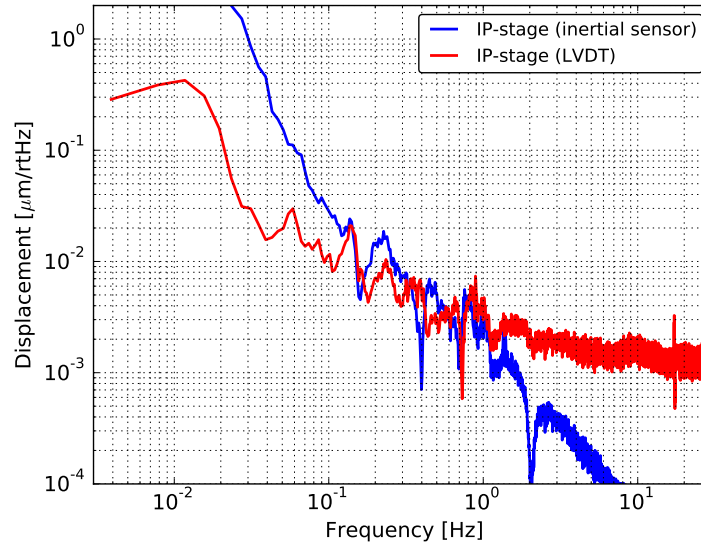

Figure 7.22: Comparison between the sensor-corrected IP-LVDT signal and the geophone signal when the IPsc is on.

BF-stage and TM-stage spectra

Figure 7.23 (*left*) shows the comparison of the BF-stage displacement spectrum measured by the LVDT, when the IPsc in L DoF is on and off. The BF-LVDTs in this measurement are not sensor-corrected and thus they observes the relative motion between the security frame (mechanical ground) and the BF-body. The plot shows that the amplitude of the spectra in the frequency region between 0.1 Hz to 1 Hz is suppressed with the IPsc. In addition, the amplitude below 30 mHz is enhanced due to the seismometer self-noise and the correction filter. This result implies that the IPsc works for the whole upper part. We must note that the detailed suppression level at the BF-stage (below 0.6 Hz) cannot be estimated from the plot. This is so since when the IPsc is on, the motion of the BF-body becomes smaller than seismic motion. All the feature of the BF-body displacement below 0.6 Hz is buried into the seismic spectrum.

Figure 7.23 (*right*) shows the TM-stage displacement spectrum measured by the length-oplev when the IPsc is on and off. A consistent improvement is observed, however, the sensitivity of the TM length-oplev is not good enough to measure the TM motion.
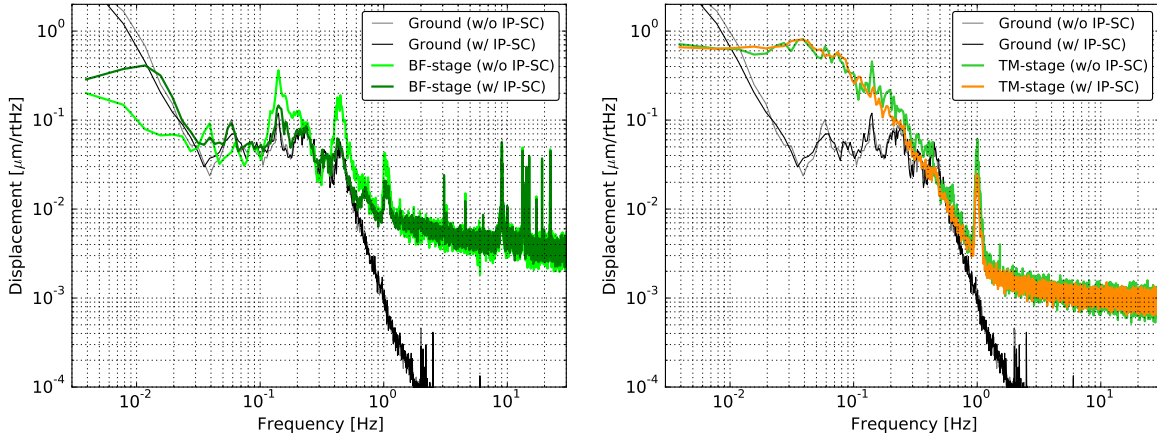
Figure 7.23: Displacement spectrum of the BF-stage measured by the LVDTs (*left*) and of the TM-stage measured by the length-optical lever (*right*), when the IPsc is on and off.

Displacement transfer function measurement in L DoF

After testing the single-DoF correction system, we install the IPsc to both L and T DoF, and then measure the performance of the mirror motion suppression control.

In order to evaluate the suppression performance, the displacement transfer function from the ground to the mirror in L DoF is measured by combining two displacement transfer functions; the displacement transfer function from the

ground to the IP-stage, and that from the IP-stage to the TM-stage. The first transfer function is passively measured with the seismometer on the ground and the geophone on the IP-stage. The second one is measured by exciting IP-stage and the geophone signal is used at frequency higher than 0.1 Hz, while LVDT signal is used at frequency lower than 0.1 Hz. Those signals are selected based on the measured coherence. The resulting transfer function from the ground to the mirror in L DoF is shown in Figure 7.24.

Using these transfer functions and the measured ground motion at KAGRA site, Figure 7.25 estimates the mirror displacement and velocity with the 90 percentile ground motion in Figure 1.13. The estimated RMS displacements and velocities of the mirror with the integration down to 20 mHz are summarized in Table 7.3.

RMS velocity satisfies its requirement even without the IPsc though, the RMS velocity is suppressed by factor of 5 using the IPsc technique. On the other hand, RMS displacement satisfies the requirement at 20 mHz though, this is not the case at 10 mHz and the RMS value can become larger than 1 μm. This performance is as expected as described in the following subsection.

Table 7.3: The estimated RMS displacements and velocities of the mirror with the integration down to 20 mHz.

Configuration	velocity [μm/s]	Displacement [μm]
Without IPsc	0.79	0.64
With IPsc	0.14	0.23

Comparison with simulation

Figures 7.26 and 7.27 show the comparison between the measurement and the simulation, where the IP-stage is controlled by IP-LVDTs without IP_{sc}, and by IP-LVDTs and with IP_{sc} respectively. These simulated curves are obtained by assuming that the inter-calibration between the IP-LVDTs and the seismometer is perfect, which corresponds to the case where the gain is equal to 1 in Figure 6.9.

In the case without IP_{sc} (shown in Figure 7.26), there is mismatch in the velocity/displacement spectrum (by factor of about 1.5 in RMS), even though the measurement qualitatively agrees with the simulation. Taking into account the additional stiffness/dissipation due to the cabling condition might explain the difference though, the details are to be investigated for further step.

On the other hand, in the case with IP_{sc} (shown in Figure 7.27), the measurement agrees with the simulation, especially below 0.5 Hz. The discrepancy between the measurement and the simulation comes from a fact that this sim-

ulation does not include the feedback loops for the payload, which affects the spectrum especially at above 0.5 Hz.

Consequently, it is confirmed that the implemented IP_{sc} suppresses the mirror RMS velocity/displacement as designed.
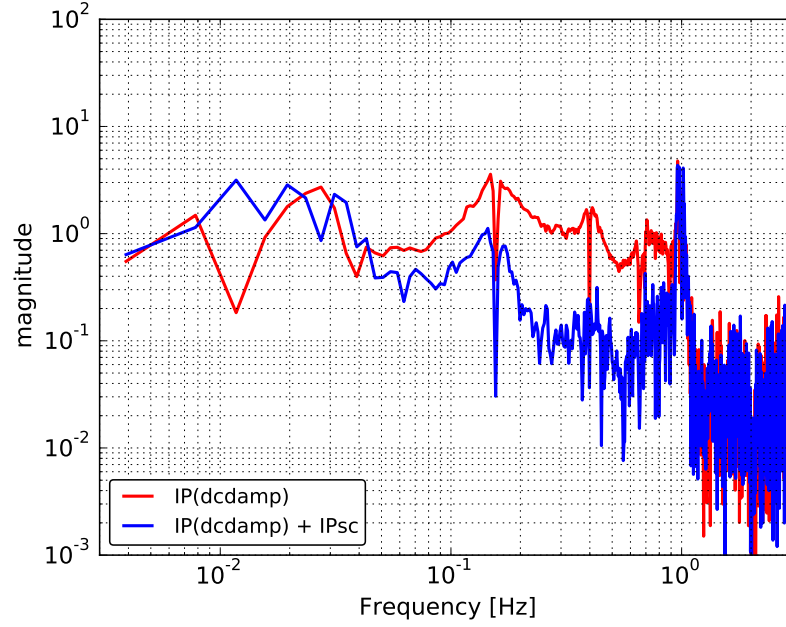
Figure 7.24: The measured displacement transfer function from the ground to the mirror in L DoF. The colors show the difference of the configuration. At the frequency region higher than 1 Hz the sensor noise becomes dominant.
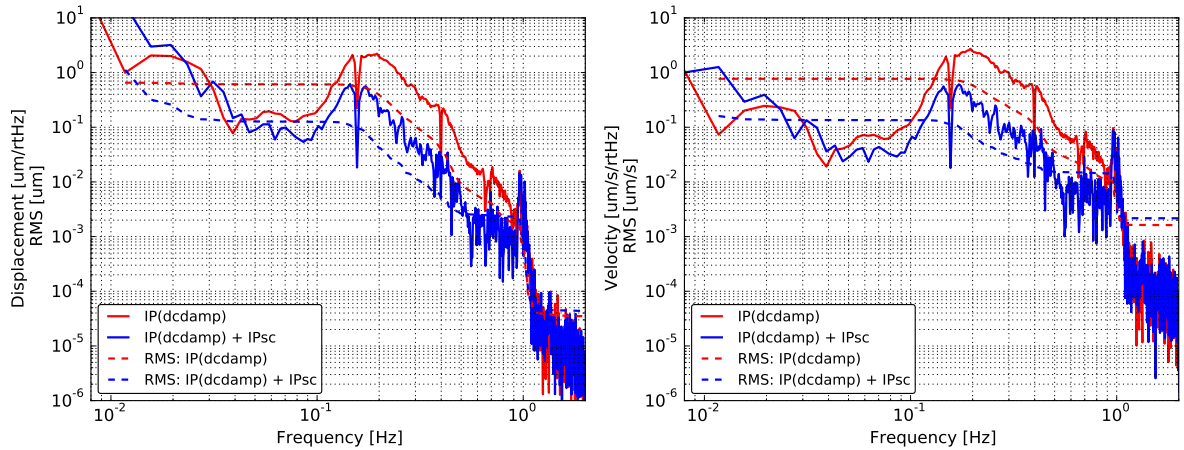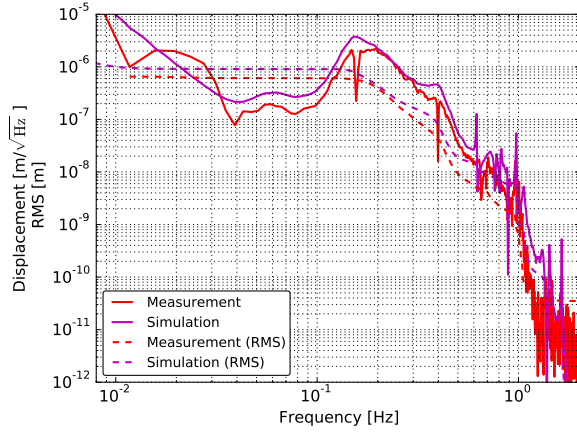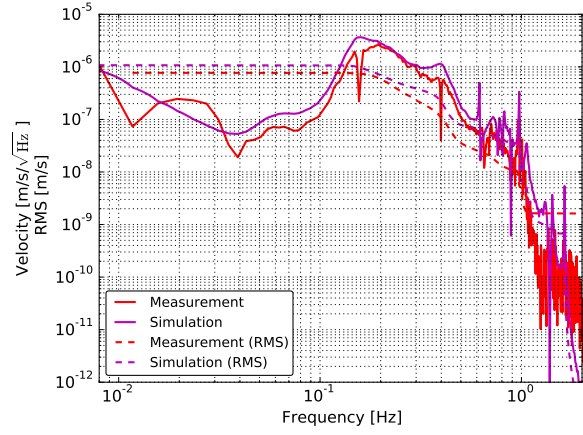

Figure 7.25: Comparison of the expected TM residual displacement (*left*) and TM velocity (*right*) in L DoF when the IPsc is on and off. In this calculation 90 percentile ground motion is used.

(a) Mirror displacement

(b) Mirror velocity

Figure 7.26: Measured mirror residual motion in L DoF, compared to the simulation shown in section 6.6.1 in displacement (*left*) and in velocity (*right*) with IP-stage controls *without IP*$_{sc}$. The dashed curves draw the RMS values integrated down to about 10 mHz. The measured spectrum is obtained by combining the transfer function shown in Figure 7.24 and the ground spectrum shown in Figure 1.13. The high seismic noise level (90 percentile seismic motion) is assumed.
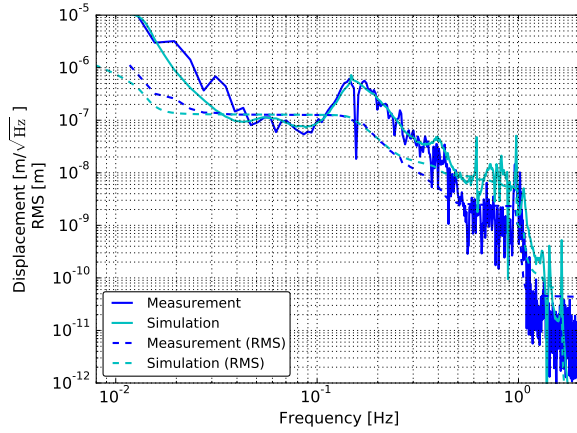
(a) Mirror displacement
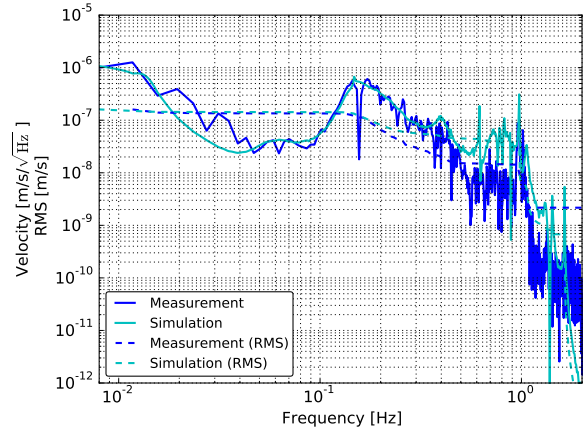
(b) Mirror velocity

Figure 7.27: Measured mirror residual motion in L DoF, compared to the simulation shown in section 6.6.1 in displacement (*left*) and in velocity (*right*) with IP-stage controls *with IP*$_{sc}$. The dashed curves draw the RMS values integrated down to about 10 mHz. The measured spectrum is obtained by combining the transfer function shown in Figure 7.24 and the ground spectrum shown in Figure 1.13. The high seismic noise level (90 percentile seismic motion) is assumed.

Performance summary

The implemented IPsc suppresses the residual motion of the mirror. It gives an RMS displacement which satisfies the requirement for the lock acquisition phase. The RMS velocity satisfies the requirement for the lock acquisition phase, independently of the IPsc system.

Since the RMS is estimated with the geophones which loses the high signal-to-noise ratio at low frequencies, these values can be upper limits. It is expected that the geophone spectra contain the tilt coupling which cannot be distinguished with the current setting.

For further performance improvement at low frequencies (below 20 mHz), a fine tuning of the high-pass cut-off frequencies of the sensor-correction filter F_{sc} might be useful. Even though it would not make drastic change from the system constructed in this work.

Another option for the improvement at low frequencies is to use blended sensors at the IP-stage (see section 4.2.3). By using the inertial sensors for the damping control, we can suppress the motion of the IP-stage itself without the sensor correction system. Thus we can avoid to re-inject the noise due to the seismometer tilt-coupling. We can also increase the damping filter gain, without inducing too much control noise coupling to the mirror above 10 Hz.

Such a system needs inertial sensors with good sensitivity at frequencies below 0.1 Hz. The required noise floor is the same level as that of the current seismometers Trillium120QA. As a reference, the typical noise floors of the inertial sensors compared to the mirror displacement due to the seismic noise, are summarized in Figure 7.28.

It is expected that, even in this configuration, we will need to compensate the tilt-coupling of the inertial sensors at low frequencies.
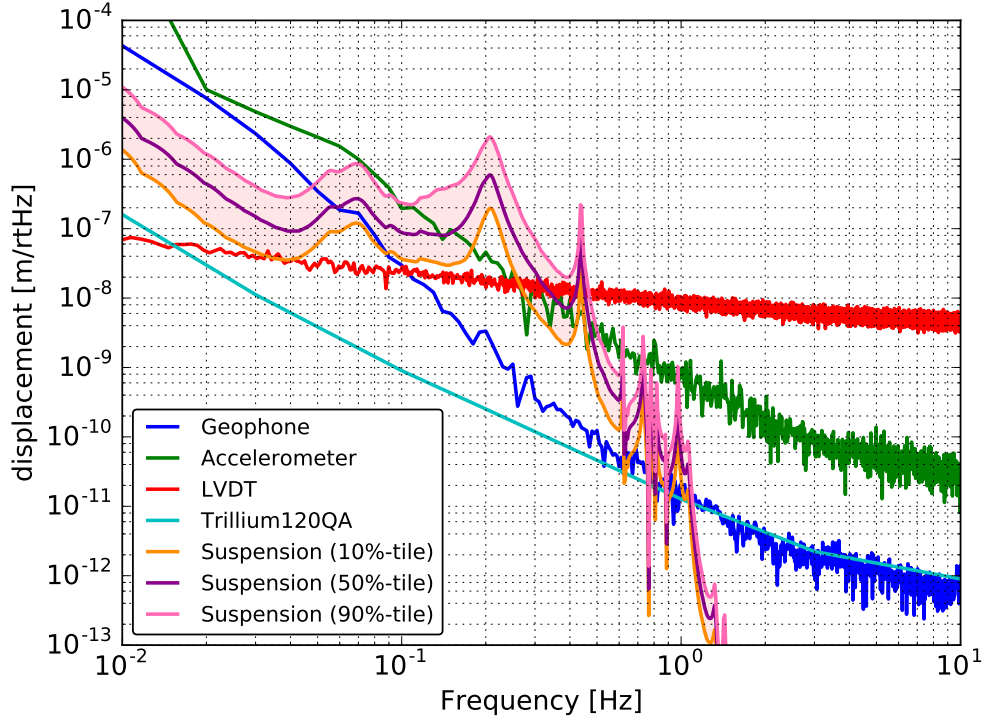
Figure 7.28: The typical noise floors of the inertial sensors used for current Type-A SAS, compared to the expected mirror displacement due to the seismic noise. The curves labeled as suspension represents the expected mirror displacement without any controls. The pink and orange curves show the expected mirror displacement when the seismic noise level is high and low respectively.

Practically, it is more natural to have another system which compensates such longer-term drift of the suspensions. One option is to use the baseline signal[3] in DC, and to feedback to the IP-stage of the end test masses. We can compensate the long-term drift by moving the ETMX/Y along with the ITMX/Y respectively (as described in section 6.6.1).

In conclusion, the implemented IPsc suppresses the residual motion of the mirror and satisfies the requirement for the lock acquisition phase. In order to construct more stabilized control system at frequencies below 0.1 Hz (in the time scale of much longer than 1 minute), another displacement drift compensation system is necessary. One option is to build a control system using blended sensors at the IP-stage with good sensitivity inertial sensors. Another option is to feedback the baseline signal to the IP-stage of the end test masses. Building such drift compensation system is set as the future step after this thesis work.

---

[3]such as interferometer signal or stain meter signal along with the arms.

7.4.3 Mirror residual motion in other DoFs

As described in section 6.2.5, it is necessary to keep the mirror orientation for the purpose of the interferometer operation.

Figure 7.29 shows the spectra of mirror residual motion in Pitch and Yaw DoF, observed by the optical lever at the TM-stage. The spectrum of the TM-stage in L DoF measured by the length-oplev is included as a reference. The TM motion in L DoF is covered by the seismic motion and the spectrum does not show the TM motion. Instead the P and Y motion of the TM is measurable. The measured RMS angular motion in Pitch and Yaw DoF is 195 nrad and 170 nrad respectively. It is confirmed that the requirements for both the lock-acquisition phase and the observation phase are satisfied.

The RMS of Pitch motion is very close to the requirement for the observation phase. However, this measurement is done when the seismic motion level is quite high at around 50 mHz. Thus, in the usual case, the requirement is satisfied with more margin.

On the other hand, it is also important to keep the mirror position in the Transverse and Vertical DoFs. Since we do not have any sensors to measure the mirror motion in the Transverse and Vertical DoFs at the payload level, we estimate the RMS motion by using the sensors in the upper part of the suspension. If the suspension is calmed down, i.e, no resonances are excited, the RMS displacement will be limited by the upper part of the suspension. Thus the RMS of the IP-stage in the Transverse DoF and of the BF-body in the Vertical DoF can represent the upper limit of the RMS TM motion in the Transverse and Vertical DoF respectively.

Figure 7.30 (*left*) reports the spectra of the residual motion the IP-stage in the Transverse DoF measured by the geophones. The measured residual RMS displacement is 0.26 μm. Assuming that the RMS displacements in these plot is the ones of TM, the requirement is satisfied.

Figure 7.30 (*right*) shows the spectra of the BF-body in the Vertical DoF measured by the displacement sensor LVDT. Since the BF-LVDTs measure the displacement between the ground and the BF-body, this RMS displacement does not represent the RMS of the BF-body itself. In particular, below 0.1 Hz, it is expected that the BF-body moves as same as the ground. Thus we can estimate the RMS displacement of the BF-body by considering that the seismic motion represents the BF-body motion. Then the estimated RMS displacements is 0.21 μm in this measurement. According to this estimate, the requirement is satisfied.

For both the Transverse and Vertical case, the requirement on the RMS displacement will be satisfied even if the seismic motion level becomes terribly high. It will be satisfied even if the seismic noise is larger than 90 percentile level.
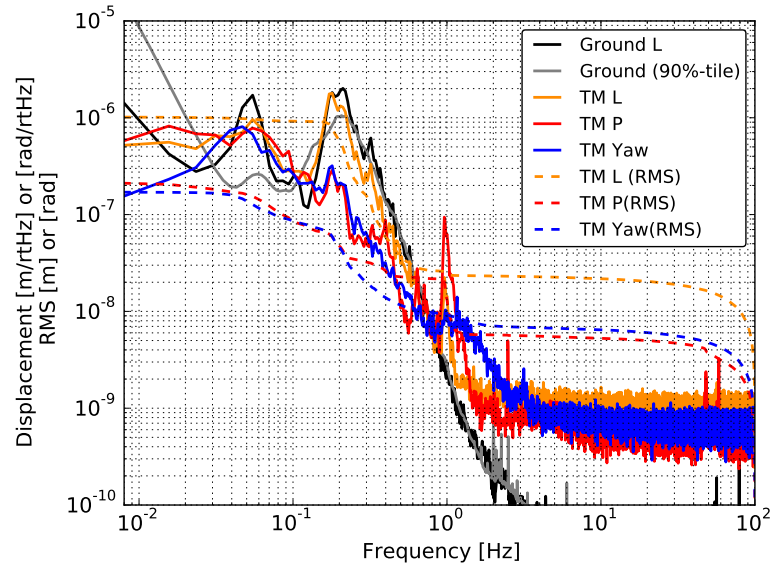
Figure 7.29: Spectra of mirror residual motion in L, Pitch and Yaw DoF, observed by the optical lever at the TM-stage. The solid curves show the amplitude spectral density and the dashed ones indicate the amplitude in RMS.
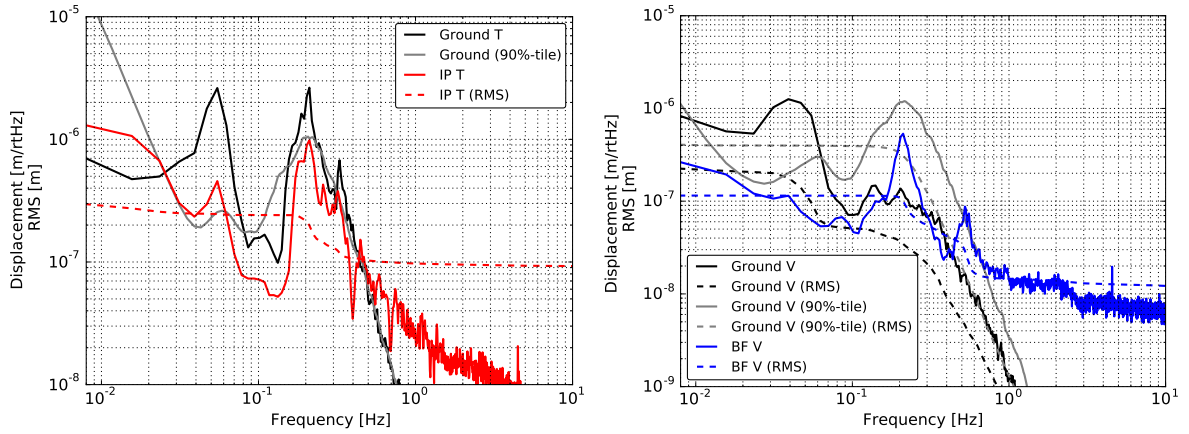

Figure 7.30: Spectra of residual motion the IP-stage in T DoF measured by the inertial sensor geophone (*left*) and that of the BF-body in V DoF measured by the displacement sensor LVDT (*right*). As a reference, the 90 percentile seismic motion level is included.

7.5 Overall frequency response measurement with interferometer

By using the implemented filters described in sections 7.3 and 7.4, the stable inteferometer lock is achieved with Fabry-Perot Michelson Interferometer (FPMI) configuration (see also section 1.3.2). We then measure the overall frequency response in L DoF of the Type-A suspension with FPMI at around a few Hz, which cannot be measured with the local sensors. The goal of this measurement is to check if the actual suspension has the performance expected from the design.

So far, the overall frequency response was measured in [41], however, the heat link vibration isolation system was not installed in that work. Thus this is the first time to measure the overall frequency response of the Type-A suspension with the full configuration.

7.5.1 Measurement set up

For this purpose, we measure the transfer functions from the actuator on the IP- and BF-stages to the mirror motion sensed with either the length-optical lever or the FPMI[4] with green and IR laser. Figure 7.31 shows the typical noise floor of the FPMI with green and IR laser.

For measuring the overall frequency response, we can measure either the displacement transfer function from a sensor to a sensor, or force transfer function from an excitation to a sensor. We select the force transfer function for this measurement. This is so since we use the LVDT for this measurement and since it was observed that the direct coupling between the LVDT signal and the actuator becomes dominant at frequencies above a few Hz when the same-stage actuators are driven, as shown in Figure 7.5a for example.

For the lower frequency part (< 1 Hz), white noise is injected to the upper stages and then the length-optical lever is used as the sensor. On the other hand, for the higher frequency part (> 1 Hz), a sinusoidal noise is injected and the FPMI is used as the sensor. In the sinusoidal noise injection measurement, the length-optical lever signal is also measured as a reference.

During the measurement with the local optical lever, all the local controls are off in order to get the open loop mechanical response.

---

[4]The difference of the wave length of the laser corresponds to the difference of the sensitivity of the sensors (interferometers). During this measurement, the ETMY is globally controlled for keeping its lock.
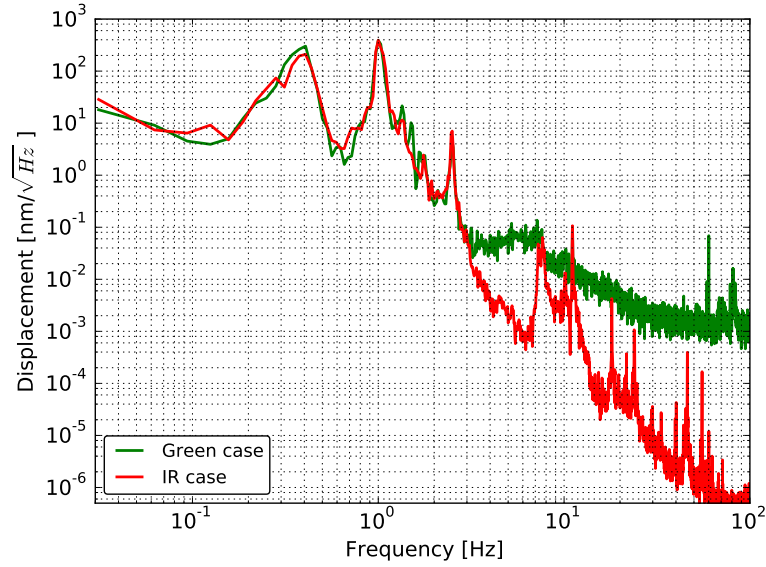
Figure 7.31: typical noise floor of the FPMI with green and IR laser during the measurement.

On the other hand, during the measurement with the FPMI, some of the loops which do not disturb the measurement are kept closed. This is necessary in order to avoid the mirror angular drift especially in yaw DoF, since otherwise we cannot keep the locked condition of the interferometer. For this purpose, during the FPMI measurement, all the payload controls are opened, however, the controls for each GAS stage, BF-stage in Yaw DoF and IP-stage in T and Yaw DoF are kept closed. The details about these filters are summarized in section 7.3.1. These loops are kept closed since the controlled DoF is different from the target L DoF, and the coupling levels are not large.

In addition to this, a DC-control filter for the longitudinal DoF at IP-stage whose unity gain frequency is lower than about 0.3 Hz is closed. The LVDTs are used for this loops. This is done since otherwise the lock of the FPMI is easily lost in the timescale of a few minutes, which is not enough for this measurement, due to the drift. It is also possible to do so since the measurement with FPMI focuses on the frequency only higher than 1Hz.

The open loop transfer function used for the IP-stage in L DoF is shown in Figure 7.32. Since the seismic motion enhanced the residual motion in the period when the measurement by FPMI with IR laser was conducted, the filter shape is changed so that the filter can also damp the 0.2 Hz mode.
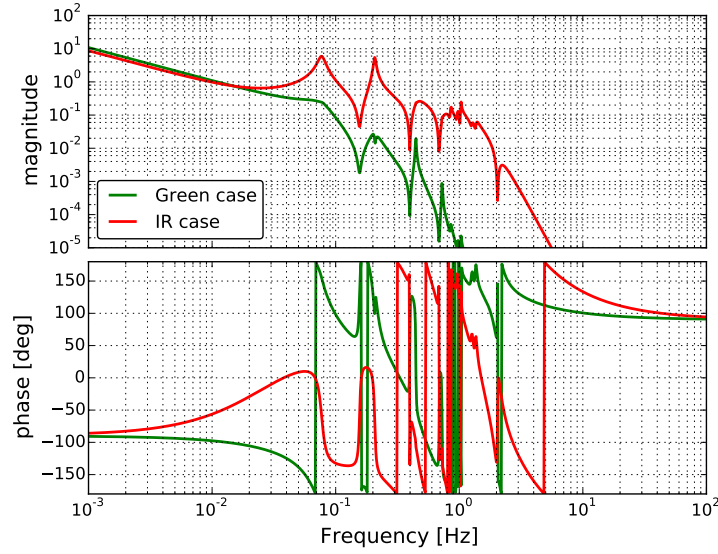
Figure 7.32: The used open loop transfer function used for the IP-stage in L DoF.

7.5.2 Overall frequency response

The measured force transfer functions when the IP- and BF-stage is excited in L DoF are shown in Figures 7.33 and 7.34 respectively.

The response at frequency below 1.1 Hz and 1.8 Hz is measured by the length-optical lever with white noise injection for IP- and BF-stage excitation respectively. The response above those frequencies is measured by both the length-optical lever and FPMI with one sinusoidal signal injection. For the measurement with sinusoidal injection, we selected the measurements whose coherence is higher than 0.7. The FPMI measurement fails above 1.4 Hz for IP-stage excitation and 4.2 Hz for the BF-stage excitation since the induced mirror displacement becomes comparable to the FPMI noise level.

Figure 7.33 indicates that except the IP-excited measurement in the frequency band between 1.1 Hz to 1.4 Hz, the model used in section 7.2, can explain the actual suspension response in both excitation cases, except for the Q factors of the lowest and the second lowest resonances. As shown in Figure 7.33, in the frequency band between 1.1 Hz to 1.4 Hz, there is no agreement among the model, the measurement by length-optical lever and that by FPMI, even though the slopes are mostly consistent. This could come from the coupling with the other DoFs. For the more details, further investigation will be necessary.

On the other hand, in the Figure 7.34 case, the actual system agrees with the model up to 4.2 Hz. At frequencies higher than 3 Hz, the coupling from the other DoFs becomes dominant in the length-optical lever signal as shown in Figure 7.34. According to the coherence in Figure 7.34, this is not due to just

249

noise but the coupling from the other DoFs. The detailed investigation is future work.

In summary, this measurement would imply that even though the actual system might not have the designed mechanical response in the the frequency band between 1.1 Hz to 1.4 Hz[5], the vibration isolation performance is as good as expected at 4.2 Hz.
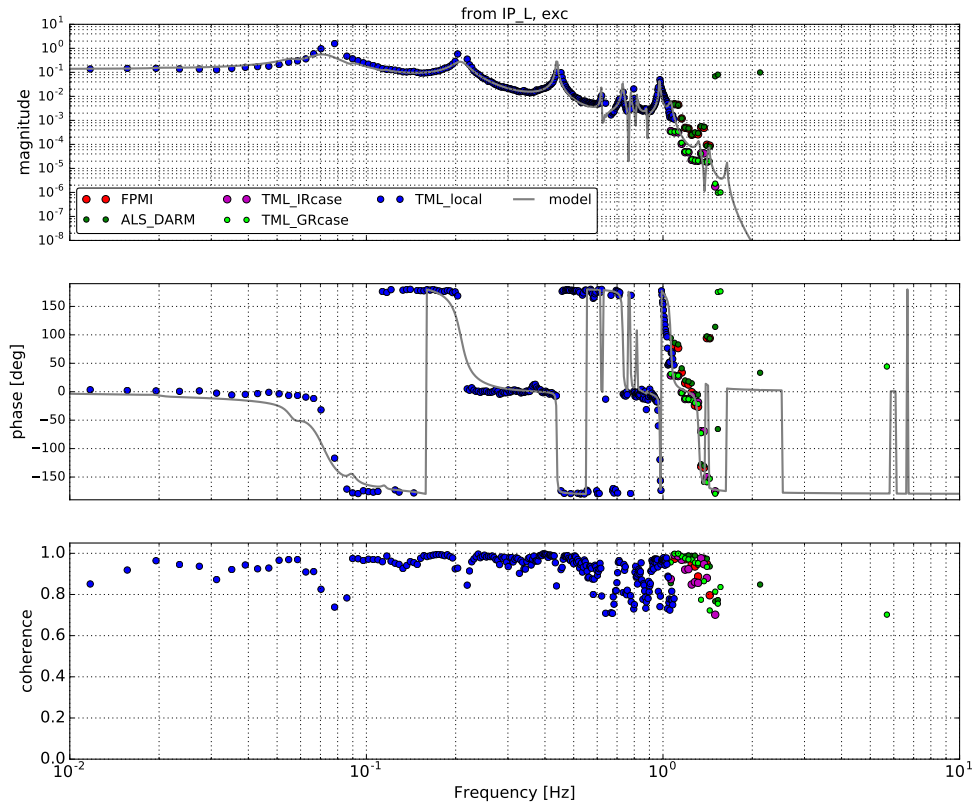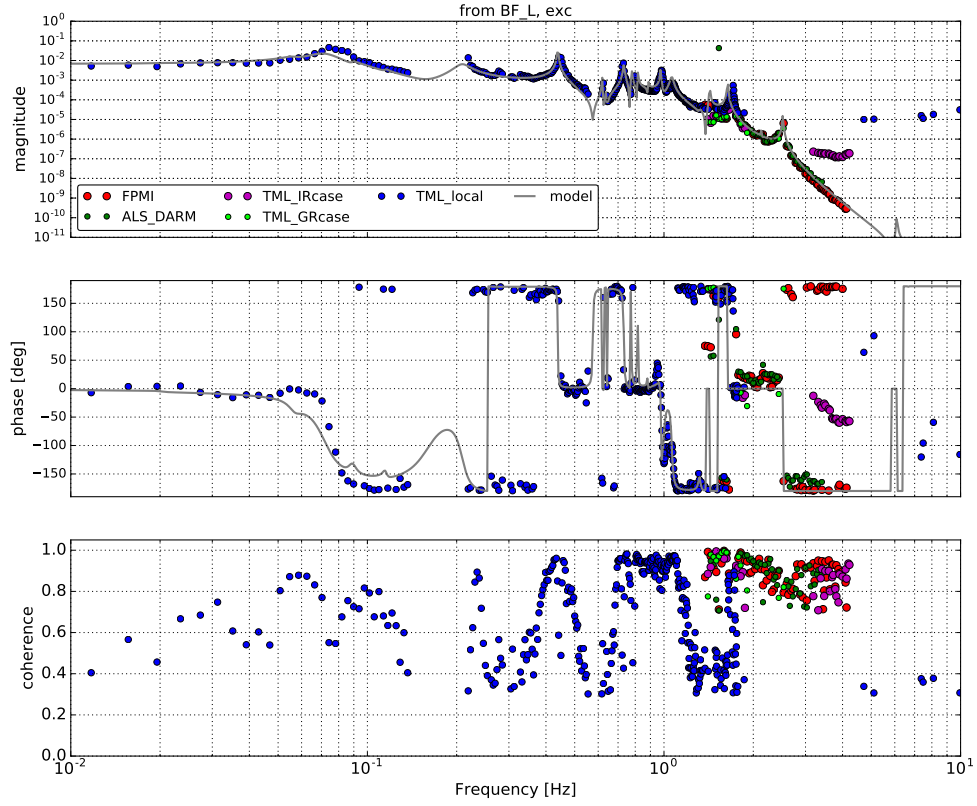

Figure 7.33: Measured force transfer functions from the IP-stage excitation in L DoF. The grey colored curves show the prediction of the model used in section 7.2. The blue dots represents the measurement with the length-optical lever and with white noise injection. The other colored dots show the results by sinusoidal noise injection. The green and red dots are obtained from FPMI while the magenta and lime dots are the measurements by the length-optical lever when the FPMI measurements are conducted.

---

[5]Assuming that the discrepancy does not comes from the coupling from the other degree of freedoms

Figure 7.34: Measured force transfer functions from the BF-stage excitation (*b*) in L DoF. The grey colored curves show the prediction of the model used in section 7.2. The blue dots represents the measurement with the length-optical lever and with white noise injection. The other colored dots show the results by sinusoidal noise injection. The green and red dots are obtained from FPMI while the magenta and lime dots are the measurements by the length-optical lever when the FPMI measurements are conducted.

7.6 Summary

Using the methods and the measurements described above, we have constructed the active control system for the Type-A suspension that allows to lock the KAGRA interferometer. More concretely, in order to evaluate the performance of the suspension and its control system, in this work we have conducted measurements about the following topics:

1. suspension mechanical frequency response,

2. damping control performance for the calm-down phase,

3. suppression of the TM RMS motion for the lock-acquisition phase,

4. overall suspension frequency response.

From the first measurement, we conclude that the assembled Type-A suspension has the characteristics of the pendulum, although some unexpected resonances related to the heat link system are observed. From this issue, we find that we have to include the heat link system in the model of the suspension mechanics for future development.

From the second measurement, we confirm that the damping control system developed during this work satisfies its requirement for the lock-recovery mode.

The third measurement demonstrates a feed-forward system using seismometer on the ground to improve the performance of the damping control. This solution effectively suppresses the mirror residual motion and satisfies the requirement for the lock-acquisition phase.

The forth measurement shows that even if the actual system might not have the designed mechanical response in the frequency band between 1.1 Hz to 1.4 Hz, the vibration isolation performance is as good as expected at 4.2 Hz. this is the first time to measure the overall frequency response of the Type-A suspension with the full configuration. The performance at higher frequencies will be measured in the future.

From the first three results, we can conclude that the implemented control system satisfies the requirements for both the calm-down phase and the lock-acquisition phase. The measured performance is summarized in Table 7.4.

The implemented system also satisfies the RMS requirements in the observation phase. However, it is expected that some of the implemented servo filters in this thesis work need to be modified or turned off during the observation phase in order to achieve the required control noise level at 10 Hz (as described in section 6.7). This work will be the subject of a future development.

In conclusion, it is confirmed that the control system which allows to lock the interferometer has been constructed.

Without this control system the suspension resonances would not allow to achieve the operation of the interferometer. Sometimes we had to wait a few ten minutes at each locking trial when the resonances were excited. In addition, even though the resonances were calmed down after waiting a long time, the interferometer lock was lost due to the large coupling from the seismic motion to the mirrors when the ground motion level is high.

In this thesis work we have damped the mechanical resonances disturbing the locking within 1 min (in terms of $1/e$ decay time). We have also reduced the seismic noise coupling to achieve robust interferometer operation. Consequently this thesis work largely contribute to the KAGRA interferometer locking and its robust operation. This is also the first time to control the full Type-A suspension system.

Table 7.4: Requirements on the Type-A suspension control and the achieved results. The column labeled as ref. describes the section which explains the reason of the requirements.

Items	Requirements	Achieved results	ref.
The calm-down phase			
$1/e$ decay time	< 1 min.	< 59 sec.	§ 7.3.2
RMS displacement (T, V)	< 1 mm	(0.26 μm, 0.21 μm)	§ 7.4.3
The lock acquisition phase			
RMS velocity (L)	< 2.0 μm/sec.	0.14 μm/s	§ 7.4.2
RMS angle (P, Y)	< 880 nrad	(195 nrad, 170 nrad)	§ 7.4.3
RMS displacement (L)	< 0.39 μm	0.23 μm	§ 7.4.2
RMS displacement (T)	< 1 mm	0.26 μm	§ 7.4.3
RMS displacement (V)	< 39 μm	0.21 μm	§ 7.4.3
The observation phase			
Control noise at 10 Hz (L)	$< 8.0 \times 10^{-20}$ m/$\sqrt{\text{Hz}}$	not measured	
RMS displacement (L)	< 0.39 μm	0.23 μm	§ 7.4.2
RMS displacement (T)	< 1 mm	0.26 μm	§ 7.4.3
RMS displacement (V)	< 39 μm	0.21 μm	§ 7.4.3
RMS angle (P, Y)	< 200 nrad	(195 nrad, 170 nrad)	§ 7.4.3
DC angle Drift (P, Y)	< 400 nrad/h	not measured	

Chapter 8

Conclusion and future works

8.1 Conclusion

8.1.1 Fast localization with heterogeneous detector network

We investigate the expected performance regarding fast sky localization of co-alescing binaries with a network of three or four GW detectors having hetero-geneous sensitivities, such as the LIGO-Virgo, LIGO-KAGRA and LIGO-Virgo-KAGRA network by using a hierarchical search. In the hierarchical approach, the presence of an event seen in coincidence in the two more sensitive detectors triggers a focused search in the data of the third (and fourth), less sensitive, detector(s) with a lower SNR threshold. In this work, we show the expected fast localization performance for GWs from CBC when a hierarchical search is implemented into a GW-EM follow-up pipeline using MBTA and Bayestar.

We confirm that the hierarchical search improves both the localization accu-racy and precision compared to those achieved by a double coincidence search with the two LIGO detectors alone with low-latency analysis pipeline.

The hierarchical network effectively improves the localization accuracy and precision when threshold SNR for the lower sensitivity detector is set to around 3.5 provided that the BNS range of that the detector is greater than 20% of the more sensitive detectors in the case where the detector network is composed of the two LIGO detectors and the Virgo detector. As the sensitivity of Virgo approaches half of the LIGO one, the accuracy and precision of the localization can be improved by about a factor of 7.

In the case where the detector network is composed of the two LIGO detectors and the KAGRA detector, we find a clear sky localization improvement when the relative sensitivity of KAGRA becomes greater than 28% of the more sensitive detectors. As the sensitivity of KAGRA approaches half of the LIGO one, the accuracy and precision of the localization can be improved by about a factor of 3.5.

In addition, the hierarchical network by four detectors improves the localiza-tion accuracy and precision when threshold SNR for the lowest sensitivity detector is set to around 3.5 provided that the BNS range of that the detector is greater than 28% of most sensitive detectors. This result assumes that the sensitivity of

the middle sensitive Virgo detector is half of the LIGO one. As the sensitivity of KAGRA approaches half of the LIGO one, the accuracy and precision of the localization can be improved by about a factor of 2 and 2.5 respectively, compared to LIGO-Virgo hierarchical network.

Consequently, we conclude that once the sensitivity of the third or fourth detector reaches the required one, the search with this hierarchical approach will be most useful when adding new, less sensitive detectors to the network, as they are undergoing commissioning.

8.1.2 Type-A local suspension control

In this work I have conducted the following tests for the evaluation of the suspension and its control system:

1. suspension mechanical response,

2. damping control performance for the calm-down phase,

3. RMS suppression control performance for the lock-acquisition phase.

From the first test, it is confirmed that the assembled Type-A suspension has the characteristics of the pendulum. It is also confirmed that it is possible to realize a local control system achieving the required performances. However, some unexpected resonances related to the heat link system are observed. It is found that we have to include the heat link system in the model of the suspension mechanics for further more precise simulation.

From the second test, it is confirmed that the installed damping control system satisfies the requirement for the lock-recovery mode. We damp all the mechanical resonances disturbing the lock acquisition, within 1 min. as $1/e$ decay time. This is the most important requirement in the calm-down phase.

From the third test, it is confirmed that the feedback control system using displacement sensors by a feed-forward system with seismometer on the ground effectively suppressed the mirror residual motion. It is also confirmed that this system satisfies the requirement on the residual mirror motion. This is the most difficult requirement in the lock-acquisition phase.

Consequently, I have realized the local control system for the Type-A suspension to allow interferometer locking.

In conclusion, including the first part about the fast localization in heterogeneous network, through this research I have contributed to the KAGRA joining to the network as the fourth detector.

8.2 Future works

8.2.1 Type-A local suspension control

Mechanical suspension characterization

During this test we find that the model without the heat link system cannot fully explain the actual mechanical system, especially the BF motion in Y DoF. The most probable origin is the heat ink system. We have to include the heat link system in the model of the suspension mechanics for more precise studies.

In addition this work could not investigate the feature of the suspension system at frequencies above 4.2 Hz, where the heat link system can introduce external vibration from the inner shield of the cryostat. We have to confirm that the vibration induced by the actual heat link system satisfies the displacement requirement at 10 Hz.

Payload control

In order to improve the operation robustness, the use of more sensitive photo-sensors is demanded. The control system using the optical levers only is possible using the band-pass comb (BP-comb) filters. However since it takes time to tune and maintain the BP-comb filters. Indeed the filters are very sensitive to the target resonant frequency and the mechanical resonant frequencies can be shifted by the temperature change. More sensitive photo-sensors would help avoiding this issues.

Residual motion suppression control

In this work, a seismometer on the ground is used for the RMS suppression control. We observe that the residual displacement below 10 mHz is enhanced due to the seismometer noise at low frequencies. In order to avoid this, it will be interesting to have inertial sensors that are more sensitive enough below 100 mHz.

Long-term tidal compensation

The mirror displacement is suppressed locally with the sensor correction technique. However, the arm cavity drift due to the tidal deformation has to be compensated to keep the interferometer locked over long period. To do so it is possible to use the signal used to keep the interferometer locked. The compensation of the tidal deformation can then be realised by sending the interferometer correction signal to the IP-stage actuators to finely move the whole suspension.

Chapter A

Supplemental note for study of fast localization

A.1 Typical parameters for data analysis

Effective distance

The effective distance D_{eff} is the distance of an optimally located and oriented source that would produce the same signal strength. The distance D_{eff} is defined as

$$D_{\text{eff}} = \frac{R}{\sqrt{\frac{1}{4}F_+{}^2(1 + \cos^2 \iota)^2 + F_\times{}^2 \cos^2 \iota}}, \tag{A.1}$$

where R is the actual physical distance to the source, ι is the inclination angle of the source.

Horizontal distance

The horizontal distance R_{H} is the distance at which an optimally located and oriented source would produce a certain SNR ρ_0 in a detector. Usually, the ρ_0 is set at 8. The horizontal distance is defined by using sensitivity of a detector. Using an inner product is defined as:

$$(a|b) = 4Re\left[\int_0^\infty df \, \frac{\tilde{a}(f)\tilde{b}^*(f)}{S(|f|)}\right], \tag{A.2}$$

the SNR of the detector ρ for a given signal h is calculated by

$$\rho^2(t) = (h|h). \tag{A.3}$$

The corresponding detector sensitivity σ in dimension of length is expressed by

$$\sigma^2 = \rho^2 \times D_{\text{eff}}{}^2. \tag{A.4}$$

The signal amplitude ρ is proportional to the $D_{\text{eff}}{}^{-1}$. Then, the horizontal distance, which is described as the effective distance at the SNR $\rho_0 = 8$, is described by

$$R_{\text{H}} = D_{\text{eff}}(\rho = \rho_0) = \frac{\sigma}{\rho_0} = \frac{\sigma}{8}. \tag{A.5}$$

Detection range

The detection range R_{det} is the spherical radius, whose volume is equal to the volume surrounded by detection radius r_{det}. The detection radius r_{det} is the distance that the detector can sense the signals in each direction for an orientation of the source. The detection radius r_{det} is defined as

$$r_{\mathrm{det}} = R_{\mathrm{H}} \sqrt{\frac{1}{4}F_+{}^2(1 + \cos^2\iota)^2 + F_\times{}^2\cos^2\iota}, \tag{A.6}$$

where R_{H} is the horizontal distance. By using the detection radius r_{det}, the detection range R_{det} is obtained as follows.

$$
\begin{aligned}
R_{\mathrm{det}}(\iota, \psi) &= \left(\frac{3}{4\pi}V(\iota, \psi)\right)^{1/3} \\
&= \left(\frac{3}{4\pi}\int_0^{r_{\mathrm{det}}(\theta,\phi,\iota,\psi)} dr \int_0^\pi d\theta \int_0^{2\pi} d\phi \; r^2 \sin\theta\right)^{1/3} \\
&= \left(\frac{1}{4\pi}\int_0^\pi d\theta \int_0^{2\pi} d\phi \left(r_{\mathrm{det}}(\theta,\phi,\iota,\psi)\right)^3 \sin\theta\right)^{1/3}. \tag{A.7}
\end{aligned}
$$

Relation between Horizontal distance and detection range

Due to the directional sensitivity or antenna pattern of the detectors, the detection range R_{det} is smaller than the horizontal distance R_{H} by a factor of 2.26, for the same SNR threshold[47, 91]. Then the relation is given by

$$\frac{R_{\mathrm{H}}}{R_{\mathrm{det}}} = 2.26. \tag{A.8}$$

Expected SNR

The SNR of a detector is deduced from the detection range and the effective distance. By combining (A.4), (A.5), (A.8), the SNR ρ is given by

$$\rho = \frac{\sigma}{D_{\mathrm{eff}}} = \frac{\rho_0 \; R_{\mathrm{H}}}{D_{\mathrm{eff}}} = \frac{\rho_0 \; \times \; 2.26 \; \times R_{\mathrm{det}}}{D_{\mathrm{eff}}} = \frac{8 \; \times \; 2.26 \; \times R_{\mathrm{det}}}{D_{\mathrm{eff}}}. \tag{A.9}$$

A.2 Triggered event population

A.2.1 LIGO-Virgo network case

The population of the HL, HLV_i and HLV_n events are summarized in Figure A.1. In these plots, V_r denotes V_n triggers.

A.2.2 LIGO-KAGRA network case

The population of the HL, HLK_i and HLK_n events are summarized in Figure A.2. In these plots, K_r denotes K_n triggers.

A.2.3 LIGO-Virgo-KAGRA network case

The population of the HL, HLV_i, HLV_n, HLK_i, HLK_n, HLV_iK_i, HLV_nK_i, HLV_nK_i and HLV_nK_n events are summarized in Figure A.3 to A.8. In these plots, V_r and K_r denote V_n and K_n triggers respectively.
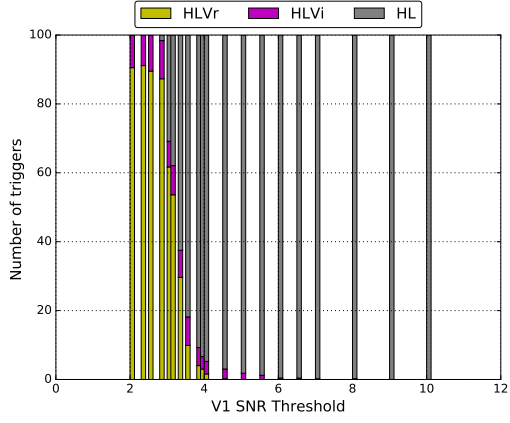
(a) HLV: 1-1-0.13 case
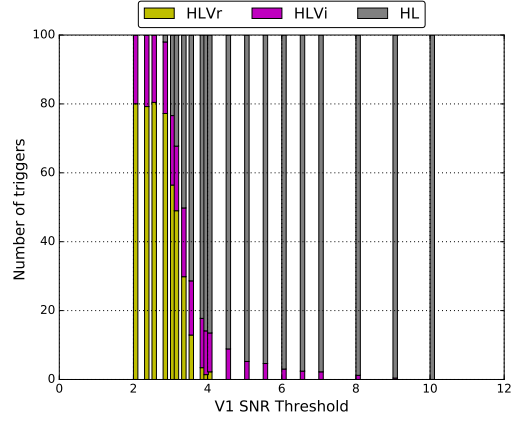
(b) HLV: 1-1-0.20 case
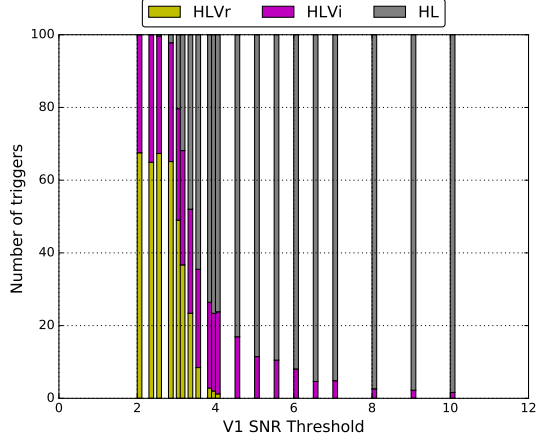
(c) HLV: 1-1-0.28 case
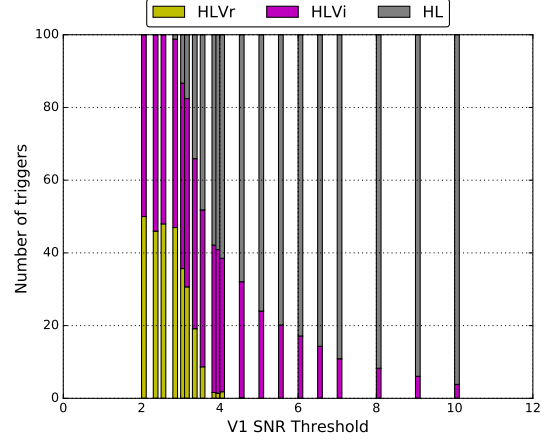
(d) HLV: 1-1-0.39 case
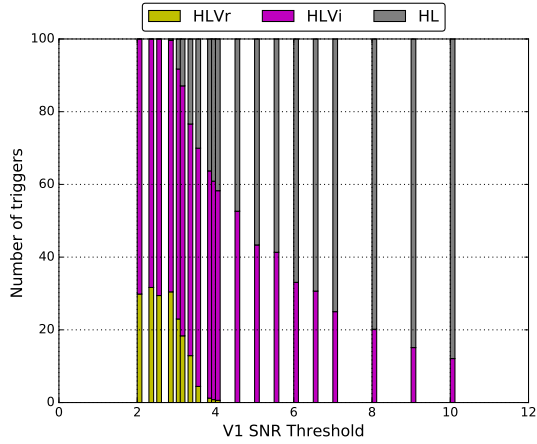
(e) HLV: 1-1-0.56 case

Figure A.1: The trigger population, HL, HLV_i and HLV_r events, in percentage with LIGO-Virgo network. The relative detector sensitivities are written down as 1-1-x, with x the ratio of the Virgo sensitivity compared to the two LIGO detectors.
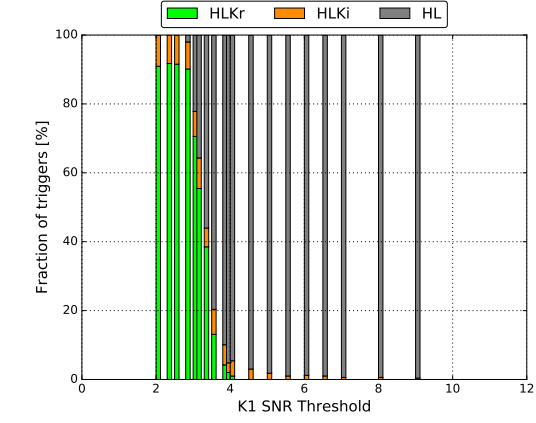
(a)   HLK: 1-1-0.13 case
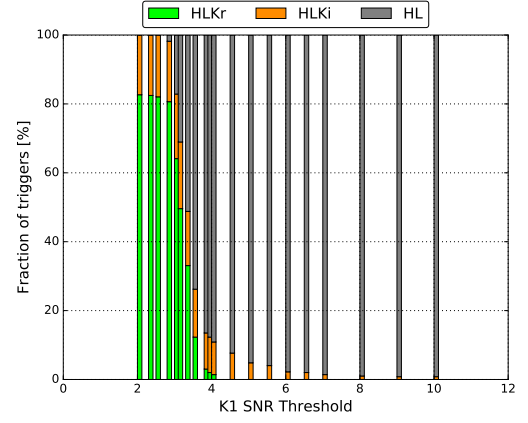
(b)   HLK: 1-1-0.20 case
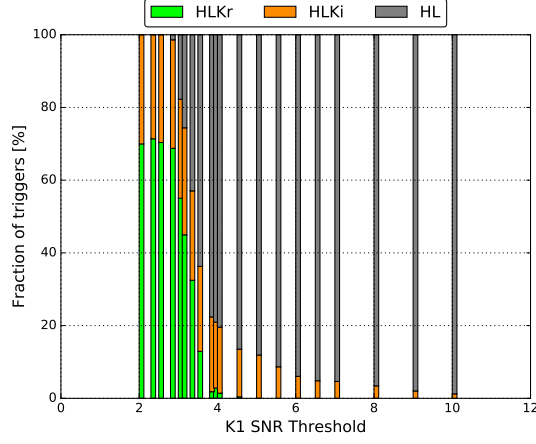
(c)   HLK: 1-1-0.28 case
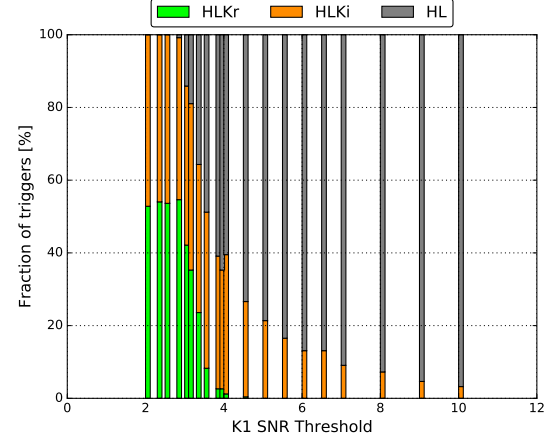
(d)   HLK: 1-1-0.39 case
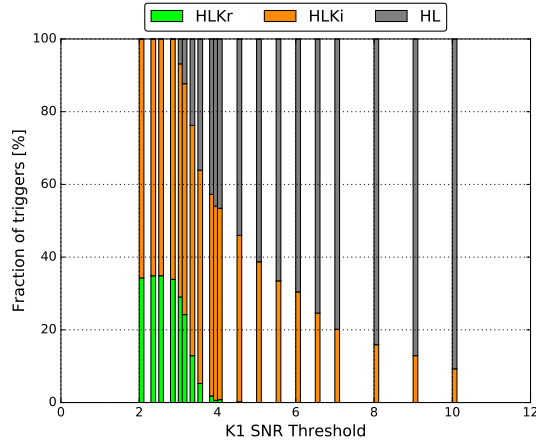
(e)   HLK: 1-1-0.56 case

Figure A.2:   The trigger population, HL, HLK_i and HLK_r events, in percentage with LIGO-KAGRA network. The relative detector sensitivities are written down as 1-1-x, with x the ratio of the KAGRA sensitivity compared to the two LIGO detectors.
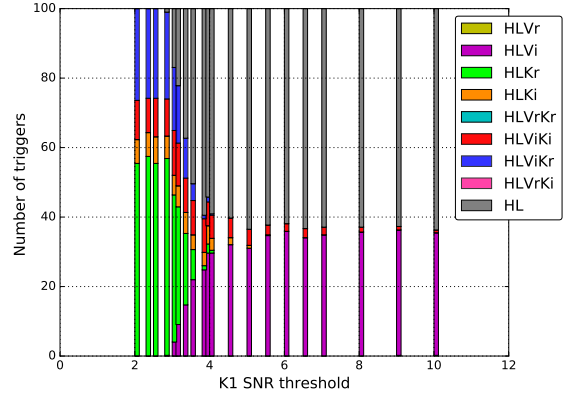
263
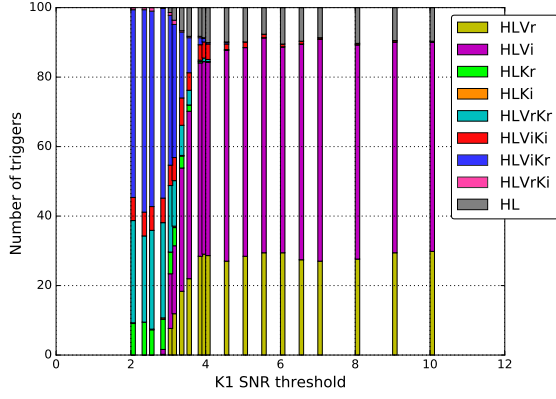
(a) SNR threshold for HLV: 5-5-3.0 case
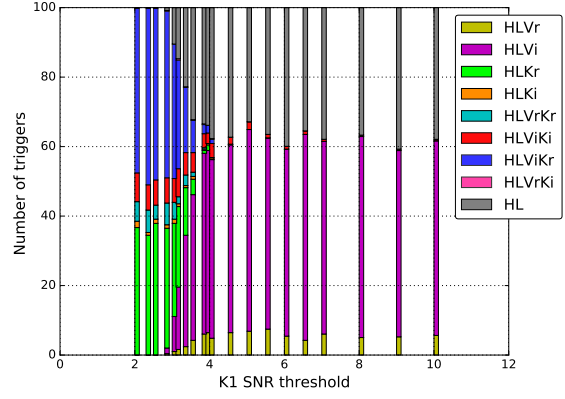
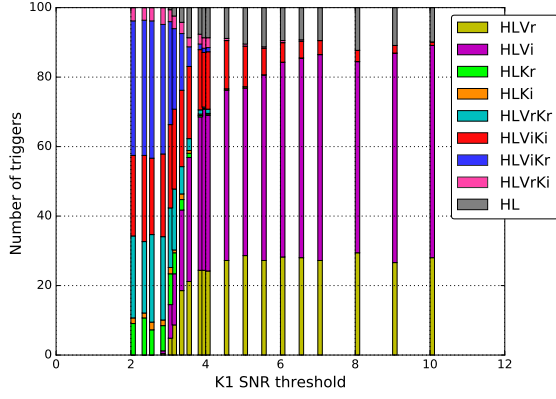(b) SNR threshold for HLV: 5-5-3.5 case
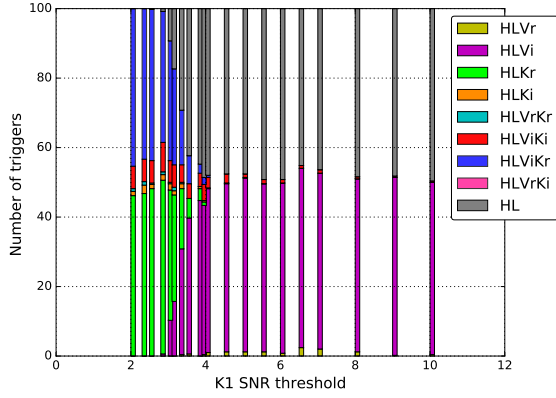
(c) SNR threshold for HLV: 5-5-4.0 case
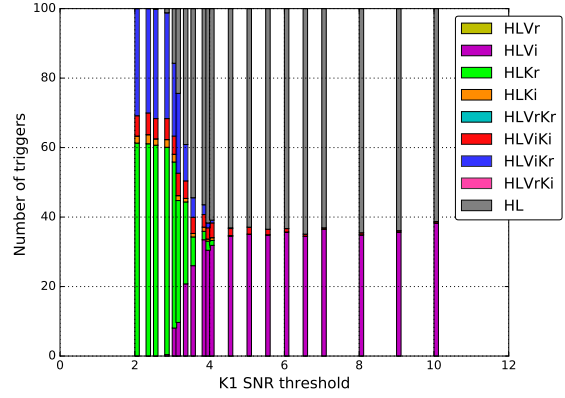
(d) SNR threshold for HLV: 5-5-5.0 case

Figure A.3: The trigger population in percentage with LIGO-Virgo-KAGRA network, where the relative detector sensitivities are set to HLVK: 1-1-0.5-0.13, with the ratio of the Virgo and KAGRA sensitivities compared to the two LIGO detectors.
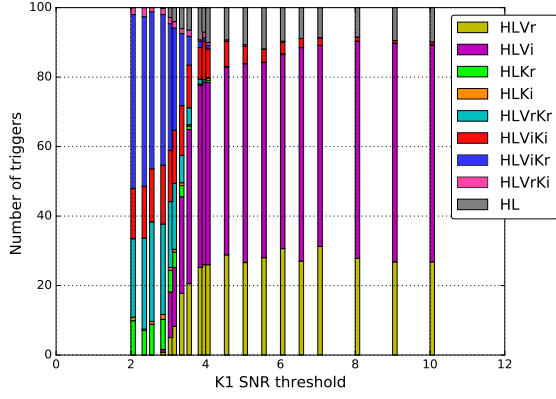
(a) SNR threshold for HLV: 5-5-3.0 case   (b) SNR threshold for HLV: 5-5-3.5 case
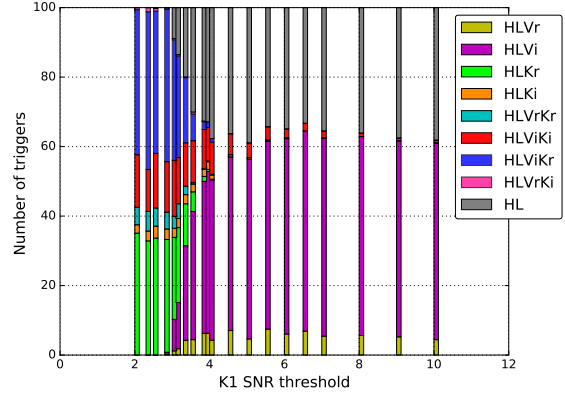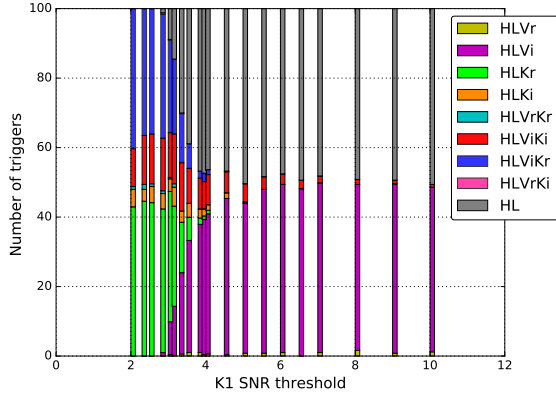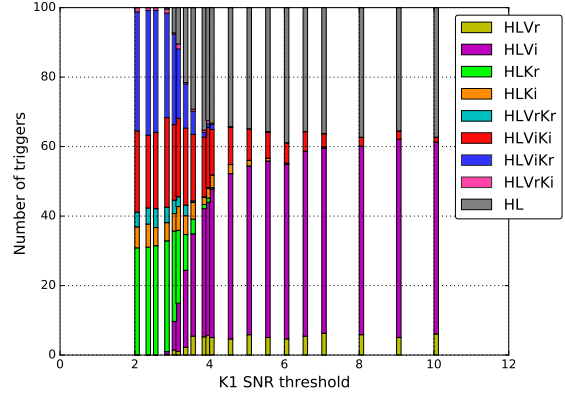
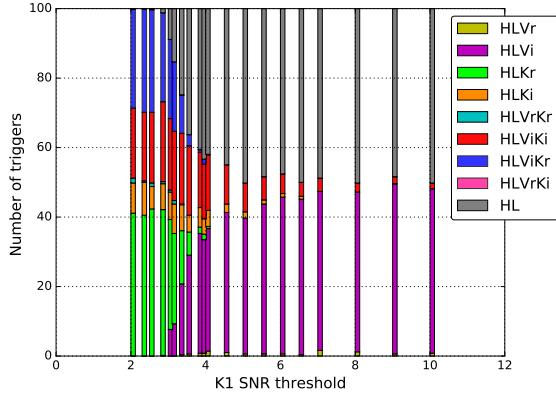(c) SNR threshold for HLV: 5-5-4.0 case   (d) SNR threshold for HLV: 5-5-5.0 case

Figure A.4: The trigger population in percentage with LIGO-Virgo-KAGRA network, where the relative detector sensitivities are set to HLVK: 1-1-0.5-0.20, with the ratio of the Virgo and KAGRA sensitivities compared to the two LIGO detectors.
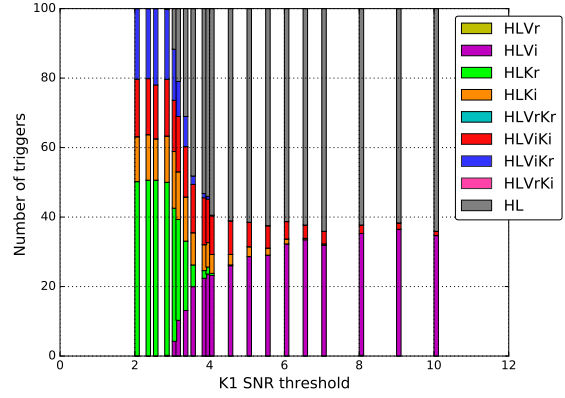
(a) SNR threshold for HLV: 5-5-3.0 case

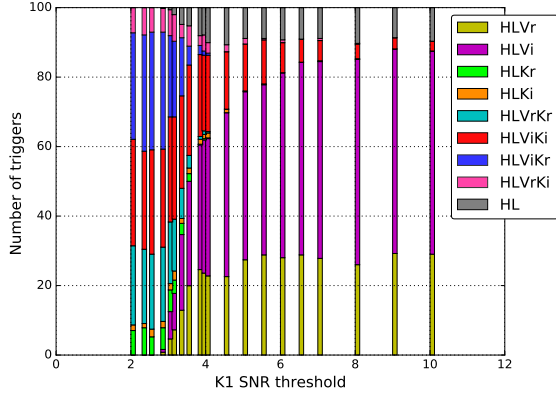(b) SNR threshold for HLV: 5-5-3.5 case

(c) SNR threshold for HLV: 5-5-4.0 case

(d) SNR threshold for HLV: 5-5-5.0 case

Figure A.5: The trigger population in percentage with LIGO-Virgo-KAGRA network, where the relative detector sensitivities are set to HLVK: 1-1-0.5-0.28, with the ratio of the Virgo and KAGRA sensitivities compared to the two LIGO detectors.

(a) SNR threshold for HLV: 5-5-3.0 case   (b) SNR threshold for HLV: 5-5-3.5 case

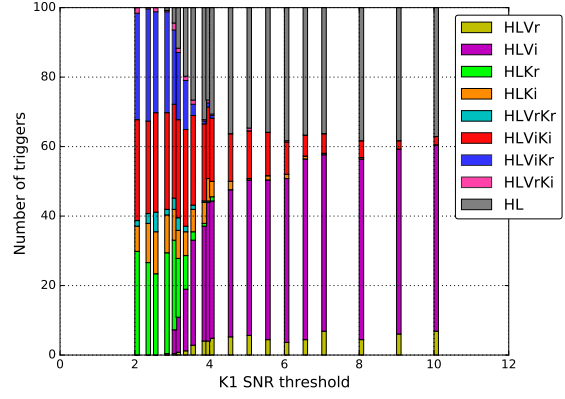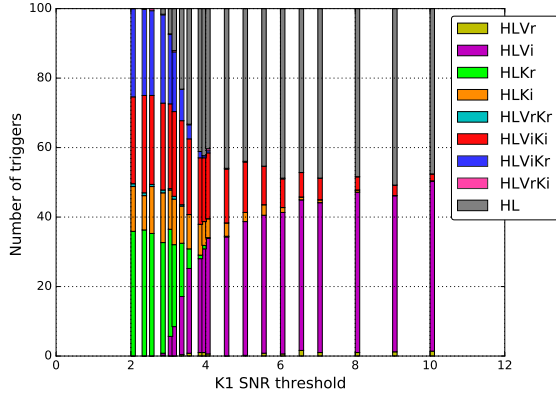(c) SNR threshold for HLV: 5-5-4.0 case   (d) SNR threshold for HLV: 5-5-5.0 case

Figure A.6:   The trigger population in percentage with LIGO-Virgo-KAGRA network, where the relative detector sensitivities are set to HLVK: 1-1-0.5-0.33, with the ratio of the Virgo and KAGRA sensitivities compared to the two LIGO detectors.

(a) SNR threshold for HLV: 5-5-3.0 case

(b) SNR threshold for HLV: 5-5-3.5 case

(c) SNR threshold for HLV: 5-5-4.0 case
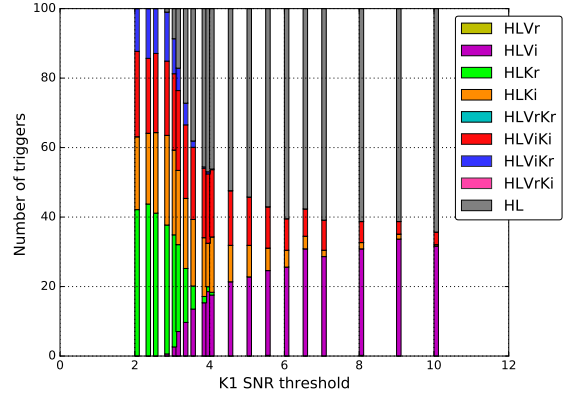
(d) SNR threshold for HLV: 5-5-5.0 case

Figure A.7: The trigger population in percentage with LIGO-Virgo-KAGRA network, where the relative detector sensitivities are set to HLVK: 1-1-0.5-0.39, with the ratio of the Virgo and KAGRA sensitivities compared to the two LIGO detectors.
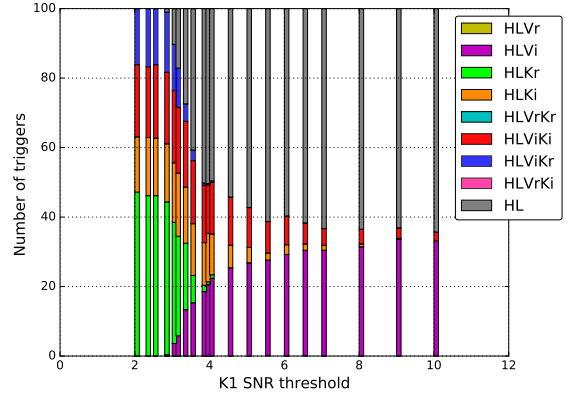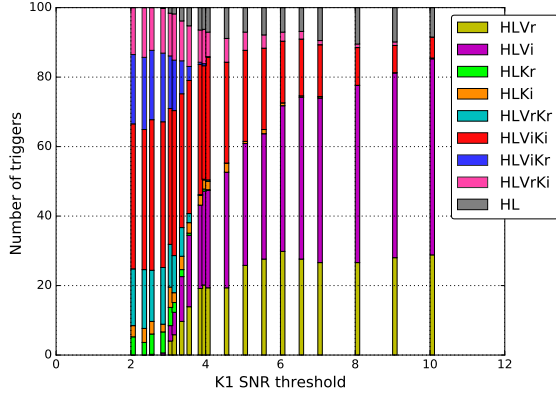
(a) SNR threshold for HLV: 5-5-3.0 case
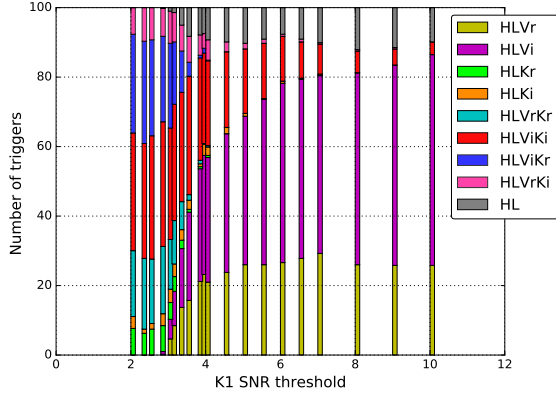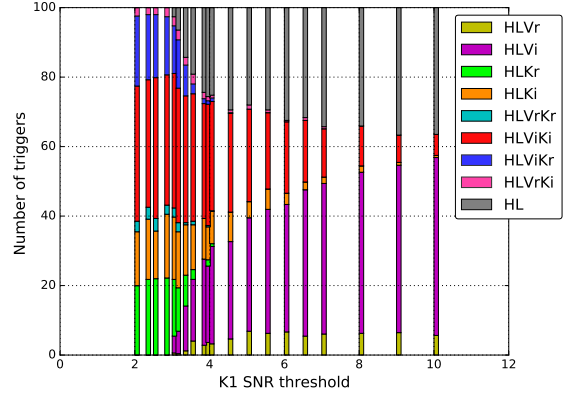
(b) SNR threshold for HLV: 5-5-3.5 case
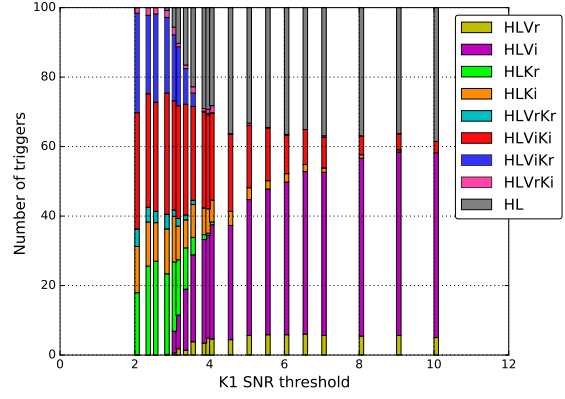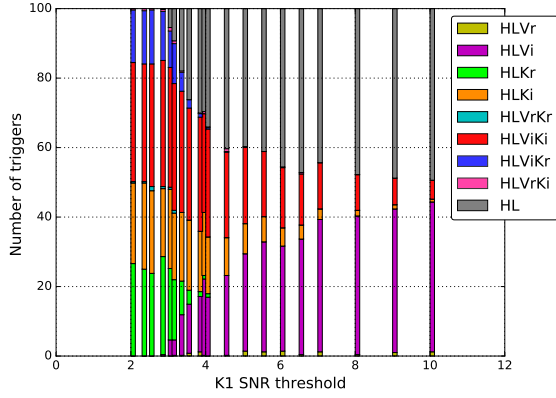
(c) SNR threshold for HLV: 5-5-4.0 case
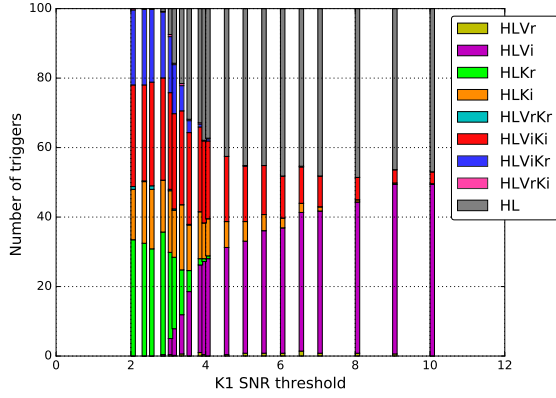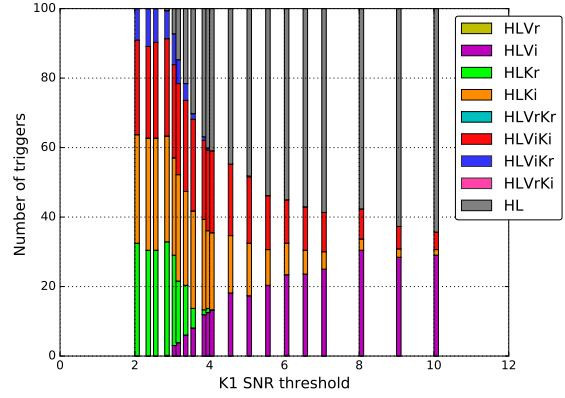
(d) SNR threshold for HLV: 5-5-5.0 case

Figure A.8: The trigger population in percentage with LIGO-Virgo-KAGRA network, where the relative detector sensitivities are set to HLVK: 1-1-0.5-0.5, with the ratio of the Virgo and KAGRA sensitivities compared to the two LIGO detectors.

A.3 Dependence on the sensitivity of the fourth detector KAGRA with different SNR thresholds in Virgo

The expected performances of the searched area and the 90% confidence area with different SNR thresholds in Virgo are summarized in this subsection. Figure A.9 and A.10 are the case where the SNR threshold for Virgo is set to 4.0, while Figure A.11 and A.12 are the case where it is set to 3.0.
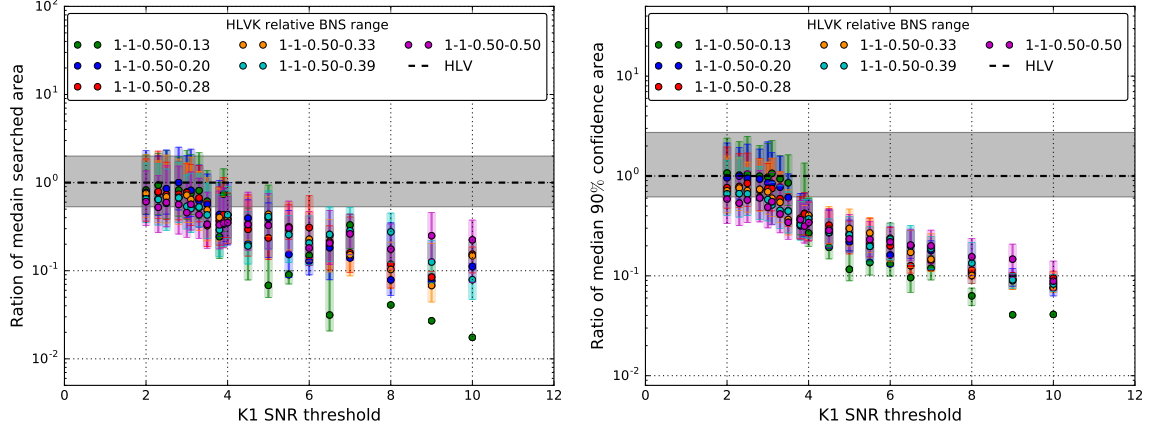
Figure A.9: Ratio of the median searched area (*left*) and 90% confidence area (*right*) of HLVK triggers to that of the same triggers treated as HLV coincidences, when the sensitivity of the KAGRA detector is varied. The colors show the network configuration. This is the case where the sub-threshold for Virgo is to 4.0.
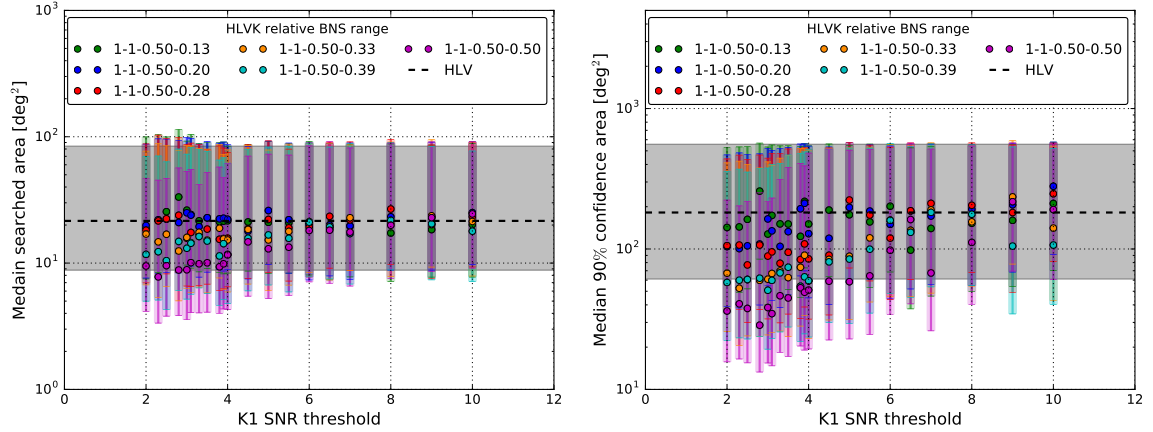
Figure A.10: The median searched area (*left*) and 90% confidence area (*right*) are shown as a function of the SNR threshold used in KAGRA. Expected sky localization performance with the hierarchical search when the sensitivity of the KAGRA detector is varied. The colors show the network configuration. This is the case where the sub-threshold for Virgo is to 4.0.

271
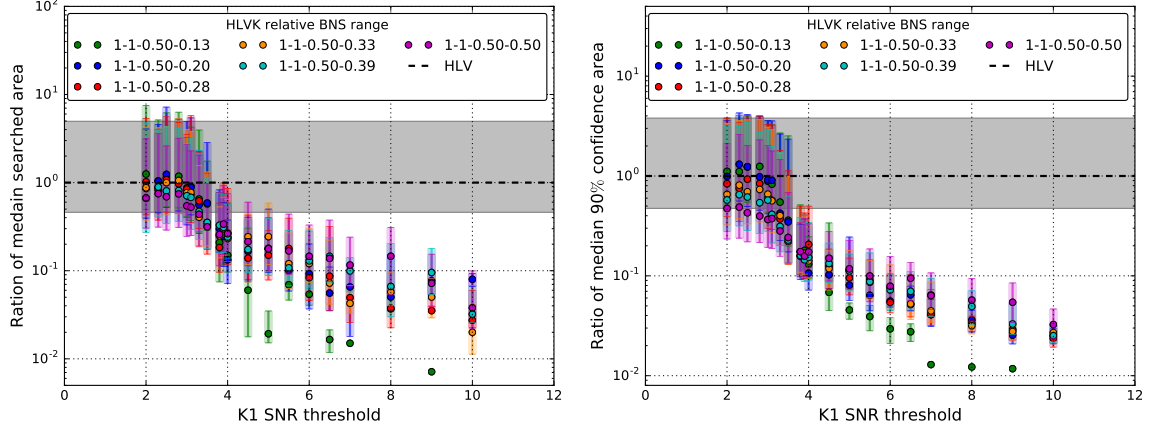
Figure A.11: Ratio of the median searched area (*left*) and 90% confidence area (*right*) of HLVK triggers to that of the same triggers treated as HLV coincidences, when the sensitivity of the KAGRA detector is varied. The colors show the network configuration. This is the case where the sub-threshold for Virgo is to 3.0.
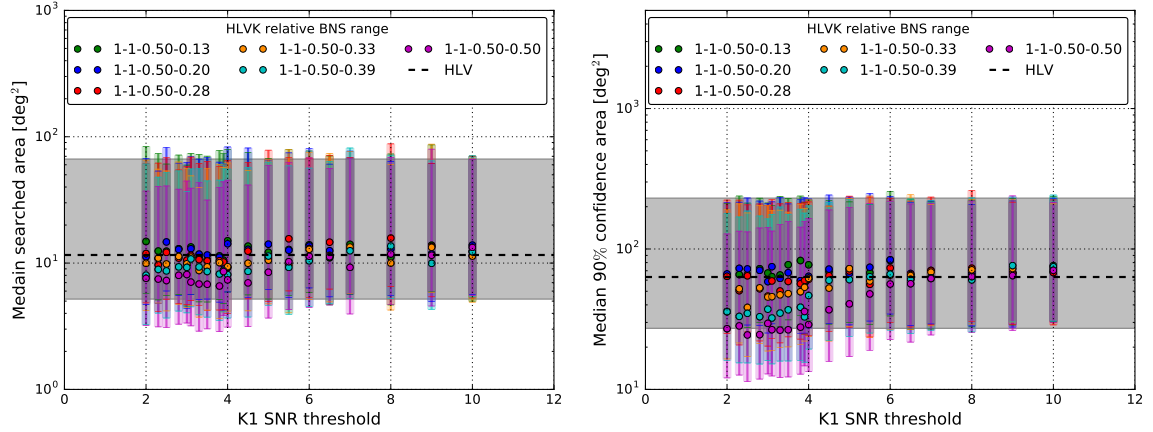
Figure A.12: The median searched area (*left*) and 90% confidence area (*right*) are shown as a function of the SNR threshold used in KAGRA. Expected sky localization performance with the hierarchical search when the sensitivity of the KAGRA detector is varied. The colors show the network configuration. This is the case where the sub-threshold for Virgo is to 3.0.

Chapter B

Detailed characteristics of Type-A suspension

B.1 Simulated eigen mode list of Type-A suspension

The eigen mode shapes of the designed Type-A suspension is listed here.

#25 0.694Hz More
#26 0.694Hz More
#27 0.701Hz More
#28 0.787Hz More
#29 0.799Hz More
#30 0.799Hz More
#31 0.817Hz More
#32 0.745Hz More

#33 0.746Hz More
#34 0.951Hz More
#35 0.972Hz More
#36 0.974Hz More
#37 1.061Hz More
#38 1.061Hz More
#39 1.171Hz More
#40 1.189Hz More

275

#73   **#74**   **#75**

150.563Hz More 151.723Hz 183.437Hz
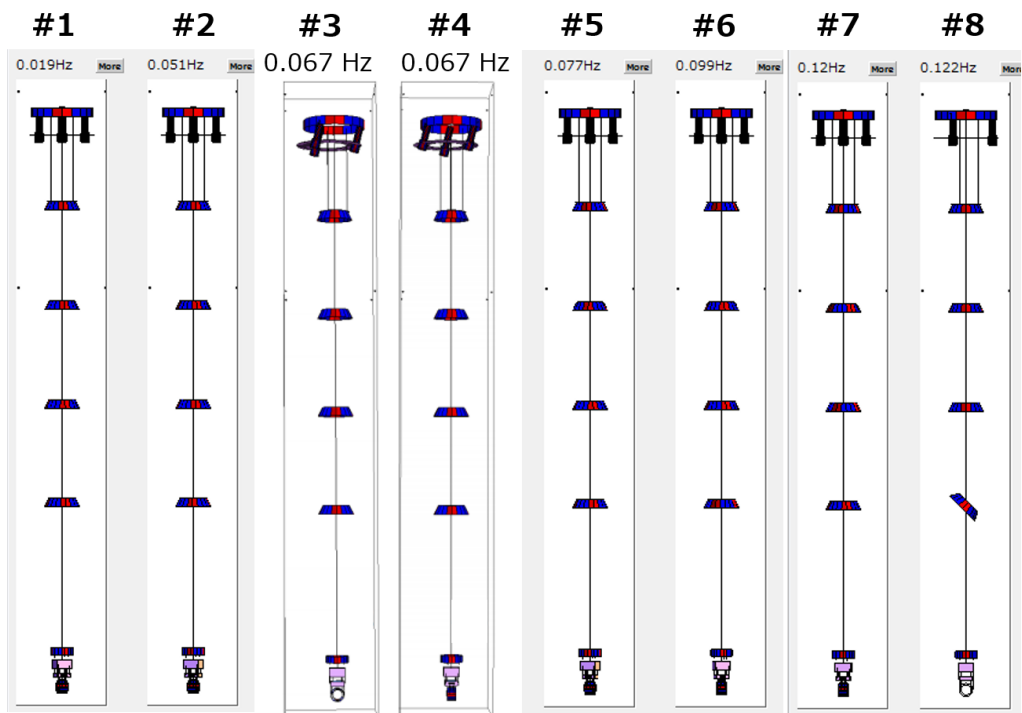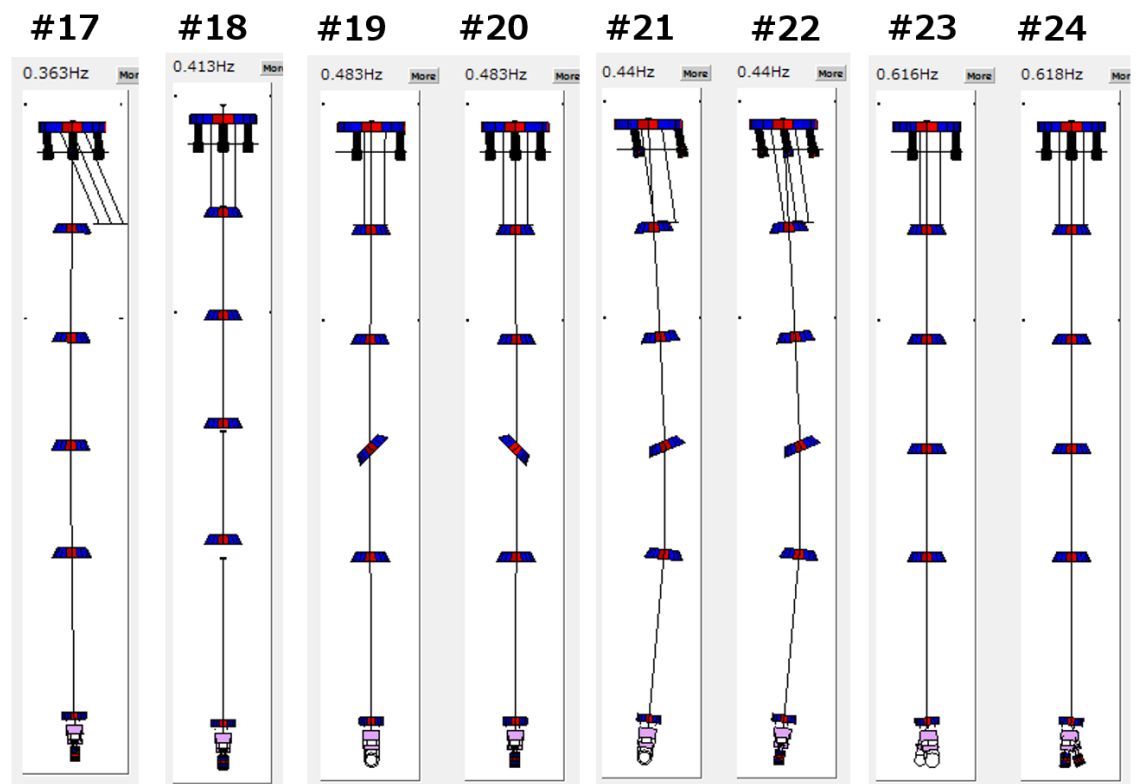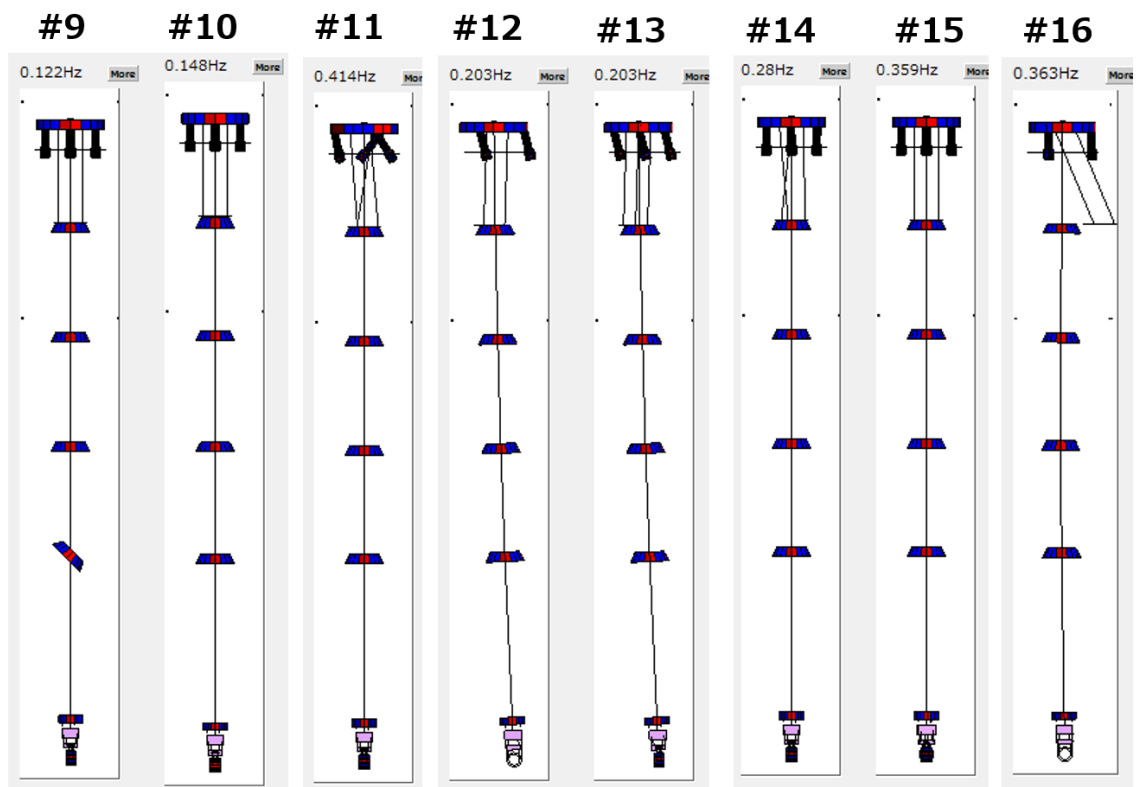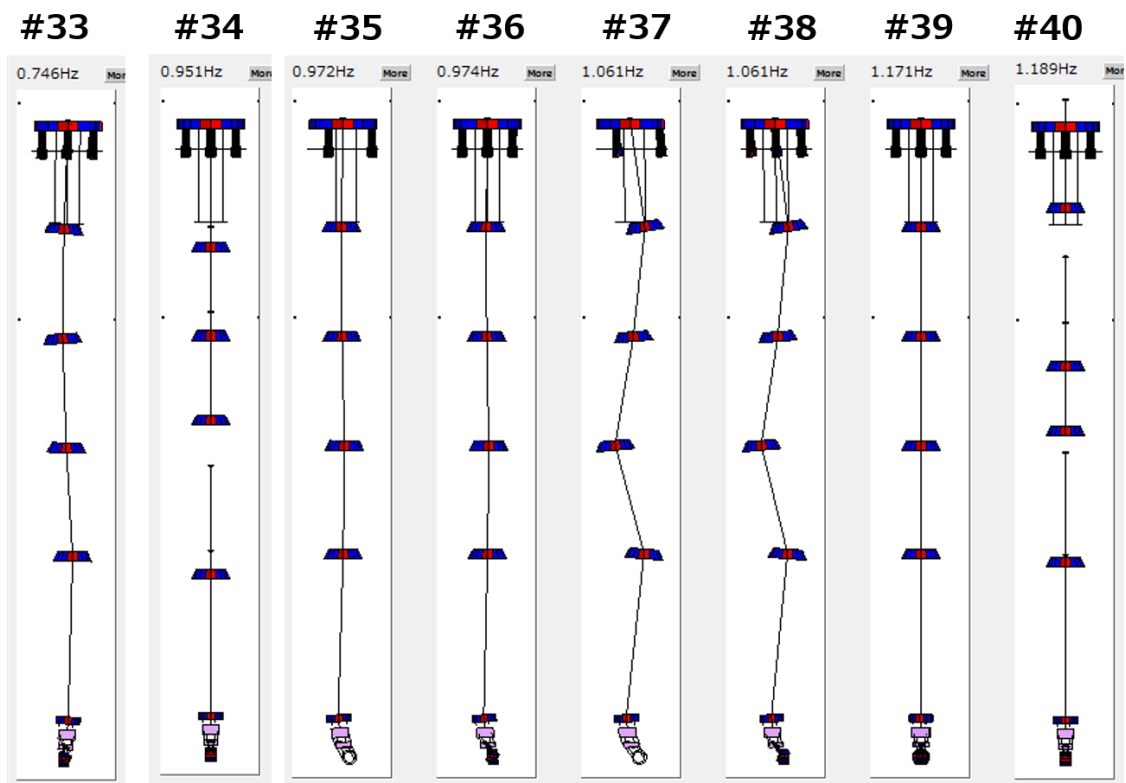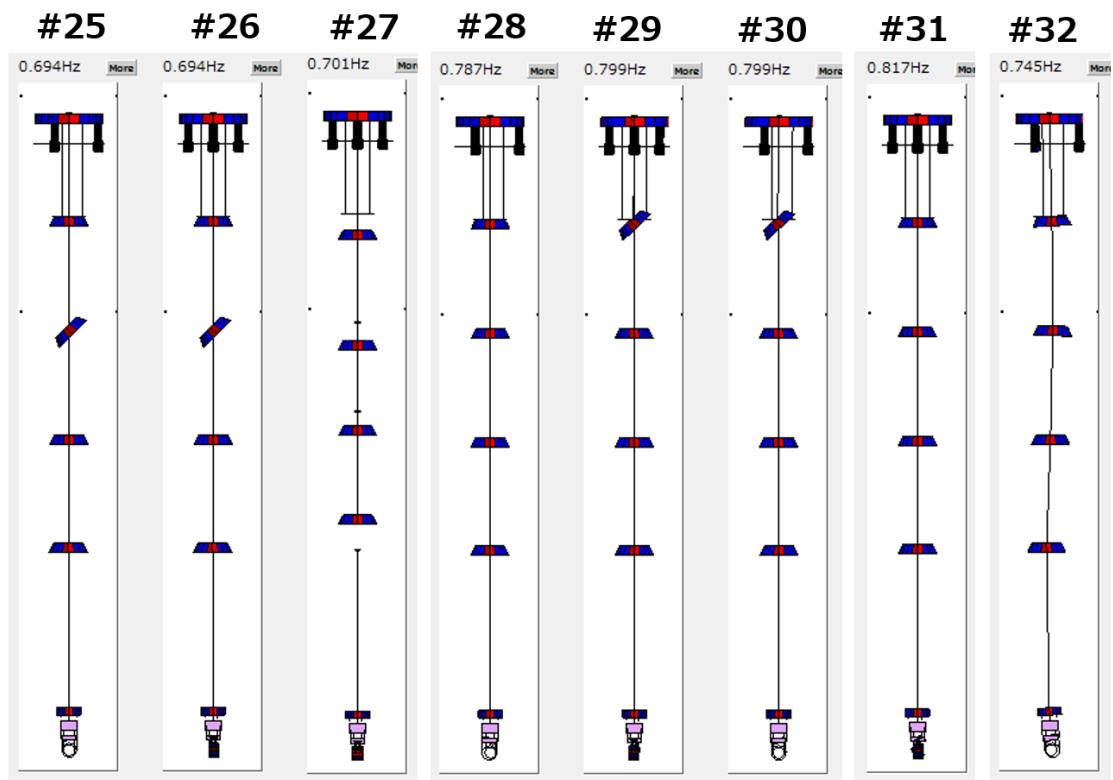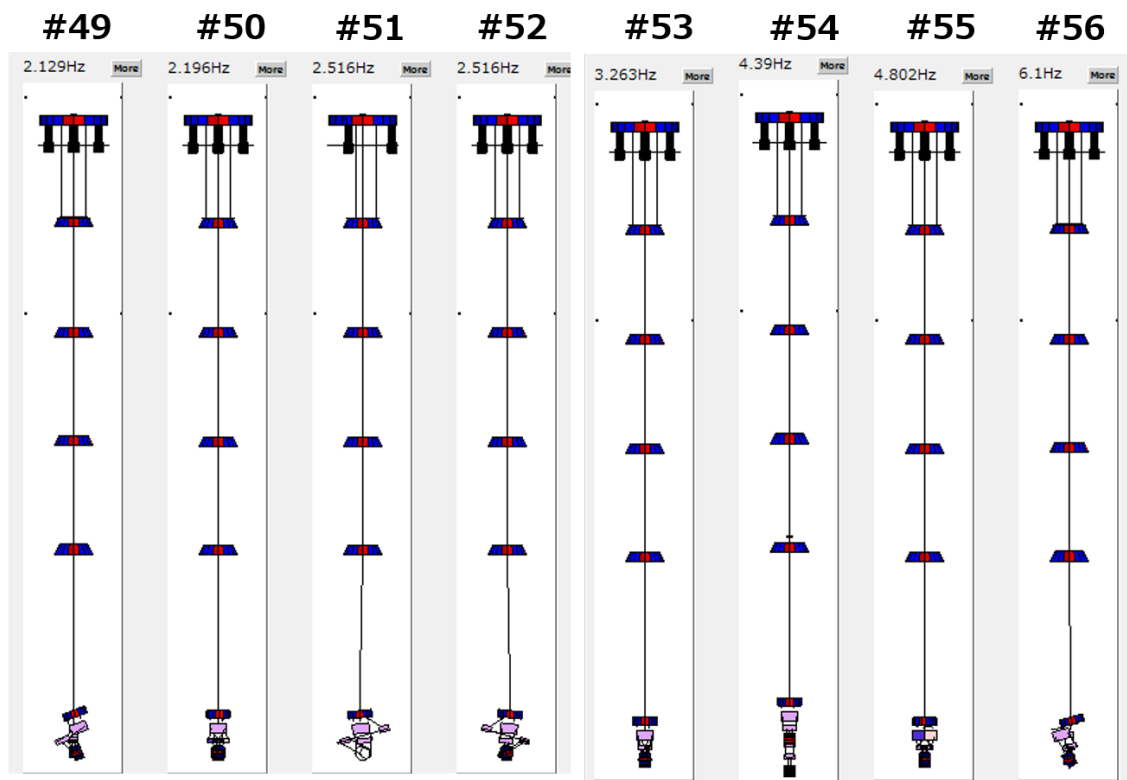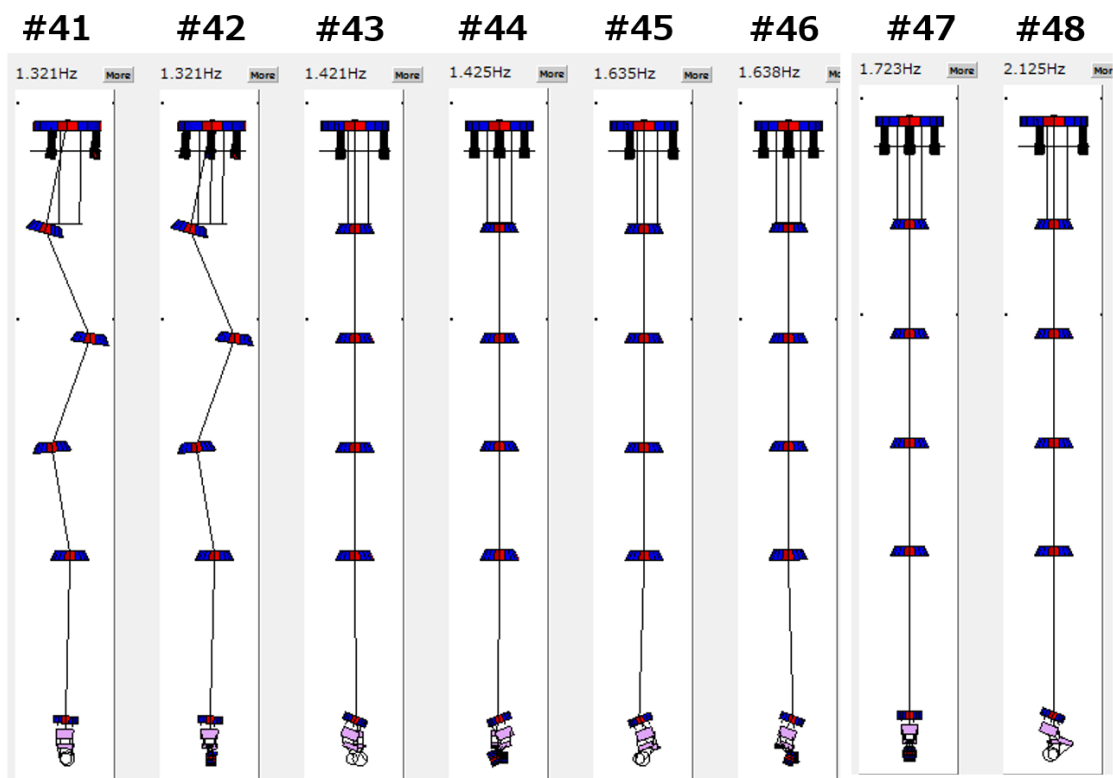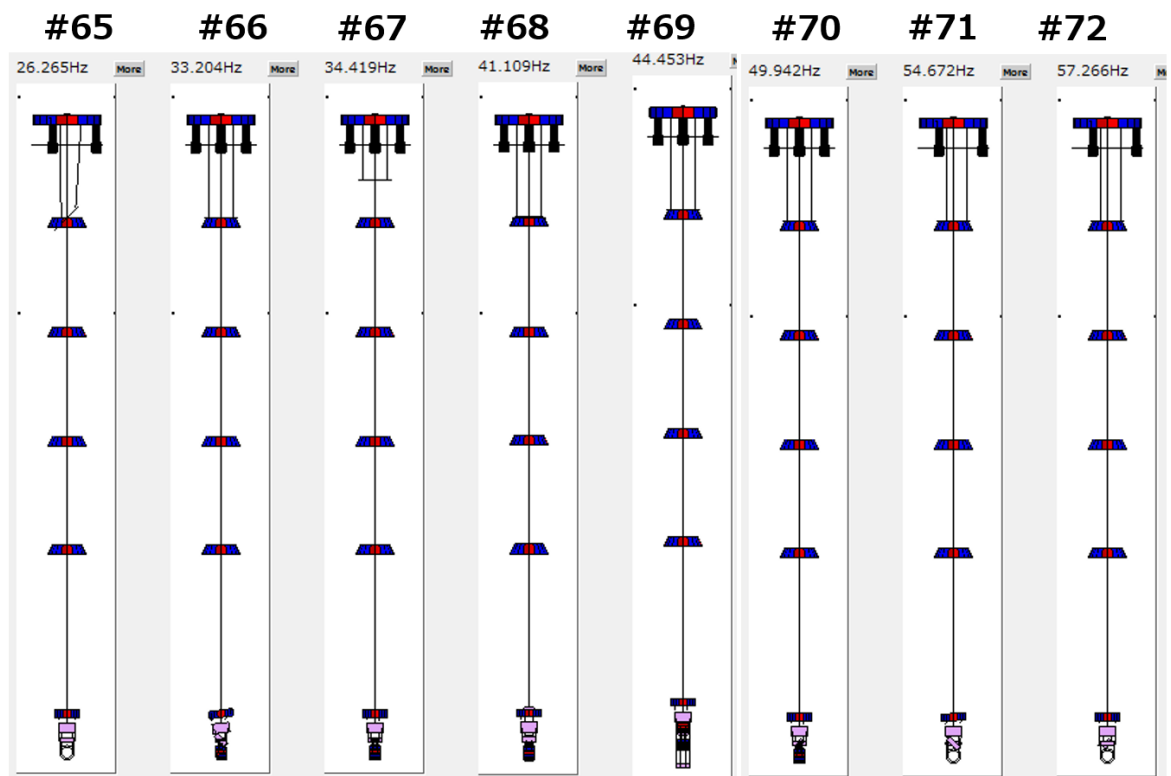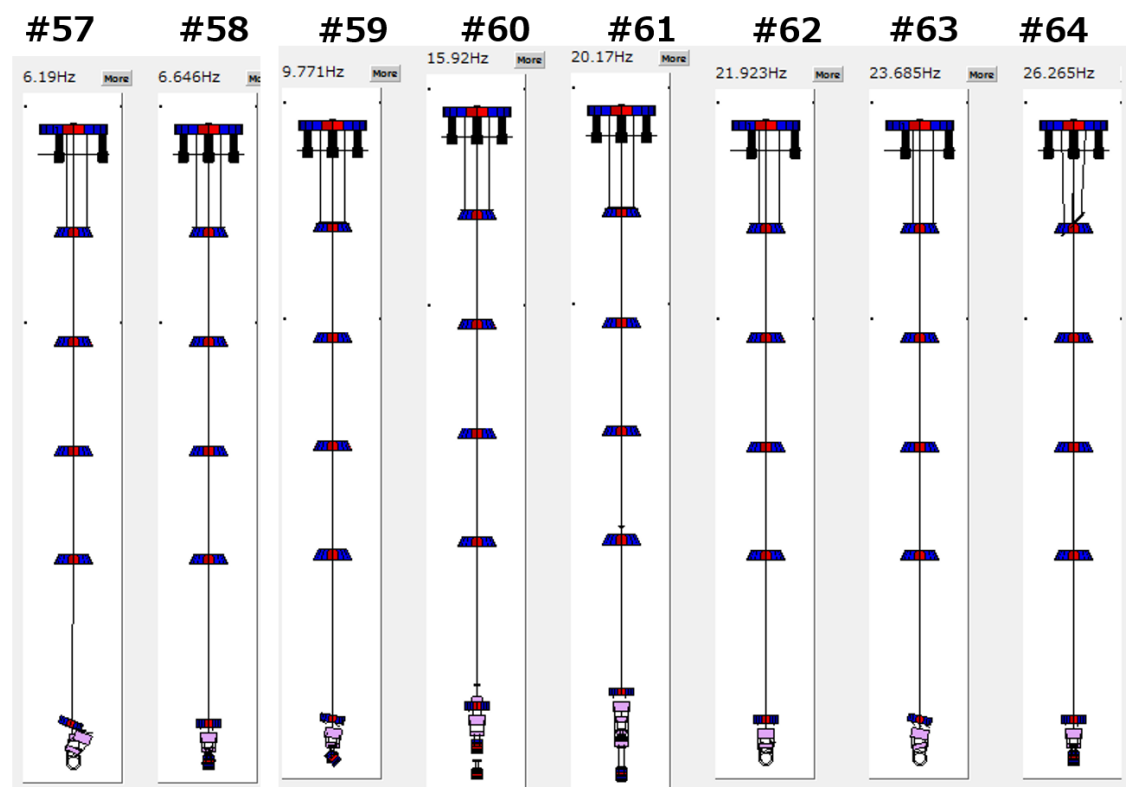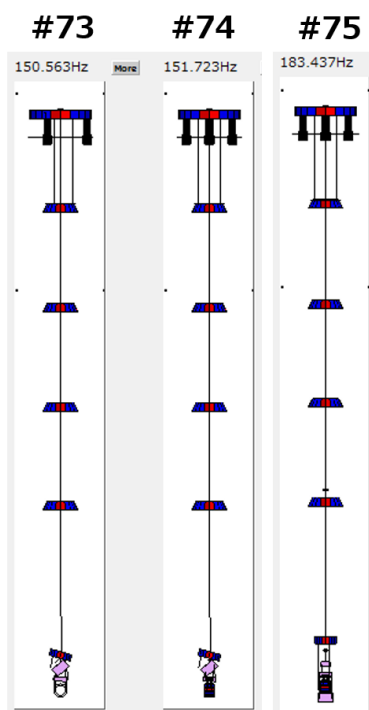
B.2 Type-A suspension configuration during the measurement

During the measurement period, we had to faced on a situation where at least on GAS filter is mechanically stack or locked in all the Type-A suspensions. Concerning ETMY suspension, we found that second and third GAS stages seemed to be mechanically stack with same reason as the issue of ETMX F2-GAS filter. For the two input suspensions, we had to intentionally lock the first GAS filter (called F0-GAS) keystone in order to hold the other suspension components, especially the mirror, at the target height[1]. For all these suspensions we decided to keep using them with such configuration for the O3 period. Figure B.7 shows the expected mechanical seismic attenuation performance where one or two GAS stage are not working as spring, assuming the vertical mirror vibration couples to the longitudinal DoF by 1%.
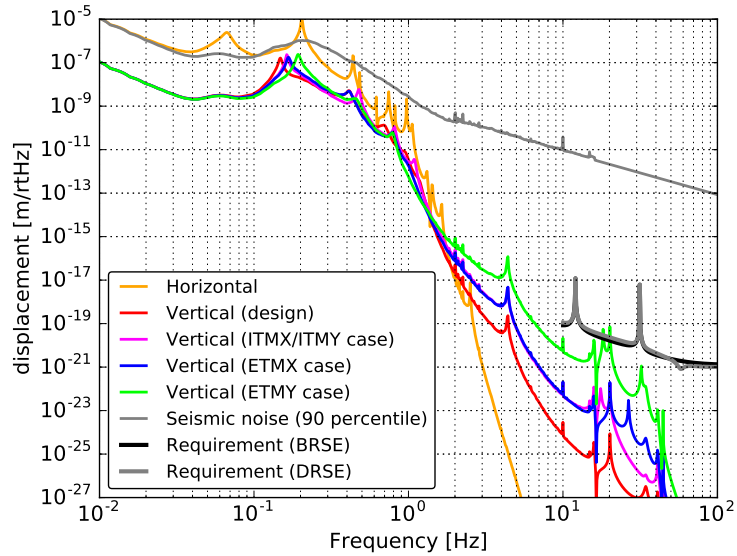
Figure B.7: Expected mechanical seismic attenuation performance where one or two GAS stage are not working as spring, assuming the vertical mirror vibration couples to the longitudinal DoF by 1%.

---

[1]This issue has the following history: we originally had GAS blades made in abroad which would suspend the mirror properly. We then found that the original blade was actually broken, cracked because of hydrogen embrittlement in Maraging steels [92]. We remade and replaced the blades with the new ones made in Japan, we finally found that the newly made GAS blades were too weak to hold the whole suspension at the desired height.

B.3 Position dependence of LVDT noise floor

The sensor noise floor of the LVDT at several point inside its linear range is measured as illustrated in Figure B.8 and B.9. This reports that of the primary coil is much close to the secondary one (at the edge of the linear range), the noise floor can be enhanced by factor of 10 in the current system.
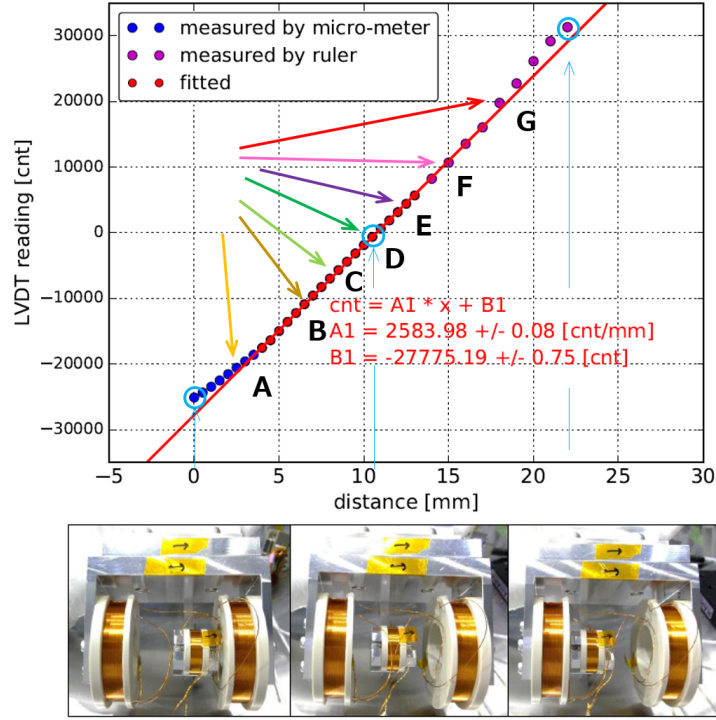
Figure B.8: A LVDT calibration curve. he noise floor is measured at the points which are denoted by the alphabets from A to B.
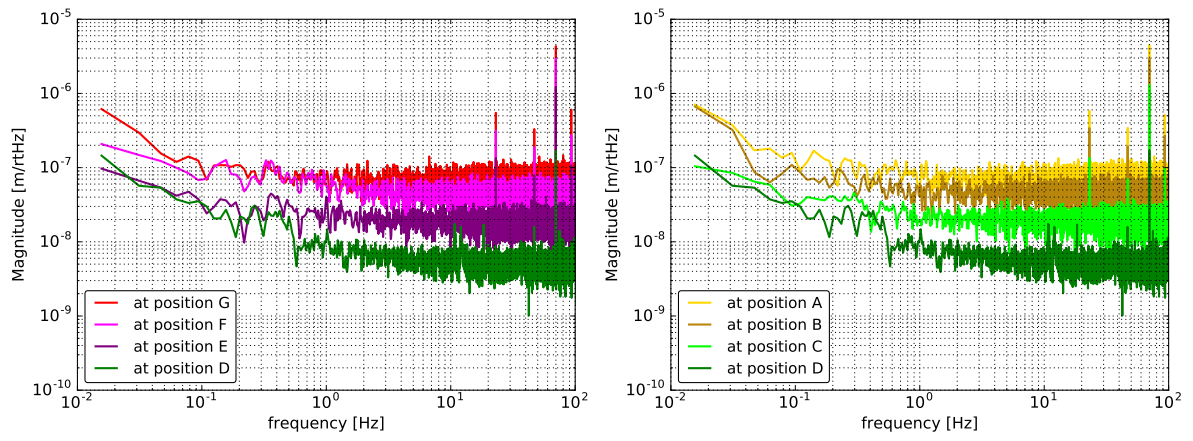
Figure B.9: LVDT sensor noise floors measured at the points shown in Figure B.8.

B.4 Details of maintenance and repairing

B.4.1 Maintenance and repairing

The details about the suspension maintenance and the repairing work are summarized in this section. During the initial interferometer alignment period, several problems are reported around the suspension system. Some of the examples, which are reported oftenly, are listed in the following. More details are found in [84].

LVDT circuit replacement

Sometimes the electrical circuits which drives the LVDT (for its sensor part) become broken and the circuits have to be replaced to new one. Since the calibration of the LVDT sensors are depended on the circuit, we have to re-calibrate the LVDTs every time when the circuits become broken.

re-cabling

Soldering point of some cables, which has been already laid inside the vacuum chambers in complicated way, are sometimes disconnected and they have to replaced to new ones.

OSEM body positioning

For the OSEM shadow sensors, it was required to finely adjust the relative position between the OSEM body and the flag so that they were at the center of its linear range (about 1 mm). This position adjustment is done in outside the vacuum chamber, however, we have to work on this even after installing the suspension inside the chamber due to the mirror slip as described below. An example of the unsuitable/suitable case is shown in Figure B.10.

Mirror slip compensation

Sometimes the mirrors, especially for the PR mirrors which are suspended by the Type-Bp SAS, has been slipped when the mirrors are kicked by a large external disturbance. The mirror orientation is recovered by tilting the upper stage, i.e, IM. After finely adjust the orientation, we work on the OSEM positioning. Basically we have to iterate this IM tilt tuning and the OSEM positioning.

For mechanical rubbing of GAS-keystone

It is found that the GAS keystone, more concretely the primary coil holder, is rubbing to the other coil holder. The tilt of the secondary coil holder have to be finely adjusted.

(unsuitable case)   **(suitable case)**
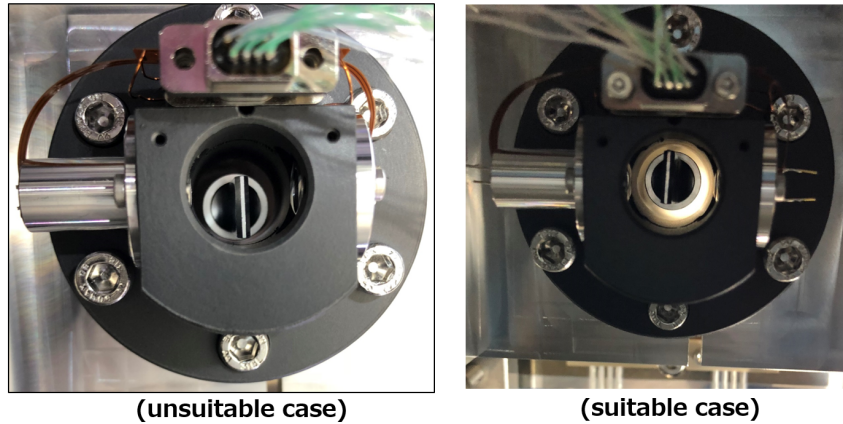
Figure B.10: Example of OSEM positioning at IM-stgae of the Type-Bp SAS. The *left* and *right* figures show unsuitable and suitable cases respectively.

Magnet re-gluing for TM of Type-Bp SAS

In PR2 and PRM suspension, it is reported that some of the magnets (flag-shaped) are come off form the mirror surface and the we are not able to actuate the TM. We then re-glue the detached magnets to the suspended mirror.

B.4.2   Contribution to integration

I have worked on the followings for the KAGRA SAS integration/maintenance for the mechanical part in the mine:

- PR2: in-vacuum cable repairing, LVDT circuit replacement, magnet re-gluing for TM, IM-OSEM positioning, rubbing-debugging at BF-GAS

- PR3: upgrading the air-shield for the optical lever (see Figure 5.31), IM-OSEM positioning

- PRM: LVDT circuit replacement, magnet re-gluing for TM, IM-OSEM positioning

- SR2: Geophone pod assembly[2] and calibration/noise estimation

- SR3: Geophone pod assembly and calibration/noise estimation, GAS blade compression tuning, rubbing-debugging at TM-stage

- SRM: Geophone pod assembly and calibration/noise estimation, TM assembly

- BS: rubbing-debugging at TM-stage

---

[2]Since the Geophone L-4C is not vacuum compatible and it has to be installed inside a pod in order to use in pumped-down condition.

- ITMX: mechanical installation of the tower part, BF-LVDT calibration/ noise estimation, in-air cabling for the room-temperature part, accelerometer/LVDT noise estimation, payload-tower connection[3]

- ITMY: in-vacuum cable repairing, in-air cabling for the room-temperature part, payload-tower connection, accelerometer noise estimation

- ETMX: in-air cabling for the room-temperature part

- ETMY: Geophone pod assembly and calibration/noise estimation, in-air cabling for the room-temperature part.

In addition to the above, I have also measure the Q factors of PR3 mechanical resonances for its characterization. Concerning the IM-OSEM positioning, its rubbing part localization and for the debugging is done by myself alone in the most of part, especially for the Type-Bp SASs.

Indeed these works were the main tasks in the time period from 2018 March to 2019 July, oftenly I have stayed inside the small vacuum chambers.

Thanks to this, however, I've gained a good knowledge about the mechanics of KAGRA SAS. I have also realized how crucial it is to design the mechanical systems in order to make easier the repairing and maintenance of such a complex system.

---

[3]The cryogenic payload of the Type-A SAS is mechanically connected to the already installed upper (tower) part.

B.5 Measured decay time constant table

The measured resonant frequencies and the decay time constants are listed in Figure B.11 and B.12. The yellow colored modes are the ones which we pay less attention, while the red colored one is the mode which is not found in this work. The mode numbers correspond to ones in section B.1. Standard deviations are removed from the below figures however, they are included in Figure 7.3.2.

mode number	fitted frequemcy[Hz]	decay time [s]	excittion point
#1	0.04	233.6	BFY
#2	0.07	193.2	BFY
#3	0.08	83.9	IPT
#4	0.08	100.9	IPL
#5	0.09	116.0	BFY
#6	0.09	174.1	BFY
#7	0.12	191.8	MNoplevY
#8			
#9			
#10	0.19	48.1	F0GAS
#11	0.42	49.1	IPY
#12	0.21	233.1	IPT
#13	0.21	111.5	IPL
#14			
#15	0.32	726.6	IMY
#16			
#17			
#18	0.47	14.7	F0GAS
#19			
#20			
#21	0.45	152.0	IPT
#22	0.45	169.3	IPL
#23	0.63	671.4	MNR
#24	0.63	982.3	MNR
#25			
#26			
#27	0.76	8.9	F3GAS
#28	0.75	316.9	IPT
#29	0.79	73.3	MNP
#30	0.79	177.2	MNR
#31	0.75	157.7	MNR
#32	0.72	268.8	IPT
#33	0.73	328.7	IPL
#34	0.94	9.5	F1GAS
#35	0.97	167.6	IPT
#36	0.98	42.6	IPL

mode number	fitted frequemcy[Hz]	decay time [s]	excittion point
#37	1.03	51.4	IPT
#38	1.04	24.7	IPL
#39	1.15	811.7	MNY
#40	1.31	8.0	F1GAS
#41	1.34	2.9	IPT
#42	1.31	26.3	IPL
#43	1.48	288.2	MNR
#44	1.52	488.6	MNP
#45	1.71	365.9	MNP
#46	1.67	615.8	MNP
#47	1.68	2201.1	MNY
#48	2.16	192.2	MNT
#49	2.16	176.6	MNL
#50	2.12	555.2	MNY
#51	2.49	845.5	MNT
#52	2.49	1241.0	MNL
#53	3.20	2552.2	MNY
#54			
#55	4.14	44.6	MNY
#56	5.20	42.2	MNT
#57	5.09	61.3	MNL
#58	7.52	172.9	MNP
#59	9.70	86.9	BFGAS
#60	15.05	38.6	MNR
#61	19.39	49.6	BFGAS
#62	22.89	1.1	MNR
#63	23.49	134.9	MNR
#64			
#65			
#66			
#67			
#68			
#69			
#70			
#71			
#72			
#73			
#74			
#75			
NOT_IDed	0.14	329.6	MNoplevY

Figure B.11: Measured decay time constants without controls.

mode number	fitted frequemcy[Hz]	decay time [s]	excittion point
#1	0.05	47.1	BFY
#2	0.08	36.6	BFY
#3	0.15	18.8	IPT
#4	0.15	10.6	IPL
#5	0.08	42.9	BFY
#6	0.09	37.9	BFY
#7	0.13	7.2	BFY
#8			
#9			
#10	0.18	4.2	F0GAS
#11	0.48	1.4	IPY
#12	0.25	2.0	IPT
#13	0.22	2.6	IPL
#14			
#15	0.23	1.3	MNY
#16			
#17			
#18	0.50	2.9	F0GAS
#19			
#20			
#21	0.46	4.2	IPT
#22	0.45	4.9	IPL
#23	0.61	10.2	MNR
#24	0.64	20.1	MNP
#25			
#26			
#27	0.82	5.1	F3GAS
#28	0.71	17.2	MNR
#29	0.71	3.2	MNP
#30	0.81	12.4	MNR
#31	0.79	6.5	MNP
#32	0.70	9.2	IPT
#33	0.72	3.7	IPL
#34	0.89	1.5	F1GAS
#35	0.95	2.9	IPT
#36	0.97	26.2	IPL

mode number	fitted frequemcy[Hz]	decay time [s]	excittion point
#37	1.03	10.8	IPT
#38	1.01	6.7	IPL
#39	1.16	17.7	MNY
#40	1.29	3.1	F1GAS
#41	1.36	25.7	IPT
#42	1.36	13.5	MNP
#43	1.48	197.4	MNT
#44	1.52	26.3	MNL
#45	1.73	0.5	MNR
#46	1.60	3.6	MNP
#47	1.70	1.7	MNY
#48	2.08	2.3	MNR
#49	2.00	3.0	MNP
#50	2.13	0.6	MNY
#51	2.49	58.6	MNT
#52	2.49	25.6	MNL
#53	3.19	13.3	MNY
#54			
#55	4.19	5.6	MNY
#56	5.20	12.6	MNT
#57	5.09	25.1	MNL
#58	7.53	19.7	MNP
#59	9.68	9.5	BFGAS
#60	14.97	0.5	MNR
#61	19.85	0.6	MNR
#62	20.17	0.5	MNR
#63	23.48	21.8	MNR
#64			
#65			
#66			
#67			
#68			
#69			
#70			
#71			
#72			
#73			
#74			
#75			
#NOT_IDed	0.13	168	BFY

Figure B.12: Measured decay time constants with controls.

Bibliography

[1] Cody Messick et al. Analysis framework for the prompt discovery of compact binary mergers in gravitational-wave data. *Phys. Rev. D*, 95:042001, Feb 2017.

[2] Alexander H. Nitz, Tito Dal Canton, Derek Davis, and Steven Reyes. Py-CBC Live: Rapid Detection of Gravitational Waves from Compact Binary Mergers. 2018.

[3] T. Adams et al. Low-latency analysis pipeline for compact binary coalescences in the advanced gravitational wave detector era. *Class. Quant. Grav.*, 33(17):175012, 2016.

[4] L. P. Singer and L. R. Price. Rapid bayesian position reconstruction for gravitational-wave transients. *Phys. Rev. D*, 93:024013, Jan 2016.

[5] A. Einstein. Die grundlage der allgemeinen relativitätstheorie. *Annalen der Physik*, 354(7):769–822, 1916.

[6] B. P. Abbott et al. Observation of gravitational waves from a binary black hole merger. *Phys. Rev. Lett.*, 116:061102, Feb 2016.

[7] B. P. Abbott, R. Abbott, T. D. Abbott, F. Acernese, K. Ackley, C. Adams, T. Adams, P. Addesso, R. X. Adhikari, V. B. Adya, and et al. Multi-messenger observations of a binary neutron star merger. *The Astrophysical Journal Letters*, 848:L12, October 2017.

[8] Michele Maggiore. *Gravitational Waves: Volume 1: Theory and Experiments.* Oxford University Press, 2007.

[9] CURT CUTLER and KIP S. THORNE. *AN OVERVIEW OF GRAVITATIONAL-WAVE SOURCES*, pages 72–111.

[10] B. P. Abbott et. al. Multi-messenger observations of a binary neutron star merger. *The Astrophysical Journal*, 848(2):L12, oct 2017.

[11] GraceDB. https://gracedb.ligo.org. (Cited April 2019).

[12] Hiroki Takeda et al. Prospects for gravitational-wave polarization tests from compact binary mergers with future ground-based detectors. *Phys. Rev. D*, 100:042001, Aug 2019.

[13] B. P. Abbott et al. A gravitational-wave standard siren measurement of the Hubble constant. *Nature*, 551(7678):85–88, 2017.

[14] Adam G. Riess, Lucas M. Macri, Samantha L. Hoffmann, Dan Scolnic, Stefano Casertano, Alexei V. Filippenko, Brad E. Tucker, Mark J. Reid, David O. Jones, Jeffrey M. Silverman, Ryan Chornock, Peter Challis, Wenlong Yuan, Peter J. Brown, and Ryan J. Foley. A 2.4% DETERMINATION OF THE LOCAL VALUE OF THE HUBBLE CONSTANT. *The Astrophysical Journal*, 826(1):56, jul 2016.

[15] Planck Collaboration and P. A. R. Ade et. al. Planck 2015 results. xiii. cosmological parameters. *A&A*, 594:A13, Sep 2016.

[16] B. D. Metzger and E. Berger. WHAT IS THE MOST PROMISING ELECTROMAGNETIC COUNTERPART OF a NEUTRON STAR BINARY MERGER? *The Astrophysical Journal*, 746(1):48, jan 2012.

[17] C Markakis, J S Read, M Shibata, K Uryū, J D E Creighton, J L Friedman, and B D Lackey. Neutron star equation of state via gravitational wave observations. *Journal of Physics: Conference Series*, 189:012024, oct 2009.

[18] Eemeli Annala, Tyler Gorda, Aleksi Kurkela, and Aleksi Vuorinen. Gravitational-wave constraints on the neutron-star-matter equation of state. *Phys. Rev. Lett.*, 120:172703, Apr 2018.

[19] Christian D Ott. The gravitational-wave signature of core-collapse supernovae. *Classical and Quantum Gravity*, 26(6):063001, feb 2009.

[20] Takami Kuroda, Kei Kotake, and Tomoya Takiwaki. A NEW GRAVITATIONAL-WAVE SIGNATURE FROM STANDING ACCRETION SHOCK INSTABILITY IN SUPERNOVAE. *The Astrophysical Journal*, 829(1):L14, sep 2016.

[21] Thibault Damour and Alexander Vilenkin. Gravitational radiation from cosmic (super)strings: Bursts, stochastic background, and observational windows. *Phys. Rev. D*, 71:063510, Mar 2005.

[22] K. Kawabe. PhD Thesis, University of Tokyo. 1998.

[23] Akito Araya, Akiteru Takamori, Wataru Morii, Kouseki Miyo, Masatake Ohashi, Kazuhiro Hayama, Takashi Uchiyama, Shinji Miyoki, and Yoshio Saito. Design and operation of a 1500-m laser strainmeter installed at an underground site in kamioka, japan. *Earth, Planets and Space*, 69(1):77, 2017.

[24] William J. Startin, Mark A. Beilby, and Peter R. Saulson. Mechanical quality factors of fused silica resonators. *Review of Scientific Instruments*, 69(10):3681–3689, 1998.

[25] S. Rowan, G. Cagnoli, P. Sneddon, J. Hough, R. Route, E.K. Gustafson, M.M. Fejer, and V. Mitrofanov. Investigation of mechanical loss factors of some candidate materials for the test masses of gravitational wave detectors. *Physics Letters A*, 265(1):5 – 11, 2000.

[26] T Tomaru, T Suzuki, T Uchiyama, A Yamamoto, T Shintomi, C.T Taylor, K Yamamoto, S Miyoki, M Ohashi, and K Kuroda. Maximum heat transfer along a sapphire suspension fiber for a cryogenic interferometric gravitational wave detector. *Physics Letters A*, 301(3):215 – 219, 2002.

[27] M. G. Beker. PhD Thesis, Vrije Universiteit. 2013.

[28] Eric D. Black. An introduction to pound–drever–hall laser frequency stabilization. *American Journal of Physics*, 69(1):79–87, 2001.

[29] Adam J. Mullavey, Bram J. J. Slagmolen, John Miller, Matthew Evans, Peter Fritschel, Daniel Sigg, Sam J. Waldman, Daniel A. Shaddock, and David E. McClelland. Arm-length stabilisation for interferometric gravitational-wave detectors using frequency-doubled auxiliary lasers. *Opt. Express*, 20(1):81–89, Jan 2012.

[30] Xavier Siemens, Bruce Allen, Jolien Creighton, Martin Hewitson, and Michael Landry. Making h(t) for LIGO. *Classical and Quantum Gravity*, 21(20):S1723–S1735, sep 2004.

[31] B. P. Abbott and et. al. Calibration of the advanced ligo detectors for the discovery of the binary black-hole merger gw150914. *Phys. Rev. D*, 95:062003, Mar 2017.

[32] Y. Aso et al. Interferometer design of the kagra gravitational wave detector. *Phys. Rev. D*, 88:043007, Aug 2013.

[33] K. Komori et. al. JGW-T1707038. (Cited March 2020).

[34] K. Somiya. Detector configuration of kagra–the japanese cryogenic gravitational-wave detector. *Classical and Quantum Gravity*, 29(12):124007, 2012.

[35] Y Aso, K Somiya, and O Miyakawa. Length sensing and control strategies for the LCGT interferometer. *Classical and Quantum Gravity*, 29(12):124008, jun 2012.

[36] Jon R. Peterson. Observations and modeling of seismic background noise. Technical report, 1993. Report.

[37] Seismic noise at KAGRA. https://gwdoc.icrr.u-tokyo.ac.jp/cgi-bin/private/DocDB/ShowDocument?docid=10436. (Cited January 2020).

[38] Trillium120QA user's guide. https://gwdoc.icrr.u-tokyo.ac.jp/cgi-bin/private/DocDB/ShowDocument?docid=7554. (Cited December 2019).

[39] Peter M. Shearer. *Introduction to Seismology.* Cambridge University Press, 2 edition, 2009.

[40] M. G. Beker, G. Cella, R. DeSalvo, M. Doets, H. Grote, J. Harms, E. Hennes, V. Mandic, D. S. Rabeling, J. F. J. van den Brand, and C. M. van Leeuwen. Improving the sensitivity of future gw observatories in the 1–10 hz band: Newtonian and seismic noise. *General Relativity and Gravitation*, 43(2):623–656, Feb 2011.

[41] K. Okutomi. PhD Thesis, SOKENDAI. 2019.

[42] B. P. Abbott et al. Prospects for observing and localizing gravitational-wave transients with advanced ligo and advanced virgo. *Living Reviews in Relativity*, 19(1):1, Feb 2016.

[43] L. P. Singer et al. The first two years of electromagnetic follow-up with advanced ligo and virgo. *The Astrophysical Journal*, 795(2):105, 2014.

[44] T. Sekiguchi. PhD Thesis, University of Tokyo. 2016.

[45] Y. Fujii. Master's Thesis, University of Tokyo. 2017.

[46] Y Akiyama et. al. Vibration isolation system with a compact damping system for power recycling mirrors of KAGRA. *Classical and Quantum Gravity*, 36(9):095015, apr 2019.

[47] Bruce Allen, Warren G. Anderson, Patrick R. Brady, Duncan A. Brown, and Jolien D. E. Creighton. Findchirp: An algorithm for detection of gravitational waves from inspiraling compact binaries. *Phys. Rev. D*, 85:122006, Jun 2012.

[48] Rana X. Adhikari. Gravitational radiation detection with laser interferometry. *Rev. Mod. Phys.*, 86:121–151, Feb 2014.

[49] Stephen Fairhurst. Triangulation of gravitational wave sources with a network of detectors. *New Journal of Physics*, 11(12):123006, dec 2009.

[50] L. P. Singer. GW170817 localization and triangulation annuli. 2017.

[51] A. H. Nitz et al. PyCBC Software, http://github.com/ligo-cbc/pycbc. (Cited April 2020).

[52] Samantha A Usman, Alexander H Nitz, Ian W Harry, Christopher M Biwer, Duncan A Brown, Miriam Cabero, Collin D Capano, Tito Dal Canton, Thomas Dent, Stephen Fairhurst, Marcel S Kehl, Drew Keppel, Badri Krishnan, Amber Lenon, Andrew Lundgren, Alex B Nielsen, Larne P Pekowsky, Harald P Pfeiffer, Peter R Saulson, Matthew West, and Joshua L Willis. The PyCBC search for gravitational waves from compact binary coalescence. *Classical and Quantum Gravity*, 33(21):215004, oct 2016.

[53] B. P. Abbott et al. Gwtc-1: A gravitational-wave transient catalog of compact binary mergers observed by ligo and virgo during the first and second observing runs. *Phys. Rev. X*, 9:031040, Sep 2019.

[54] Surabhi Sachdev et al. The GstLAL Search Analysis Methods for Compact Binary Mergers in Advanced LIGO's Second and Advanced Virgo's First Observing Runs. 1 2019.

[55] S Klimenko, I Yakushin, A Mercer, and G Mitselmakher. A coherent method for detection of gravitational wave bursts. *Classical and Quantum Gravity*, 25(11):114029, may 2008.

[56] J. Veitch et al. Parameter estimation for compact binaries with ground-based gravitational-wave observations using the lalinference software library. *Phys. Rev. D*, 91:042003, Feb 2015.

[57] Neil J Cornish and Tyson B Littenberg. Bayeswave: Bayesian inference for gravitational wave bursts and instrument glitches. *Classical and Quantum Gravity*, 32(13):135012, jun 2015.

[58] Summary page. https://summary.ligo.org/ detchar/summary/O3a/. (Cited January 2020).

[59] Masaomi Tanaka and Kenta Hotokezaka. RADIATIVE TRANSFER SIMULATIONS OF NEUTRON STAR MERGER EJECTA. *The Astrophysical Journal*, 775(2):113, sep 2013.

[60] Shaon Ghosh and Gijs Nelemans. Localizing gravitational wave sources with optical telescopes and combining electromagnetic and gravitational wave data. In Carlos F. Sopuerta, editor, *Gravitational Wave Astrophysics*, pages 51–58, Cham, 2015. Springer International Publishing.

[61] Yoshinori Fujii, Thomas Adams, Frédérique Marion, and Raffaele Flaminio. Fast localization of coalescing binaries with a heterogeneous network of advanced gravitational wave detectors. *Astroparticle Physics*, 113:1 – 5, 2019.

[62] B. P. Abbott et al. Implementation and testing of the first prompt search for gravitational wave transients with electromagnetic counterparts. *Astron. Astrophys.*, 539:A124, 2012.

[63] The LIGO Scientific Collaboration, the Virgo Collaboration, the KA-GRA Collaboration, and B. P. Abbott et. al. Prospects for observing and localizing gravitational-wave transients with advanced ligo, advanced virgo and kagra, 2013.

[64] Henry A. Sodano, Jae-Sung Bae, Daniel J. Inman, and W. Keith Belvin. Improved Concept and Model of Eddy Current Damper. *Journal of Vibration and Acoustics*, 128(3):294–302, 11 2005.

[65] A. Takamori. PhD Thesis, University of Tokyo. 2002.

[66] G. Cella, V. Sannibale, R. DeSalvo, S. Márka, and A. Takamori. Monolithic geometric anti-spring blades. *Nuclear Instruments and Methods in Physics Research Section A: Accelerators, Spectrometers, Detectors and Associated Equipment*, 540(2):502 – 519, 2005.

[67] Alberto Stochino, Riccardo DeSalvo, Yumei Huang, and Virginio Sannibale. Improvement of the seismic noise attenuation performance of the monolithic geometric anti-spring filters for gravitational wave interferometric detectors. *Nuclear Instruments and Methods in Physics Research Section A: Accelerators, Spectrometers, Detectors and Associated Equipment*, 580(3):1559 – 1564, 2007.

[68] L. Trozzo. PhD Thesis, Universitá di Siena. 2018.

[69] F Matichard et al. Seismic isolation of advanced LIGO: Review of strategy, instrumentation and performance. *Classical and Quantum Gravity*, 32(18):185003, aug 2015.

[70] Y. Sakakibara. PhD Thesis, University of Tokyo. 2015.

[71] T. Yamada. Master's Thesis, University of Tokyo. 2018.

[72] T. Ochi. Master's Thesis, University of Tokyo. 2018.

[73] F. Cordero, F. Corvasce, R. Franco, G. Paparo, E. Maiorana, P. Rapagnani, F. Ricci, S. Braccini, C. Casciano, R. De Salvo, F. Frasconi, R. Passaquieti, M. De Sanctis, A. Solina, and R. Valentini. Elastic and anelastic properties of marval 18 steel. *Journal of Alloys and Compounds*, 310(1):400 – 404, 2000. Intern. Conf. Internal Friction and Ultrasonic Attentuation in Solids (ICIFUAS-12).

[74] Hareem Tariq et al. The linear variable differential transformer (lvdt) position sensor for gravitational wave interferometer low-frequency controls. *Nuclear Instruments and Methods in Physics Research Section A: Accelerators, Spectrometers, Detectors and Associated Equipment*, 489(1):570 – 576, 2002.

[75] Virgo Internal Document. Advanced Virgo Technical Design Report, VIR-0128A-12. 2012.

[76] Riccardo Desalvo. Review: Accelerometer development for use in gravitational wave-detection interferometers. *Bulletin of the Seismological Society of America*, 99, 05 2009.

[77] R. Sleeman. Three-Channel Correlation Analysis: A New Technique to Measure Instrumental Noise of Digitizers and Seismic Sensors. *The Bulletin of the Seismological Society of America*, 96(1):258–271, Feb 2006.

[78] S. Aston. LIGO Internal Document, T050111-04-K. 2009.

[79] S. Zeidler. KAGRA Internal Document, JGW-T1605788. 2016.

[80] M. Fukunaga. Master's Thesis, University of Tokyo. 2019.

[81] Yuta Michimura et al. Mirror actuation design for the interferometer control of the KAGRA gravitational wave telescope. *Classical and Quantum Gravity*, 34(22):225001, oct 2017.

[82] A. Shoda et al. KAGRA Internal Document, JGW-T1604756. 2016.

[83] M. A. Barton et al. KAGRA Internal Document, JGW-E1504235. 2017.

[84] KAGRA Logbook. http://klog.icrr.u-tokyo.ac.jp/osl/?c=1. (Cited February 2020).

[85] K. Izumi. Master's Thesis, University of Tokyo. 2009.

[86] Y. Michimura Y. Enomoto and K. Izumi. KAGRA Internal Document, JGW-T1808343. 2018.

[87] Y. Michimura. KAGRA Internal Document, JGW-T1202403. 2014.

[88] 3D rigid body suspension modeling tool. https://gwdoc.icrr.u-tokyo.ac.jp/cgi-bin/private/DocDB/ShowDocument?docid=3729. (Cited January 2020).

[89] KAGRA wiki page for ETMX. http://gwwiki.icrr.u-tokyo.ac.jp/JGWwiki/KAGRA/Subgroups/VIS/TypeA/ETMX. (Cited January 2020).

[90] D. Martynov. PhD Thesis, California Institute of Technology. 2015.

[91] J. Abadie et al. Sensitivity Achieved by the LIGO and Virgo Gravitational Wave Detectors during LIGO's Sixth and Virgo's Second and Third Science Runs. 2012.

[92] M. Barsanti, M. Beghini, F. Frasconi, R. Ishak, B.D. Monelli, and R. Valentini. Experimental study of hydrogen embrittlement in maraging steels. *Procedia Structural Integrity*, 8:501 – 508, 2018. AIAS2017 - 46th Conference on Stress Analysis and Mechanical Engineering Design, 6-9 September 2017, Pisa, Italy.